Multi–Wavelength Investigations on Galactic Star Forming Regions

Lokesh Kumar Dewangan

Multi-Wavelength Investigations on Galactic Star Forming Regions

A Thesis Submitted to

Gujarat University

for the Degree of

Doctor of Philosophy

in

Physics

by

Lokesh Kumar Dewangan

Astronomy and Astrophysics Division

Physical Research Laboratory

Ahmedabad-380 009, India

Year of Submission : July 2010

To

Ma, Babuji,

Devendra, Dhanendra,

Reena & little Reyans

CERTIFICATE

I hereby declare that the work presented in this thesis is original and carried out by me at Physical Research Laboratory, Ahmedabad. It has not formed the basis for the award of any degree or diploma by any University or Institution.

Signature of the Candidate
Lokesh Kumar Dewangan
Date:

Certified by,

Signature of the Thesis Supervisor
Prof. B. G. Anandarao
Astronomy and Astrophysics Division
Physical Research Laboratory
Navarangpura
Ahmedabad 380009
INDIA
Date:

Acknowledgements

Nothing is particularly hard if you divide it into small jobs.
Henry Ford

It is great pleasure and honour to thank my thesis supervisor Prof. B. G. Anandarao for inspiring me towards the most wonderful and exciting field of Astronomy and for providing his valuable guidance and advice throughtout my PhD tenure. I thank him for his constant encouragement, support and affection which helped me overcome many difficulties during my research career. I have learnt a lot from his experience, systematic way of working and approach towards problem at hand. I express my sincere gratitude to him for his great deal of independence and all his efforts in establishing collaborations with international institutes which has given me sufficient exposure to stand in the global scientific arena.

I would like to express my sincere gratitude to Dr. M. S. N. Kumar (Nanda) for his help, suggestions and criticism about my work and personal life. He has made efforts in arranging my visit to Centro de Astrofísica da Universidade do Porto (CAUP), Portugal and allowed to stay at his home and provided very friendly and enjoyable environment. I also thank Prof. Mário J. P. F. G. Monteiro, Director, CAUP for providing me partial funds to visit CAUP, Porto.

I am thankful to my co-guide Dr. Santosh Vadawale for his interaction and discussions related to my work. I pay my sincere gratitude to Dr. P. Janardhan and Dr. A. K. Singal for their fruitful suggestions and discussions. I have always enjoyed their company and they are always friendly, helpful & always open for discussion, not only on science, but also on practicalities of life. I thank Dr. P. Janardhan for carefully going through my thesis and giving useful inputs to further improve it.

Physical Research Laboratory has provided me with excellent facilities, for which I am thankful and also to the Dept. of Space, Govt. of India for funding my research. I would like to thank Prof. J. N. Goswami, Director, PRL for providing necessary funds to visit CAUP, Porto. I am also thankful to the Academic Committee members of PRL (former and present) for their suggestions regarding my thesis work.

I would like to express my sincere gratitude to the team members involved in 2MASS, SPITZER/GLIMPSE, MSX, IRAS, SCUBA, HST projects for archival data, which was used in making this thesis. Also, I would like to thank Dr. H. Beuther for providing me observed outflow CO images of HMPOs. I thank Jorge Grave (CAUP, Porto) for his help in IDL. In addition, I am thankful to all the members involved in IRAF, NASA's IDL Astronomical Library, MOPEX softwares, SED modeling tool and SIMBAD Database.

I pay my gratitude to the Area Chairmen of the Astronomy & Astrophysics Division (AAD), Prof. N. M. Ashok (former) and Prof. T. C. Chandrashekhar (present) for their support throughout my PhD tenure. I would like to thank the faculties of AAD: Prof. U. C. Joshi, Prof. D. P. K. Banerjee, Dr. K. S. Baliyan, Dr. Hari Om Vats and Dr. Abhijit Chakraborty for their concern about my research work. I would like to acknowledge the help and support of all the staff members of Mt. Abu observatory, Mr. Rajesh Shah, Mathurbhai, Rajpurohitji, Jainbhai, P. S. Patwalbhai, Naransinghji, Padamsinghji and Kothariji during my observational trip to Mt. Abu Observatory.

I am heartily thankful to my School/College teachers specially, Shree Bhushan Dewangan, Shree K. L. Tulkar, Shree K. D. Manikpuri, Prof. T. K. Sengupta, Prof. R. C. Agrawal, Prof. D. K. Chakarvorty and Prof. S. Bhushan for their encouragement and words of motivation.

Prof. S. K. Pandey was the first teacher, who introduced me to the excitement of astronomy and astrophysics. I owe my deepest gratitude to him for his great help, support, encouragement and guidance since the days of my M.Sc. till date.

I am greatful to Prof. R. Ramesh and Dr. J. S. Ray for their interaction, discussion and encouragement during my initial days at PRL. I have some memorable moments, which I had spent with Dr. J. S. Ray and Mr. A. D. Shukla during my project associateship at PRL. I convey my special thanks to Dr. J. S. Ray and Mr. A. D. Shukla for their help, affection and always caring nature for me.

I am glad to acknowledge Mr. I. J. Thakker (Thaltej Library) for his affection, support and help for my work specially for books, research materials and prints whenever needed. Also, I would like to thank staff members of library particularly Mrs. Nishtha, Mrs. Uma Desai, Zubedaben and Ms. Pragaya for their help and support related to library issues.

I would like to convey thanks to all the staff members of computer centre, administration and medical for their help and support, particularly to Dholakiaji, Subhedarji, Jigarbhai, Hitendraji, Alokbhai, Girishbhai, Gangadhariaji, Rangnathanji, Parulben, Pritiben, Keyurbhai, Ms. Jayashree, Dr. Shital Patel and Dr. Sameer Dani.

I am thankful to all the staff members of AAD particularly Mr. N. S. Jog, Mr. Muraleedharan, Mrs. Meera, Pathanbhai and Mr. Madhavan for their help and support on various occasions.

A special thanks to Mr. V. Venkat for his friendship, scientific as well as personal help during my PhD. I always enjoy his company and also I would like to thank his wife Punitha and son Karunya for memorable interactions.

I am grateful to Dr. Shashikaran Ganesh for his help, especially on computer related issues. Also, I would like to thank Prof. D. B. Vaidya (Gujarat Arts and Science College, Ahmedabad) for his interaction and concern about my work.

It is my great pleasure to acknowledge Mr. S. L. Kayastha (Kaka), D. B. Pancholi, Thakkarbhai, Dr. Baliyan, Dr. Singal, Dr. Vats, Murlibhai, Vishal bhai, Amishbhai and Vadherbhai for cheerful company and friendly environment everyday during the bus journey from PRL main campus to Thaltej Campus. I would like to convey my special thanks to Kaka, Pancholibhai and Doshibhai for their personal affection and support and adding tangy flavor to my life during PhD tenure. They had always encouraged me for my research work.

I heartily thank to Subimal (Dada) and Rohan for their affection, suggestions and help whenever I needed regarding work or life. I am thankful to Dr. Nandita Shrivastva for her concern about my research work and sharing her time to join at dinner parties with me and Rohan during her visit to PRL, Ahmedabad. Also, I thank Dr. Shibu Mathew for his interaction and concern over my work. I thank Jayant for his friendship, cheerful company, suggestions, help and sharing his valuable experience with me.

I am very fortunate to have friends like Deepak Sahu, Amit Kashayp, Harish Dewangan, Suchi, Aadarsh, Umesh, Tarkeshavar, Abhishek, Subhash, Aanand, Bharat, Vinod, Basant, Santosh Dewangan, Roshan, Santosh Verma and Harish Sinha. I acknowledge their affection and concern for me and my work. Also, I acknowledge Hemu, Ram and Gopi for their respect and affection for me. In particular, I am greatful to Jitendra Soni (Baba) for his friendship, affection and help during my school and college days.

I can never forget the help, efforts and support of Ghanshyambhai and Shaileshbhai regarding my trip to Portugal. I am heartily thankful to them for their selfless help and support.

During my stay at Ahmedabad, I am fortunate to have friends like Shishir and Milap. I convey my special thanks to them for their love, friendship and cheerful company. Also, I thank Ruchira for her concern and delicious food. I thank Shishir and Milap's families for their affection.

I have gained new experiences and many good moments of my life during my stay of about five and half years at PRL hostel. I would like to thank Gyana for his help and care during my illness in 2005. In particular, I am greatful to Kallol, Bhavik, Dattatray Shinde, Bindu Manthena, Radhunandan Sharma, Satish Chandra, Jitendra Bhatt, Kripa Ram, Sumanta and Ram Ajor for their affection and support. I thank Lokesh Sahu, Arinbanda, Santoshbhai, Prashanta Shanyal, Narendra Sahu, Bhavesh, Murali (Balamurali), Ganguly, Jayesh, Madhav, Amit Misra, Morthekai, Shreyas, Sanat, Uma, Sasadhar, Rohit (senior), Santosh (theory), Ritesh, Akhilesh, Ramkrishna, Rajesh Kushawaha, Brajesh, Vishal, Waliur Rahman, Alok Saini, Harinder, Manan, Ashok, Navin Chauhan, Vimal, Soumya, Rohit (junior) and Bikkina Srinivas for their concern for me. I would like to thank Mr. Nambiarji, Shanmugam, Raja Bayanna, Deepak Panda, Deepak Dingra, Neeraj, Jayesh Pabari, T. A. Rajesh, R. P. Singh (SPA-SC), Dr. Dibyendu Chakrabarty (Dipuda), Dr. Ravi Bhushan (Ravida), Dr. M.G. Yadava, Dr. Som kumar Sharma, Jitubhai and Sandipbhai for their support and concern. I am thankful to Anish Parwage (CDAC) for his concern and cheerful company during my final year of PhD. Also, I thank Manjunatha (CDAC) for bearing my strong comments.

I am happy to acknowledge Ganeshbhai and Devilalbhai for their help and support on many occasions during my stay at PRL Hostel. Also, I am thankful to Madhaiji and his group members particular, Alok, Gautam, Vijay, Gopal and Deepak for providing and arranging food on time everyday.

It is also my pleasure to thank Mrs. Janaki Anandarao for her affection and delicious food on many occasions. Also, I thank Mrs. Janardhan for her help and interaction with me.

Finally, I would like to extend my heartfelt gratitude to all my family members for their love and blessings. My father has been a great source of inspiration for me; his words always make me feel confident, whenever I feel low. I miss my late grandfather for his love and blessings throughout my adulthood. I wish he could have seen my thesis. Also, I thank all my relatives for their love and care. I can never forget my parent's encouragement, support and sacrifices for my studies. I dedicate this thesis work to my father, mother, my two brothers Devendra, Dhanendra, Reena bhabhi and little Reyans.

Lokesh Kumar Dewangan

Contents

List of Figures

List of Tables

Chapter 1

Introduction

Mankind has always been fascinated by the celestial sources in the night sky such as stars seen in patterns called constellations, planets and comets. Due to their own light stars are not only one of the most conspicuous objects in the sky but also the building blocks of the Universe. Hence our curiosity to know about their birth and evolution. The study of star formation is one of the most interesting and fundamental topics in astrophysics.

In this chapter, we give an overview of star formation processes with a particular emphasis on massive stars. Towards the end of the chapter, the motivation and objectives of the present study are given along with an outline of the ensuing chapters of the thesis.

1.1 Star Formation: an overview

It is well known that stars form out of dust and gas from dense and cool regions of the molecular clouds throughout the Galaxy (Evans 1999). Star formation is generally believed to be the result of gravitational contraction and subsequent accretion of matter from the parent molecular cloud (Shu et al. 1987; Palla and Stahler 1993). The physical processes involved in star formation are mostly derived from the study of nearby star forming sites including Taurus-Auriga ($\sim$ 140 pc), Perseus ($\sim$ 315 pc) and Orion ($\sim$ 450 pc) molecular clouds. Star formation has been divided into two modes, viz. isolated and clustered modes based on the observational studies of many star forming regions situated at nearby and farther distances from us. Observational studies show that the low-mass stars (M $\lesssim$ 3 M$_\odot$) are known to form via both isolated and clustered modes of star formation (Ward-Thompson 2002), while massive stars (M $\gtrsim$ 8 M$_\odot$) form explicitly only in clustered mode together with low and intermediate mass (3 $<$ M $<$ 8 M$_\odot$) stars.

This section has been divided into four sub-sections dealing with birth sites of star formation, instability conditions for the collapse, low-mass star formation and massive star formation.

1.1.1 Nucleation sites for star formation

Observational studies in various wavelengths (such as optical, infrared, sub-mm/mm) show that the space between the stars in our Galaxy is not empty. The diffuse matter in the form of gas and dust which exists between stars is known as Interstellar Medium (ISM). Studies indicate that the ISM is present in three distinct phases: a cold phase in the form of molecular and atomic hydrogen gas co-existing with dust grains, a warm phase with partially ionised hydrogen gas, and a hot phase with shocked and fully ionised gas. These different phases and their physical properties are summarised in Table 1.1.

Most of the mass of the molecular ISM is in the form of giant molecular clouds (GMCs). Molecular clouds are observed by various molecular emission lines (in mm- and cm-wavelengths), which occur due to transitions in the rotational and vibrational levels. Hydrogen molecules (H_2) are the most abundant molecules in molecular clouds. However, direct detection of H_2 is very difficult as it is symmetric and homonuclear in nature and does not have a permanent electric-dipole moment, thereby forbidding the vibrational-rotational transitions. Shull and Beckwith (1982) have described in detail the molecular physics of the H_2 molecule in the interstellar medium. H_2 can be identified through its electric quadrupole forbidden transitions in vibrational-rotational modes in the near- and mid-infrared. The carbon-monoxide (CO) molecule is the next most abundant tracer after H_2 and its observations in dense clouds at infrared, sub-mm and millimeter suggest that the abundance ratio CO/H_2 is about 10^{-4} (about 30% of carbon in CO). CO column density is estimated using low- J ($1 \rightarrow 0$, $2 \rightarrow 1$) observations in emission. ^{12}CO molecules are optically thick (optical depth $\approx$ 100), therefore they trace only outer tenuous regions but not the inner denser regions. Denser regions of molecular clouds are traced by other molecules like NH_3, CS, rare isotopes of CO like $C^{18}O$ (see Table 1.2 for different tracers for different regions).

Table 1.1: Phases of ISM (adopted from Mathis (1990)).

Medium	Phase	H state	n (cm^{-3})	T (K)	Heating signature	Comments
Molecular clouds, cores	Cold	H_2	> 1000	10 - 50	Cosmic rays	Icy dust
H I clouds	Cold	H	30	100	Dust	Diffuse ISM
Warm H I	Warm	H	0.1	8000	Dust	Diffuse ISM
Warm H II	Warm	H^+	0.03	10^4	Photo-ionization	Faint
H II regions	Warm	H^+	> 100	10^4	Photo-ionization	Transient, expanding
Hot ISM	Hot	H^+	10^{-3}	$10^{6.5}$	SNe shocks	Low mass
SNRs	Hot	H^+	Variable	10^7	Shocks	Dynamic

1.1.2 GMCs and Gravitational Instability

GMCs are not homogeneous but have a complex structure and are clumpy in nature. GMCs can be fragmented into sub-structures by gravity and turbulent motions. Physical properties of the GMCs, clumps and cores are shown in Table 1.2.

Gravitational collapse of molecular clouds is a result of gravitational instability. Gravitational instability is defined by a condition in which self-gravity of a gaseous object overcomes the resisting forces due to thermal, magnetic, centrifugal and turbulent pressures leading to a collapse. Jeans (1902) derived a relation between the oscillation frequency ω and the wave number k for a small perturbation; assuming a non-magnetic, isothermal, infinite, homogeneous and self-gravitating medium without turbulent motions. The dispersion

Table 1.2: Physical properties of clouds, clumps and cores (from Smith (2004)).

Physical parameters	GMCs	Clumps/ Globules	Cores
Mass (in $M_\odot$)	$10^4 - 10^6$	10^2	$1 - 10$
Size (in pc)	$20 - 100$	$0.2 - 4$	$0.1 - 0.4$
Density (in cm^{-3})	$100 - 300$	$10^3 - 10^4$	$10^4 - 10^5$
Temperature (in K)	$15 - 40$	$7 - 15$	10
Magnetic Field (in μG)	$1 - 10$	$3 - 30$	$10 - 50$
Line width (km s^{-1})	$6 - 15$	$0.5 - 4$	$0.2 - 0.4$
Molecular tracers	^{12}CO, ^{13}CO	^{12}CO, ^{13}CO	NH_3, CS

relation is given below with the assumption of non-vanishing wave number

$$\omega^2 = k^2 v_s^2 - 4\pi G\varrho_0 \tag{1.1}$$

or

$$\omega^2 = v_s^2 \left(k^2 - \frac{4\pi G\varrho_0}{v_s^2}\right)$$

or

$$\omega^2 = v_s^2 \left(k^2 - k_0^2\right)$$

where $k_0^2 = 4\pi G\varrho_0/v_s^2$, G is the gravitational constant, $v_s(= \sqrt{kT/\mu m_H})$ is the isothermal sound speed, ϱ_0 the initial mass density, m_H the mass of the hydrogen atom, T is the temperature and μ the mean molecular weight (= 2.4 for a fully molecular cloud with 25 $\%$ He mass fraction).

Eq. 1.1 gives the propagation of sound waves with effect of the perturbation by self-gravity. It is clear from Eq. 1.1 that the equilibrium is stable with respect to large k $(= 2\pi/\lambda)$. In such perturbations (with shorter wavelengths), the right-hand side of Eq. 1.1 is positive, i.e., ω is real. If $k^2 < k_0^2$ then ω is imaginary and perturbations grow exponentially with time, leading to unstable equilibrium. k_0 is known as the characteristic wave number and the corresponding characteristic wavelength, called Jeans length (λ_J) is defined by

$$\lambda_J \equiv \frac{2\pi}{k_0} \equiv \sqrt{\frac{\pi}{G\varrho_0}} v_s \tag{1.2}$$

Assuming the perturbation is spherical with diameter λ_J, one gets the minimum mass, called Jeans mass (M_J) as,

$$M_J \equiv \frac{4\pi}{3}\varrho_0\left(\frac{\lambda_J}{2}\right)^3 \equiv \frac{\pi}{6}\left(\frac{\pi}{G}\right)^{3/2}\varrho_0^{-1/2}\upsilon_s^3 \tag{1.3}$$

The conditions for gravitational instability, $\lambda > \lambda_J$ and $M > M_J$, are called the $Jeans$ $criteria$. Using Eq. 1.2 and 1.3 respectively, Jeans length and Jeans mass can be written as below:

Jeans length:

$$L_J(pc) = \frac{7.82}{\mu}\sqrt{\frac{T(K)}{n_H}} \tag{1.4}$$

Jeans mass:

$$M_J(M_\odot) = \frac{11.74}{\mu^2}\sqrt{\frac{T^3(K)}{n_H}} \tag{1.5}$$

When the force of gravitational self-attraction well exceeds the internal gas pressure, then free-fall time (i.e., time required for the collapse) of clumps and cores is given by

$$t_{ff}(yr) = \sqrt{\frac{3\pi}{32G\rho}} = \frac{3.4\times10^7}{\sqrt{n_H}} \tag{1.6}$$

where, ρ (= $m_H n_H$ μ) is the mass density (gms cm^{-3}) and n_H, the number density (cm^{-3}). Eq. 1.6 shows that the free-fall time is independent of radius and depends only on the density of the GMCs (i.e., homologous collapse). For the typical mean density ($\sim$ 10^{4} cm^{-3}) of a cloud core the free-fall time is about 3.4 $\times$ 10^5 years.

Table 1.3 illustrates the value of Jeans mass (M_J), length (L_J) and free-fall time scale (t_{ff}) for clumps and cores. These values are derived using Eqs. 1.4, 1.5 and 1.6 with their typical values of temperature and density from Table 1.2. Free-fall time for core is smaller than clump for gravitational collapse. The Jeans mass is calculated by Elmegreen (1999) and Larson (1998) taking turbulence and magnetic field.

Jeans mass with turbulence is given by,

$$M_J \propto v_{rms}^4 P^{-1/2} \tag{1.7}$$

where P is gas pressure.
Jeans mass including magnetic field is given as,

$$M_J \propto B^3 \rho^{-1} \tag{1.8}$$

where B is magnetic field strength.

Another important timescale for understanding the star formation is the Kelvin-Helmholtz

Table 1.3: Jeans mass, size and free-fall time for clumps and cores

Physical properties	n(cm^{-3})	T(K)	M$_J$(M$_\odot$)	L$_J$(pc)	t$_{ff}$(years)
Clumps	10^3	10	2.0	0.3	1.1×10^6
Cores	10^5	10	0.2	0.3	1.1×10^5

contraction timescale (t$_{KH}$). It tells us the time required to start nuclear reactions in the core and reach the zero-age main-sequence (ZAMS) phase. Gravitational potential energy is converted to heat when the cloud core continues to contract due to gravity. The Kelvin-Helmholtz timescale is the ratio of gravitational energy (GM_*^2/R_*) to the luminosity and given by

$$t_{KH} = \frac{GM_*^2}{R_* L_*} = 3 \times 10^7 \left(\frac{M_*}{1M_\odot}\right)^2 \left(\frac{R_*}{1R_\odot}\right)^{-1} \left(\frac{L_*}{1L_\odot}\right)^{-1} yr \tag{1.9}$$

where M$_*$ is the stellar mass, R$_*$ the stellar radius and L$_*$ the stellar luminosity. The t$_{KH}$ value for Sun (M$_*$ = 1 M$_\odot$) is 3×10^7 yr and for a O type star (M$_*$ = 50 M$_\odot$) it is of the order of 10^4 yr.

1.1.3 Low-mass star formation

The formation process of low-mass stars is reasonably well understood both observationally as well as theoretically. The star formation process starts with the formation or development of a dense prestellar core due to the gravitational contraction of dense regions of GMCs (André et al. 2000). As further gravitational contraction continues in such a dense prestellar core, a system thus emerges with a central protostar, surrounded by an infalling envelope and a protostellar disk. In the starting phase, the central source is completely obscured by the dense envelope that provides a source of material for the accretion on the central source. With time, the envelope is destroyed or loses mass as a result of infall onto the central source/disk and an outflow into the surrounding ISM. Finally, the central young star and prostellar disk emerge when the envelope is completely consumed through both outflow and accretion.

Observational evidences, like the existence of bipolar outflows (Wu et al. 2004) and accretion disks (Burrows et al. 1996; Simon et al. 2000) associated with low-mass stars (see Fig. 1.1), support the theoretical model about their formation (van Dishoeck et al. 1995; Hogerheijde 1999; McKee and Ostriker 2007; van Kempen et al. 2008; Evans et al. 2009). In case of low-mass stars, the Kelvin-Helmholtz timescale is larger than the free-fall timescale (i.e., $t_{KH} > t_{ff}$). This implies that the pre-main-sequence (PMS) evolutionary phases of low mass stars are sufficiently long making it possible to identify and observe these phases during the evolution of low mass stars (Shu et al. 1987).

The advent of modern technology, specially in infrared and sub-mm wavelength regions, brought about a revolution in the study of star formation in the earliest phases with good spatial resolution and high sensitivity. Such facilities provide an opportunity to study the earliest stages of star formation, which are always deeply embedded in their natal material and accessible only in longer wavelengths (i.e., infrared, sub-mm) due to lower extinction in these wavelengths.

Lada and Wilking (1984) and Lada (1987) classified the PMS stages of low mass stars into three evolutionary classes, Class I, II and III, based on the slopes (i.e., spectral index) of their Spectral Energy Distributions (SEDs) in the infrared region. Later André et al. (1993) included in the classification scheme, another very early phase of the evolution called Class 0. SEDs of young stellar objects (YSOs) consist of emission not only from photospheres but also from disks and envelopes around them; the latter contributing mainly at wavelengths longer than 2 μm.

The slope of a SED is defined by

$$\alpha_\lambda = \frac{dlog(\lambda F_\lambda)}{dlog(\lambda)} \tag{1.10}$$

for wavelengths longer than 2 μm. Schematic SEDs of different classes of low-mass stars are shown in Figure 1.2. A brief description of each of the four evolutionary stages is given below:

$Class0$ sources (young protostars) are deeply embedded, having positive α_λ with ratio $L_{submm}/L_{bol} > 5 \times 10^{-3}$, where L_{submm} is the luminosity measured at wavelengths longer than 350 μm and L_{bol} is the bolometric luminosity. They have a cold single-temperature blackbody SED peaking at sub-mm wavelength region with bolometric temperature (T_{bol}) $<$ 100 K and an age of $\sim 10^4$ yr. One of the main characteristics of such sources is the presence of powerful and collimated molecular CO outflows from the central source.

$ClassI$ sources (evolved protostars) have SEDs much broader than those for a single temperature in Class 0. They too have a positive α_λ, with $T_{bol} \sim$ 70 - 650 K and contain smaller envelope masses than Class 0 sources with an age of $\sim 10^5$ yr. Molecular outflows are also present in Class I sources but are less collimated than in Class 0.

$ClassII$ sources have negative α_λ with $T_{bol} \sim$ 650 - 2880 K and their SEDs peak around 2 μm. These sources are also known as Classical T-Tauri Stars (CTTS) with an age of $\sim$ 10^6 - 10^7 yr. In this stage, sources have thick accretion disks and CO outflows are mostly absent.

$ClassIII$ sources have negative α_λ with $T_{bol} >$ 2880 K and having SEDs for a single stellar blackbody (photosphere), peaking at optical or infrared wavelengths. These sources have no or very little evidences of IR-excess and may still have thin or anemic accretion disks. These are also known as Weak-Lined T-Tauri Stars (WTTS) with age of $\sim 10^6$ - 10^7 yr.

It is obvious that there is a significant improvement in the understanding of low-mass star formation and their different evolutionary stages. But, the model described above for the low mass stars does not entirely work for massive stars due to many reasons discussed in the next sub-section.

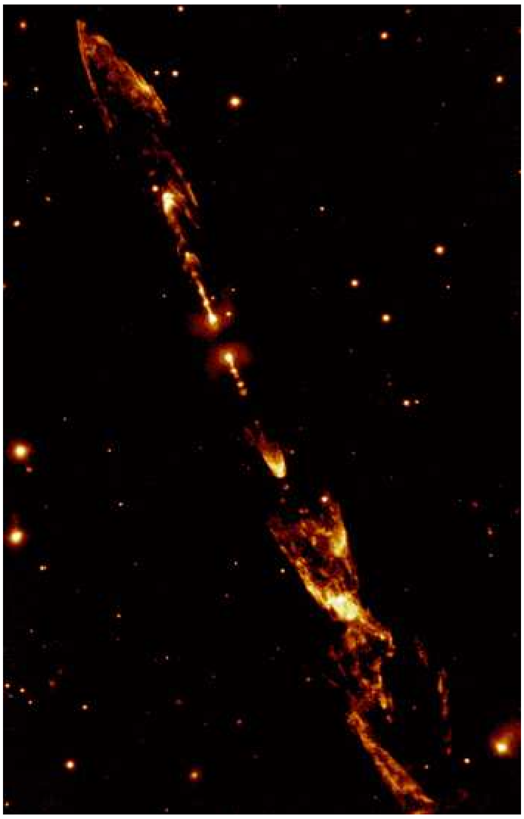

(a)

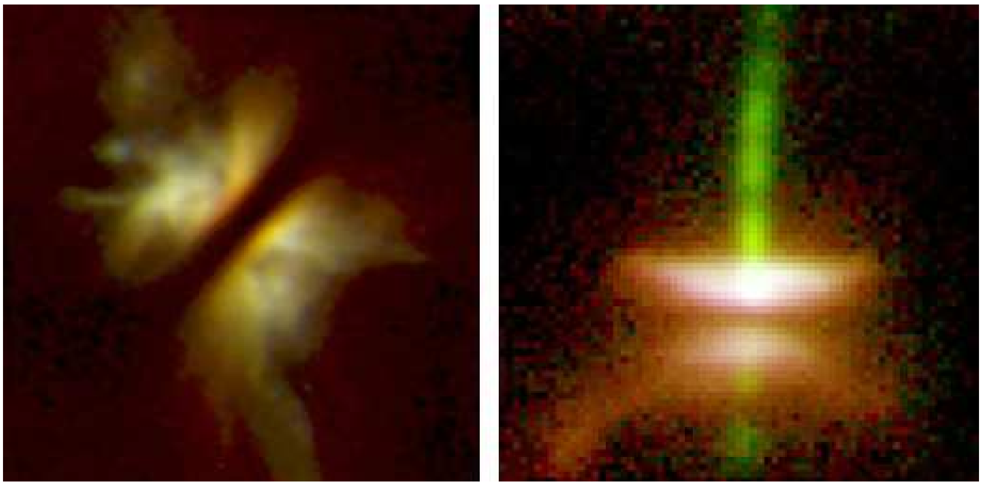

(b)

Fig. 1.1: a: Infrared view of the bipolar jet HH 212 (M.McCaughrean, ESO/VLT). b: Hubble Space Telescope infrared images of a dense circumstellar disk surrounding the young source IRAS 04302+2247 (left side) and the source HH30 (right side) with powerful jets from the central proto-star (from D.Padgett/STScl/NASA).

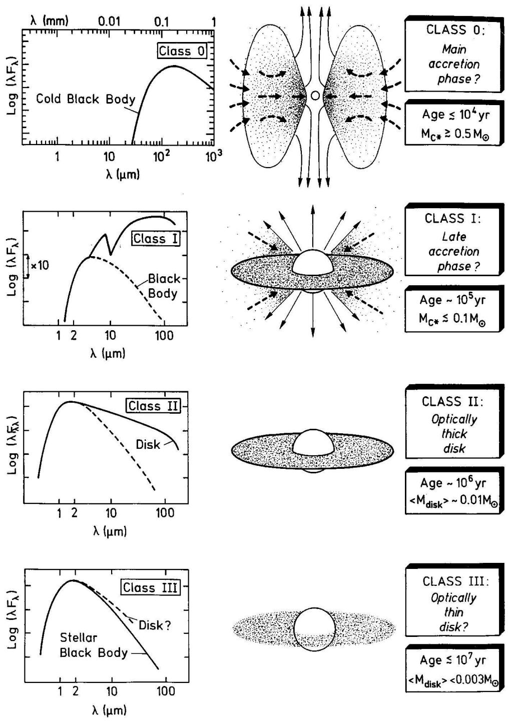

Fig. 1.2: Classification of low-mass stars in their early phases based on the slope of their Spectral Energy Distributions. (taken from C. Lada, P. André, M. Barsony, D.Ward-Thompson.)

1.1.4 High-mass star formation

Massive stars (M $\gtrsim$ 8 $M_{\odot}$) have a major impact on the evolution of the Galaxy. They are responsible for heating molecular clouds and enriching the interstellar medium with heavy elements. Massive stars are capable of changing the structure of their parent cloud and influence the star formation process via intense winds, UV radiation, massive outflows, expanding HII regions and supernovae explosions. At sufficiently farther distances, they may trigger fresh star formation.

The formation processes of high-mass stars are much less understood compared to these of low-mass stars. High-mass stars are born deeply enshrouded in the dense optically thick cores of molecular clouds present throughout the Galaxy and form mostly in cluster environment. In sharp contrast with low-mass stars, the high-mass stars have Kelvin-Helmholtz timescale shorter than the free-fall timescale (i.e., $t_{KH} < t_{ff}$). This indicates that massive stars begin their hydrogen burning (ZAMS) phase while still in their natal dense cores and accreting matter.

The smaller values of t_{KH} (compared to t_{ff}) for massive stars reflect that their PMS evolution is very rapid compared to their low-mass counterparts, making it very difficult to observe the critical earliest phases of their evolution. Going by the Salpter initial mass function (Salpeter 1955), massive stars are rare (i.e., small in number), usually situated at large distances ($\gtrsim$ 1 kpc), suffer high extinction ($A_v \gtrsim 100$) and have relatively short formation/evolution timescales compared to low-mass stars. Also they are able to produce large luminosity (10^4 – 10^6 $L_\odot$) due to their large temperature, intense flux of ionising photons and a tremendous radiation pressure ($P_{rad} \sim L_*/4\pi r^2 c$, where L_* is the stellar luminosity and c is the speed of light), which rapidly clears the material around it, hampering the process of accretion. The radiation pressure can also be defined as below:

$$P_{rad} = 10^{-6} \left(\frac{L_*}{5 \times 10^4 L_\odot}\right) \left(\frac{r}{1500AU}\right)^{-2} \tag{1.11}$$

The radiation pressure becomes an impediment for the accretion process to continue and sets a limit on the mass of a star beyond which the accretion may not contribute to star formation. This limit on stellar mass, about 10 $M_\odot$, is set by the balance between radiation force and gravitational force. Thus, the radiation pressure can halt the accretion process and set the upper limit of stellar mass function (Larson and Starrfield 1971; Wolfire and Cassinelli 1987; Jijina and Adams 1996).

All these factors inhibit the study of massive star formation, particularly the earliest phases of their evolution. A massive star emits UV photons with energy $\geq$ 13.6 eV, sufficient to ionise hydrogen and generate an ionised region called an HII region. Unlike in the high mass stars, the Lyman continuum fluxes from low-mass stars are not sufficient enough to create an HII region. The radius over which ionizing photons are effective, called the Strömgren radius (Franco et al. 1990), can be calculated from the equilibrium between the ionisation and recombination rates and is given by

$$R_s = \left(\frac{3}{4\pi\alpha}\right)^{1/3} N_{UV}^{1/3} n_e^{-2/3} \tag{1.12}$$

N_{UV} being the rate of ionising UV photons, n_e the electron density and recombination coefficient $\alpha[\mathrm{cm}^3\ \mathrm{s}^1] \simeq 2.6 \times 10^{-10}$ $(\mathrm{T[K]})^{-3/4}$, which is temperature dependent. For a O type star with T = 40,000 K, n_e = 10 cm^{-3}, α = 2.6 $\times$ 10^{-10} $\times$ $(40000)^{-3/4}$ and N_{UV} = 5

$\times\ 10^{48}$ photons/s; R_s is found to be nearly 4 pc (from Eq. 1.12).

However, it must be noted that the Strömgren sphere does not represent the true observed HII regions but provides a model for physical conditions around a hot star with uniform density. Observationally, it is known that the HII regions show different sizes and shapes. Dyson and Williams (1980) proposed a model of expansion of an HII region with time given by,

$$R(t) = R_s \left(1 + 7\frac{c_s \times t}{4R_s}\right)^{4/7} \tag{1.13}$$

where, c_s is the sound velocity in the ionised gas (c_s = 15 km s^{-1}) and R_s is defined in Eq. 1.12.

Models for massive star formation

Recent reviews by Beuther et al. (2007); Zinnecker and Yorke (2007); McKee and Ostriker (2007) cover the details of various theoretical studies on formation processes of massive stars. A brief account of different important theoretical models is presented here:

- **Monolithic collapse model**
  Low-mass star formation is explained by accretion process (with a typical accretion rate $\sim 10^{-6}$ $M_\odot$ yr^{-1}) and which cannot be directly applied to the massive stars due to their strong radiation pressure, which can directly halt the accretion of material onto the central object. McKee and Tan (2003) proposed what is called a turbulent core model to overcome the radiation pressure for the formation of massive stars through accretion process. In this model, massive stars form in the supersonic turbulent cloud cores with high accretion rates $\sim 10^{-3}$ $M_\odot$ yr^{-1}. These authors justify their model with the observed high pressure and turbulent motions associated with many dense massive cores. The high value of accretion rate is sufficient to overcome the radiation pressure of the central source. Through this process a massive star takes about 10^5 yr to form.

- **Competitive accretion in a proto-cluster environment**
  In the competitive accretion model, massive protostars in the dense cluster environment gain mass from unbound material through nearby clouds of gas with different

and higher accretion rates in a competing manner with other protostars of low- and intermediate-masses (Bonnell et al. 1997, 2001).

- **Stellar collisions and mergers in very dense systems**
  This model is very different from the low-mass star formation. Bonnell et al. (1998) proposed a model for formation of massive stars based on the cluster environment of massive stars. In this model, massive stars form through the physical collision and merging of low- and intermediate- mass stars. This process can occur only in regions of very high stellar densities of about 10^8 stars pc^{-3} for low mass stars and such high densities have not been observed so far. A stellar density of upto 10^6 stars pc^{-3} is reported in the densest regions of W3 IRS5 (Megeath et al. 2005).

Current observational scenario for high-mass star formation was summarised by Churchwell (2002); van der Tak and Menten (2005); Zinnecker and Yorke (2007); Beuther et al. (2007); McKee and Ostriker (2007). These authors have divided the evolution of individual massive stars into the following evolutionary stages based on observations from infrared through radio wavelengths that are very useful in tracing the cool dust regions, dense molecular gas and ionised emission regions, where these stages are manifested.

1. Infrared Dark Clouds (IRDCs) as birth places for high mass stars
2. High-mass protostellar objects (HMPOs) representing very early stages
3. Hypercompact (HCHII) and ultracompact HII (UCHII) regions
4. Compact classical HII regions

IRDCs were first identified as long dark filamentary features through infrared images from the Infrared Space Observatory (ISO; Perault et al. (1996)) and the Midcourse Space Experiment (MSX; Egan et al. (1998)) space missions. IRDCs are believed to be the precursors of clustered, massive star formation. IRDCs are known as the densest parts of the giant molecular clouds and are characterized by low temperatures (< 25 K), high column densities ($\sim 10^{23} - 10^{25}$ cm^{-2}) and high volume densities ($> 10^5$ cm^{-3}) (Bergin and Tafalla (2007); Rathborne et al. (2010) for more details).

HMPOs represent the second observable evolutionary stage in the high-mass star formation process. The phase in which the molecular cloud core starts to undergo free-fall collapse and form massive protostar, is known as HMPO. Hot molecular core is observationally identified with its lack of radio continuum emission. These are small (0.1 pc) and dense (n $\sim 10^5$ - 10^7 cm^{-3}) cores of the molecular gas with temperatures (T $\sim$ 100 - 200 K) associated with massive star forming regions (Keto 2002; Kurtz et al. 2000). HMPOs are younger than the hot molecular core (HMC) sub-phase that is traced by methanol maser emission (Hill et al. (2005) and references therein).

It has been suggested that HMPOs represent the early phase in the development of Hyper-compact (HCHII) and Ultra-compact HII (UCHII) stages. HMPOs have very strong dust continuum emission and lack free-free emission, while HCHII (size $<$ 0.01 pc) and UCHII (size $<$ 0.1 pc) regions are traced by strong free-free emission. HCHII regions represent individual photoevaporating disks (Keto 2007) and UCHII regions represent the disk-less stars photoionising their envelopes and cocoons. A HCHII region is known to show broad radio recombination line profiles, with typical velocity dispersions of 40 - 50 km s^{-1} (Gaume et al. 1995; Johnson et al. 1998) and a UCHII region has recombination line widths of about 30 - 40 km s^{-1} (Keto et al. 1995). Classical HII regions expand hydrodynamically and disrupt the parent molecular cloud.

Bipolar molecular outflows are commonly associated with young high-mass stars (Shepherd and Churchwell 1996; Zhang et al. 2001; Beuther et al. 2002a; Anandarao et. al. 2004; Zhang et al. 2005). These molecular outflows are much more massive and energetic with higher outflow entrainment rates than those associated with low-mass stars (Bachiller 1996). High accretion rates were noticed in the study of several massive star forming regions (which harbours HMPOs, Hyper- and Ultra compact HII regions) from molecular line observations (Fuller et al. 2005; Keto and Wood 2006). Recently Takashi and Kazuyuki (2009) numerically solved the detailed structure of the accreting protostar and reported the evolution of massive protostars with high accretion rates ($> 10^{-3}$ M$_\odot$yr^{-1}).

Interferometric observations in the sub-mm and mm bands provided evidence for the presence of accretion disk-like structures (also toroidal/ring like shapes) around young massive stars (Mundy et al. 1996; Shepherd and Kurtz 1999; Trinidad et al. 2003; Beltran et al. 2004; Patel et al. 2005; Curiel et al. 2006; Furuya et al. 2008). Cesaroni et al. (1997) and Zhang et al. (1998) observed a disk ($>$ 10,000 AU) in Keplerian rotation around one luminous young source, IRAS 20126+4104, which is also associated with an outflow (Cesaroni et al. 1997, 2005) (see Fig. 1.3).

In recent years, the *Spitzer* Space Telescope[1] (Werner 2004) has produced a wealth of useful data in mid- and far- infrared regions with better sensitivity and improved spatial resolution. *Spitzer*-IRAC images have been used to trace many signatures associated with young massive stars such as toroidal/ring structures (see Fig. 1.4), outflow lobes (see Fig. 3.9 of Chapter 3) and jets (see Fig. A.3 of Appendix A), which are similar to the observed features associated with low mass stars in their early formation phase. These observational evidences show that massive stars are formed in a similar manner to the low mass star but with higher accretion rates in clusters rather than in isolation.

Therefore, it is still not clear whether massive star formation is a scaled up version of low-mass star formation or is a result of a fundamentally different process. Crucial to this question is the study of the early stages of high-mass stars such as HMPOs and UCHII regions, to look for similar signatures (as found in disks and outflows in low-mass stars) associated with these stages.

Spectral Energy Distribution Modeling

Modeling of Spectral Energy Distributions (SEDs) of massive young protostars provide important inputs on various physical parameters of the sources, which can not otherwise be possible through direct observation. Therefore, in recent years, several workers have given much needed attention to the SED modeling of young stellar objects (YSOs) (Whitney et al. 2003a,b, 2004). The understanding of the physics of low-mass star formation has significantly progressed and the same physics has been incorporated in radiative transfer calculations to analyse SEDs of individual sources in massive star forming regions.

The SED modeling tool developed by Robitaille et al. (2006) was successfully tested on low-mass YSOs in nearby star forming regions. These models assume an accretion scenario with a central source associated with rotationally flattened infalling envelope, bipolar cavities, and a flared accretion disk, all under radiative equilibrium (Bjorkman and Wood 2001). The model provides a set of physical parameters associated with a particular source instead of analysing the shape of a single SED (see Robitaille et al. (2007)). The model grid consists of 20,000 models of two-dimensional Monte Carlo simulations of radiation transfer with 10 inclination angles, resulting in a total of 200,000 SED models. The model

[1] see http://ssc.spitzer.caltech.edu/

output gives 14 physical parameters of the individual source which can be divided into 3 categories: the central source parameters (stellar mass, radius, luminosity and temperature), the infalling envelope parameters (the envelope mass, accretion rate, outer radius, inner radius, cavity opening angle and cavity density), and the disk parameters (disk mass, accretion rate, outer radius, inner radius, flaring power, scale height and inclination). The current version of the SED fitting tool covers the mass range from $0.1M_{\odot}$ to $50M_{\odot}$. The tool fits the best fit model along with a group of models that is interpolated to different apertures at different wavelengths depending upon the beam sizes. This group of models is selected on the basis of the criterion given as below:

$$\chi^2 - \chi^2{}_{best} < 3 \tag{1.14}$$

Recently, Grave and Kumar (2009) applied these SED models for samples of HMPOs and derived their disk and envelope accretion rates to be 10^{-6} - 10^{-3} $M_{\odot}$ yr^{-1}. However, there are limitations in these SED models because they do not account for accretion luminosity from envelopes and multiplicity of sources which are very important for the study of the massive young objects (see Robitaille (2008) for justification).

1.2 Motivation for the present work

Massive stars heat their natal dust cocoons, where they are born and emit predominantly mid-infrared radiation. Hence, to understand the processes involved in the formation of massive stars and their relation to their surroundings, we need to study them at longer wavelengths which suffer lower extinction. These sites are accessible to mid- and far-infrared observations that can probe very deeply embedded objects. High spatial resolution is very important at these longer wavelengths to observationally identify individual sources from their cluster environment, where they are born. The *Spitzer* Infra-Red Array Camera (IRAC) (Fazio et al. 2004) provides an opportunity, with an unprecedented high spatial resolution in thermal infrared wavelength regime, that is very useful in identifying embedded sources in massive star forming regions. IRAC has four wavelength bands covering the region 3.6 - 8.0 μm, i.e., Ch1 (3.55/0.75), Ch2 (4.49/1.0, Ch3 (5.73/1.43) and Ch4 (7.87/2.91 μm). Thus, with the *Spitzer* Space Telescope, it is now possible to identify deeply embedded massive stars in their early phases of formation and model them. This provides the motivation for the present work, viz. to look into regions in which HMPOs

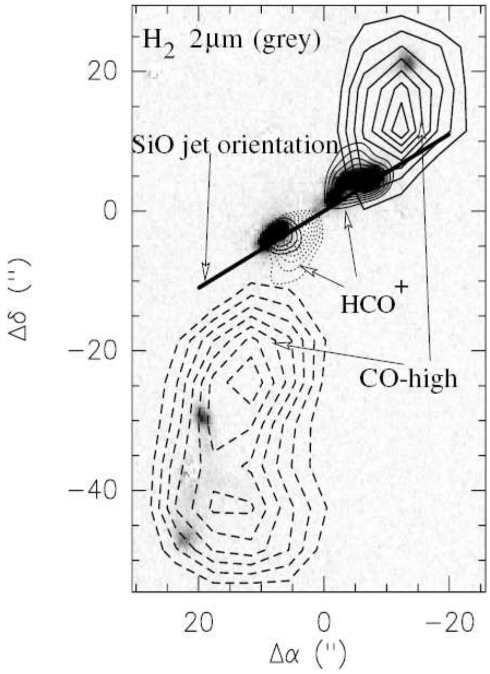

Fig. 1.3: The molecular hydrogen (H_2) image of IRAS 20126+4104 overlaid with contours of ^{12}CO(2-1) (thick solid and dashed lines) and HCO^+(1-0) (thin solid and dashed lines) outflow lobes (from Lebrón et al. (2006)).

and the driving engines of UCHIIs regions are associated and to identify their counterparts in the infrared using IRAC images and characterise their physical parameters (like mass, age, temperature, luminosity and accretion rates etc.) by modeling their SEDs.

Stars of all masses show outflows during their PMS stages. While in the case of low mass YSOs, it is fairly well-established that the outflows and disks are phenomenologically related, observations have just begun to show that massive PMS stars too have disk/disk-like structure of accretion. As far as the intermediate and high-mass PMS sources are concerned, there have been catalogues prepared from CO line survey observations (Lada (1985) for low to high luminosity objects; Shepherd and Churchwell (1996), Shepherd et al. (2000) and Zhang et al. (2007) for high luminosity objects). These studies indicated that the intermediate-/high-mass sources too follow the basic relationship between outflow parameters and those of the driving source in a way similar to the well-established case of low mass sources. However, the statistics are poor for young massive stars. Recently, there have been systematic studies of outflow phenomenon associated with HMPOs and these studies have provided improved statistics for the range of masses covering early B stars.

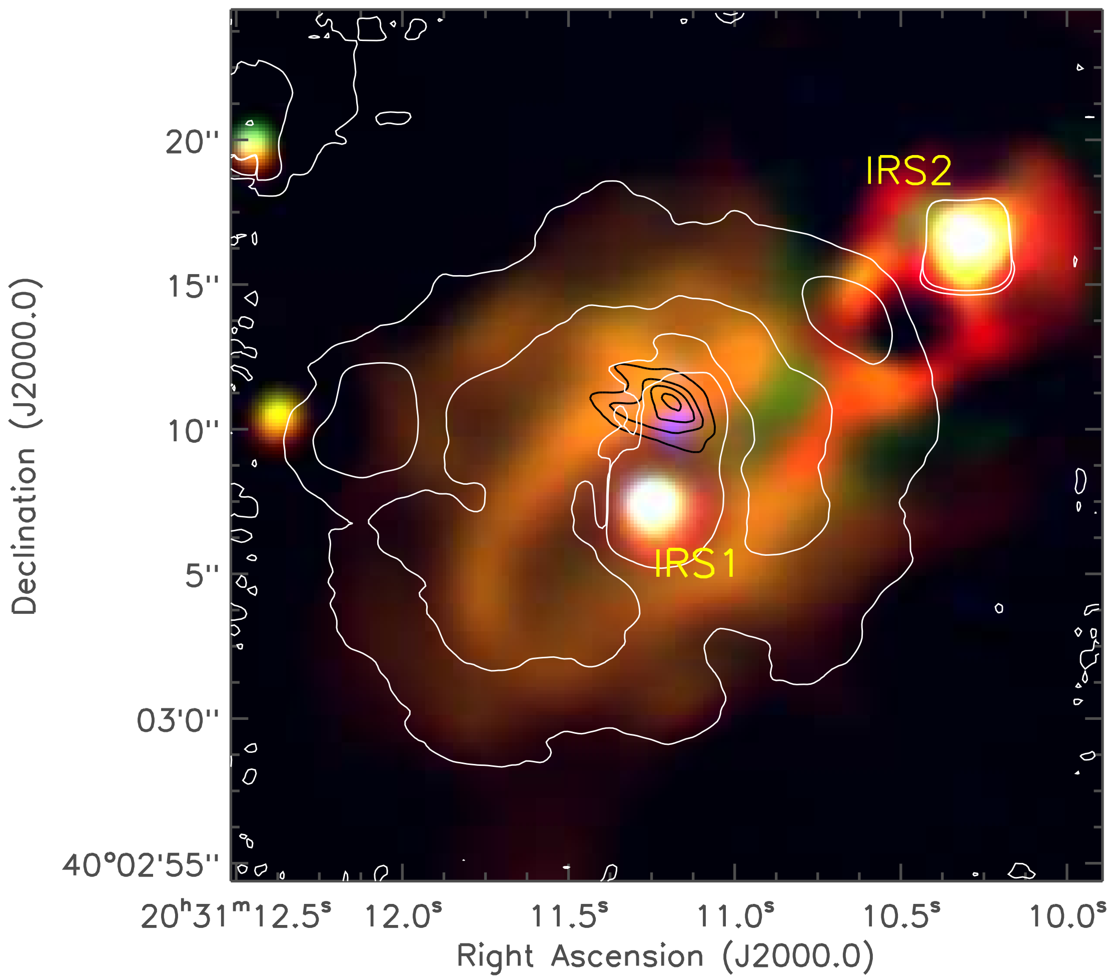

Fig. 1.4: The RGB colour-composite image of IRAS 20293+3952 from Kumar et al. (2009) obtained by coding the *Spitzer*-IRAC hi-res deconvolved IRAC Ch4, Ch3 images, and near-infrared (normal) 2.2 μm image as red, green and blue respectively. White contours (15 σ and 60 σ levels above the mean background) display continuum subtracted H_2 narrow band emission at 2.12 μm. Figure exhibits the ring structure around the IRS1 source. Location of UCHII regions is represented by 2 cm Radio contours with black solid lines.

But the possible relation between outflow parameters and physical parameters of the driving engines has not been well established. Therefore, this is one of the main motivations of the present work. IRAC provides very high sensitivity and arc-sec spatial resolution to detect embedded YSOs allowing for first time to estimate the surface density of YSOs in massive star forming regions. The surface density of YSOs provides an important input/clue for the formation of stars in embedded clusters. In addition to, IRAC photometry, ratio maps of IRAC images are very helpful to study the atomic/molecular emission regions created by massive stars due to their interaction with the immediate surroundings. The energy released (i.e., the amount of UV photons) from O and early B type stars (Panagia 1973) is different, therefore their interaction with their surrounding will be different and complex. Hence, it is very interesting to look for such regions, where O and early B type stars are present. Also, it is important to look for sites of fresh star formation triggered by winds, UV radiation and expanding HII regions associated with young massive stars.

1.3 Objectives of the Thesis

To summarise, the objectives of the present work are:

1. Identification of mid-IR counterparts of HMPOs, which represent the pre-UCHII phase. In some of the HMPOs, known to be outflow sources, it is important to identify their driving engines and derive their physical parameters such as, mass, luminosity and accretion rate through SED modeling using observed imaging data. Therefore, one of the important aims of this work is to compare the physical parameters of HMPOs against the observed outflow parameters.

2. The central ionising sources of UCHII regions are known to be O and early B stars because of their ability to ionise the regions surrounding them. Nevertheless, many of them are still deeply embedded not to be optically visible. Therefore, one of the objectives of this study is to identify the mid-IR counterparts of the driving engines of the UCHII regions and to derive their physical parameters through SED modeling using observed imaging data.

3. To carry out mid-infrared photometric study of a few massive star-forming regions, taking into advantage of arcsec spatial resolution of *Spitzer*-IRAC data, through which it is possible to identify embedded YSOs, especially young massive protostars. Determination of cluster sizes of YSOs and their spatial density which give

important clues to understanding the star formation. Finally to derive the physical properties of selected YSOs through their SED modeling. The thesis also includes the study of the interaction and feedback of massive stars to their immediate environments.

1.4 Outline of the thesis

The afore-mentioned work will be described in the ensuing chapters, the outline of which is as follows:

Chapter 2: In this chapter, we describe the driving engine-outflow relationships for the HMPOs known as the driving sources of the outflows. We will present the results of SED modeling of mid-IR counterparts of HMPOs identified through *Spitzer*-GLIMPSE images and report their relation with physical parameters like mass, age and accretion rates with observed outflow properties like outflow mass, momentum, velocity and entrainment rates. We will also present the work on the identification of the mid-IR counterparts of the driving engines of UCHII regions and characterise their physical properties through SED modeling.

Chapter 3: We report detailed studies on the massive star forming region AFGL 437 using *Spitzer*-IRAC archival images. In this work, we have identified many new YSOs using IRAC colour-colour diagram and have investigated one young high-mass protostellar source with its outflow lobes using IRAC ratio image, which indicates that the source is in its accretion phase. Also, we will highlight the results on its environment, which tells us about the interaction of massive stars with its surroundings.

Chapter 4: We present the detailed study on another massive star forming region M8 (Lagoon Nebula) using *Spitzer*-IRAC archival images. In this work, we have identified many new YSOs using IRAC colour-colour diagram and have investigated the PAH cavity structure nearby a high-mass star. Also, we will highlight the results of the interaction of massive stars with immediate and far distant environment in causing triggered star formation.

Chapter 5: In this chapter, we present ground-based near-infrared JHK photometric observations of one massive star forming region, namely, IRAS 05375+3540 from the Mt. Abu IR observatory. In addition, space-based *Spitzer*-IRAC images on this massive star forming region will be presented. We focus on and examine the photometric results obtained on this source and their surroundings using the infrared images.

Chapter 6: This chapter summarises the results produced in the thesis and outlines future directions for further study.

Chapter 2

Spitzer-IRAC GLIMPSE study of driving engines of HMPOs and UCHII regions

In this chapter, we present the physical properties of the driving engines of high mass protostellar objects (HMPOs) and Ultra-Compact HII (UCHII) regions derived from radiative transfer modeling of SED. HMPOs are known precursors to UCHII regions, some of which are associated with outflows. We have divided this chapter into two parts. In the first part, we present the identification of the outflow driving engines and their outflow relationships with SED model-derived physical parameters of HMPOs. The identification of driving engines of UCHII and their physical properties through SED modeling will be described in second part of this chapter. Towards the end of the chapter, a comparison of physical parameters of the two stages will be highlighted.

2.1 The outflow and driving source relationships

Outflows are ubiquitous sign-posts of star formation; in particular, of the accretion process (Lada 1985; Bachiller 1996; Bontemps et al. 1996). Their detailed properties, driving mechanisms and their relation with driving source properties were studied in the context of low-mass stars and a few intermediate-mass stars (Arce et al. (2007) and references therein). One of the earliest reviews on this subject by Lada (1985) addressed outflows from both low and high luminosity sources. However, many of the specific results obtained were based on the observations of low luminosity sources (Bontemps et al. 1996; Bachiller 1996). From the studies of bipolar outflows from low-mass stars, it has been established that the outflow momentum flux: (i) increases with the luminosity of the driving source, and (ii) decays as the driving source evolves, owing to reduced accretion activity. Our uncertain knowledge about the formation of massive stars coupled with the poor statistics of outflows from high luminosity sources has kept the topic of massive outflows distinct, even though Lada (1985) included outflows from low to high luminosity objects in his outflow catalog. Shepherd and Churchwell (1996) observed a sample of high luminosity sources, which cover the outflow parameters for intermediate- and high-mass sources and showed that the relations between molecular outflows and their driving sources were valid even for massive stars, probably up to O type stars. Indeed, it is the observations of massive bipolar molecular outflows from luminous infrared sources (Shepherd et al. 2000; Zhang et al. 2007) that reinforced the idea of the formation of massive stars through the accretion process, without much need to invoke alternative scenarios (i.e., coalescence scenario for details, Zinnecker and Yorke (2007)).

Massive star formation studies have become more systematic in the last decade with the availability of higher sensitivity and high spatial resolution observing facilities in the infrared (IR) and millimeter (mm) bands. Well-defined samples of HMPOs have been the targets of investigation both in millimeter (Beuther et al. 2002; Williams et al. 2004) and infrared bands (Kumar and Grave 2007; Grave and Kumar 2009). The outflow phenomenon has been systematically studied from such samples (Ridge and Moore 2001; Beuther et al. 2002a; Benedettini et al. 2004; Zhang et al. 2005; Kim and Kurtz 2006). These studies have provided an improved statistics for the range of masses covering early B type stars for which outflow-driving source relations showed similar trends as in the case of low mass sources (Beuther et al. 2002a; Arce et al. 2007). The issue of source and outflow multiplicity has also been investigated in recent years using interferometric observations (Beuther et al. 2004, 2005; Palau et al. 2007a,b). Theoretically, outflows have been shown to be important in massive star formation to channel out the radiation pressure (Krumholz et al. 2005). Banerjee and Pudritz (2007) simulated disk-driven outflows in collapsing massive cores with high accretion rates. These simulations suggest magnetically driven winds from disks as the origin of the outflows. Despite the common features between low and high mass outflows, specific observational evidences is necessary to confirm the outflow-disk connection in massive star formation.

In the first part of this chapter, we have identified the embedded infrared counterparts (IRCs) of HMPO cores and estimated their physical properties by modeling their Spectral

Energy Distributions (SEDs). The details of the SED modeling tool (Robitaille et al. 2006) used here are given in Chapter 1. Robitaille et al. (2007) applied this tool to observational data of a sample of low mass young stars in the Taurus region. They demonstrated that the tool reproduces properties such as stellar mass, disk and envelope accretion rates that are highly consistent with results obtained from other, specific and detailed methods. Although the current version of the SED fitting tool covers the mass range up to 50 $M_{\odot}$, it is thought to be highly effective only up to 20 $M_{\odot}$, at which limit, the disk accretion luminosity is computed.

This ability to model and derive source properties together with the improved sensitivity in the infrared bands enables true identification of deeply embedded protostellar objects. With the *Spitzer* Space Telescope, it is now possible to identify the driving sources in the infrared, model them and investigate the outflow-driving engine relationships for deeply embedded massive stars, which is pursued in the first section of this chapter.

2.1.1 Data Selection and Analysis: The IRCs data sample

The outflow data for the present analysis are taken from the CO observations of Ridge and Moore (2001), Beuther et al. (2002a), Benedettini et al. (2004), Zhang et al. (2005) and Kim and Kurtz (2006). We searched for infrared counterparts coinciding with the outflow center and also associated with a dense core. The reddest and brightest IRCs appearing on the *Spitzer*-IRAC image that coincide with "both" the millimeter core and the outflow centre to better than 5$''$ was chosen as the driving source. A total of 33 outflows in the sample were found to have IRCs that could be modeled. In all targets, only one point source was found within a radius of 5$''$ satisfying the required criteria. Data for the 33 sources were found by searching all programs in the *Spitzer*-IRAC/Glimpse archive (see Table 2.1 for the position of the outflow driving engines). There is a distance ambiguity (near and far distances) for 8 of the 33 sources. Photometry data for 16 sources were taken from the Glimpse data base and data for 9 sources were extracted from the individual observing program ID's 3528 (PI: Q. Zhang; four sources), 6 (PI: G. Fazio, three sources), 30734 (PI: D. Figer; one source) and 104 (PI: T. Soifer; one source). Since IRAC data are not available for 8 sources (shown by star and dagger symbols on the Table 2.1), available ground based observational data were taken for SED modeling (Dagger (†) symbol represents the single source having 24.5 μm data from Linz et al. (2009) and the seven sources having 10.47 μm data from Campbell et al. (2005) are shown by star ($\star$) symbol).

Table 2.1: List of 33 driving engines of the molecular outflows and their positions. Dagger (†) symbol represents the source having 24.5 μm data from Linz et al. (2009). Sources having 10. 47 μm data from Campbell et al. (2005) are shown by a star ($\star$) symbol.

Sources IRAS	RA (J2000)	Dec (J2000)	Distance (kpc) Near, Far
05358+3543mm1	05:39:13.07	+35:45:50.9	1.80
05373+2349s1	05:40:24.20	+23:50:54.9	1.20
05553+1631*	05:58:13.82	+16:31:57.0	2.50
06584-0852	07:00:50.99	-08:56:30.2	4.50
18151-1208	18:17:58.14	-12:07:24.7	3.00
18182-1433	18:21:09.14	-14:31:48.5	4.50, 11.70
18264-1152mms1	18:29:14.69	-11:50:23.6	3.50, 12.50
18345-0641mms1	18:37:16.92	-06:38:29.8	9.50
18511+0146s1	18:53:37.89	+01:50:30.7	3.90
18566+0408mms1	18:59:09.95	+04:12:15.7	6.70
19012+0536mms1	19:03:45.30	+05:40:42.4	4.60, 8.60
19035+0641mms1	19:06:01.63	+06:46:36.2	2.20
19217+1651mms1	19:23:58.80	+16:57:41.1	10.50
19266+1745mms1	19:28:55.66	+17:51:59.5	0.30, 10.00
19368+2239	19:38:57.22	+22:46:23.8	4.40
19374+2352	19:39:34.58	+23:59:48.6	4.30
19388+2357	19:40:59.32	+24:04:44.2	4.30
19410+2336mms1	19:43:11.23	+23:44:03.7	2.10, 6.40
19410+2336mms2	19:43:10.70	+23:44:00.0	2.10, 6.40
19411+2306mms1	19:43:17.97	+23:14:01.5	2.90, 5.80
20050+2720s2	20:07:06.60	+27:28:47.6	0.73
20216+4107*	20:23:23.79	+41:17:39.0	1.7
20293+3952	20:31:12.43	+40:03:19.9	1.30, 2.00
20343+4129*	20:36:07.55	+41:40:09.3	1.4
22134+5834*	22:15:09.14	+58:49:08.2	2.6
22172+5549s2	22:19:09.50	+56:05:00.1	2.87
22305+5803	22:32:24.00	+58:19:01.9	5.40
22570+5912*	22:59:06.19	+59:28:30.0	5.1
23033+5951*	23:05:25.14	+60:08:15.2	3.5
23151+5912*	23:17:21.42	+59:28:49.9	5.7
M8E†	18:04:53.20	-24:26:41.3	1.5
HH80	18:19:12.09	-20:47:30.0	1.9
WK34	03:07:24.58	+58:30:52.8	2.0

A typical example of the outflow driving engine with its SED is shown in Fig.2.1. Figure A.1 of Appendix A displays the association of the identified IRCs with the outflows. This association is shown for 13 sources (12 images) from the Beuther et al. (2002a) sample. The outflows are shown as contours (dotted: red-shifted lobe, solid: blue-shifted lobe) on the *Spitzer*-IRAC 8 μm grey scale images. Black circles mark the identified IRCs as the outflow driving engine. Similarly, Fig. A.2 of Appendix A shows the six outflow sources (from the Beuther et al. (2002a) sample that do not have IRAC images) with the outflow data overplotted on the inverted grey scale 2MASS K-band image. Figure A.3 of Appendix A shows the 3-colour-composite *Spitzer*-IRAC image (Ch4(red), Ch2(green) and Ch1(blue)) of other 11 sources including one common source IRAS 18182-1433 from Figure A.1 of Appendix A. The jet structure is associated with the source IRAS 18182-1433 as is clearly seen in the image (Figure A.3 of Appendix A). The jet may be due to shock-excited molecular H_2 emission. Figure A.4 of Appendix A shows the 3-colour-composite image of four sources (using IRAC images for three sources and 2MASS for one source) along with the location of outflow driving engines.

2.1.2 The outflow data

The outflow parameters such as mass, momentum, outflow entrainment rate and velocities were obtained from the tables of Ridge and Moore (2001), Beuther et al. (2002a), Benedettini et al. (2004), Zhang et al. (2005) and Kim and Kurtz (2006). The spatial resolution and quality of the Beuther et al. (2002a) sample of 20 outflows are better than those of the 13 outflows (1 from Ridge and Moore (2001), 1 from Benedettini et al. (2004), 10 from Zhang et al. (2005) and 1 from Kim and Kurtz (2006)); owing to the observations with a larger telescope (30m vs 12m). In the analysis, we will compare the outflow mass and momentum against the modeled properties of the driving protostar. The outflow mass and momentum are relatively direct measurements from the CO line flux and velocity spreads, whereas, the outflow force or mechanical luminosity involves additional measurements such as size and dynamical time. Measuring the size brings additional uncertainties due to the limited spatial resolution and the large distances to our targets. Therefore, we do not use the outflow force or mechanical luminosity for comparisons, which is contrary to the traditional choice made in studying outflows from low mass objects (Lada 1985; Cabrit and Bertout 1992; Bontemps et al. 1996). The errors on the outflow mass and momentum are assumed to be 50% and 10% respectively, following recommendations from the original papers presenting the data.

2.1.3 SED modeling of the IRCs

The SEDs were constructed for the 33 driving sources by using 2MASS, MSX, IRAS, and (sub)millimeter data (from literature). The resulting SEDs were fitted using the SED fitting tool of (Robitaille et al. 2007) and analysed as described by Grave and Kumar (2009).

The photometric data used for SED fitting involve different apertures for different bands depending upon the beam sizes. The SEDs here are strongly constrained by the highest spatial resolution data between 1-8 μm from 2MASS and *Spitzer* for 25 sources. The SEDs of the remaining 8 sources are constrained by using 2MASS with ground based mid-infrared data points. At the longer wavelength side, it is constrained by the (sub)mm data points which typically have beam sizes of 10-15″. The fitting was done separately using both the near and far distance estimates in the case where the distance was not resolved. However, the parameters obtained by using the far distance only were used to make the plots. The SED plots for all the 33 sources are shown in Figure A.5 of Appendix A. The solid line shows the best fit model which is interpolated to different apertures at different wavelengths depending upon the beam sizes. The dotted line represents the input photosphere. Filled circles and triangles show the data points and upper limits respectively. The grey lines display the group of models that satisfy the criterion:

$$\chi^2 - {\chi^2}_{best} < 3 \qquad (2.1)$$

In many cases, when the quality of the longer wavelength data was thought not to be the best, we use it as an upper limit rather than data point.

Figure A.6 from Appendix A display the best fit model (shown for a single aperture of 2.4″ for 23 sources only) and its decomposition into three components, namely, envelope (red), disk (green) and scattered (yellow) fluxes. It is evident from this figure that the disk flux (when present) traces the shorter wavelength data and the envelope flux is better represented by the longer wavelength data. Therefore, the 2MASS and *Spitzer* data are indeed representative of the disk emission. In a few cases, either the disk is not present or deeply embedded in the envelope. When there is a disk and envelope together, it can be seen that at shorter wavelengths, there is a significant overlap between the two curves. This can indicate that the decompositions of the disk and envelope parameters may not be efficient unless sufficient data points in the millimeter range are present, which will strongly constrain the envelope emission.

The SED fitting works by using a large grid of 200,000 models to scale and match the observed SED. In doing so, the most reliable parameters from the results are the luminosity and temperature. Subsequently using evolutionary models, these parameters are translated into the mass and age of the protostar. Also, the shape of the SED at shorter wavelengths, particularly in the *Spitzer* bands constrain the disk emission. Indeed, Robitaille et al. (2007)

demonstrated that quantities such as accretion rates obtained from the SED fitting of low mass stars are in remarkable agreement with measurements using classical methods. Although the case for intermediate- and massive stars is different from that for the low-mass stars, we will proceed with the assumption that the physics of disks incorporated in the SED models would be valid for the mass range dealt here.

2.1.4 Outflow properties vs driving source properties

The physical properties of the driving sources estimated from SED modeling are listed in Table A.1 of Appendix A with corresponding outflow properties (such as outflow mass, outflow momentum and entrainment rate) obtained from literature. Additionally, each column of physical parameters (i.e., mass, luminosity, age, envelope mass ,envelope accretion rate, disk mass, disk accretion rate) is accompanied by another column with the corresponding standard deviation. All models with criterion given in Eq. 2.1 for each data point are used to compute the weighted means and standard deviations. As we mentioned earlier, the SED modeling is done separately for both the near and far distances for sources having a distance ambiguity.

In the following, the outflow mass and momentum for 33 sources are compared with various properties of the driving protostar. This analysis has two specific advantages: (i) The outflow driving sources for the massive protostellar candidates are identified based on the highest spatial resolution data available to date in the infrared and millimeter bands, thus reducing the source confusion; and (ii) the identified sources have been modeled with an effective SED fitting tool to derive the mass, age of the star and accretion rates, allowing direct comparison with outflow properties. The net result is compared with the stellar mass instead of source luminosity and also with a stellar age on a continuous scale unlike the three or four evolutionary classes such as Class 0, I, etc.

Luminosity, Mass and Age

In this subsection, we will explore the various trends between outflow parameters and model derived physical properties of outflow driving engines of HMPOs. For this purpose, we made log-log plots of outflow parameters against physical parameters of sources. For each graph that is plotted, we also show as error bars, the standard deviations in SED fitted parameters and uncertainties from the outflow observational data. In Fig. 2.2 the outflow mass is plotted against total luminosity and effective temperature respectively. The luminosity and temperature are the two most reliable results from the SED modeling. Subsequently the model tool estimates the mass and the age of YSO using evolutionary models. It turns out that the age is a less certain parameter compared to the mass (Robitaille et al. 2006). Fig. 2.3 plots the stellar photospheric mass with the outflow mass and momentum. The figure shows that the net outflow mass (M_{out}) and momentum (P_{out}) increase with increasing stellar mass, despite considerable scatter in the data points. These results are valid up to a mass range of 25 $M_{\odot}$, mostly limited by the analysed data. The increasing tendency for both P_{out} and M_{out} with stellar mass may be noticed. The outflow mass and momentum are plotted against the stellar age in Fig. 2.4. One may notice a slight trend or tendency to decrease. The plots indicate that the outflow mass and momentum show a declining trend with the evolution of massive protostars. This result, however, is in good agreement with what is known from the study of low-mass stars (Wu et al. 2004).

Disk and Envelope: Masses and Accretion Rates

Fig. 2.5 plots the outflow mass and momentum against the envelope accretion rate. Similarly, Fig. 2.6 plots the outflow mass and momentum against the disk accretion rate. It can be seen that the outflow mass and momentum tend to increase with increasing accretion rates with the trend more clear for disk accretion. In Fig. 2.7, we display the variation of outflow mass with mass of the envelope and mass of the disk. The outflow mass shows a trend of increase with increasing disk and envelope masses (again, the trend is better seen with disk mass). It can be seen from Figs. 2.3, 2.4 and 2.5 that the linear trend is better between outflow mass and momentum with stellar mass and accretion rates, but not with the age.

Accretion rates and Outflow Entrainment rates

The scatter plots between the measured outflow entrainment rates and the accretion rates (disk and envelope) are shown in Fig. 2.8. One may notice a faint trend in the plots (better in disk accretion rate than envelope accretion rate).

2.1.5 Discussion

One of the most important correlations found in the present study is between the outflow entrainment rate with the source accretion rate, even if it is a trend in the scatter diagrams. This is the key to understanding the connection between the outflow phenomenon and ac-

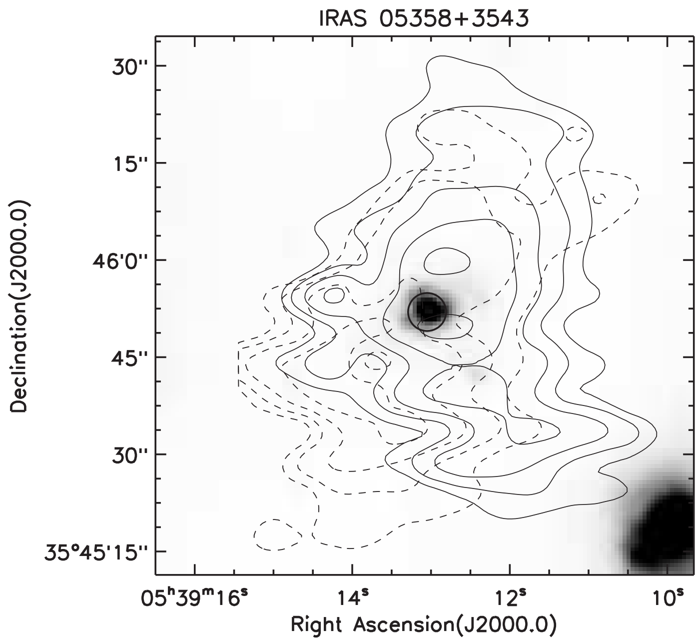

(a)

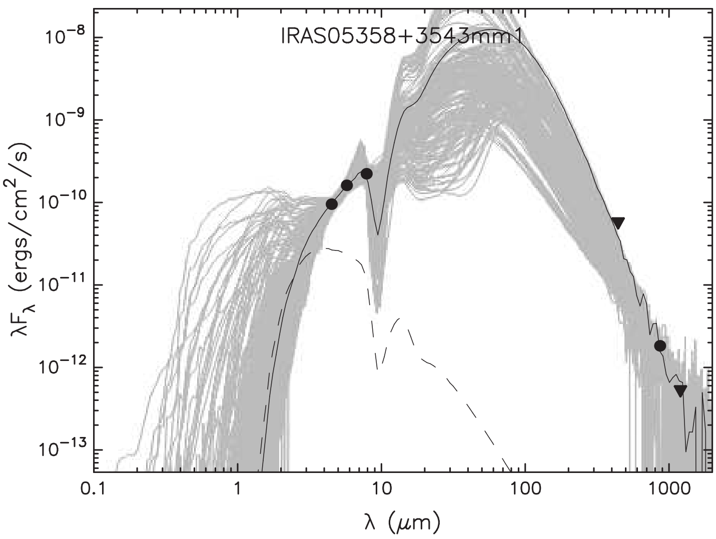

(b)

Fig. 2.1: a: Mid-IR (IRAC 8 μm) counterpart of the outflow driving engine for IRAS 05358+3543 is shown in figure and indicated by the the black circle. Overplotted the contours are the observed red shifted (dashed curves with maximum velocity 13.6 km s^{-1}) and blue shifted (solid curves with maximum velocity 14.4 km s^{-1}) components of molecular ^{12}CO (J = 2 - 1 transition) outflow taken from (Beuther et al. 2002a). b: Shows the SED model for the HMPO source.

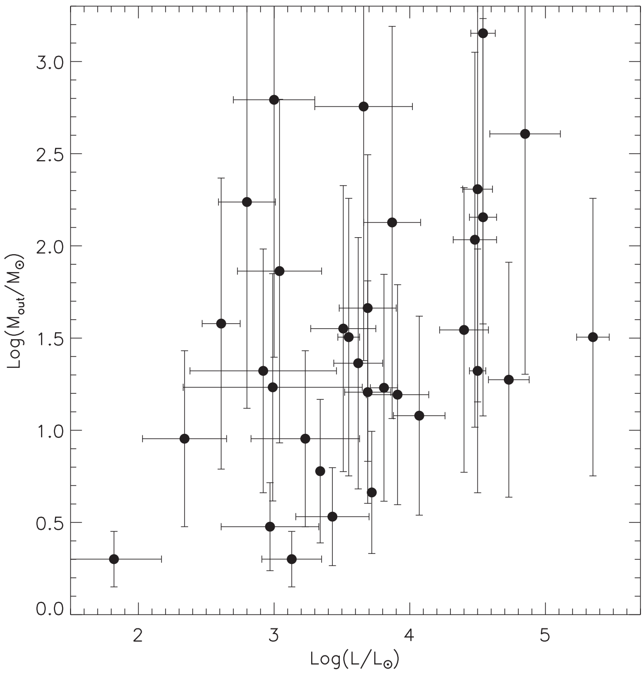

(a)

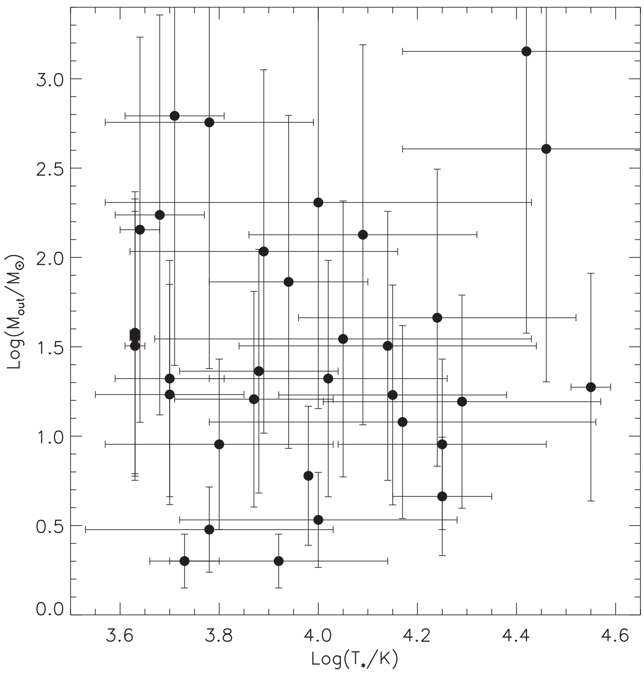

(b)

Fig. 2.2: a: Observed outflow mass is shown as a function of model-obtained total luminosity of the HMPOs. b: Outflow mass vs temperature.

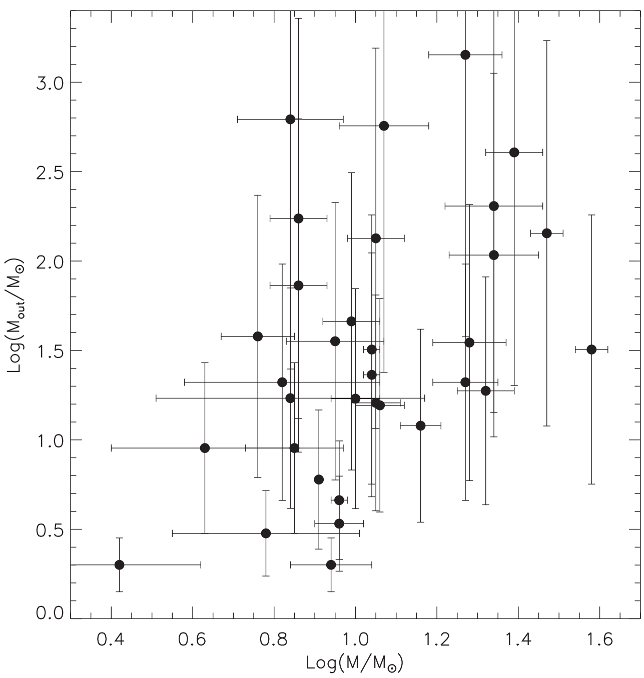

(a)

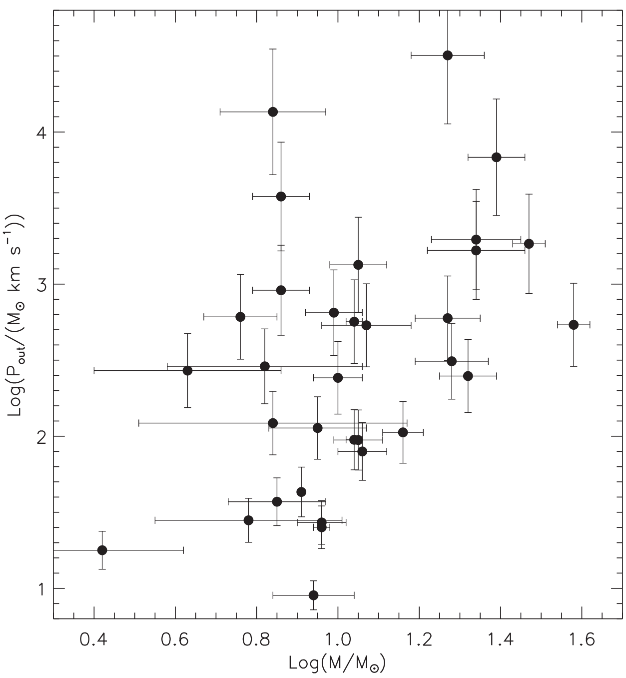

(b)

Fig. 2.3: a: Observed outflow mass is shown as a function of model-obtained stellar mass of the HMPOs. b: Outflow momentum vs stellar mass.

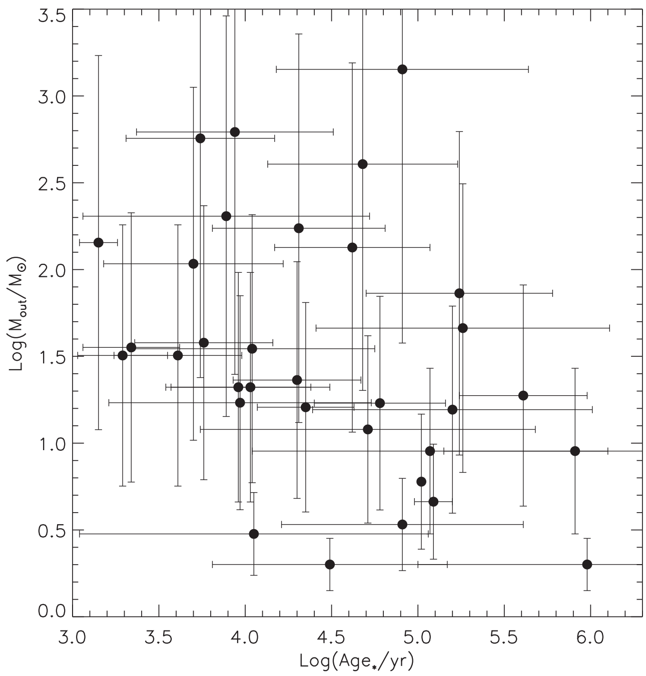

(a)

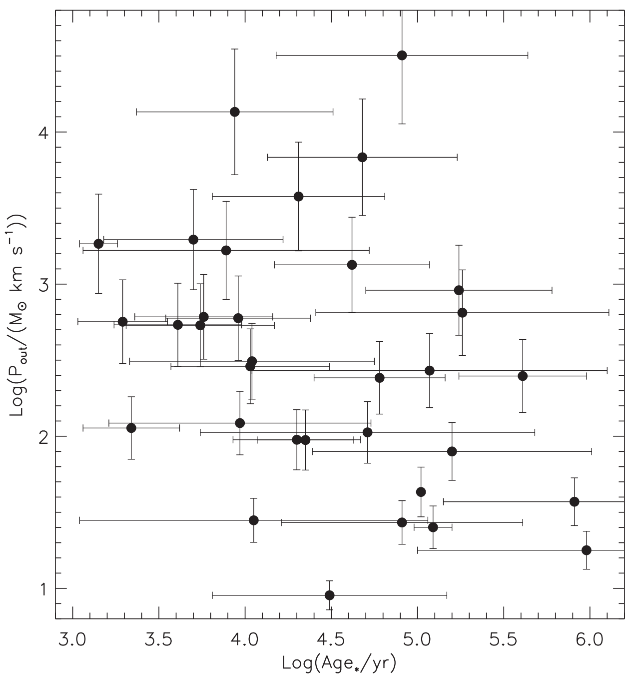

(b)

Fig. 2.4: a: Observed outflow mass is shown as a function of model-obtained stellar age of the HMPOs. b: Outflow momentum vs stellar age.

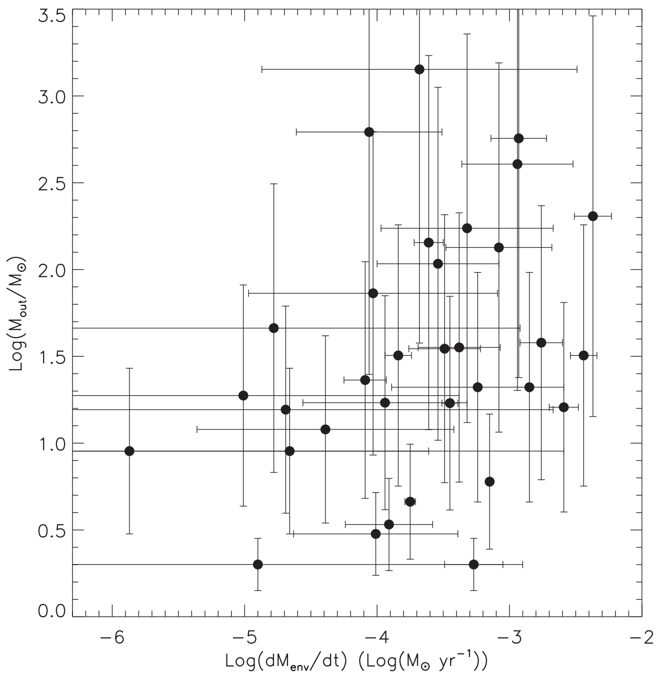

(a)

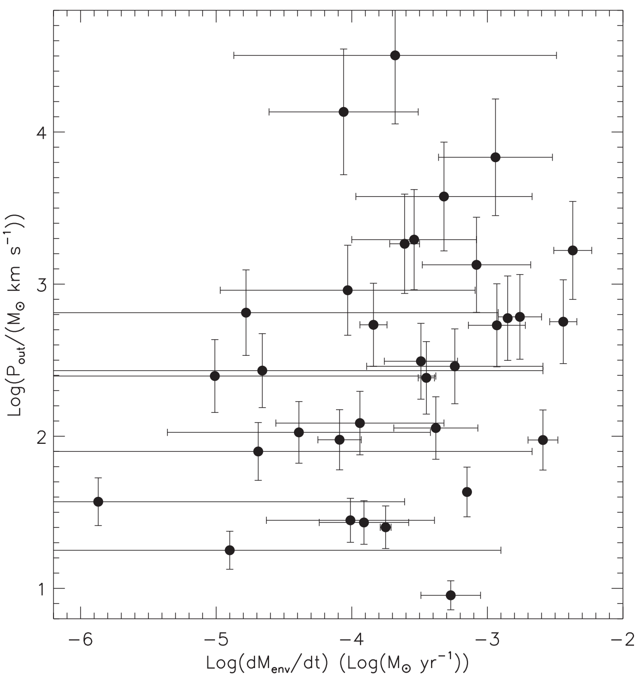

(b)

Fig. 2.5: a: Observed outflow mass is shown as a function of model-obtained envelope accretion rate of the HMPOs. b: Outflow momentum vs envelope accretion rate.

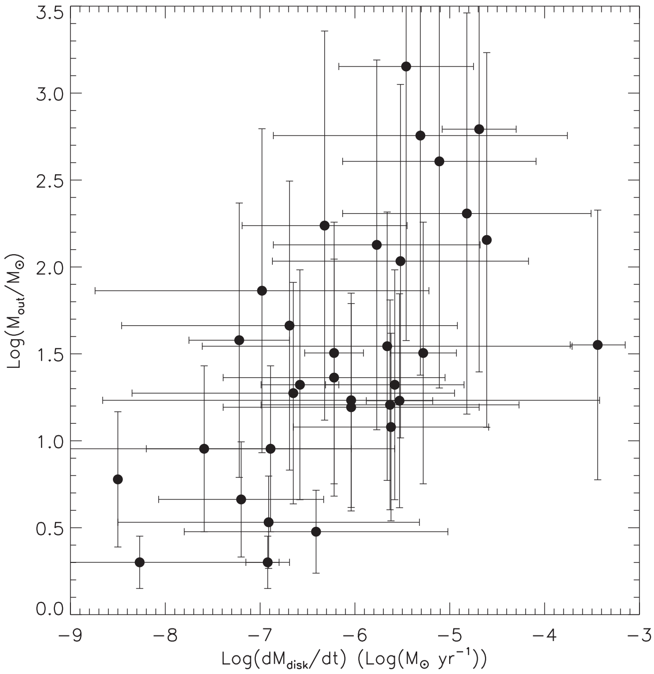

(a)

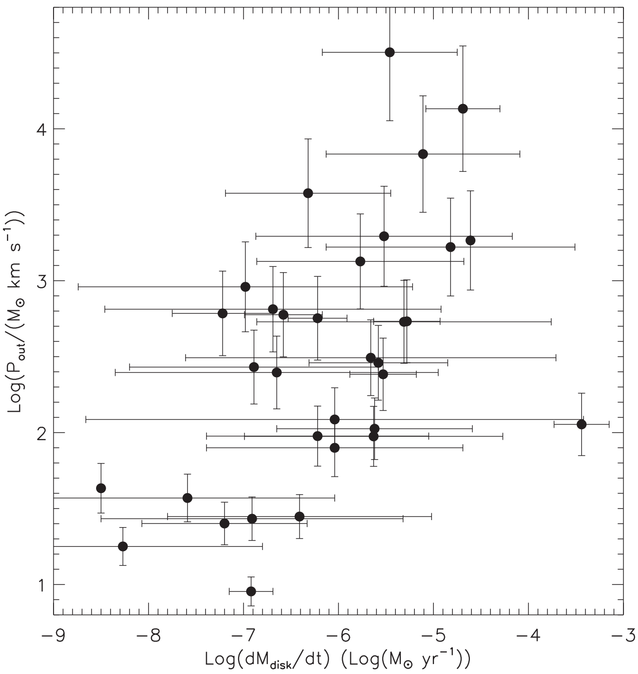

(b)

Fig. 2.6: a: Observed outflow mass is shown as a function of model-obtained disk accretion rate of the HMPOs. b: Outflow momentum vs disk accretion rate.

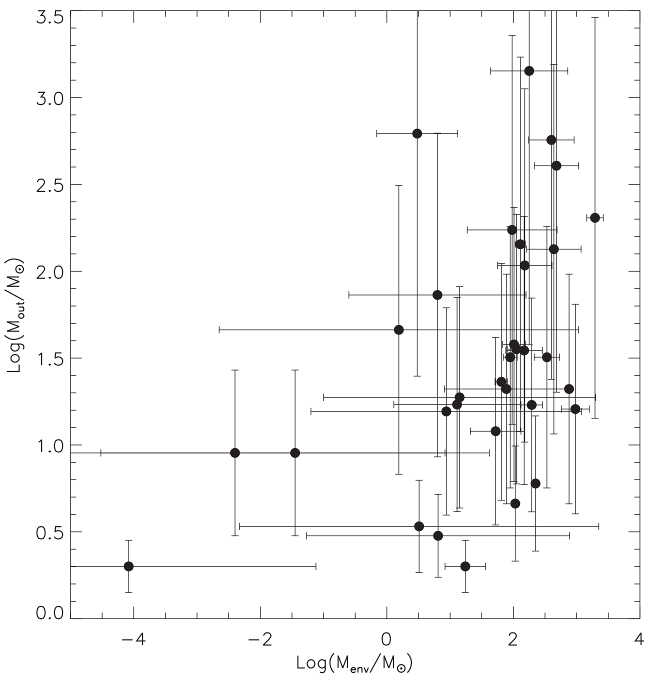

(a)

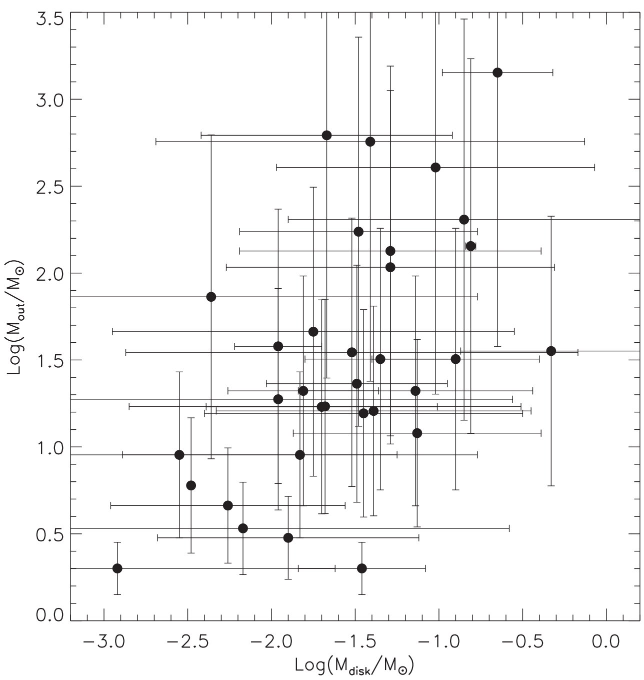

(b)

Fig. 2.7: a: Observed outflow mass is shown as a function of model-obtained envelope mass of the HMPOs. b: Outflow mass vs disk mass.

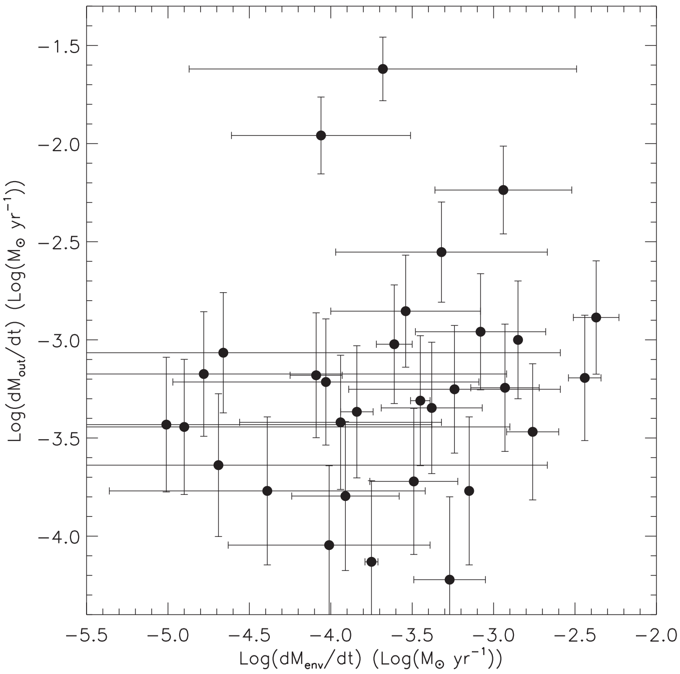

(a)

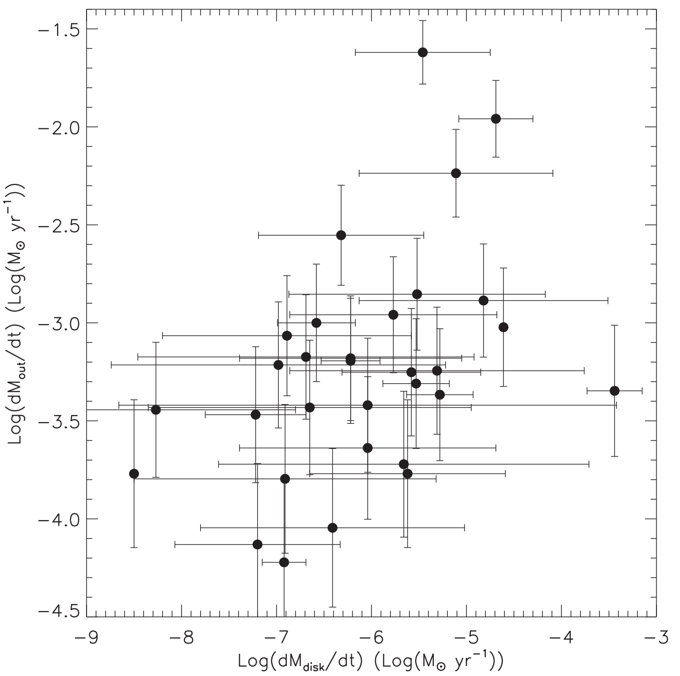

(b)

Fig. 2.8: a: Observed outflow entrainment rate is shown as a function of model-obtained envelope accretion rate of the HMPOs. b: Outflow entrainment rate vs disk accretion rate.

cretion mechanism. Measuring disk accretion rates is observationally challenging. For massive stars, it is obtained by combining the disk surface density from millimeter dust continuum observations with infall velocities from line observations under the assumption of a certain disk geometry and inclination angle (e.g., Beltran et al. 2004). Accretion rates obtained by such measurements are found to be high ($10^{-2} - 10^{-4}$ M$_\odot$ yr^{-1}) which agrees well with the *envelope accretion rates* obtained from SED modeling. It should be noted that the theoretical concepts of disks and envelopes (Pringle 1981; Bjorkman 1997) assumed in the SED modeling and by observational methods such as above are quite similar. However, the SED modeling is an independent way of estimating the accretion rates based on computing the spectral contribution of the disk and envelope (see Robitaille et al. (2006) for details). Our SED modeling shows that the disk accretion rates ($10^{-4} - 10^{-6}$ M$_\odot$ yr^{-1}) are approximately two order of magnitude lower than the envelope accretion rates ($10^{-2} - 10^{-4}$ M$_\odot$ yr^{-1}).

The outflow entrainment rates (used for the study here) obtained by single dish observations by Beuther et al. (2002a) have a relatively smaller spread ($10^{-4} - 10^{-3}$ M$_\odot$ yr^{-1}) (see Fig.2.8) and do not depend critically on the source luminosity. *These entrainment rates are smaller than the modeled $\dot{M}_{env}$ but larger compared to the modeled $\dot{M}_{disk}$. If we suppose that the disks modeled by the SED are responsible for driving the outflow, then we would encounter the problem of throwing out more matter than we are putting into the system*. Interestingly, high spatial resolution observations of some of these massive sources, made with the Sub-Millimeter Array (JCMT) and Plateau de Bure Interferometer, resolve the outflows into multiple components and the entrainment rates of the individual components are $\sim 10^{-5}$ M$_\odot$ yr^{-1} (Palau et al. 2007a,b), which is in better agreement with the modeled $\dot{M}_{disk}$ values. It was argued by Grave and Kumar (2009) that the SED modeling may not be very sensitive to the disks for massive embedded sources, which may be the reason why the outflow entrainment rates are consistent with $\dot{M}_{env}$ rather than $\dot{M}_{disk}$. Alternatively, these facts allow us to speculate: (i) that the massive molecular outflows are probably composed of multiple components, or (ii) that the massive molecular outflows may be driven by larger scale envelopes. These speculations are based on the observational evidences from mm interferometric observations of massive cores that display large scale flattened structures and circumcluster toroids (Cesaroni et al. 2006).

Given that our SED modeling largely relies upon high spatial resolution data, in particular, the IRAC bands and NIR bands, with about $1''$ resolution, the modeled sources represent relatively isolated or point sources. First, the outflow entrainment rates are consistent with the modeled envelope accretion rates and NOT with the disk accretion rates. Second, the observational evidences for disks around massive protostars is little. Although the disks are thought to be present (e.g., Cesaroni et al. (2003)), the most common observational evidences are flattened rotating structures which are called circumstellar toroids (Cesaroni et al. 2006; Furuya et al. 2008). Recent outflow models by Machida et al. (2008) demonstrate that the large scale infalling envelope which produces the first core (see the last figure in their paper) is responsible for launching the poorly collimated component of the outflows. The characteristic feature of this component is the lower velocity and poor collimation. In contrast, the fast, highly collimated central jet is thought to be driven by the central (second) core, launched closer to the protostar and from the inner disk. In this scenario, the outflows from the HMPO candidates can be explained as the poorly collimated low velocity wind launched in the larger infalling envelopes. It can then explain the measured outflow entrainment rates and the apparently poor collimation factors of outflows from HMPO sources compared to their low mass counterparts (Kumar et al. 2002; Beuther et al. 2002).

The positive connection between the outflow entrainment rates and accretion rates points to a magneto-hydrodynamic origin (Konigl and Pudritz 2000) of the outflows even in the massive stars. The real problem for now is the lack of clear observational data that can disentangle disks and envelopes around massive stars and measure accretion rates from each entity.

A total of 95 HMPO candidates have been observed in CO emission line (69 by Zhang et al. (2005) and 26 by Beuther et al. (2002a)) and 86 of these objects showed spatially confined CO emission with high velocity features attributed to outflows. The mean velocity of the line wing emission measured from these observations is $\sim$ 20-30 km s^{-1}. Even the "jet-like" outflows from massive stars such as IRAS 20126+4104 (Cesaroni et al. 1999; Su et al. 2007), IRAS 18566+0408 (Zhang et al. 2007) and IRAS 05358+3543 (Beuther et al. 2002b) display velocities of only up to 40 km s^{-1}. Outflows from low mass stars also have similar mean velocities (30 km s^{-1}) (Bachiller 1996; Arce et al. 2007), but several jet-like outflows show intermediate and extremely high velocity components (IHV and EHV). L1448 IRS3 (Bachiller et al. 1990) and IRAS 04166+2706 (Santiago-Garcia et al. 2009) have IHV components of $\sim$ 50 km s^{-1}; while sources such as HH7-11 display EHV as high as 100-140 km s^{-1} (Bachiller and Cernicharo 1990). While the outflows from

HMPO sources stand up against the low mass objects in terms of total mass and momenta, the high mass outflows do not show either the IHV or EHV components found in the low mass outflows. It may be noted that even the Shepherd and Churchwell (1996) sample, which included sources with luminosity even higher than studied here, does not display the IHV and EHV components in the CO spectra. The lack of these high velocity components can not be entirely attributed to a lower sensitivity at the large source distances. Therefore, we speculate that the lack of IHV and EHV components in massive protostars is possibly related to the origin of the outflows.

2.1.6 Summary and Future Work

We have examined the relations between the properties of 33 massive molecular outflows and of their driving protostars. Several trends were found in the scatter diagrams, which are in accordance to previously known relations from the studies of outflows from low mass stars.

- The mass and momentum of the outflow tend to scale directly as the mass of the star and inversely as the age of the star.
- The outflow mass and momentum also show similar but weaker trends with the accretion rate.
- The outflow entrainment rates obtained from single dish measurements can be explained by the modeled envelope accretion rates rather than the disk accretion rates.
- The modeled disk accretion rates are in better agreement with the individual components of the outflows, resolved by interferometric observations.

Most observational data of intermediate and massive protostars are suggestive of the wind driven origin for the outflows. However, our results point to a scenario where the wind is driven from envelopes rather than disks. This is because the outflow entrainment rates are about two orders of magnitude larger than disk accretion rates. Unambiguous identification and characterisation of disks and envelopes in isolated massive protostars with outflows are necessary to understand the true connection between the outflow and the protostar. More importantly, it is necessary to identify independent indicators of accretion rates, similar to the emission lines of magnetospheric origin in low mass stars. Such results are expected to be possible with future high resolution facilities such as the Atacama Large Millimeter Array and the James Webb Space Telescope.

2.2 Physical Properties of the driving engine of Ultra-Compact HII (UCHII) regions

The study of the embedded photospheres of the HMPOs (younger stages than UCHII regions) revealed that they are associated with early B stars and not many O stars are detected. The central ionising sources of the UCHII regions, in comparison, are known to be O and early B stars (Beuther et al. 2002; Grave and Kumar 2009). In this section, we present the identification of the driving engines of the UCHII regions and characterisation of their associated physical parameters through SED modeling. UCHII regions are characterised by sizes < 0.1 pc, large electron densities $n_e \geq 10^4$ cm^{-3} and temperatures $T_e \approx 10000$ K. These regions are referred to as one of the most reliable tracers of massive star formation (stars of type earlier than $\sim$ B3). The UCHII regions are known as a little more evolved stage of massive star formation than the HMPOs (as mentioned in Chapter 1). In this evolutionary stage, the central young massive star is hot enough to produce Lyman continuum photons that ionise the surrounding regions. Nevertheless, many of them are still deeply embedded and are not optically visible. The driving engine of UCHII regions can be identified in mid-IR due to lower extinction in these wavelengths. *Spitzer*-IRAC/GLIMPSE (mid-IR) data for a significant sample of such objects are available. The recent sub-millimeter survey by Thompson et al. (2006) provided an opportunity to model the SED from infrared to (sub-)millimeter in a similar way as for HMPOs, to obtain the properties of the driving engines of the outflows.

The main goal of this work is to use the SED modeling in the framework of an accretion scenario and analyse the derived properties of the central stars, in particular, to see if the central stars of UCHII regions have photospheres suffering large extinction, and/or accreting protostars. We discussed earlier about the advantage of SED modeling using available high spatial resolution data on mid-infrared region compared to previous mid/far-infrared surveys like MSX and IRAS.

2.2.1 Data selection

We looked into the catalogs of sub-mm observations of the UCHII regions (Thompson et al. 2006) and available *Spitzer*-IRAC/Glimpse archive. We followed a similar procedure to identify the mid-IR counterpart of the driving engine of a UCHII region as described in the first part of this chapter. Since some UCHII regions are found to have more than one counterpart we found 56 infrared counterparts (for a total of 42 UCHII regions) of the driving engines of UCHII regions using of *Spitzer*-IRAC/Glimpse archive. This multiplicity may have arisen because of the fact that the sub-mm observations (in 450 and 850 μm) (Thompson et al. 2006) have a large beam size (8-14$''$) compared to IRAC observations (about 2$''$ spatial resolution in all four bands). Table 2.1 gives the positions of the UCHII driving engines and their offsets (in arcsecond) from the peak of sub-mm positions. Some of the UCHII regions have multiple infrared counterparts which are also included in Table 2.1. There is a distance ambiguity (near and far distances) for 6 sources. Photometry data for 43 sources (total 32 UCHII regions) were taken from Glimpse data base and 13 sources (10 UCHII regions) were extracted from the individual observing program ID's 3528 (PI: Q. Zhang; one source), 6 (PI: G. Fazio, four sources), 623 (PI: G. Fazio, two sources), 20778 (PI: Sean Carey; four sources), 30726 (PI: Jeroen Bouwman; one source) and 201 (PI: Giovanni Fazio; one source).

Three colour-composite IRAC images of all the 42 UCHII regions along with the identified 56 central sources (marked by orange circles) are shown in the Figure B.1 of Appendix B. It may be noted that the source of G133.95+1.06 region has only two IRAC images (Ch4 and Ch2), therefore 2MASS K-band was used to make the 3-colour-composite image.

2.2.2 SED modeling of the driving engines of UCHII regions

The SEDs were modeled using the SED fitting tool of Robitaille et al. (2007) for all the 56 sources (separately for sources having near and far distances, i.e., six sources). The fitted SEDs are strongly constrained by the high spatial resolution data between 1 - 8 μm from near-infrared (JHK) and *Spitzer*-IRAC. In addition, we have used MSX, IRAS, sub-mm (Thompson et al. 2006) and published data at different wavelengths (Alvarez et al. 2004; Cabrera-Lavers et al. 2006; De Buizer et al. 2003; de Wit et al. 2009; Fang and Yao 2004; Faundez et al. 2004; Giveon et al. 2007; Hill et al. 2006; Hunter et al. 2000, 2008; Longmore and Burton 2009; Mueller et al. 2002; Pozzo et al. 2003; Qiu et al. 2008), wherever available. Figure 2.9 shows a typical example of the driving engine of UCHII region using IRAC colour-composite image (left side) and its fitted SED plot (right side). Table B.1 of Appendix B gives the weighted mean values of the model-derived physical parameters, viz. age, mass, temperature, luminosity, radius of the central driving engine, and envelope and disk masses and accretion rates; along with the corresponding standard deviations. Additionally, the first two columns give the name of the source and χ^2 per

Table 2.2: Driving engines of the UCHII regions with their positions and offsets(in arcsec) from the sub-mm peaks. Sources having distance ambiguity are represented by the symbol '†'. The images of the sources marked with '⋆' are generated by mosaicing IRAC BCD images.

id	Source	RA [2000]	Dec [2000]	offset($''$)
1	G5.89-0.39	18:00:30.46	-24:04:01.1	07.44
2	G6.55-0.10	18:00:50.00	-23:20:33.1	05.01
3	G8.14+0.23smmb	18:03:00.96	-21:48:07.5	08.72
4	G10.30-0.15smma1	18:08:55.60	-20:05:57.3	09.67
5	G10.30-0.15smma2	18:08:55.96	-20:06:05.5	04.84
6	G10.62-0.38a1	18:10:28.68	-19:55:54.2	05.51
7	G10.62-0.38a2	18:10:28.86	-19:55:49.0	02.77
8	G10.62-0.38a3	18:10:28.49	-19:55:49.9	07.28
9	G10.84-2.59⋆	18:19:12.11	-20:47:31.0	07.03
10	G11.94-0.62smma	18:14:01.12	-18:53:26.5	06.41
11	G18.30-0.39smma	18:25:41.95	-13:10:19.7	01.88
12	G19.07-0.27	18:26:48.91	-12:26:24.4	01.44
13	G20.08-0.14smma1	18:28:10.36	-11:28:48.5	03.35
14	G20.08-0.14smma2	18:28:10.53	-11:28:50.9	01.00
15	G20.08-0.14smmb	18:28:10.80	-11:29:28.4	01.98
16	G23.46-0.20	18:34:44.93	-08:31:07.4	07.95
17	G23.87-0.12smma†	18:35:12.77	-08:06:50.6	10.00
18	G23.87-0.12smmb†	18:35:14.38	-08:06:48.9	06.82
19	G25.72+0.05smmb	18:38:03.15	-06:24:15.2	03.81
20	G26.54+0.42smmb†	18:38:16.06	-05:29:32.9	06.66
21	G27.49+0.19smma†	18:40:50.00	-04:45:12.1	04.95
22	G28.20-0.05	18:42:58.10	-04:13:57.3	05.83
23	G31.28+0.06	18:48:12.38	-01:26:30.4	01.90
24	G31.40-0.26smma	18:49:33.01	-01:29:05.0	02.85
25	G32.80+0.19a	18:50:30.97	-00:01:55.3	06.22
26	G32.80+0.19b	18:50:30.68	-00:02:00.3	01.87
27	G33.13-0.09a	18:52:08.35	00:08:07.2	02.89
28	G33.13-0.09b	18:52:07.94	00:08:12.0	04.89
29	G33.13-0.09c	18:52:08.30	00:08:12.8	04.09
30	G33.13-0.09d	18:52:08.37	00:08:16.7	08.08

Table 2.2: contd.

id	Source	RA [2000]	Dec [2000]	offset($''$)
31	G33.92+0.11s1	18:52:50.22	00:55:28.8	02.85
32	G33.92+0.11s2	18:52:49.66	00:55:24.5	02.97
33	G34.26+0.15smma	18:53:18.57	01:14:57.9	03.93
34	G35.02+0.35	18:54:00.55	02:01:18.0	03.11
35	G35.57+0.07	18:56:01.51	02:22:59.8	01.66
36	G35.58-0.03	18:56:22.59	02:20:27.7	02.35
37	G37.55-0.11	19:00:16.04	04:03:18.9	08.78
38	G37.77-0.20	19:01:02.01	04:12:01.5	04.58
39	G37.87-0.40	19:01:53.60	04:12:49.6	03.04
40	G41.74+0.10a†	19:07:15.54	+07:52:44.0	03.84
41	G41.74+0.10b†	19:07:15.34	+07:52:46.8	05.35
42	G42.42-0.27smmb	19:09:49.95	+08:19:44.0	02.23
43	G43.18-0.52smma1	19:12:09.00	+08:52:12.9	01.93
44	G43.18-0.52smma2	19:12:09.60	08:52:07.9	09.43
45	G43.80-0.13	19:11:54.01	+09:35:49.9	01.63
46	G45.07+0.13	19:13:22.10	+10:50:53.4	03.81
47	G45.12+0.13	19:13:27.85	+10:53:35.7	04.05
48	G70.29+1.60*	20:01:45.74	+33:32:42.4	02.28
49	G76.38-0.62smmb*	20:27:26.62	+37:22:47.9	06.45
50	G106.80+5.31smma2*	22:19:19.77	+63:18:49.6	11.03
51	G106.80+5.31smma3*	22:19:18.23	+63:19:03.8	06.59
52	G110.21+2.63smmb	22:57:02.15	+62:38:25.1	05.37
53	G111.28-0.66smma*	23:16:04.82	+60:01:58.9	06.66
54	G133.95+1.06*	02:27:03.87	+61:52:24.8	06.13
55	G138.30+1.56*	03:01:31.32	+60:29:13.1	07.79
56	G213.88-11.84*	06:10:50.33	-06:11:57.8	12.12

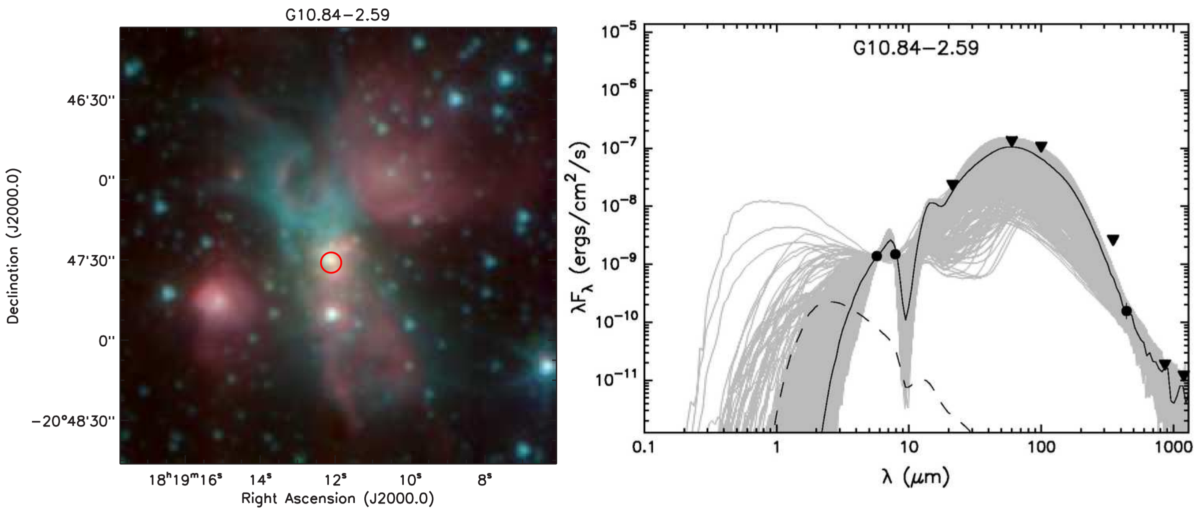

Fig. 2.9: An example of the location of a driving engine of the UCHII region G10.84-2.59 using IRAC 3-colour-composite image (Ch4(red), Ch2(green) and Ch1(blue)). On the right side is the corresponding SED model plot.

data point. The SED fitted plots are also shown in Figure B.2 for all the sources. For six sources, the SED modeling was done for both the near and far distances separately whose results are shown in the Table B.1.

2.2.3 Results and Discussion

Figure 2.10 shows the distribution of mass, age and temperature for all the fitted sources compared with the full model grid. These histograms are presented with the normalised frequency in order to compare them with the grid distribution. The dotted blue line represents the results for the sources without distance ambiguity. For the sources having distance ambiguity, the short dashed red line represents the near distance and the long dashed black line represents the far distance. In all the subsequent plots, for the sources having distance ambiguity (total six), we use values of parameters corresponding to the far distances. The solid orange line represents the histograms of the full model grid (200,000 models). It can be inferred from Figure 2.10 that the derived SED results are not biased with the inherent trend in the model grid. We found that the masses of the sources are between $\sim$ 5 - 43 $M_\odot$ with a median mass about 12.9 $M_\odot$; while the total luminosities are between $10^{2.7}$ and $10^{5.6}$ $L_\odot$. All the fitted sources have a median stellar age of $\sim 10^{4.5}$ years (in the range of $\sim 10^{3.5-6.5}$ years) showing that many of the sources are very young. We obtained the radii of photospheres typically large, in the range between 3 - 250 $R_\odot$. The stellar temperatures

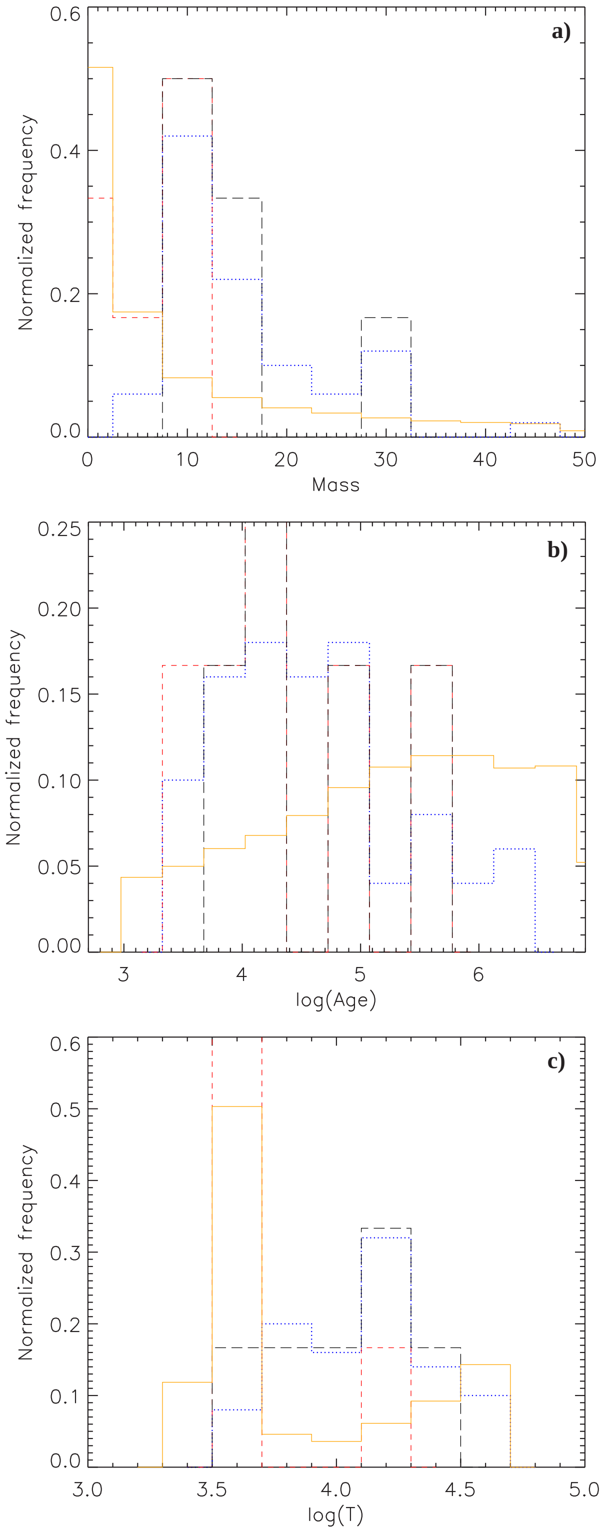

Fig. 2.10: Histograms of physical parameters: a) stellar mass; b) stellar age and c) stellar temperature for all the 56 sources. Figure shows the distributions of the sources without any distance ambiguity with a dotted blue line. For the sources having distance ambiguity, distributions corresponding to the near distances shown by short dashed red line; and those corresponding to the far distances are shown by long dashed black line. All the models in the grid of Robitaille et al. (2006) are shown by the solid orange line.

are between 4300 - 40000 K.

Figure 2.11 represents the H-R diagram (luminosity vs temperature) of all 56 sources with zero-age main sequence (ZAMS) up-to 7 $M_\odot$ from Siess et al. (2000) and birth line above 7 $M_\odot$ from Bernasconi and Maeder (1996). The largest and smallest circles in Fig. 2.11 show the youngest and oldest sources respectively; the size of the circle going inversely with age. As can be seen in the figure, old sources (small circles) are close to the ZAMS locus and young sources are approaching the ZAMS. Geneva isochrones (dashed lines) and mass evolutionary tracks (dotted lines) upto 7 $M_\odot$ are overplotted in the H-R diagram. Most of the sources are young massive stars (above the 7 $M_\odot$ mass evolutionary tracks) approaching ZAMS stage. These sources are identified as the infrared counterpart(s) of the driving engine of UCHII region. The sources may be associated with powerful ionised winds or accretion flows at a very early stage of formation.

We have plotted the total luminosity against stellar mass for all the sources (see Fig. 2.12a). The symbols and error bars in the figure represent the weighted mean and standard deviations obtained from the SED modeling. It shows a very tight correlation between stellar mass and total luminosity of the sources. It indicates that the mass increases with luminosity as follows:

$$L \sim 10^{0.4\pm0.1} \times M^{3.2\pm0.1} \tag{2.2}$$

Stellar temperature and mass are plotted against stellar radii in Figs. 2.12b and 2.13a. Our results show that the temperature decreases with stellar radii and stellar mass increases with stellar radii. Fig. 2.13b exhibits the decreasing trend between disk mass and age of sources as expected. Similarly, as shown in Fig. 2.14a envelope mass also decreases with age, as expected. We have found the median values of the disk ($\dot{M}_{disk}$) and envelope accretion rates ($\dot{M}_{env}$) to be $\sim 10^{-5.8}$ and $10^{-3.6}$ $M_\odot$ yr^{-1} respectively. Our results show that in general the envelope accretion rates for the sources are higher than the disk accretion rates. Disk and envelope accretion rates are plotted against the age in Figs. 2.14b and 2.15a. These plots show that the accretion rates decrease with age. Figures 2.15b and 2.16a exhibit an increasing trend between disk/envelope accretion rate and stellar radii. Recently, Takashi and Kazuyuki (2009) studied using numerical simulations the evolution of massive protostars with high accretion rates and found stellar radii are larger for the sources having

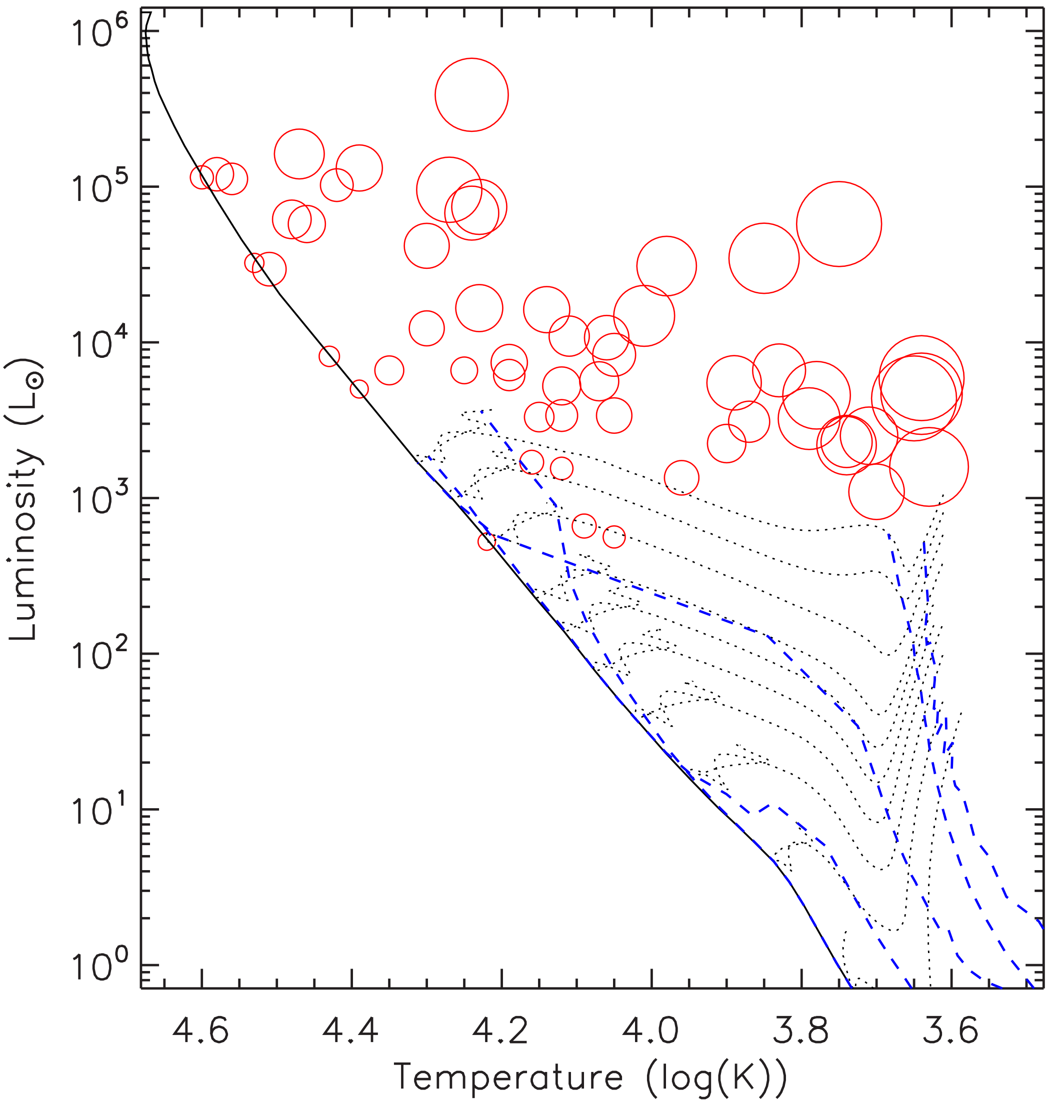

Fig. 2.11: Exhibits the stellar luminosity vs stellar temperature (H-R diagram): solid line represents the birth-line track (above 7 $M_\odot$ Bernasconi and Maeder (1996)) and ZAMS (up-to 7 $M_\odot$ from Siess et al. (2000)). Geneva isochrones up-to 7 $M_\odot$ are shown by dashed blue lines with ages of 8, 7, 6, 5 and 4 in log units (years) from left to right. Dotted lines show the mass evolutionary tracks for 0.1, 1.0, 1.5, 2, 2.5, 3.0, 3.5, 4.0, 5.0, 6.0 and 7.0 $M_\odot$ from lower to higher values of the luminosity respectively (Siess et al. 2000) (see text for more details).

higher accretion rates. Our results are consistent with these theoretical simulations. The disk and envelope accretion rates are plotted against the stellar mass in Figs. 2.16b and 2.17. We have estimated the the dependence of the disk and envelope accretion rates with stellar mass. We found that the envelope accretion rate scales with stellar mass by the following power law relation:

$$\dot{M}_{env} = 10^{-6.6\pm0.7} \times M^{2.6\pm0.6} \tag{2.3}$$

It is known that some of the UCHII regions are associated with ionised inward flow (Keto 2002a; Keto and Wood 2006), therefore it may possible that the ionised accretion with high rate is important for massive star formation. However, our SED modeling results predict very high (envelope) accretion rates, even without taking ionised accretion flows into account. Therefore, it calls for (i) improved SED modeling to take into account the ionised flows, non-spherical accretion and envelope accretion luminosity; and (ii) observations that unambiguously identify and characterise disks and envelopes.

2.2.4 Comparison of SED results: HMPOs and UCHII regions

It may be instructive to compare the physical parameters obtained from SED modeling for HMPOs (33 sources) with those of the UCHII regions (48 regions). The following table gives a few parameters for the comparison:

Physical Parameters	HMPOs	UCHII regions
Mass range (median mass)	3 - 38 $M_\odot$ ($\sim$ 10.2 $M_\odot$)	5 - 43 $M_\odot$ ($\sim$ 12.9 $M_\odot$)
Age range (median age)	$10^{3.2-6.0}$ yr ($\sim 10^{4.4}$ yr)	$10^{3.5-6.5}$ yr ($\sim 10^{4.5}$ yr)
Temperature range	4300 - 35500 K	4300 - 40000 K
Median $\dot{M}_{disk}$ and $\dot{M}_{env}$	$10^{-6.0}$ and $10^{-3.6}$ $M_\odot$ yr^{-1}	$10^{-5.8}$ and $10^{-3.6}$ $M_\odot$ yr^{-1}

One may notice that there is no significant difference between the derived physical parameters of HMPOs and UCHII regions.

The UCHII regions are traced by the detection of free-free emission, whereas HMPOs are characterised by the lack of free-free emission and presence of strong dust continuum emission. The models of massive YSOs in the tool grid assume an accretion scenario and are scaled up versions of the processes leading to low-mass star-formation (Robitaille et al.

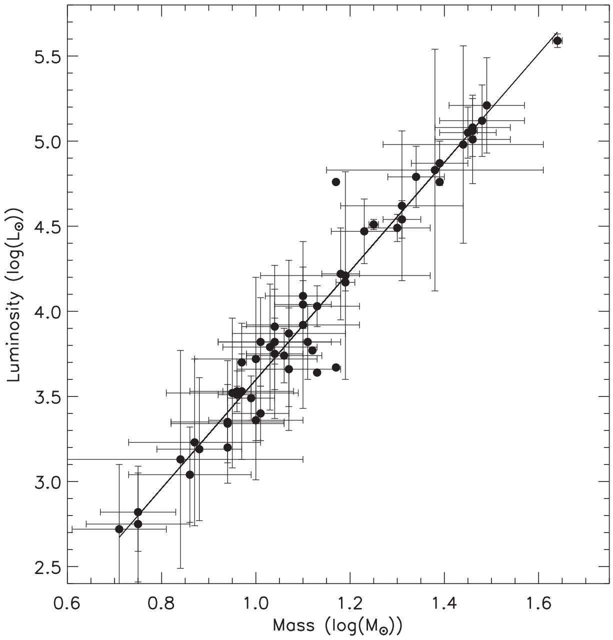

(a)

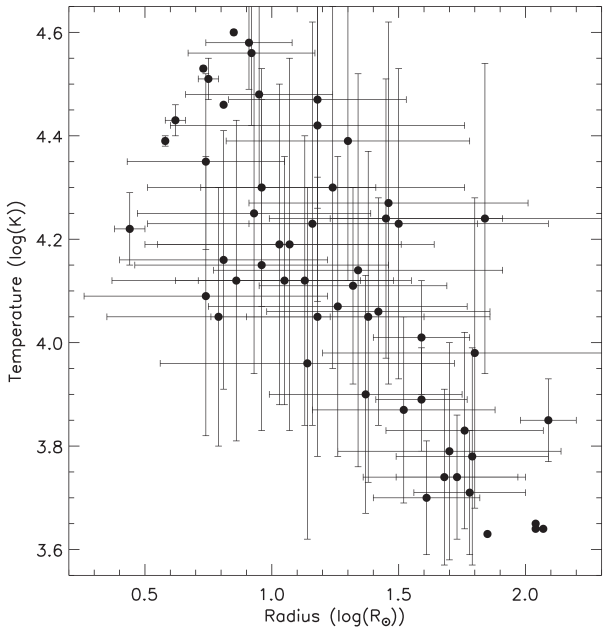

(b)

Fig. 2.12: a: Shows model-derived total luminosity as a function of mass of the driving engines of the sample UCHII regions. The solid line is the linear fit: $L \sim 10^{0.4\pm0.1} \times M^{3.2\pm0.1}$. b: The Scatter diagram shows the model-derived stellar temperature vs stellar radius for the driving engine of the UCHII regions.

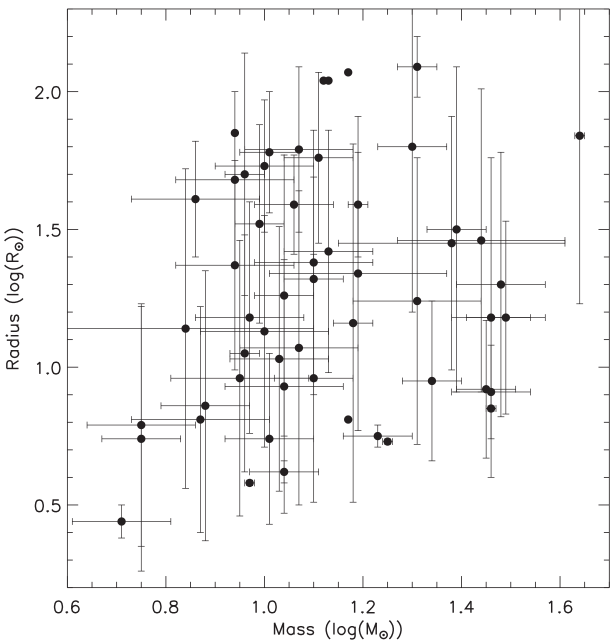

(a)

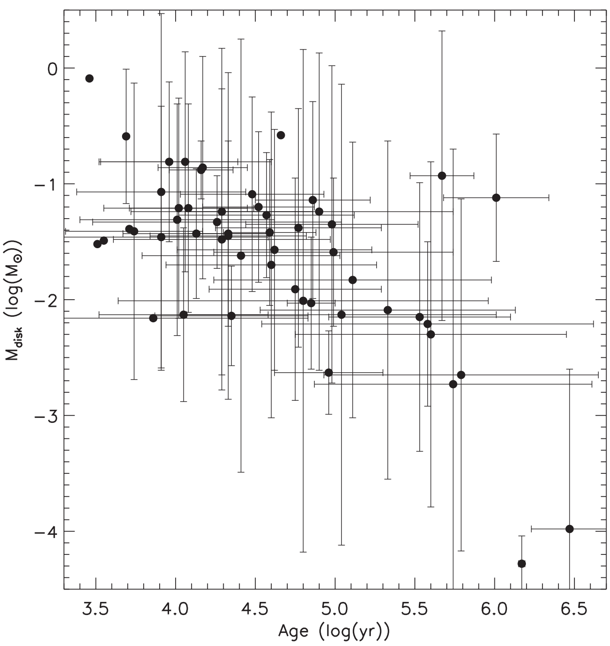

(b)

Fig. 2.13: a: The Scatter diagram shows the model-derived stellar mass vs stellar radius for the driving engine of the UCHII regions. b: The Scatter diagram shows the model-derived disk mass vs stellar age for the driving engine of the UCHII regions.

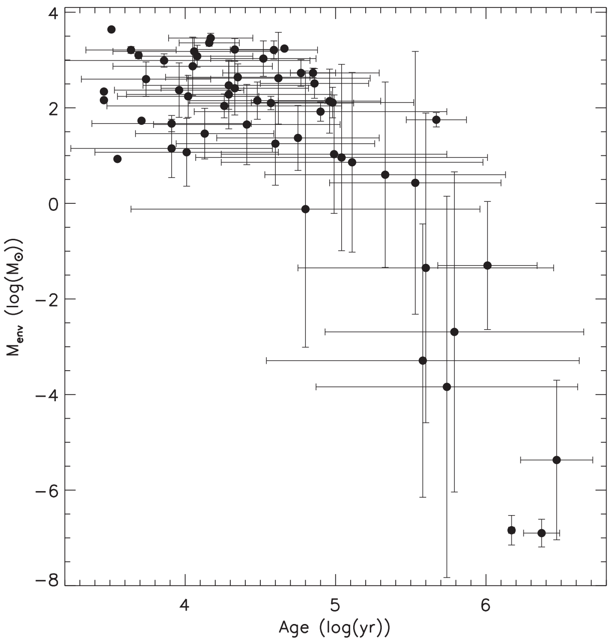

(a)

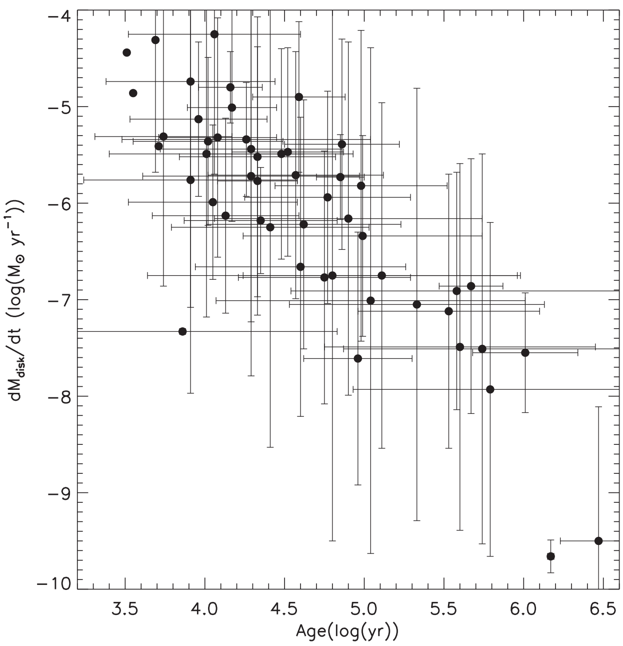

(b)

Fig. 2.14: a: The Scatter diagram shows the model-derived envelope mass vs stellar age for the driving engine of the UCHII regions. b: The Scatter diagram shows the model-derived disk accretion rate vs stellar age for the driving engine of the UCHII regions.

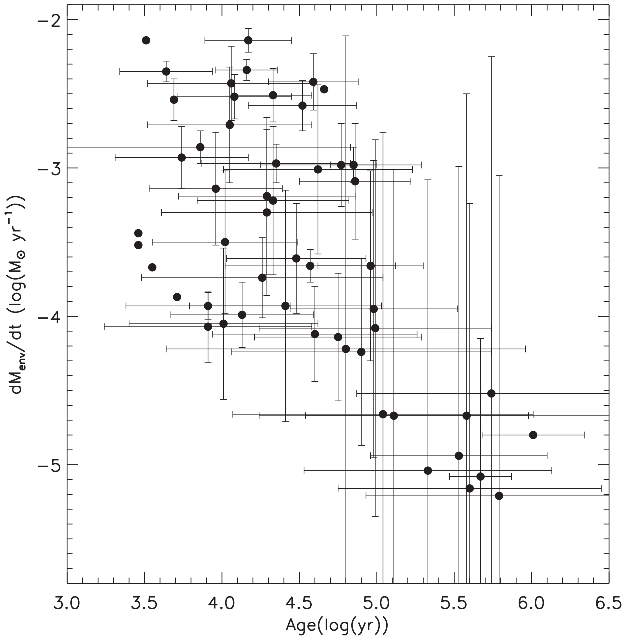

(a)

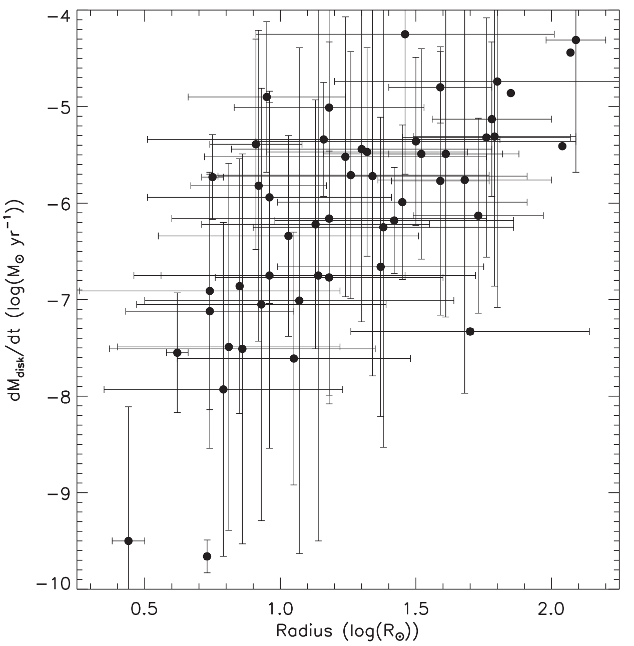

(b)

Fig. 2.15: a: The Scatter diagram shows the model-derived envelope accretion rate vs stellar age for the driving engine of the UCHII regions. b: The Scatter diagram shows the model-derived disk accretion rate vs stellar radius for the driving engine of the UCHII regions.

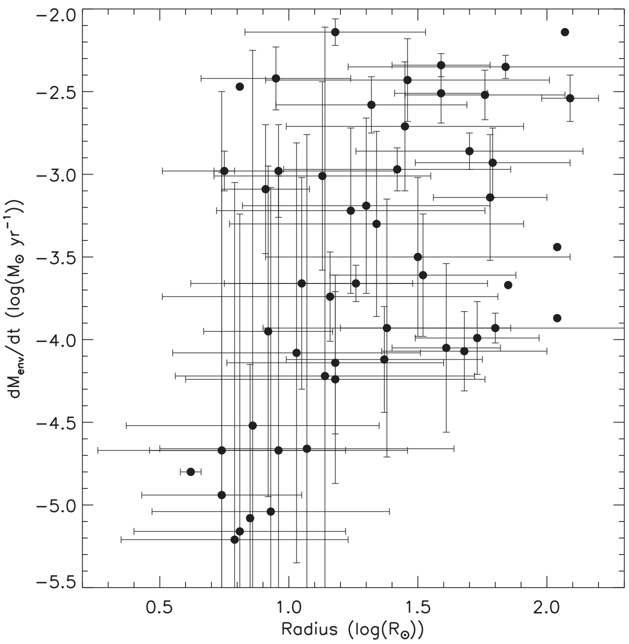

(a)

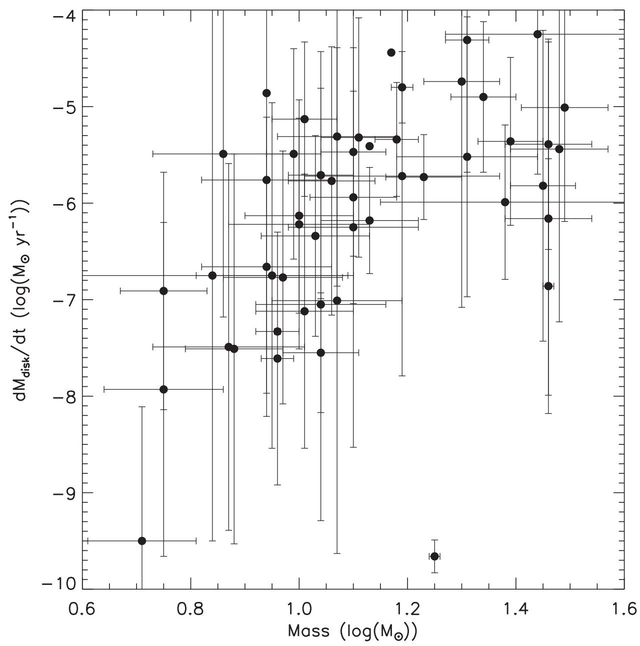

(b)

Fig. 2.16: a: The Scatter diagram shows the model-derived envelope accretion rate vs stellar radius for the driving engine of the UCHII regions. b: The Scatter diagram shows the model-derived disk accretion rate vs stellar mass for the driving engine of the UCHII regions.

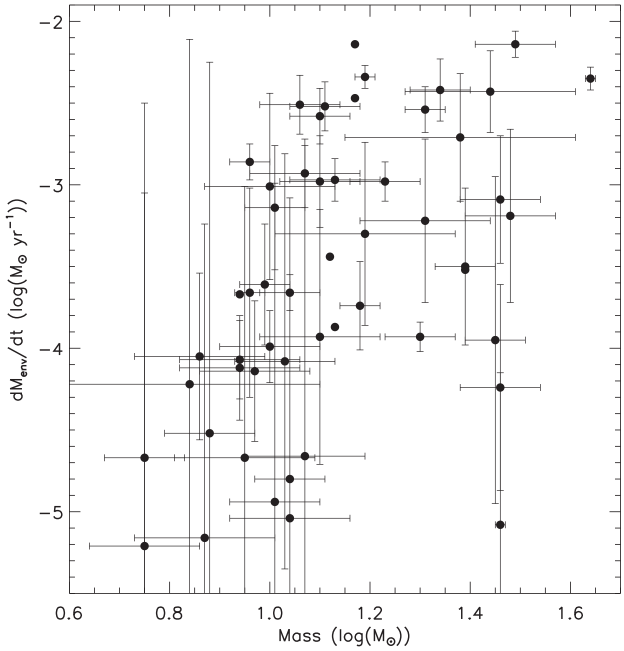

Fig. 2.17: The Scatter diagram shows the model-derived envelope accretion rate vs stellar mass for the driving engine of the UCHII regions.

2006). The SED models give the disk accretion luminosities for all mass ranges but does not consider the accretion luminosity from envelopes. However, it is believed that the accretion luminosity from envelopes have significant importance for sources having masses larger than 20 $M_\odot$. Further, the geometries assumed in the grid of SED models may not be appropriate for masses above 20 $M_\odot$ (Robitaille et al. 2006). These limitations in the SED models reflect probably as over-estimations of the results on sources having masses above 20 $M_\odot$. Still, the results (trends from scatter diagrams of the model-derived physical properties) obtained from the SED modeling for the driving engines of UCHII regions are consistent with the results of numerical simulations of Takashi and Kazuyuki (2009) on the evolution of massive protostars with high accretion rates.

2.2.5 Conclusions

The SED modeling of the UCHII regions gives the following physical parameters for their driving infrared counterparts:

a) Ranges and median values of the various physical parameters:

Mass range (median mass)	$\sim$ 5 - 43 $M_\odot$ ($\sim$ 12.9 $M_\odot$)
Age range (median age)	$\sim 10^{3.5-6.5}$ yr ($\sim 10^{4.5}$ yr)
Radii range	$\sim$ 3 - 250 $R_\odot$
Temperature range	$\sim$ 4300 - 40000 K
Median disk and envelope accretion rate	$\sim 10^{-5.8}$ and $10^{-3.6}$ $M_\odot$ yr^{-1}

b) Envelope and disk masses decrease with stellar age.

c) Envelope and disk accretion rates decrease with stellar age.

d) Mass and luminosity have a tight correlation: $L \sim 10^{0.4\pm0.1} \times M^{3.2\pm0.1}$

e) The higher the accretion rate (both disk and envelope), the larger the radii of the sources.

f) Temperature decreases with increasing radii of sources.

g) The envelope accretion rate has a power law relation with stellar mass:
$\dot{M}_{env} = 10^{-6.6\pm0.7} \times M^{2.6\pm0.6}$.

The parameters derived for UCHII regions are very similar to those obtained for HMPOs.

Chapter 3

Spitzer-IRAC imaging photometric study of the massive star forming region AFGL 437

In this chapter, we present *Spitzer*-IRAC mid-infrared photometry of one massive star forming region AFGL 437. The region harbours early B type stars and a young source associated with powerful outflows.

3.1 Introduction

Compact clusters embedded in giant molecular clouds provide an opportunity to study recent star formation over a wide range of masses in a small volume (e.g., Lada and Lada (2003)). Due to the large visual extinction suffered by the protostars in such clusters, infrared, especially mid- and far-infrared, observations help in studying them. AFGL 437 (IRAS 03035+5819; G139.909+0.197) is one such compact embedded cluster of size $\sim$ $15''$ (Kleinmann et al. 1977; Lada and Lada 2003) situated at a distance of 2.0 $\pm$ 0.5 kpc (Arquilla and Goldsmith 1984) and having a total luminosity of $\sim$2 $\times$ 10^4 $L_\odot$ (Weintraub and Kastner 1996). The cluster is associated with an optical reflection nebula and contains at least four embedded sources called AFGL 437N, S, E and W (Cohen and Kuhi 1977). Rainer and McLean (1987) and later Weintraub and Kastner (1996) resolved a highly embedded source known as WK 34, $\sim$$2.5''$ to the South-East of AFGL 437N. The bright sources in the cluster suffer a large extinction of A_v $\sim$ 7 mag (Cohen and Kuhi 1977). Radio observations revealed that AFGL 437W and S, identified as early B type ZAMS stars, are associated with Ultra-Compact (UC) H II regions (Wynn-Williams et al. 1981; Torrelles et al. 1992; Kurtz et al. 1994). Wynn-Williams et al. (1981) and Torrelles et al. (1992) have detected water masers towards AFGL 437N and W, which indicate the youth of the region of star formation. Gomez et al. (1992) found a compact, poorly collimated bipolar CO outflow oriented in North-South direction. Studies of the cluster in near-IR polarimetry (Weintraub and Kastner 1996) and diffraction-limited imaging in 3.8 μm (Weintraub et al. 1996) have attributed the outflow to the highly-embedded, low-luminosity source WK 34; this was later confirmed by the HST polarimetric imaging studies (Meakin et al. 2005). HST results showed further that the reflection nebulosity is due to the source WK 34. Davis et al. (1998) found H_2 emission 'wisps' towards the south-west of the compact cluster, but not associated with the outflow. Recent high-resolution $C^{18}O$ study of the region by Saito et al. (2006, 2007) revealed a few dense cores/clumps around the central cluster in AFGL 437, indicating star formation activity in the region and de Wit et al. (2009) provided spatially resolved 24.5 μm observation on the main sources of the cluster. Sub-mm/mm observations of the cluster were made by Dent et al. (1998) using beam sizes of 16-19$''$ which do not resolve the cluster members. Devine et al. (2008) determined the age of the cluster to be 1-5 Myr. In the background of a number of these important observations and inferences made already on this interesting massive star forming region, our motivation for the present study has been to look into the available (space) infrared imaging observations beyond 3 μm, which have not been studied so far, in order to understand the evolutionary stages of the highly embedded cluster members as well as the regions beyond the cluster and to compare them with the earlier results.

The *Spitzer* Infra-red Array Camera (IRAC) provides an opportunity to study embedded sources in massive star forming regions with an unprecedented high spatial resolution and very good sensitivity in the 3.6 - 8.0 μm wavelength regime. The *Spitzer*-IRAC bands include molecular emissions such as those from H_2 and Polycyclic Aromatic Hydrocarbon (PAH) molecules. The aims of the present study are to identify the embedded sources using the IRAC bands in order to classify the different stages of their evolution; to use ratio maps of the four IRAC bands in order to identify possible H_2 emission regions (or PAH regions) following the suggestion of Smith and Rosen (2005) and Povich et al. (2007); and to present the nebulosity associated with the cluster in all the IRAC bands. Further, we construct SEDs of the identified embedded sources in the cluster using not only the IRAC channels but also observations in JHK bands (Weintraub and Kastner 1996; Meakin et al. 2005), mid-IR (de Wit et al. 2009), sub-mm/mm (Dent et al. 1998) regions; and model the SEDs using the on-line tool developed by Robitaille et al. (2006).

In Section 3.2, we describe the data used for the present study and the analysis tasks utilised. Section 3.3 presents the results on the *Spitzer*-IRAC photometry on 21 embedded sources associated with the dense young cluster AFGL 437. In the same section, we discuss our results in the light of what is already known about AFGL 437. Further in Section 3.3, we present the results and discussion on the ratio maps and on the SED modeling of the YSOs. In Section 3.4, we give the conclusions.

3.2 *Spitzer*-IRAC Data on AFGL 437 and Data Reduction

The *Spitzer* Space Telescope (SST) IRAC archival images were obtained from the Spitzer public archive, using the 'leopard' software (see Fazio et al. (2004), for details on the IRAC instrument). The observations relevant for AFGL 437 were taken in the High Dynamic Range (HDR) mode with 12s integration time in all filters. These observations were a part of the project entitled, "The Role of Photo-dissociation Regions in High Mass Star Formation" (Program id 201; PI: G. Fazio). Basic Calibrated Data (BCDs) images were processed for 'jailbar' removal, saturation and 'muxbleed' correction before making the final mosaic using Mopex and IDL softwares (Makovoz and Marleau 2005). A pixel ratio (defined as the ratio of the area formed by the original pixel scale, 1.22 arcsec/px, to that of the mosaiced pixel scale) of 2 was adopted for making the mosaic (giving a mosaic pixel scale of 0.86 arcsec/pixel) [1]. Using these procedures, a total number of 60 BCD images each of 5.2 $\times$ 5.2 arcmin^2 were mosaiced to make a final image of 17.4 $\times$ 14.2 arcmin^2 commonly in all the four bands. Aperture photometry was performed on the mosaic with 2.8 pixel aperture and sky annuli of 2.8 and 8.5 pixels using the APPHOT task in the IRAF package. The zero points for these apertures (including aperture corrections) were, 17.80, 17.30, 16.70 and 15.88 mag for the 3.6, 4.5, 5.8, 8.0 μm bands, here onwards referred to as Ch1, Ch2, Ch3 and Ch4 respectively. The photometric uncertainties vary between 0.01 to 0.22 for the four channels, with Ch3 and Ch4 on the higher side. Ratio maps were produced from the IRAC channel images by using the standard procedure, with a pixel ratio of 8, that reveals the features prominently.

For the purpose of SED modeling, JHK photometric data were taken from Weintraub and Kastner (1996) and Meakin et al. (2005) as well as from 2MASS archives (Skrutskie et

[1] see http://ssc.spitzer.caltech.edu/dataanalysistools/tools/mopex/mopexusersguide

al. 2006). The 24.5 μm photometric fluxes were obtained from de Wit et al. (2009) (at a diffraction-limited resolution of 0.6″), for the three main sources, WK34, S and W, in the compact central cluster. In addition, the sub-mm/mm data from Dent et al. (1998) were used as upper limits on the central sources, being unresolved due to the large beam sizes. The details of the data compiled on individual sources are given in section 3.3.3. We modeled the SEDs so constructed using the on-line SED-fitting tool due of Robitaille et al. (2006). A criterion χ^2 - $\chi^2_{best} < 3$ was chosen to obtain weighted means and standard deviations of individual physical parameters from sets of models for each object. For the SED modeling, we followed a similar procedure as described in Chapter 2.

3.3 Results and Discussion

Fig. 3.1 shows the IRAC images of the entire extent of AFGL 437 in all four bands and IRAC 3-colour-composite image (Ch1 (blue), Ch2(green) and Ch4 (red)) is presented in Fig. 3.2. The central compact cluster is shown marked by a square box in the Ch3 image (bottom left). As shown in Fig. 3.1, the IRAC 8.0 μm band image (bottom right) reveals a diffuse bubble-/fan-like nebulous structure associated with and extended from the compact cluster in the south-west to the north-east direction (with a size of $\sim$ 8.0 pc). We find that the brightness of the nebulosity gradually increases from 3.6 to 8.0 μm (Ch1-Ch4), as seen in Fig. 3.1. One can also notice in Fig. 3.1, several filamentary structures probably due to the UCHII regions associated with AFGL 437S and W in the compact cluster. Just below the box in the south-west in Fig. 3.1 (between the two arrows in the Ch3 image at bottom left), one can notice a dense cross-/boxcar-shaped structure that seems to be expanding into the surrounding interstellar medium (ISM). It has bright components in NE & SW (separated by $\sim$ 1.70 pc) and in SE & NW (separated by $\sim$ 1.5 pc) directions. The corners of this boxcar-like structure are seen faintly (as 'wisps') in the narrow band H_2 image by Davis et al. (1998). We find that this feature becomes more prominent in longer wavelengths (see Fig. 3.1). It may be possible that this was generated through interaction of stellar wind from the sources AFGL 437W & S with the surrounding dense material. The compact cluster (inside the box in Fig. 3.1: Ch3) is shown enlarged in Fig. 3.3 (in a colour-composite of three images: Ch1 (blue), Ch2(green) and Ch4 (red)), in which we have marked the central main sources namely AFGL 437 N, S, W and WK34 (E is not detected in IRAC) as well as other YSOs identified in the region (see Section 3.3.1).

The compact cluster appears very nebulous in all the four bands. As shown by the earlier authors (e.g., Wynn-Williams et al. (1981)), the source AFGL 437W is associated with a blister HII region. It appears like a diffuse source with its brightness increasing progressively in the four IRAC channels Ch1-4 (and is also seen in the 24.5 μm image by de Wit et al. (2009)). A dense filamentary structure, seen to the right of AFGL 437W in all the bands, is probably associated with the source and extends to about 38.3$''$ (0.4 pc) in NE-SW direction (see Section 3.3.2).

3.3.1 Cluster Sources

The IRAC [3.6]-[4.5] vs [5.8]-[8.0] colour-colour diagram is shown to be a very powerful tool in classifying proto-stellar objects into their evolutionary stages, such as Class 0/I, Class II and Class III (Allen et al. 2004). However, the IRAC colour-colour diagram may give incorrect YSO classifications due to contamination from PAH galaxies, active galactic nuclei (AGNs), unresolved shocked emission knots and PAH-emission aperture contaminations. Gutermuth et al. (2009) proposed selection criteria based on the IRAC magnitude and the colour-colour scheme to remove these contaminations and to obtain a genuine sample of YSOs (the details of the criteria are described in Chapter 4). However, our study is mainly focused on the region near the compact cluster and most of the sources detected in IRAC bands were at least identified in K-band (Weintraub and Kastner 1996). Criteria based on the IRAC spectral index α_{IRAC} $(dlog(\lambda F_\lambda)/dlog(\lambda))$ also indicate that the classification of the sources is consistent with the Allen et al. (2004) criteria (see Section 4.3.1 of Chapter 4 for the details of criteria based on α_{IRAC}). For some of the sources, our identification of YSOs matches with that of Weintraub and Kastner (1996). Using Gutermuth et al. (2009) criteria, we find that some of the YSO candidates turn out to be contaminants (about 20%). However, based on the α_{IRAC} criteria and the SED modeling (presented later in Section 3.3.3), we consider these sources as YSOs rather than contaminants.

The IRAC [3.6]-[4.5] vs [5.8]-[8.0] colour-colour diagram for the sources is shown in Fig. 3.4, along with divisions shown by boxes for Class 0/I, Class II and Class III sources. The Class II sources have colour criteria 0 $<$ [3.6] - [4.5] $<$ 0.8 & 0.4 $<$ [5.8] - [8.0] $<$ 1.1, and Class 0/I sources have [3.6] - [4.5] $>$ 0.8 & 0.4 $<$ [5.8] - [8.0] $<$ 1.5. Colours represented by ([3.6]-[4.5],[5.8]-[8.0]) $\approx$ (0,0) are Class III or photosphere sources. The criteria for Class I/II, [5.8] - [8.0] $>$ 1.1 & [3.6] - [4.5] $<$ 0.4, are taken from Megeath et al. (2004).

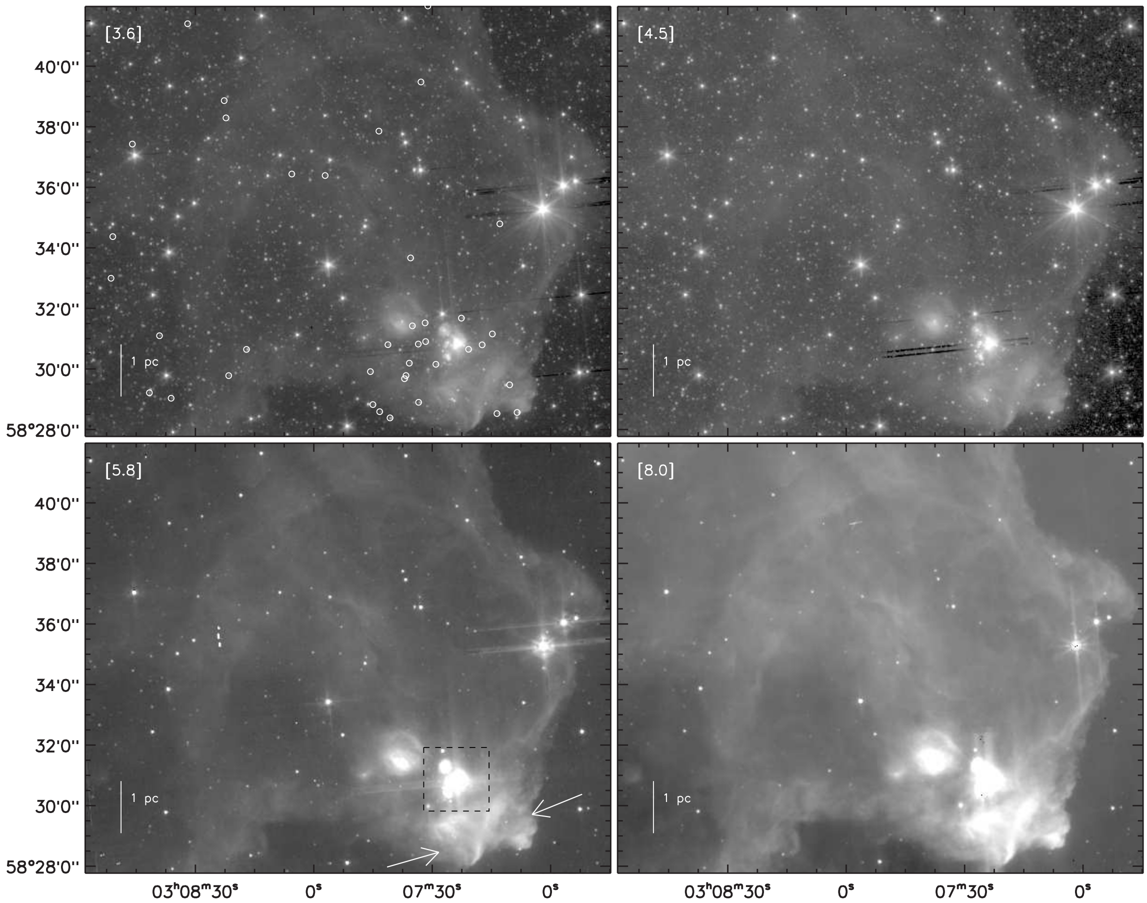

Fig. 3.1: IRAC images of AFGL 437 (size $\sim$ 17.4 $\times$ 14.2 arcmin^2) are shown in all four channels (in log scale). The central compact cluster is marked by the square box (of side $\sim$ 129$''$ or 1.2 pc) in Ch3 image (bottom left). The associated bubble-like extended nebulosity is of size $\sim$ 8.0 pc in the SW-NE direction. The cross-like or boxcar-shaped dense nebula expanding into the local ISM is shown marked by the two arrows in the Ch3 image (bottom left). The open circles in Ch1 (top left) mark the Class II sources identified from IRAC photometry (All four band IRAC magnitude is shown in Table C.1 of Appendix C).

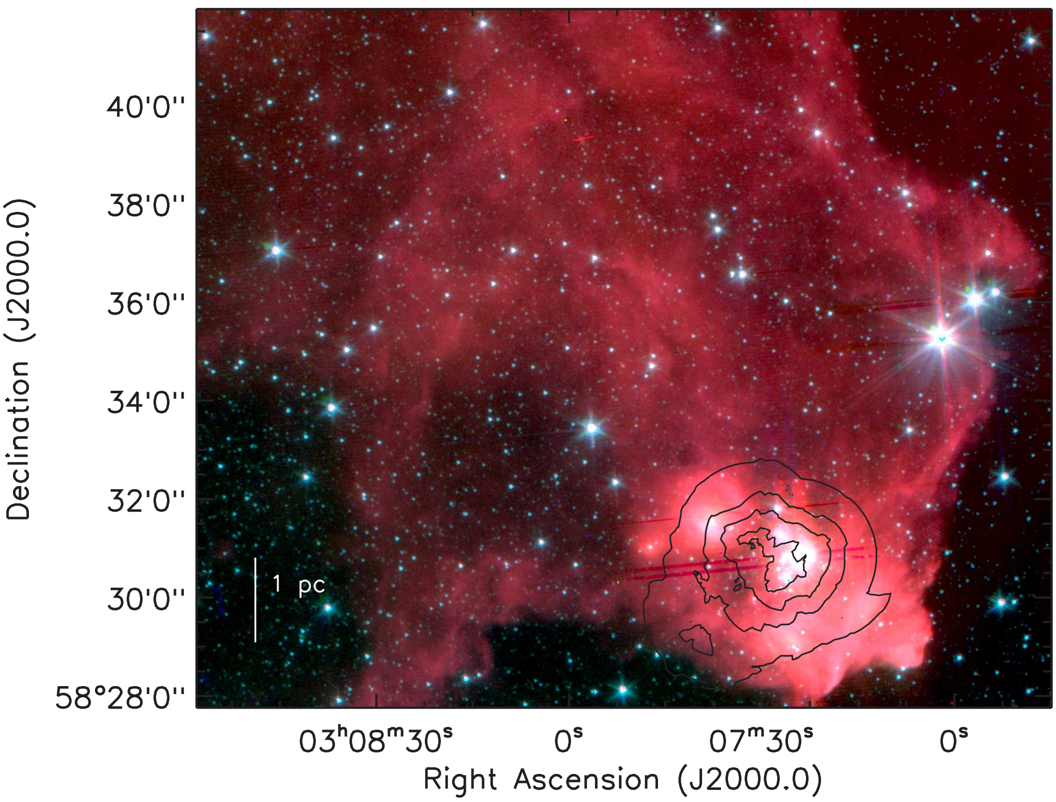

Fig. 3.2: RGB colour-composite IRAC image (8.5 (red), 4.5 (green) and 3.6 (blue) μm) is shown here. Surface density contours are over-plotted on the image representing 2, 5, 10, 25 YSOs per pc^{-2} from outer to inner side.

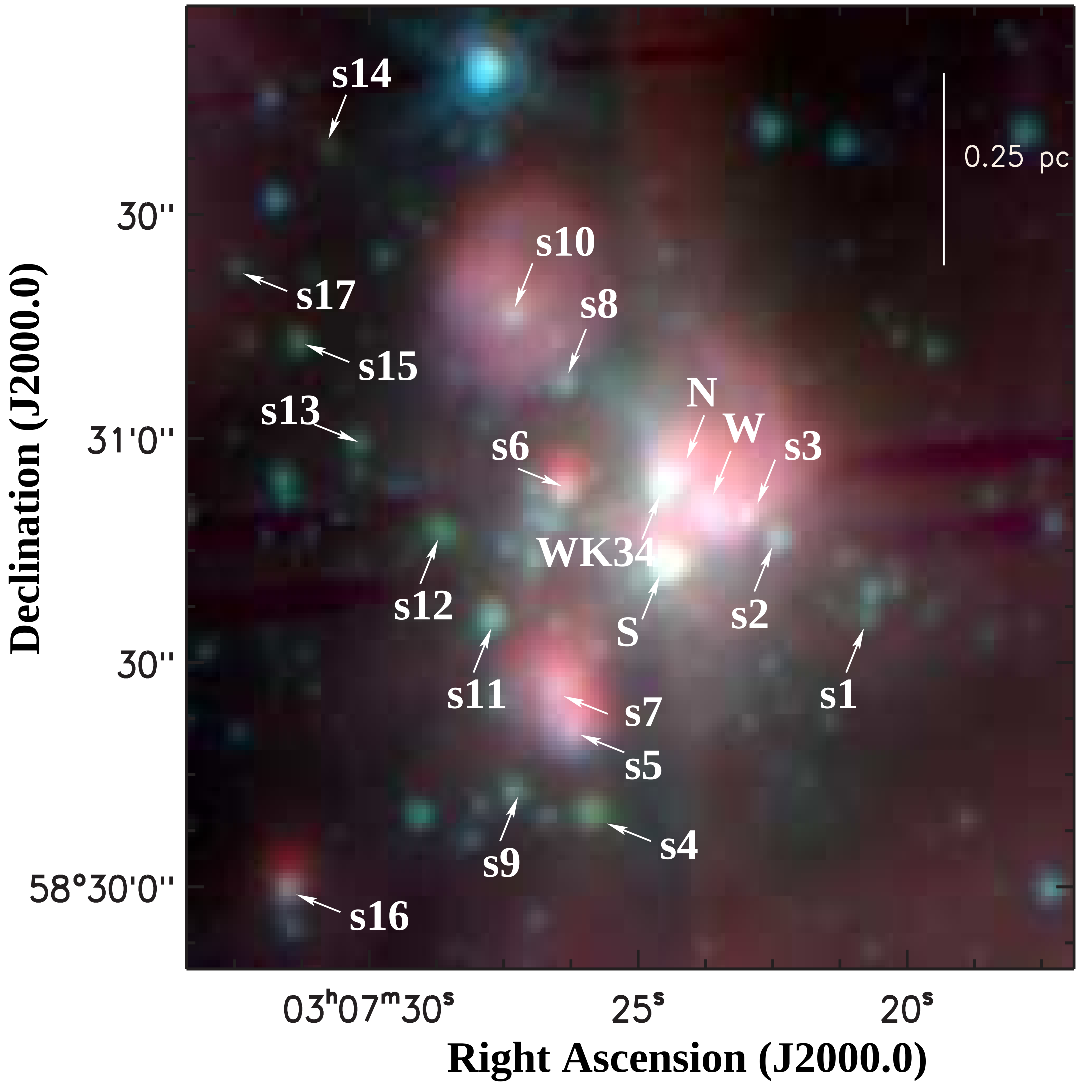

Fig. 3.3: The compact cluster (see the dashed-line box in Fig. 3.1) is shown in a colour-composite zoomed-in image (8.5 (red), 4.5 (green) and 3.6 (blue) μm). The identified YSOs are shown as s1, s2, etc. along with the brighter sources AFGL 437S, W and WK34 (see Table 3.1).

Based on the above criteria, we identify 13-14 sources (including AFGL 437S and WK34) as Class 0/I and 4-5 as Class I/II (including AFGL 437W) in the vicinity (within 64″) of the central compact cluster (see Fig. 3.3). Table 3.1 gives the photometric magnitudes, of these sources, marked as s1, s2 etc. in Fig. 3.3. It may be noted that only 18 sources were detected in all the four channels and the calculation of the slopes of their SED (i.e., spectral index (α_{IRAC}); see Eq. 1.10 of Chapter 1) using the four IRAC channels are listed in Table 3.1. Criteria based on α_{IRAC} also indicate that the classification of sources is consistent with the Allen et al. (2004) criteria (see Chapter 4 for the details of criteria based on α_{IRAC} and Fig. 3.5). We applied the α_{IRAC} criteria on sources given in Table 3.1 and found 1 Class 0/I (i.e., id 7), 24 Class II, 24 Class III (sources with faint or anemic disks) and 3 photospheric sources. It may noted here that the Allen et al. (2004) criteria do not distinguish the Class III sources from photosphere sources. A histogram of the spectral index is shown in Fig. 3.5 for sources from Table 3.1 and Class II sources from Table C.1 of Appendix C.

We have included in Table 3.1 three sources (s2, s3 and AFGL 437N) that were not detected in all the four bands, but satisfy one of the two colour criteria for Class I/II or Class II. In the Object column in Table 3.1, the numbers in parentheses correspond to the sources identified earlier by Weintraub and Kastner (1996) (see their Table 3.1 and Fig. 3.3). Some of these sources are seen in the K band image of Weintraub and Kastner (1996), but are not detected in J and H bands. From IRAC photometry, we have identified a number of new YSOs, apart from the sources AFGL 437W, S, WK34, s2, s5-s8 and s10 that have been classified earlier by Weintraub and Kastner (1996). A large number of these sources are highly embedded and suffer large extinction. We have determined the visual extinction A_v for the sources that have JHK photometry (Weintraub and Kastner 1996; Meakin et al. 2005) and have found that WK34 is the most embedded of all, with A_v = 30-35 mag. In addition to the Class I and Class I/II cluster sources, about 35 Class II sources (from Fig. 3.4) are also identified outside the cluster, spread over the nebular bubble. These are shown as open circles in the Ch1 image in Fig. 3.1 (top left). Most of these sources occur within a distance of about 1.6 pc (165.4″) southeast of the cluster. For about 23 of these sources, good quality (S/N $\geqslant$ 5) 2MASS JHK photometric colours have provided confirmation of their low mass Class II nature. This supports our conjecture that the filamentary structures and the expanding boxcar-like nebula are possibly driven by the central cluster sources.

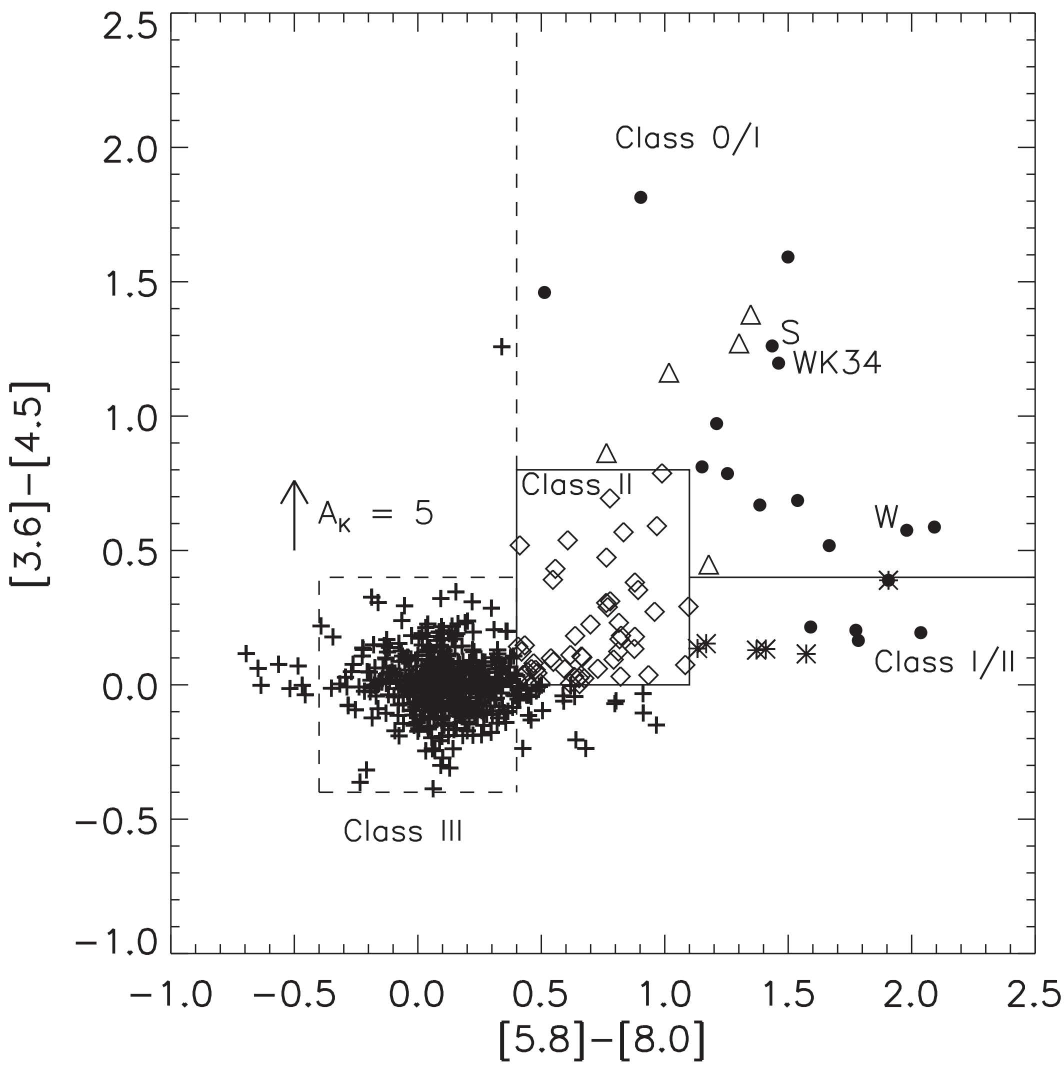

Fig. 3.4: Mid-IR colour-colour diagram constructed using the *Spitzer*-IRAC bands. The boxes indicate possible regions of Class 0/I, Class II, and Class III sources based on (Allen et al. 2004). Class I/II sources share the properties of both Class I and Class II sources. The filled circles represent the sources within 64 arcsec of the centre of the cluster (see Table 3.1 and Fig. 3.3); the asterisks are Class I/II stars and the diamonds are for Class II (see Fig. 3.1 for their locations). The Class III stars are shown as plus-signs. The triangles are Class I sources found quite far away from the central cluster. The principal sources of the cluster, AFGL 437 S, W, and WK34 can be seen marked inside the box designated for Class 0/I protostars. Extinction vector for K band, A_K = 5 is shown in the diagram, which is calculated using averaged reddening law from Flaherty et al. (2007).

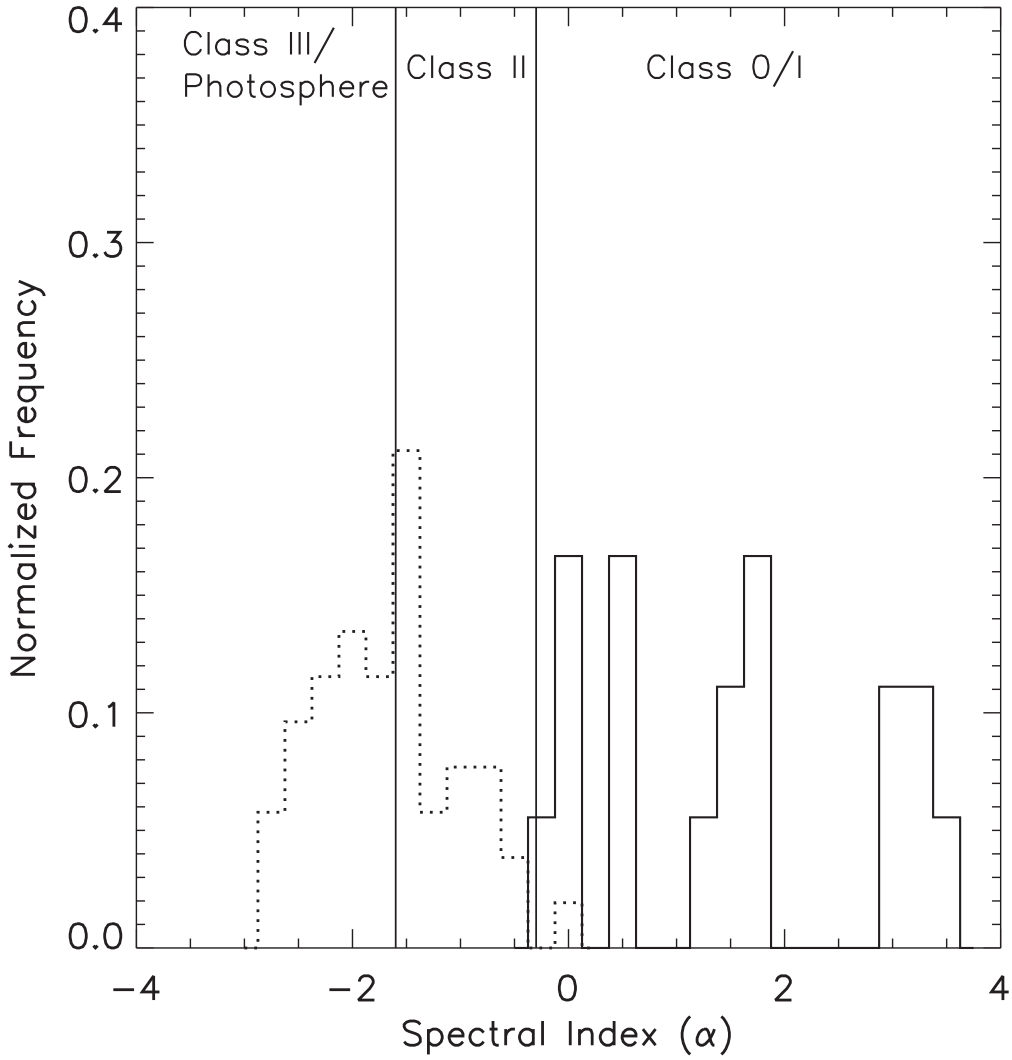

Fig. 3.5: Histogram of spectral index (α_{IRAC}) of sources in AFGL 437 is shown here with regions of different evolutionary stages of star formation shown by vertical lines (see text for more details). Dotted line represents the distribution of photospheric sources and distribution of YSOs is shown by solid line.

YSO density

In order to obtain quantitatively the spatial distribution of YSOs, we adopted the nearest-neighbour technique (Chavarria et al. 2008; Guieu et al. 2009; Evans et al. 2009) on the Class 0/I, I/II and II of AFGL 437 region. These authors used surface number density as defined below:

$$\rho_n = n/A_n \tag{3.1}$$

where, A_n is the surface area defined by the radial distance r_n to the n nearest-neighbours. But, Casertano and Hut (1985) showed that the above formula leads to an over-estimation of surface density by a factor of (n / (n-1)). Therefore, we have followed the suggestion of Casertano and Hut (1985) to obtain surface density distribution, without a bias towards over-estimation. We have used a 5 arcsec grid to compute the surface number density, defined now as

$$\rho_n = (n-1)/A_n \tag{3.2}$$

where, we have used r_n to the n (= 6) nearest-neighbours. In Fig. 3.2 the IRAC RGB colour-composite image is overlaid by YSO spatial density contours with levels 2, 5, 10, 25 YSOs/pc^2 going from the outer side to the inner side. We have calculated the empirical cumulative distribution function of the nearest-neighbour distance for the identified YSOs. The separation between the clustered and scattered YSOs is obtained by using an (arbitrarily chosen) inflection distance d_c = 1.08 pc (0.03 degree at a distance of 2.0 kpc)(see Fig. 3.6a). We have used d_c = 1.08 pc to find the cluster members and found about 53% of the YSOs are clustered occurring inside the surface density contours with a maximum density of about 20-25 YSOs/pc^2 (see Fig. 3.6b).

3.3.2 IRAC Ratio Maps

As mentioned earlier, the IRAC bands contain a number of prominent molecular emissions lines (see Table 3.2 and Fig. 3.7). Ch1 contains H_2 vibrational-rotational lines while Ch2-4 mostly contain pure rotational lines. Ch1, 3 and 4 also contain the PAH features at 3.3, 6.2, 7.7 and 8.6 μm; but Ch2 does not include any PAH features. de Muizon et al. (1990) have detected some of the above mentioned PAH features in AFGL 437. As mentioned earlier, Davis et al. (1998) have reported some ‘wisp’-like features of H_2 emission (in 2.121 μm narrow band filter that contains the 1-0S(1) line) at a few locations in AFGL 437. Several authors have utilised these IRAC ratio maps to identify some of the molecular diagnostics mentioned above (e.g., Smith and Rosen (2005); Povich et al. (2007); Neufeld and Yuan

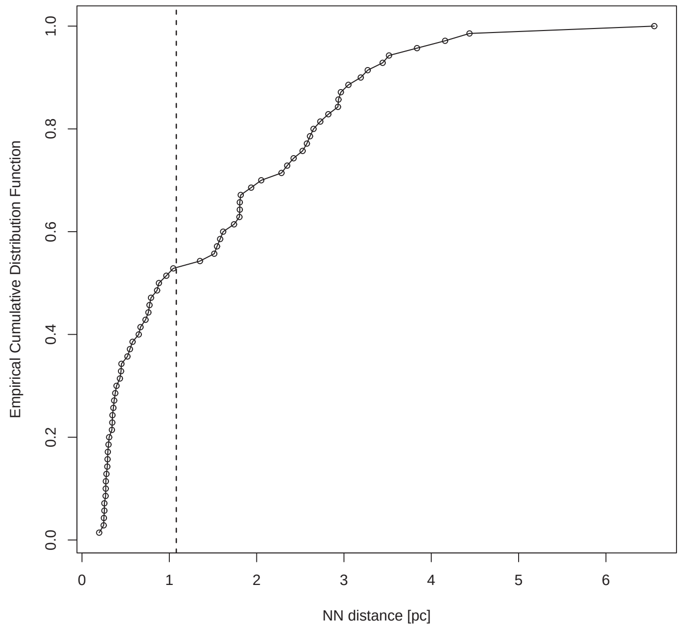

(a)

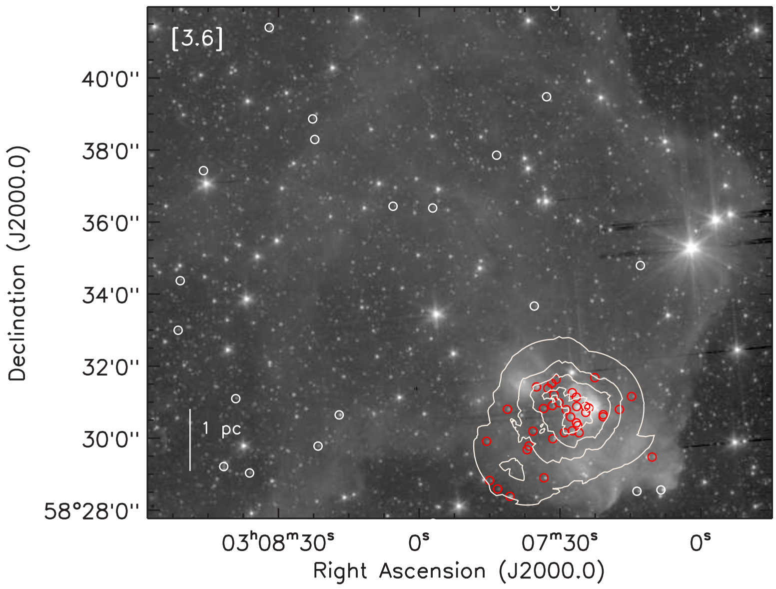

(b)

Fig. 3.6: a: The Empirical cumulative distribution function of nearest-neighbour distance for the all identified YSOs in the whole AFGL 437 region is shown here. An arbitrary inflection distance d_c = 1.08 pc (0.03 degree at a distance of 2.0 kpc) is chosen to find cluster members in the region. b: IRAC Ch1 overlaid with surface density contours (same levels as used in Fig. 3.2) and positions of YSOs. Sources with red circles represent the clustering of YSOs having sizes less than or equal to d_c and white ones for larger than the d_c value.

Table 3.1: *Spitzer*-IRAC 4-channel photometry (in mag) of the YSOs identified in the central cluster of AFGL 437; the numbers in parentheses in the Object column are Weintraub & Kastner (1996) designations (see text)

Object	RA [2000]	Dec [2000]	Ch1	Err-Ch1	Ch2	Err-Ch2	Ch3	Err-Ch3	Ch4	Err-Ch4	α_{IRAC}	Class
s1 (22)	3:07:20.81	58:30:35.6	12.65	0.03	11.97	0.01	11.56	0.19	10.02	0.12	0.09	I
s2 (23)	3:07:22.53	58:30:45.6	9.65	0.01	8.97	0.01	7.97	0.04	—	—	—	—
s3 (29)	3:07:23.04	58:30:48.9	8.86	0.04	8.16	0.03	—	—	—	—	—	—
W (28)	3:07:23.88	58:30:50.2	8.34	0.05	7.77	0.05	5.50	0.05	3.52	0.05	3.03	I
N (35)	3:07:24.29	58:30:54.8	—	—	—	—	5.23	0.04	3.34	0.04	—	—
S (20)	3:07:24.53	58:30:42.9	6.72	0.01	5.46	0.01	4.11	0.00	2.68	0.01	1.83	I
WK34 (34)	3:07:24.55	58:30:52.8	7.24	0.03	6.05	0.01	4.98	0.03	3.51	0.05	1.42	I
s4	3:07:25.94	58:30:08.9	12.36	0.02	10.55	0.01	9.26	0.01	8.35	0.04	1.71	I
s5 (7)	3:07:26.21	58:30:21.0	9.71	0.02	9.54	0.02	6.52	0.02	4.73	0.02	3.46	I/II
s6 (31)	3:07:26.45	58:30:52.6	9.47	0.01	8.89	0.02	6.63	0.01	4.53	0.01	3.16	I
s7 (11)	3:07:26.50	58:30:25.4	9.60	0.02	9.40	0.02	6.63	0.02	4.85	0.05	3.13	I/II
s8 (36)	3:07:26.53	58:31:08.3	10.76	0.03	10.24	0.02	8.98	0.02	7.32	0.04	1.24	I
s9	3:07:27.38	58:30:12.2	11.97	0.02	11.16	0.01	10.51	0.06	9.36	0.09	0.12	I
s10 (40)	3:07:27.40	58:31:15.8	10.05	0.02	9.66	0.02	8.36	0.06	6.46	0.06	1.43	I/II
s11 (17)	3:07:27.76	58:30:35.3	10.66	0.02	9.69	0.01	8.87	0.04	7.66	0.05	0.57	I
s12	3:07:28.69	58:30:47.4	12.68	0.03	11.22	0.01	10.81	0.08	10.30	0.22	-0.28	I
s13	3:07:30.22	58:30:58.9	13.43	0.02	12.65	0.02	12.06	0.09	10.81	0.12	0.12	I
s14	3:07:30.83	58:31:37.8	15.62	0.07	14.03	0.02	12.99	0.14	11.49	0.16	1.81	I
s15	3:07:31.32	58:31:12.4	13.20	0.01	12.53	0.01	11.74	0.03	10.35	0.03	0.44	I
s16	3:07:31.56	58:29:59.0	11.86	0.01	11.67	0.01	9.22	0.01	7.18	0.01	2.97	I/II
s17	3:07:32.60	58:31:23.0	13.94	0.02	13.72	0.02	12.70	0.13	11.11	0.22	0.53	I/II

(2008)). Since it is difficult to assess the contribution of different molecular transitions to different channels, ratio maps are only indicative; until/unless supplemented by spectroscopic evidences.

The Ch2 channel is more sensitive to H_2 lines of high excitation temperatures while the Ch4 channel represents rotational lines of low excitation temperatures (Neufeld and Yuan 2008). Likewise, the Ch2 channel does not have any PAH features while the Ch4 channel has. Thus, in the ratio image of Ch2/Ch4, the brighter regions indicate emission regions from higher excitations of H_2 and the darker regions indicate PAH emission. This trend is reversed in the image of Ch4/Ch2 (i.e., bright regions show PAH emission and dark regions the H_2 emission).

Ratio maps for the AFGL 437 are generated using residual images for each band, by removing point sources from the IRAC image. The extended PSF flux calibration is very important for making such ratio maps, because it is known to hold a fraction of the total flux in the 5.8 and 8.0 μm bands (Reach et al. 2005). Therefore, residual images are created by using an extended aperture of 12.2 arcsec and sky annulus of 12.2 - 24.4 arcsec in IRAF/DAOPHOT software. These residual images were then subjected to median filtering with 9 pixels and smoothed with 3 $\times$ 3 pixels by "box-car" algorithm in IRAF package, before obtaining the final ratio maps (Povich et al. 2007).

Fig. 3.8 shows the ratio maps of Ch2/Ch4 (a) and Ch4/Ch2 (b) in a region surrounding the central cluster. The bright regions in Fig. 3.8a probably correspond to H_2 emission; and those in Fig. 3.8b correspond to PAH emission. The ratio map Ch2/Ch4 (Fig. 3.8a) brings out clearly the cross-like features towards the south-west edge of the cluster; positions of which match well with the faint 'wisps' seen in Davis et al. (1998). These emission features could be the result of the expansion of HII regions or stellar winds interacting with the local ISM. We have looked for PAH features by examining the ratio images of Ch4/Ch2; Ch3/Ch2 and Ch1/Ch2 (since Ch2 does not have any PAH features).

Fig. 3.8b shows the ratio map of Ch4/Ch2. The ratio map shows bright regions around AFGL 437W, s5, s7 and s10; as well as towards north of the NE corner of the boxcar nebula. The ratio Ch3/Ch2 (possible indicator for the 6.2 μm PAH feature) does not show any bright features. The ratio map shows the boxcar/cross shaped feature in dark, probably because of a lack of PAH emission. The bright narrow linear filament seen to the right

Table 3.2: Important H_2 and PAH lines in IRAC bands (compiled from Smith and Rosen (2005); Povich et al. (2007)).

Line	Wavelength (μm)	IRAC bands
H_2 (1, 0) O(5)	3.234	Ch1
H_2 (2, 1) O(5)	3.437	Ch1
H_2 (1, 0) O(6)	3.500	Ch1
H_2 (2, 1) O(6)	3.723	Ch1
H_2 (0, 0) S(14)..........................	3.724	Ch1
H_2 (1, 0) O(7)	3.807	Ch1
H_2 (0, 0) S(13)..........................	3.845	Ch1
H_2 (0, 0) S(12)..........................	3.996	Ch1
H_2 (0, 0) S(11)..........................	4.180	Ch2
H_2 (0, 0) S(10)	4.408	Ch2
H_2 (1, 1) S(11)	4.416	Ch2
H_2 (0, 0) S(9)	4.694	Ch2
H_2 (1, 1) S(9)	4.952	Ch2
H_2 (0, 0) S(8)	5.052	Ch3
H_2 (0, 0) S(7)	5.510	Ch3
H_2 (1, 1) S(7)	5.810	Ch3
H_2 (0, 0) S(6)	6.107	Ch3
H_2 (0, 0) S(5)	6.907	Ch4
H_2 (1, 1) S(5)	7.279	Ch4
H_2 (0, 0) S(4)	8.024	Ch4
HI Pfδ	3.30	Ch1
HI Pfγ	3.70	Ch1
HI Brα	4.05	Ch2
HI Pfβ	4.65	Ch2
HI Pfα	7.50	Ch3
PAH C-H stretching	3.3	Ch1
PAH C-C stretching	6.2	Ch3
PAH C-C stretching	7.7	Ch4
PAH C-H in-plane bending	8.6	Ch4

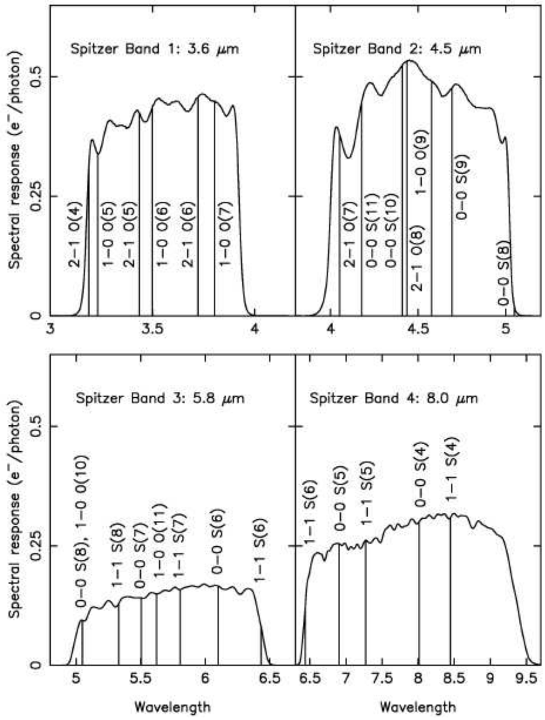

Fig. 3.7: IRAC bands encompassing several molecular hydrogen lines (see Table 3.2 and Smith and Rosen (2005) for more details).

of AFGL 437W (between the dashed lines in Fig. 3.8b) probably indicates the ionisation front from the massive star in the wake of which the PAH is excited (Povich et al. 2007). It is possible that the requisite UV photon flux for exciting the PAH features comes from the source AFGL 437W. The detection of the 'PAH filament' corroborates the blister model for AFGL 437W presented by Wynn-Williams et al. (1981).

We have examined more closely the ratio map of Ch2/Ch4 to look for the infrared counterpart of molecular outflow originating from the highly embedded YSO WK34. Fig. 3.9 shows a zoomed-in image of Ch2/Ch4 ratio contours over-laid on the Ch4 image. One can notice the prominent lobe/outflow stretched northwards of WK34 and slightly bent towards the NE, with a total extension of $\sim$ 0.16 pc. The outflow direction and size are consistent with the earlier reports. The bending itself is attributed to the presence of the nearby source AFGL 437N (Weintraub and Kastner 1996).

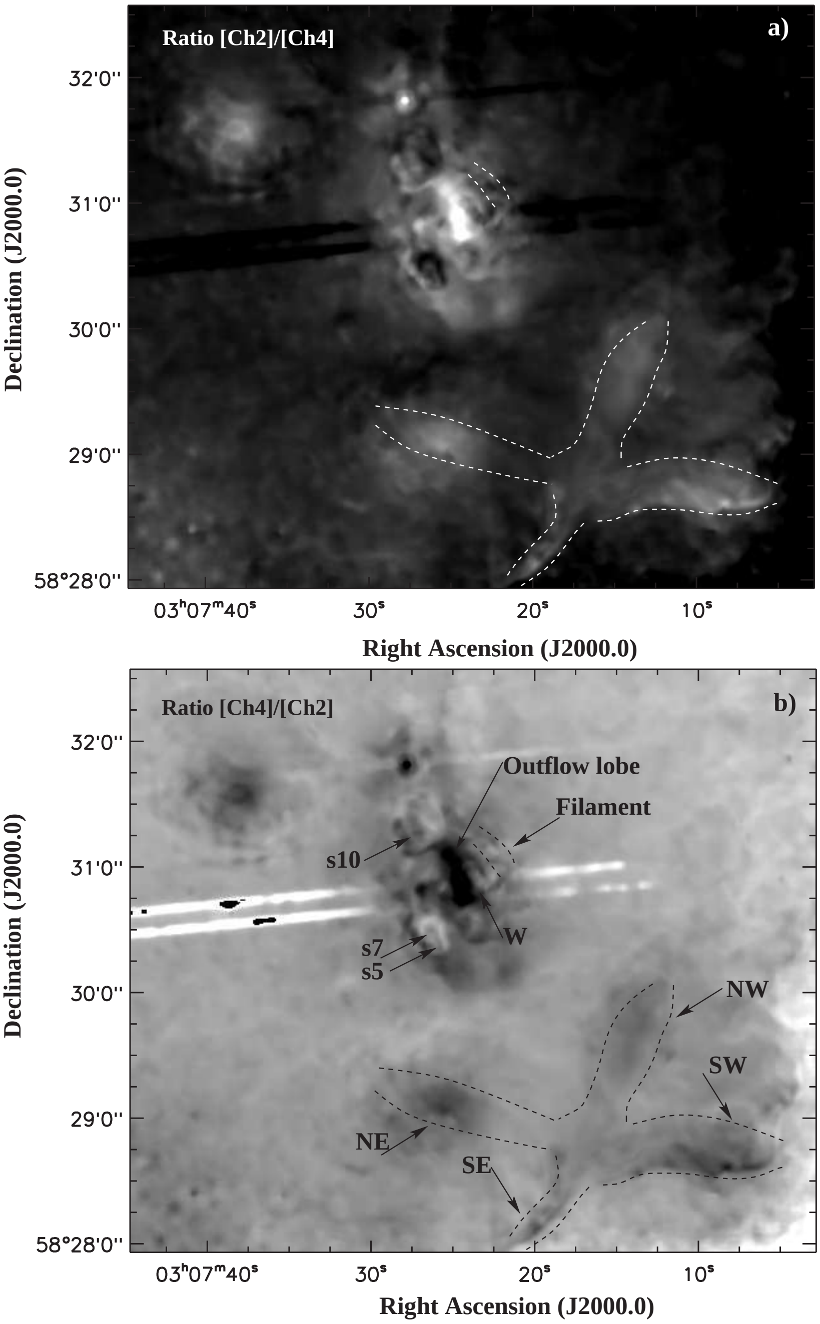

Fig. 3.8: IRAC Ch2/Ch4 (a) and Ch4/Ch2 (b) ratio images in log scale (from mosaics made with pixel ratio of 2). The central cluster and the cross- or boxcar-like structure to its south-west can be noticed. This structure has a size of 1.7 pc in the NE-SW and 1.5 pc in NW-SE directions. The bright patches in the image on the top (a) show regions dominated by H_2 emission; while in the image on the bottom (b) the bright patches indicate regions that are emitting PAH bands. The prominent outflow lobe, some of the YSOs, and the H_2 emission patches in the four corners of the cross-like structure are marked (by dashed curves). The near-horizontal tracks across the image are artifacts. The filament-like structure to the right of AFGL 437W is marked by dashed lines in the upper half of both the figures.

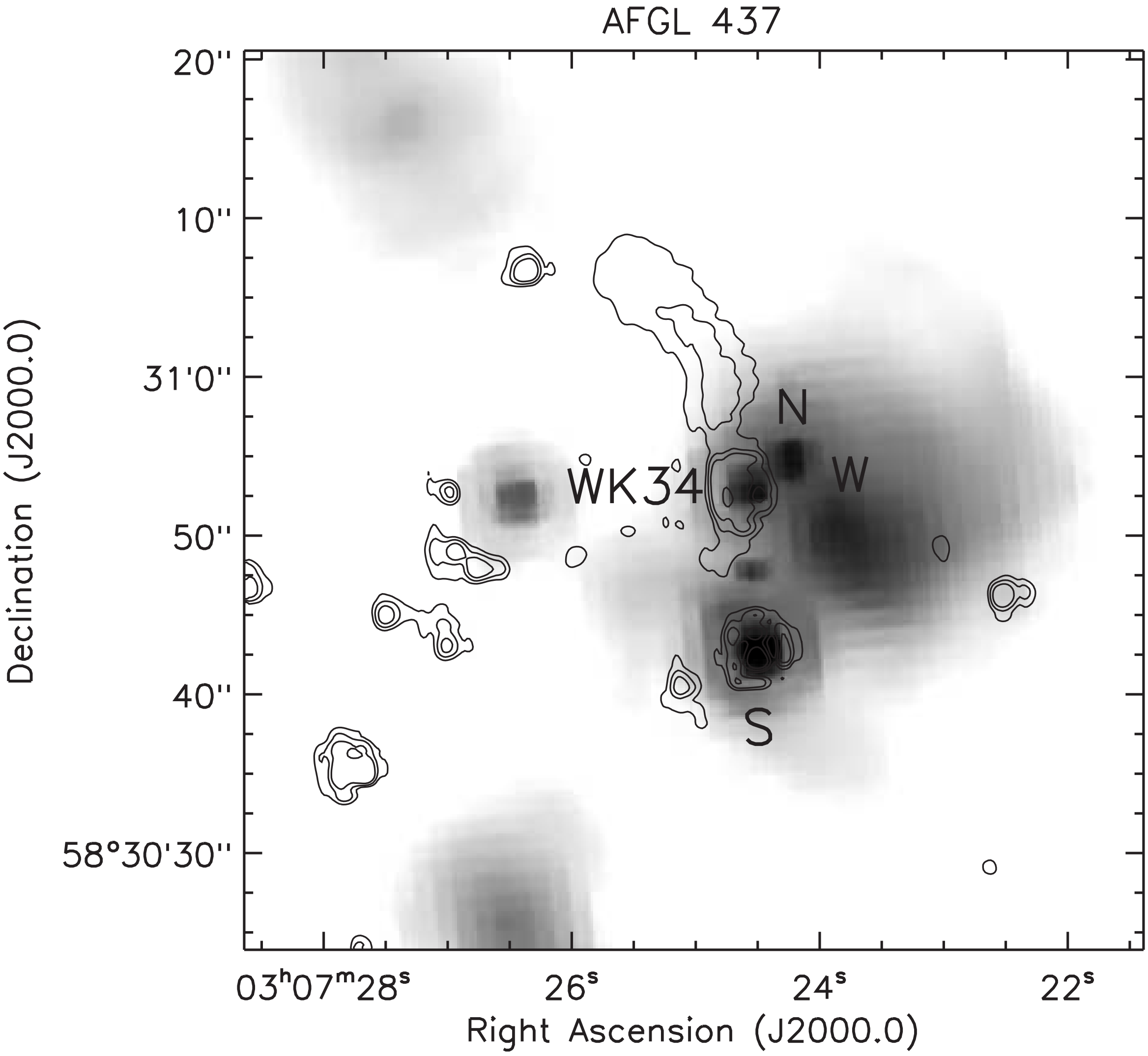

Fig. 3.9: IRAC 8 μm zoomed-in image of the cluster is shown in log scale overlaid by the contours of IRAC ratio image of (Ch2/Ch4). Contours show the outflow lobes associated with the source WK34. Outflow lobes are stretched in north direction with a bend towards east. The IRAC Ch 4 (8 μm) image is made with a pixel ratio of 8 in a spatial extent of $\sim 55 \times 55$ arcsec^2; while the ratio contours are plotted with a minimum of 0.178 and maximum of 8 MJy/Sr.

3.3.3 SED modeling of Cluster Sources

By modeling the SEDs of the identified YSOs, we derive physical parameters of both their photospheres and mass accreting disks/envelopes. For this purpose, we constructed the SEDs for all the 21 sources listed in Table 3.1, from the optical to sub-mm data depending upon the availability in the archives and published literature. The optical data[2] are available only for the sources W (B,V bands), s7 (V upper limit) and s16 (B,V,R upper limits). In fact, the lack of optical data is indicative of the large extinction that most of the sources suffer. The JHK fluxes for the sources s10, s16 and s17 are taken from the 2MASS survey and for the sources s2, s3, s5-s8 and s11 from Weintraub and Kastner (1996). While the source s1 has only K band flux from Weintraub and Kastner (1996), s4, s9, and s12-s15 do not have near-infrared counterparts. The JHK photometric fluxes for WK 34 are taken from Meakin et al. (2005). We have used sub-mm/mm data (Dent et al. 1998) as upper limits for WK34, S, W and N (because of the large beam sizes that nearly encompass the entire central region of the cluster), only to constrain the models. The rest of the sources listed in Table 3.1 are outside the field of view of the sub-mm observations. The SEDs are then modeled using an on-line 2D-radiative transfer tool due of Robitaille et al. (2006) (see Chapter 2 for details). In our sample all the 21 sources have at least three good quality data points, the minimum requirement of the tool. For a source that has a meager number of data points, the tool picks out a large number of solutions that can fit the data well, within the specified limit on χ^2 (as earlier, we have used χ^2 - $\chi^2_{best} < 3$). If the SED has larger data, spread over the wavelength region of 0.5 to 1000 μm, then the model would be better constrained to yield results with the least standard deviations (Robitaille et al. 2007). The distance to the source and visual extinction are to be given as input parameters, usually as a range of values. This leads to a further degeneracy in the models. In our case, however, the cluster distance is fairly well-determined and the extinctions were estimated from the available JHK data on individual sources. But, in order to avoid 'over-interpretation' of SEDs (Robitaille et al. 2007), we have provided a range of visual extinction values for each object to account for the uncertainties in their determination from JHK photometry.

We show in Fig. 3.10 the SED modeling results for the sources AFGL 437W, S, N and WK34. Table 3.3 gives the weighted mean values of the derived physical parameters for the four sources along with their standard deviations. The table also lists the model-derived weighted mean values of A_v with standard deviations and the degeneracy of the mod-

[2]from http://vizier.u-strasbg.fr/viz-bin/VizieR

Table 3.3: Physical parameters derived from SED modeling of the main sources AFGL 437 W,S,N and WK34 (see text)

Source Name	Age log(yr)	M_* $M_\odot$	T_* log(T(K))	L_* log($L_\odot$)	$\dot{M}_{env}$ log($M_\odot$ yr^{-1})	$\dot{M}_{disk}$ log($M_\odot$ yr^{-1})	A_v mag	Degeneracy/ No. of models
W	5.36±0.19	8.28±1.48	4.28±0.11	3.55±0.23	-4.84±0.17	-7.01±1.16	4.0±0.7	16
S	4.35±0.90	7.79±1.72	3.86±0.31	3.14±0.39	-4.12±1.30	-5.84±1.12	9.2±1.8	72
N	4.82±0.46	9.36±1.62	3.99±0.19	3.48±0.30	-3.96±0.94	-6.02±0.84	18.0±8.0	132
WK34	3.94±0.57	7.23±1.91	3.71±0.10	3.00±0.30	-4.06±0.55	-4.69±0.39	23.0±5.6	3

els (i.e., the number of solutions that satisfy the criterion mentioned above). The model-derived parameters listed in Table 3.3 indicate that all the four sources are likely to be massive (early B type). This is consistent (within the standard deviations) with the observations on W and S that are associated with UCHII regions. It may be noted that observationally very little is known about the spectral type of the source N. The modeling results of the rest of the 21 sources (s1 - s17) are shown in Appendix C (see Fig. C.1, C.2 and Table C.2).

The model parameters for WK34 suggest that the source is young and massive, with an effective temperature still not sufficient to create an HII region (see Table 3.3). Its low luminosity is suggested by earlier workers also. This is also reflected in its outflow, which shows emission in H_2 (as revealed by the ratio map in Fig. 3.9) but not in PAH; indicating that WK34 is still not hot enough to produce sufficient UV flux. The modeling suggests that the source AFGL 437W and S are also massive stars but more evolved to attain sufficiently large effective temperature to excite an HII region. Qin et al. (2008) derived a CO outflow entrainment rate of 7.4×10^{-4} $M_\odot$/yr for the outflow source (WK34), which agrees with that observed for massive stars (e.g., Beuther et al. (2002a)). In comparison, the low mass stars show much less entrainment rates (Wu et al. 1996). In a study of the molecular outflows from high mass YSOs, Ridge and Moore (2001) have concluded that these outflows are often poorly collimated. This again points to the possibility that WK34 is a massive protostellar object. From the SED modeling of the 21 sources, we infer that the weighted mean values of the mass and ages of the YSOs in the central cluster (for the 21 sources listed in Table 3.1) are in the ranges 1 - 10 $M_\odot$ and $10^{4.1-6.4}$ yr respectively; while the luminosities are in the range of $10^{0.47-3.48}$ $L_\odot$.

3.4 Conclusions

The important conclusions of this work are as follows:

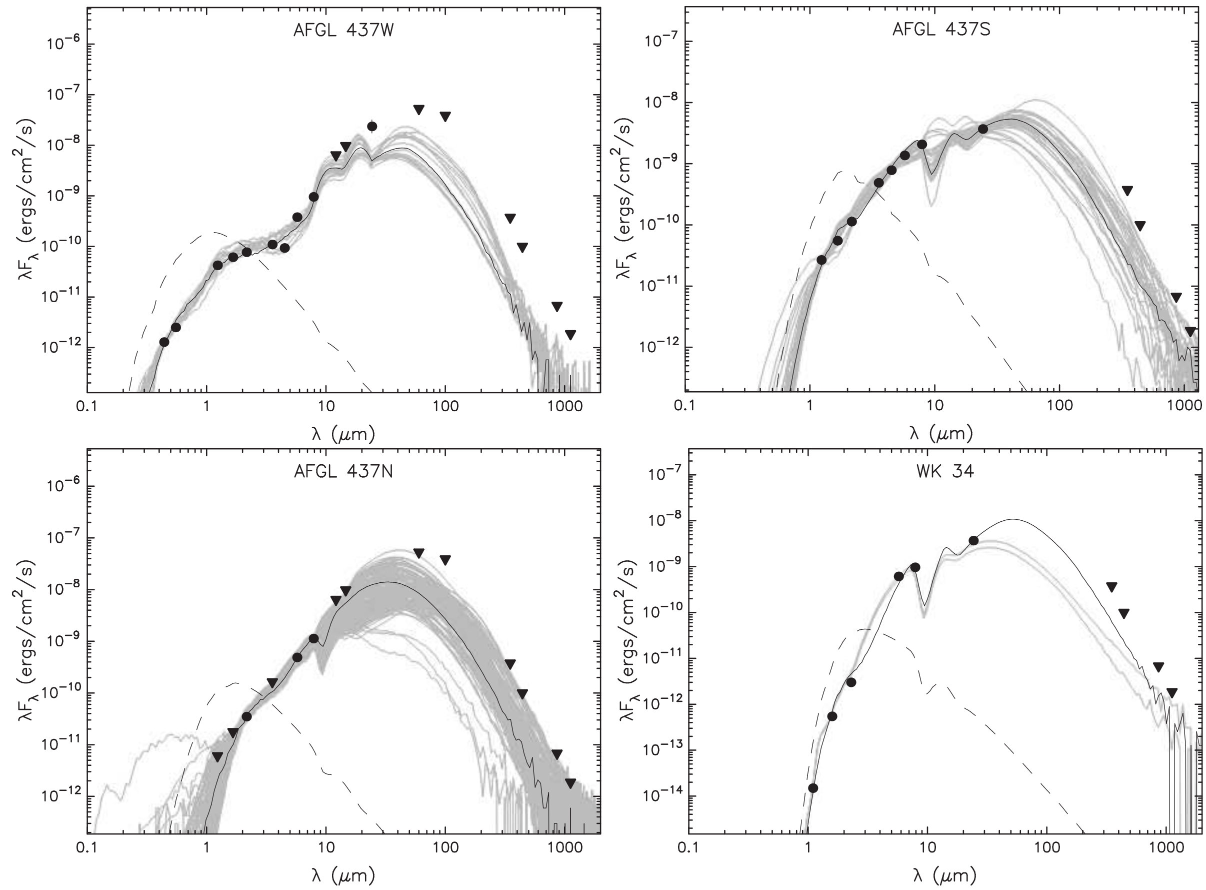

Fig. 3.10: Spectral Energy Distributions for four YSOs in the central cluster: AFGL 437W, S (top panels) N and WK34 (bottom panels). Filled circles are observed fluxes of good quality (with filled triangles as upper limits) taken from archives or published literature (see text for references) and the curves show the model fits. The thin black curve corresponds to the best fit model. The dashed curves represent photospheric contributions. The model parameters of the YSOs are listed in Table 3.3.

1. *Spitzer*-IRAC imaging photometry is presented on the massive star forming region AFGL 437;

2. Several new embedded YSOs are identified within 64 arcsec of the central compact cluster with a maximum surface density of about 25 YSOs/pc^2;

3. The IRAC ratio maps indicate molecular outflow corresponding to WK34 which is possibly due to H_2;

4. The SED modeling of the outflow driving source WK34 indicates that it is a massive but very young protostar not yet able to drive an HII region;

5. SED modeling of the 21 sources gives their mass, age and luminosities in the range 1-10 $M_\odot$, $10^{4.1-6.4}$ yr and $10^{0.47-3.48}$ $L_\odot$ respectively.

Chapter 4

A study of the massive star forming region M8 using *Spitzer*-IRAC images

In the previous chapter, IRAC photometry was presented on a massive star forming region, which contained only early B type stars. In this chapter, *Spitzer*-IRAC images and photometry of another star forming region will be discussed. This region is very complex due to the presence of many O and early B type stars. Here we present our study on the massive star forming region, M8 using *Spitzer*-IRAC images.

4.1 Introduction

Messier 8 (M8), also known as the Lagoon Nebula (or NGC 6523) is a well known galactic HII region (comprehensively reviewed in Tothill et al. (2008), and the references therein) situated at a distance of 1.25 kpc (Arias et al. 2006) in the Sagittarius-Carina spiral arm of the Galaxy. The core of M8 contains a spectacular blister-type HII region, called the Hourglass nebula, ionised by the O7.5 V star Herschel 36 (Her 36) (Woolf 1961). The HII region is embedded within a giant molecular cloud that extends eastwards to the young star cluster NGC 6530 of age 2×10^6 yrs (Lada et al. 1976). While Her 36 is responsible for the Hourglass and the ionised bubble surrounding it, the other early type stars in the M8 complex, 9 Sgr (O4 V(f)) and HD165052 (O6.5V+O7.5V) are believed to account for the ionised regions east of the central core/bubble (Goudis 1976; Lada et al. 1976; Lynds and Oneil 1982; Woodward et al. 1986). Allen et al. (1986) discovered a few near-IR sources in the vicinity of Her 36, designated by Woodward et al. (1990) as KS 1 to KS 5. From a high resolution near-IR study, Arias et al. (2006, 2007) found the existence of a very young star cluster around Her 36, having an age of $\sim 10^6$ yrs. Barba and Arias (2007) discovered a number of HH objects in M8, which confirms by implication, the existence of very young stars undergoing the accretion phase of formation. Narrow-band imaging by the Hubble Space Telescope (HST) revealed the presence of proplyds in the neighbourhood of Her 36 (Stecklum et al. 1998). The core of M8 is detected by the Mid-course Space Experiment (MSX) in mid-infrared as a luminous extended source (Crowther and Conti 2003). Colour-composite maps of M8 in mid-infrared (mid-IR) bands of *Spitzer* Infrared Array Camera (IRAC) shows a ridge extending in east-west direction to the south-east of the Hourglass (Tothill et al. 2008). A number of filamentary structures extending in the NE-SW direction to the east of Her 36 or the Hourglass are also seen. Among the new compact star forming regions in the M8 complex, M8E stands out with its compact HII region powered by an early B type star (M8E-Radio) (Lada et al. 1976; Wright et al. 1977; Brand and Zealey 1978; Mitchell et al. 1991; Linz et al. 2009). White et al. (1997) discovered very intense CO line emission in mm and sub-mm wavelength regions from the central core of M8. Later, from a larger survey in mm and sub-mm continuum and CO lines, Tothill et al. (2002) found bright rims and dark lanes stretching in the east-west direction. White et al. (1997) found from CO (J=3–2) line observations, a loose bipolar structure extending NW-SE from Her 36; while Stecklum et al. (1995) found the presence of a jet-like object very close to Her 36. These observations provide evidences for outflow activity around Her 36 region. As for the spectral diagnostics in the infrared region, Woodward et al. (1986) detected Brγ (2.17 μm), Brα (4.05 μm) as well as Pfϵ (3.03 μm) and the 3.28 μm PAH emission to the west of Her 36. Burton (2002) observed H_2 1–0 S(1) line at 2.12 μm near the Hourglass/Her 36 region attributed primarily to shock-excited molecular gas; but UV excitation can not be ruled out.

The M8 region seems to be quite complex and very interesting, owing to the presence of stellar winds and expanding HII region bubbles from massive stars, which can trigger fresh star formation by sweeping up and compressing the local dense interstellar matter. The afore-mentioned near-IR surveys studied the regions around Her 36 and NGC 6530, leaving the ridge regions far-east and south-east of Her 36 relatively under-explored in near-IR (except for the 2MASS survey) and mid-IR regions (except for the MSX survey). In view of this, we have examined in detail the extended region of M8 in the near-/mid-infrared images provided by *Spitzer*, which are so far not looked into.

The aims of the present study are to identify the embedded sources using the IRAC bands in order to classify the different stages of their evolution; to use ratio maps of the four

IRAC bands in order to identify possible H_2, PAH or H emission regions, following the suggestions of Smith and Rosen (2005) and Povich et al. (2007).

In Section 4.2, we describe the data used for the present study and the analysis tasks utilised. Section 4.3 presents the results and discussion on *Spitzer*-IRAC photometry of embedded sources associated with the M8 complex. In this section, we also present the results and discussion on the ratio maps. In Section 4.4, we give the conclusions.

4.2 *Spitzer*-IRAC Data on Messier 8 and Data Reduction

The observation of M8 presented in this chapter were obtained with the *Spitzer* Space Telescope IRAC camera by *Spitzer* Science Center (SSC) on 16 September 2005 and Basic Calibrated Data (BCDs) images were processed by SSC using software version S14.0.0 for all four bands (see Fazio et al. (2004), for details on the IRAC instrument). The observations were obtained in the High Dynamic Range (HDR) mode with 12s integration time in all filters. These observations were a part of the project entitled, “Spitzer Follow-up of HST Observations of Star Formation in H II Regions” (Program id 20726; PI: Jeff Hester). The IRAC archival images of M8 were obtained by us on 8 April 2009 from the *Spitzer* public archive, using the ‘leopard’ software. The final mosaic of the M8 region was made using the Mopex and IDL software (Makovoz and Marleau 2005) to remove ‘jailbar’, saturation and ‘muxbleed’ artifacts from BCD images. A single BCD image has a 5.2 $\times$ 5.2 arcmin^2 field of view on the sky, therefore a total number of 320 BCDs were used to make a final mosaiced image of 42.5 $\times$ 30.0 arcmin^2 commonly in all the four bands. The mosaic image was generated for pixel ratio of 2. The photometric magnitude of sources in M8 were extracted through aperture photometry on the mosaic with 2.8 pixel aperture and sky annuli of 2.8 and 8.5 pixels using APPHOT task in the IRAF package. The zero points for these apertures (including aperture corrections) are, 17.80, 17.30, 16.70 and 15.88 mag for the 3.6, 4.5, 5.8, 8.0 μm bands, here onwards called as Ch1, Ch2, Ch3 and Ch4 respectively (see Reach et al. (2005)). The photometric uncertainties vary between 0.01 to 0.25 for the four channels, with Ch3 and Ch4 on the higher side.

We have looked into the 2MASS archives (Skrutskie et al. 2006) as well as published literature for JHK photometric data on sources identified from IRAC and have succeeded in extracting for nearly half of them. From 2MASS archives, we have considered only the data with tags of A, B or C (or a signal-to-noise ratio of ≥ 5) in all the JHK bands.

4.3 Results and Discussion

We divide the results and discussion into two subsections: one in which we discuss the IRAC photometry and the pre-main-sequence (PMS) sources or the young stellar objects (YSOs) detected and their possible formation scenario; and the second in which we describe the ratio maps produced from IRAC images and discuss possible interpretations and their implications.

4.3.1 IRAC Photometry

Fig. 4.1 shows the IRAC Ch4 (8μm) image of $\sim 42.5\times30.0$ arcmin^2 of M8 region with Her 36 situated near the center. Following earlier workers, M8 may be divided into a few distinct regions for convenience (see Fig. 4.1): the Her 36 region comprising of the bubble-like structure around Her 36 with the massive stars 9 Sgr and HD 164816 forming the eastern/north-eastern bounds; the central ridge that includes filamentary structures seen in the NE-SW direction; the massive star HD 164906 and the cluster NGC 6530; the east-west ridge region consisting of the finger-like filamentary structures starting from far-east to the south of Her 36; and the compact young cluster region M8E (see Fig. D.1 of Appendix D for IRAC 3-colour-composite image of similar field of view as shown in Fig. 4.1).

Using the [3.6]-[4.5] vs [5.8]-[8.0] colour-colour diagrams, Allen et al. (2004) and Megeath et al. (2004) formulated division criteria for various PMS classes such as Classes 0/I, I, II and III. These criteria have since been refined by several authors (e.g., Harvey et al. (2006, 2007); Gutermuth et al. (2008, 2009); Evans et al. (2009) and the references therein), in order to account for possible contaminations from broad-line AGNs, PAH-emitting galaxies, unresolved shocked emission blobs/knots and PAH-emission contaminated apertures, which may lead to wrong identifications of YSOs. We used the updated criteria given clearly by Gutermuth et al. (2009) to delineate the PMS sources. We have applied these criteria (see also Section D.1 of Appendix D) to the sources identified in IRAC photometry. The total number of point sources identified, that are common to all the four IRAC bands is 3376; of these, 235 sources are found to be contaminations (1 PAH galaxy, 6 shocked emissions, 228 PAH aperture-contaminations), while there are 327 YSOs (see the criteria for YSOs selection in the Section D.2 of Appendix D).

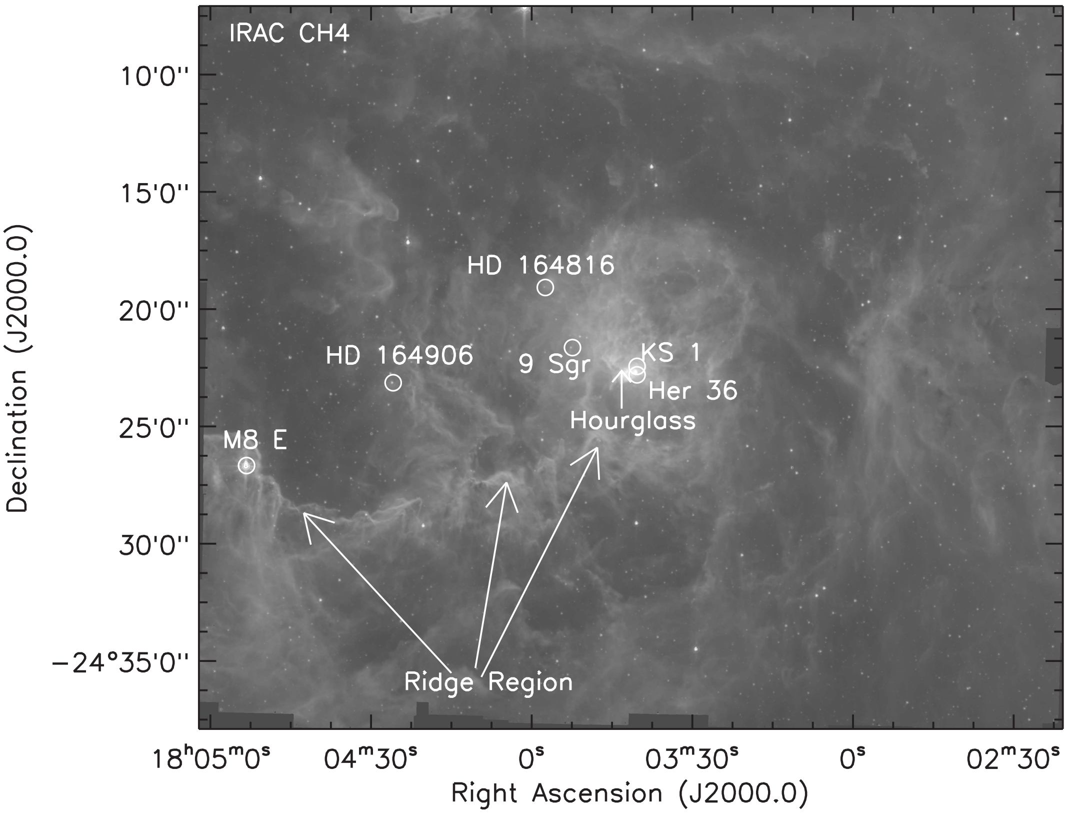

Fig. 4.1: *Spitzer*-IRAC Ch4 (8.0 μm) image of Lagoon Nebula region ($\sim 42.5 \times 30.0$ arcmin^2). The locations of well known sources are shown circled: the massive O type stars Her 36 and 9 Sgr; the early B type stars HD 164906 and HD 164816; the near-infrared source KS1 just north of Her 36; and the young compact massive star-forming region M8E to the extreme east. The Hourglass HII region is shown by the arrow near the core of M8. The young cluster NGC 6530 is situated just to the west of the massive star HD 164906. The arrows at the bottom show the ridge region in the east-west direction. One can also notice filamentary features in the central ridge running north-south near the star HD 164906. The massive star HD 165052 is towards the east of M8E but it is not covered by the IRAC observations.

After removing the contaminants, we used the criteria based on the IRAC spectral index (see Eq. 1.10 of Chapter 1), to classify the YSOs (numbering 327 as shown above) into different evolutionary classes (see e.g., Green et al. (1994); Smith (2004); Lada et al. (2006)). We followed Billot et al. (2010) in the classification of Class 0/I as sources whose α_{IRAC} is > -0.3; Class II as those having -0.3 > α_{IRAC} > -1.6; and Class III as those having -1.6 > α_{IRAC} > -2.6 (termed as sources with faint or anemic disks by Lada et al. (2006)). In applying these classifications to M8, we have not considered the flat-spectrum sources (e.g., Green et al. (1994)) as a separate class but included them in the Class 0/I, the sources with in-falling envelopes (see Billot et al. (2010)). The sources with α_{IRAC} < -2.6 are taken as stars with purely photospheric emissions (see histogram plot of α_{IRAC} for sources in Fig. 4.2). With the α_{IRAC} classification, we have obtained 64 Class 0/I, 168 Class II sources and 95 Class III sources. The rest of the sources, numbering 2814, are purely photospheric sources.

We then verified the selected sample of YSOs for possible interstellar extinction/reddening bias (see Muench et al. (2007) and the references therein). Muench et al. (2007) showed that only for very large values of A_v do sources, with α_{IRAC} ranges relevant here, get misclassified as YSOs. Such large values are seen as being intrinsic for YSOs as may be inferred from the H-K colour. Typically, we can identify the bias by comparing the ratio (N) of number of Class II sources to that of the Class 0/I, for different values of extinction and see if the ratio changes substantially (Guieu et al. 2009). In the case of M8, the visual extinction and the reddening (defined as the ratio of total to selective extinction, R_v = A_v/E(B-V)) varies from region to region; and a value of A_v = 3.2 was determined towards the Hourglass region for standard reddening (R_v = 3.1) (Arias et al. 2006; Tothill et al. 2008). For the present purpose, however, we compared the ratio N, for A_v values 0.0, 3.2 and 5.0. The ratio N remains at 2.63 with a Poisson error of $\pm$ 0.39 for A_v 0.0 and 3.2. For A_v = 5.0, we get N = 2.73$\pm$0.42. The value of N obtained here for M8 is comparable with that obtained for the Serpens (Harvey et al. 2006) and North American Nebula (Guieu et al. 2009) star forming regions, indicating the similarity of ages of these regions.

Fig. 4.3 shows the mid-infrared colour-colour diagram constructed from the IRAC photometry for [3.6]-[4.5] vs [5.8]-[8.0] colour. In this diagram, we show the photospheric sources as black dots, and the Class 0/I, Class II and Class III sources as open circles, open triangles and open squares respectively. Table D.1 in Appendix D lists the Class 0/I sources

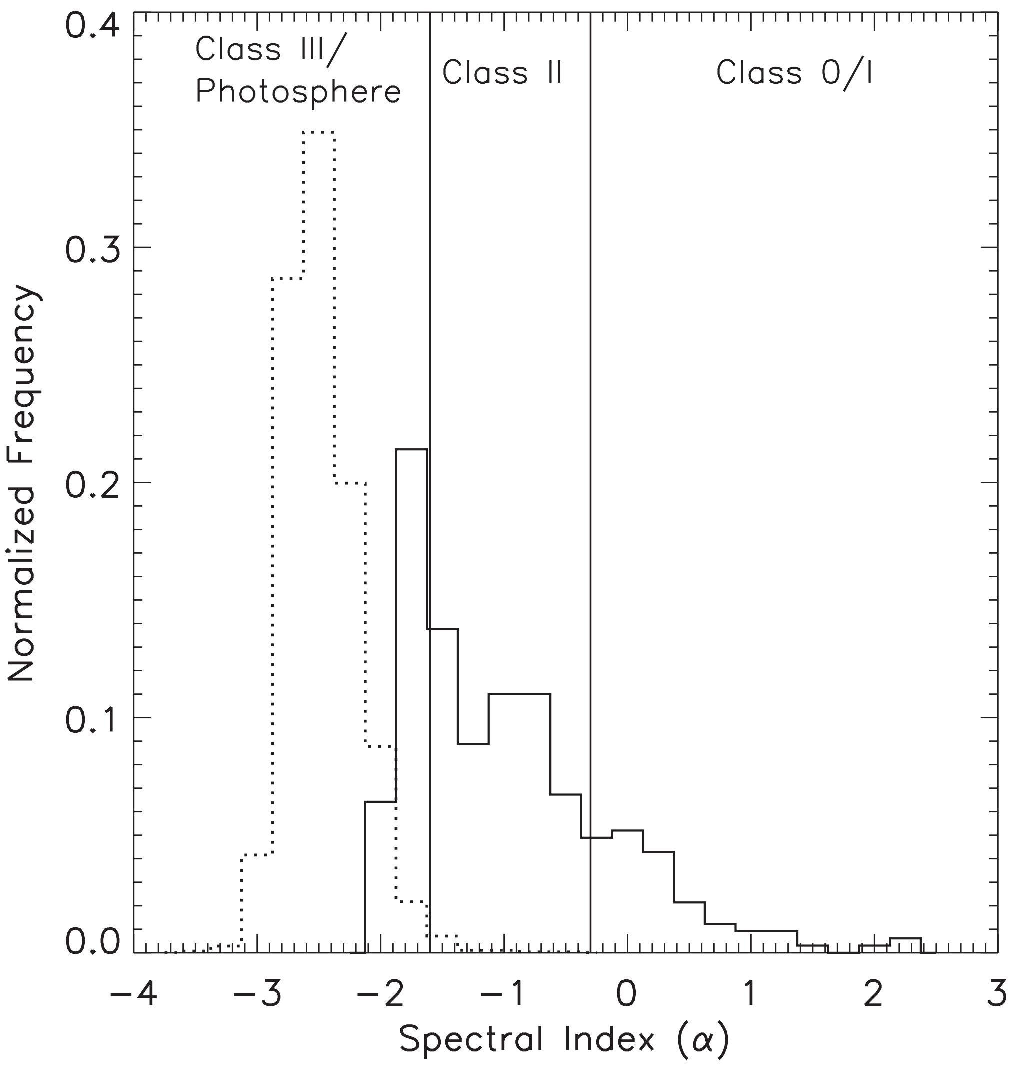

Fig. 4.2: Histogram of spectral index (α_{IRAC}) of sources in M8 is shown here with regions of different evolutionary stages of star formation shown by vertical lines (see text for more details). Dotted line represents the distribution of photospheric sources and distribution of YSOs is shown by solid line.

while Table D.2 gives the Class II sources. Also included in Table D.1 is the source KS 4 (No. 26; classified as YSO by Arias et al. (2006)) for which IRAC has detections in Chs. 1 & 2 only. Where available, the colours [J-H] and [H-K] along with the H magnitude from JHK surveys are also given in the Tables along with references.

Following the discovery of a companion, called Her 36 SE, about 0.25 arcsec south-east of Her 36 by Stecklum et al. (1995), Goto et al. (2006) observed the Her 36 region using VLT with adaptive optics. The latter authors conclude that the bulk of the mid-IR flux is infact accounted for by Her 36SE. The IRAC fluxes therefore represent contributions from both Her 36 and Her 36SE. Dividing the fluxes in each band following Goto et al. (2006), it may be concluded that Her 36SE could be a Class I (of B2 spectral type). Her 36 itself could be Class II or pre-ZAMS star of O spectral type. This corroborates with the age estimate of 5 $\times$ 10^4 yr for Her 36 by Chakraborty and Anandarao (1997).

The un-biased spatial distribution of YSOs is calculated using a 5 arcsec grid (see Chapter 3 for more details). The surface density is estimated using 5 and 6 nearest-neighbour YSOs for each grid point using the formula, given by Eq. 3.2 in Chapter 3. There is no significant difference for 5 and 6 NN density calculation; therefore we have used only 5 nearest-neighbour YSOs for the surface density calculation. Fig. 4.4 shows the YSO spatial density contours with the inner and outer contours representing 10 and 5 YSOs/pc^2 respectively. The maximum densities are about 20 YSOs/pc^2. Also shown in the figure are the spatial distributions of all the 327 sources (232 YSOs and 95 Class III) (a) and the contaminants (b). One can notice in Fig. 4.4 several small clusters (about 7) isolated by the technique used as above. These clusters are mostly confined to the Hourglass, NGC 6530, M8E and the ridge regions along with two more clumps east of H36.

In order to identify the cluster members rather than the isolated or scattered cases, we computed the empirical cumulative distribution as a function of nearest-neighbour distance. We found that the sources were within an (arbitrarily chosen) inflection distance d_c (that signifies the maximum separation between the cluster members) of $\sim$ 0.75 pc (0.03^o at 1.25 kpc distance). By varying d_c between 0.65 and 0.85 pc, the number of cluster members does not change significantly (see Fig. 4.5). The Class 0/I and Class II YSOs in clusters constitute about 60% of the total number detected and are confined mainly within the YSO density contours (corresponding to about 7 clusters) shown in Fig. 4.4. In comparison, only about 26% of the Class III sources (having “anemic” disks) occur in the clusters.

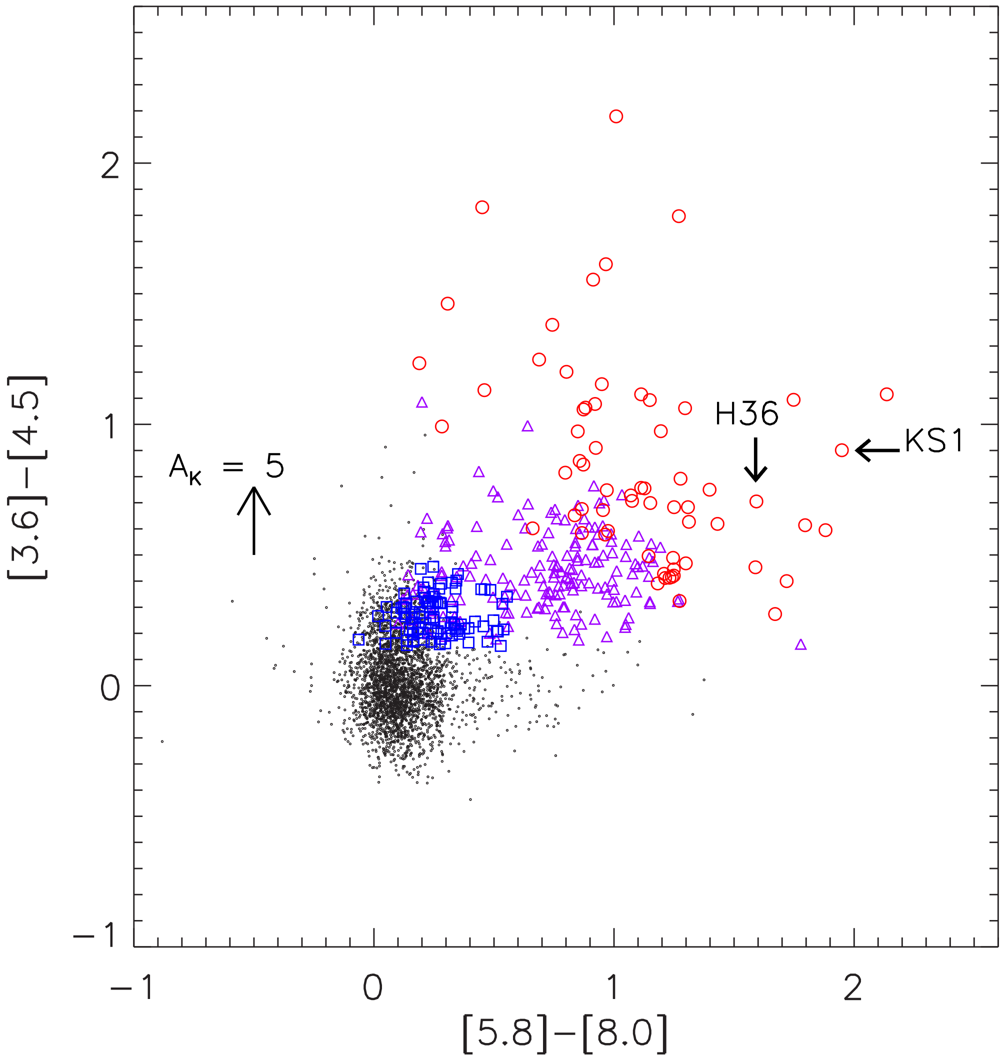

Fig. 4.3: Mid-IR colour-colour diagram using the *Spitzer*-IRAC bands for all the sources identified within the region shown in Fig. 4.1. The sources KS1 and Her 36 are marked by arrows. The upward arrow on the left shows the extinction vector for A$_K$ = 5 mag, using average extinction law from Flaherty et al. (2007). The black dots around the center (0,0) locate the stars with only photospheric emissions. The open squares (blue), open triangles (violet) and open circles (red) represent respectively, Class III, Class II and Class 0/I sources, obtained from the α_{IRAC} criteria.

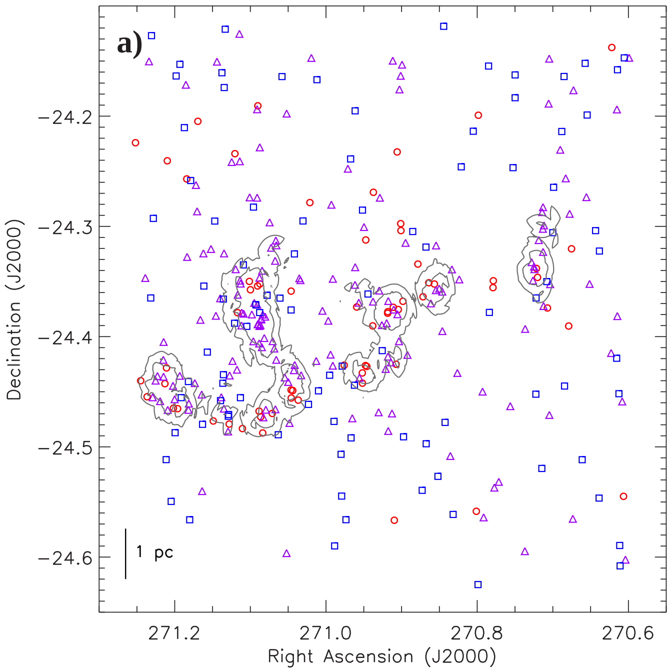

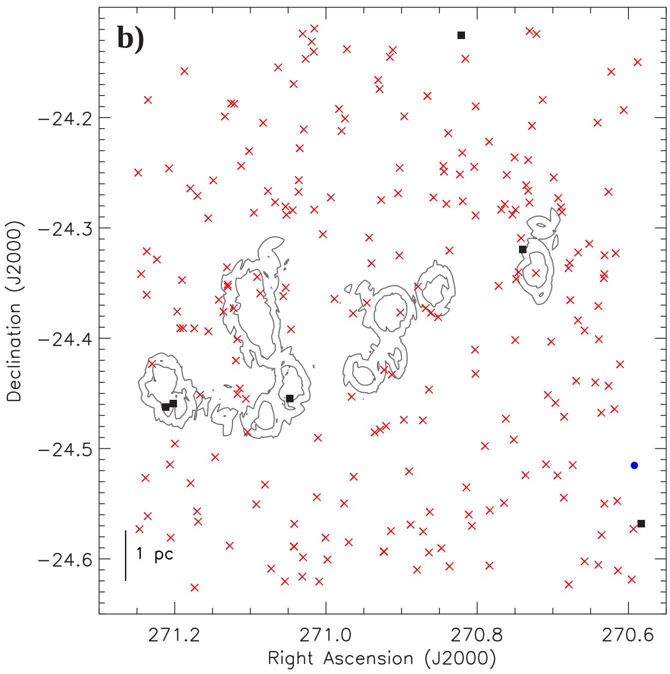

Fig. 4.4: a: *Spitzer*-IRAC field of M8 showing all the 327 sources (232 YSOs and 95 Class III): open circles (red) show Class 0/I sources, open triangles (violet) show Class II and open squares (blue) show Class III sources; b: *Spitzer*-IRAC field of M8 showing contaminants: crosses (red) show unresolved PAH aperture contaminations, filled squares (black) show shocked emission knots and the lone filled circle (blue) the PAH galaxy contaminant. In both the figures, the contours show YSO iso-density at 5 (outer) and 10 (inner) YSOs/pc^2.

The ratio N mentioned before varies from cluster to cluster with an average of 2.29 which is comparable to the one for the entire sample (2.63) within the Poisson errors. It may be noted here that the surface density of YSOs derived by us is very close to the values obtained for star forming regions elsewhere such as VULPECULA OB ASSOCIATION (see Billot et al. (2010) and references therein).

It may be noted here that since M8 (l = 5.958; b = -1.167) is located near the mid-plane of the Galaxy, there exists a possibility of our YSO sample being still contaminated from other intrinsically "red sources", such as asymptotic giant branch (AGB) stars. Recently Robitaille et al. (2008) prepared an extensive catalog of such "red sources" based on the *Spitzer*-GLIMPSE and MIPSGAL surveys. While the best way to distinguish between YSOs and AGB stars is spectroscopy, these authors showed that the two classes are well separated in the [8.0-24.0] colour space, with YSOs being redder than AGB stars in this space (see also Whitney et al. (2008)). Since in the present case of M8 we do not have the 24 μm data (from MIPS), we have estimated the AGB contamination by using the criteria based on the IRAC magnitudes and colour space (Robitaille et al. 2008). Since AGB stars are unlikely to occur in clusters, we have removed the clustered YSOs from our estimates. We find that our Class 0/I and II samples may be contaminated by AGB stars up to about 19%, while we do not find any contamination for our Class III sources. As pointed out by Robitaille et al. (2008), these separation criteria (including [8.0-24.0] colour) are "only approximate and there is likely to be contamination in both directions" (see the criterion for Red source selection in the Section D.3 of Appendix D).

Fig. 4.6 shows the Ch3 (5.8 μm) image overlaid by the IRAC Class 0/I (open circles) and Class II (open triangles) sources identified by using the α_{IRAC} criteria (see Tables D.1 and D.2 of Appendix D). Also shown (as black star symbols) in the figure are the positions of sub-mm (850μm) gas clumps (taken from Table 1 of Tothill et al. (2008)). The YSO density contours (in white) are also shown in the figure. A number of the Class 0/I and Class II sources occur very close to the dense filamentary/pillar-like structures seen all along the ridge region in the east-west direction as well as perpendicular to it in the central ridge or NGC 6530 region (see Fig. 4.1). A majority of these sources are found to be present in the vicinity of the sub-mm gas clumps (marked by black star symbols in Fig. 4.6). As mentioned earlier, M8E is a young compact high-mass star forming region. The central source of this cluster was resolved into a protostar M8E-IR and M8E-Radio, a B2 type star that is responsible for the compact HII region (Simon et al. 1984). While

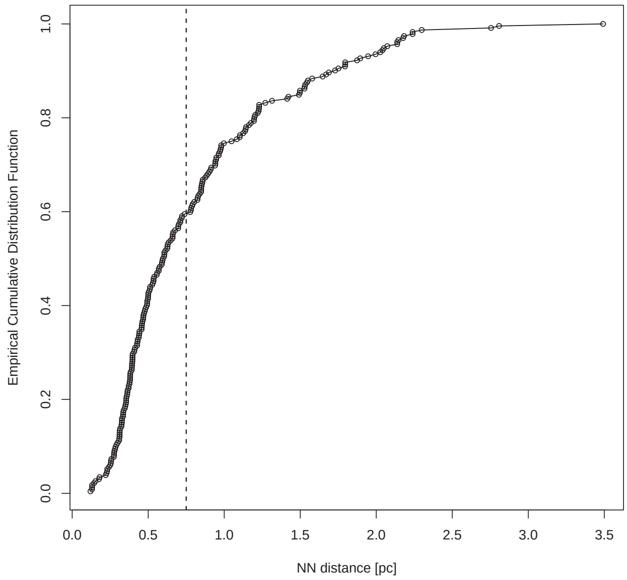

(a)

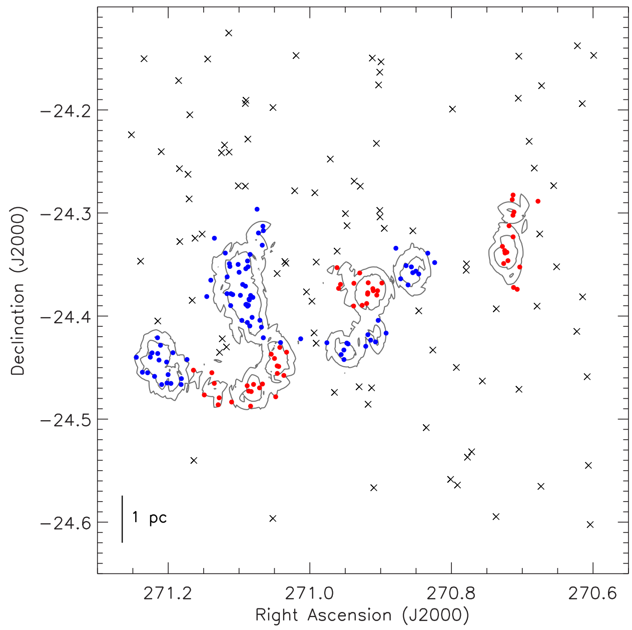

(b)

Fig. 4.5: a: Empirical cumulative distribution function of nearest-neighbour distance for the YSOs. The separation between clustered and scattered YSOs was done by (arbitrary) distance of inflection (d_c) of 0.75 pc at a distance of 1.25 kpc. b: The inflection distance d_c = 0.75 pc is used to distinguish the clustered and scattered members. YSOs occurring at larger than d_c value are shown by the cross symbols, lying outside the density contours and about 7 clusters are shown by circles. Red and blue colours are used only to distinguish the different cluster.

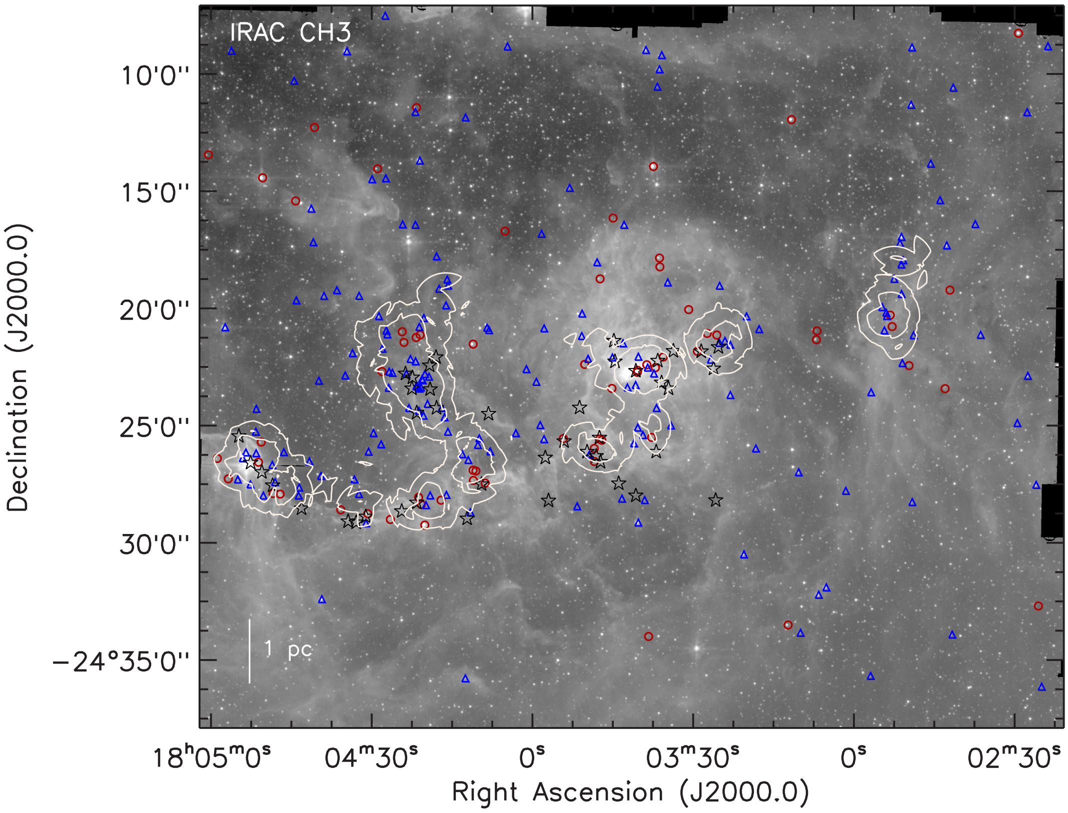

Fig. 4.6: *Spitzer*-IRAC Ch3 (5.8 μm) image of M8 ($\sim$ 42.5×30.0 arcmin^2) superposed by IRAC Class 0/I and II sources and sub-mm gas clumps. The open circles (red) and open triangles (blue) show the IRAC Class 0/I and II sources respectively (from Tables 1 and 2 in Appendix D); the black star symbols represent the locations of the sub-mm gas clumps (from Table 1 of Tothill et al. (2008)). The overlaid contours (white) are YSO density contours generated using a grid size of 5 arcsec: the inner contours are 10 YSOs/pc^2 and the outer contours represent 5 YSOs/pc^2.

the IRAC bands are saturated for M8E-IR itself, about 6 Class I or flat-spectrum and 10 Class II sources have been identified by IRAC in a region of 4 arcmin^2 around M8E. These sources are not common with those listed in Table 6 of Tothill et al. (2008). We did not find any IRAC PMS sources in the vicinity of the source IRAS 18014-2428, believed to be another young star forming region (corresponding to the sub-mm gas clump called SE3 (Tothill et al. 2002)).

Triggered star formation by the "Collect and Collapse" process (Elmegreen and Lada 1977) could be responsible for the existence of the IRAC sources, possibly started by the stellar winds or expanding HII regions associated with the nearby massive stars, viz. HD 165052, M8E, HD 164806, HD 164816, 9 Sgr and Her 36 (see Tothill et al. (2002)). While the ionization fronts from 9 Sgr and Her 36 have expanded well into the molecular cloud, that from M8E seems to have started later, as is evident from the bright narrow rim in front of M8E seen in Fig. 1. Thus the small cluster in M8E region may be younger than others in the region. Linz et al. (2009) modeled the spectral energy distribution of M8E-IR and concluded that it is a B0 type YSO. That the star formation is sequential in M8 starting from north-west regions to southern edge regions has been shown by Damiani et al. (2004), based on the Chandra X-ray survey of the NGC 6530 region and its neighbourhood in conjunction with 2MASS data and optical surveys (see Tothill et al. (2008) for a discussion).

4.3.2 IRAC Ratio Maps

As mentioned in Chapter 3, in the ratio image of Ch2/Ch4, the brighter regions indicate emission regions from higher excitations from H_2 and the darker regions indicate PAH emission. This trend is reversed in the image of Ch4/Ch2 (i.e., bright regions show PAH emission and dark regions show the H_2 emission). In addition to these molecular lines/features, IRAC bands also contain hydrogen recombination lines, notably the Brα line (4.05 μm) in Ch2, which can be used to trace HII regions. Thus, in HII regions, the H recombination lines (Brα and Pfβ) are more significant contributors to Ch2 rather than the H_2 lines. Several authors have utilised the ratios of IRAC bands to identify some of the atomic and molecular features/regions mentioned above (e.g., Smith and Rosen (2005); Povich et al. (2007); Neufeld and Yuan (2008)). It is important to note that the ratio maps are only indicative; until/unless conformed by spectroscopic evidences.

In order to make the ratio maps, point sources from all the IRAC images are removed by using an extended aperture of 12.2 arcsec and a sky annulus of 12.2-24.4 arcsec in IRAF/DAOPHOT software (Reach et al. 2005). Then these residual frames are subjected to median filtering with a width of 15 pixels and smoothing by 3$\times$3 pixels using the "boxcar" algorithm (Povich et al. 2007). Fig. 4.7 gives the ratio map of Ch2/Ch4 in a region of 0.67 $\times$ 0.46 pc^2 around Her 36. Contours overlaid on the ratio map represent the Hα emission observed by HST (in F656N filter image extracted from HST public archive). The minimum and maximum values of the contours are 5288 and 14100 counts respectively; six contours have been drawn with an interval of 1762 counts. In the vicinity of Her

36, the ratio map Ch2/Ch4 shows bright regions coinciding very nicely with the Hourglass HII region (as traced out by the contours of Hα). The bright regions coinciding with the Hourglass can not be attributed to molecular hydrogen lines of higher excitation temperature present in Ch2 in comparison with those of lower excitation temperature present in Ch4 (see Smith and Rosen (2005)). Further, the molecular hydrogen (1-0 S(1) at 2.12 μm) images presented by Burton (2002) do not show substantial emission around the Hourglass region (refer Figs. 3 and 4 of Burton (2002)). Considering the fact that the IRAC Ch2 also contains Hydrogen Brα line (as well as Pfβ (4.65 μm)), we may attribute the bright regions in the ratio map of Ch2/Ch4 coinciding with Hourglass, as due to Brα (and Pfβ) emission. One can notice narrow bright regions surrounding Her 36 (and the near-IR source KS1) in the ratio map of Ch2/Ch4. These regions are coincident with those of molecular hydrogen in Burton (2002). In these regions, it is likely that molecular hydrogen transitions of high excitation temperature may be responsible rather than Brα. A similar trend is also seen in the ratio image of Ch2/Ch3. Fig. 4.8 gives the ratio image Ch4/Ch2 in the same region as in Fig. 4.7. In this figure, ratio contours are overlaid on the ratio image for better clarity and insight. One can notice a bright (corresponding to dark region in Fig. 4.7) "cavity"-like structure to the east of the Hourglass. Actually, this structure occurs towards the east of the regions of very high column density reported by Arias et al. (2006) towards north and east of the Hourglass. It is possible that the PAH molecules can be shielded from high energy UV photons by these dense regions. But the molecules may be excited by the low energy (non-ionising) UV photons that can escape from the narrow dense regions between the Hourglass and the "cavity". Thus we may attribute the bright tubular structure to PAH emissions.

It may be mentioned here that the ratio image of Ch2/Ch1 does not show the Hourglass as prominently as in Ch2/Ch4 or Ch2/Ch3. This could be because of the fact that Ch1 contains the Pfγ (3.7 μm) and Pfδ (3.3 μm) lines which may be partly canceling the contribution of the recombination lines in Ch2. In fact we do clearly see the Hourglass HII region in the ratio images of Ch1/Ch3 and Ch1/Ch4 also. Thus, Ch1 and Ch2 bring out well the H recombination emission in the Hourglass. Ch4 is unable to depict the HII region in spite of the presence of Pfα (7.5 μm), mainly because of the fact that its spectral response is inferior to that of Ch1 (or that of Ch2) (Smith and Rosen 2005). For a HII region under Case B situation (Hummer and Storey 1987) with a kinetic temperature of 10^4 K and electron densities of 10^2-10^6 cm^{-3}, the combined relative intensities of Pfγ and Pfδ are only a factor of $\sim$ 1.4 times lower than that of Pfα. Hence the combined detected

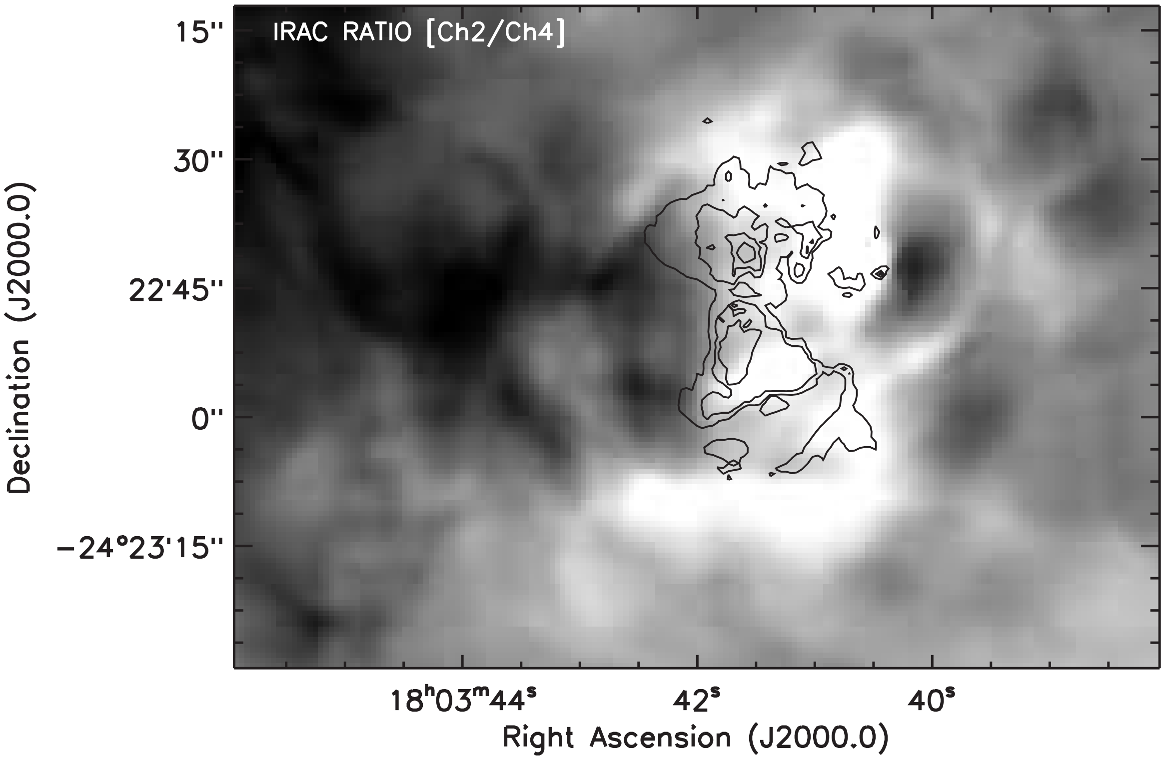

Fig. 4.7: Ratio image of Ch2/Ch4 of M8 (Lagoon Nebula) in log scale overlaid by HST Hα (F656N filter) contours, in a region around Her 36 of size 110$\times$76 arcsec^2. The contour levels are between 5288 and 14100 counts. The bright regions indicate the prominence of Ch2 over Ch4, while the dark regions have the reverse trend. The bright "3" shaped structure is more extended than the Hα contours and nearly coincide with them.

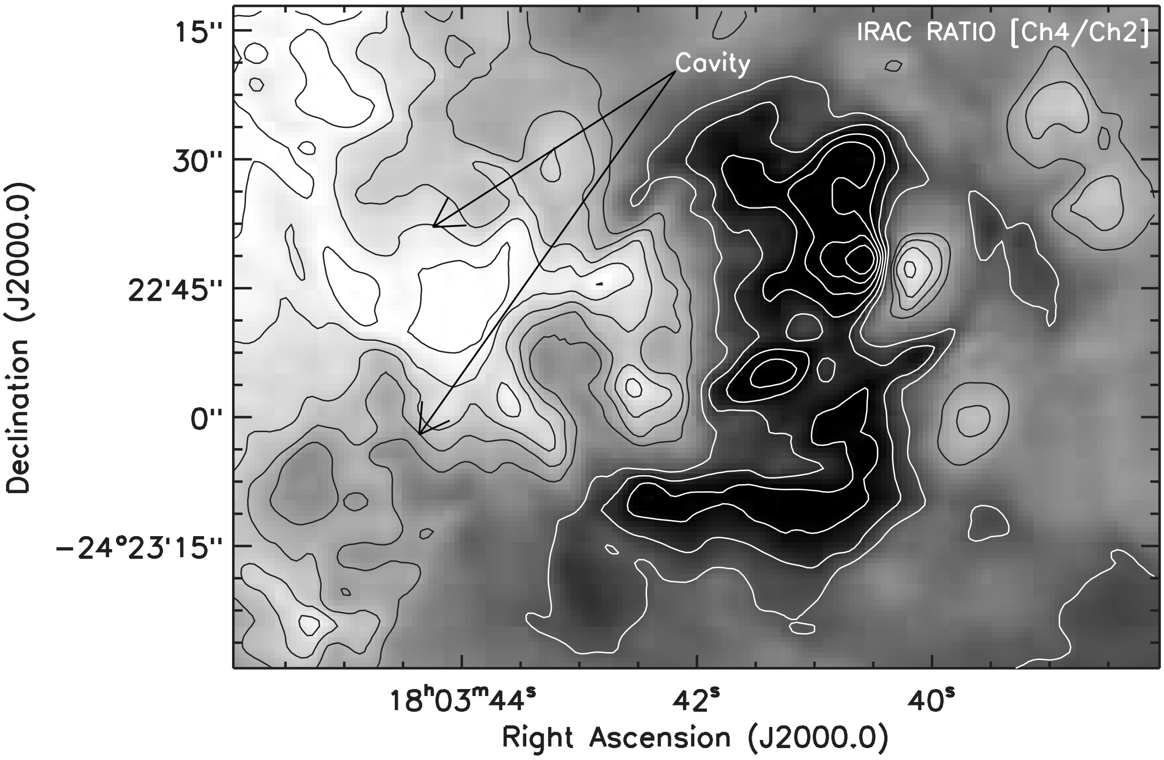

Fig. 4.8: Ratio image of Ch4/Ch2 of M8 (Lagoon Nebula) in log scale. The bright regions indicate the prominence of Ch4 over Ch2. For better insight, the ratio image is overlaid by the ratio contours: the black contours in the bright regions represent ratio levels between 17.4 and 22.8; and the white contours in the dark regions indicate the ratio levels between 8.4 and 14.3. The region of possible PAH emission is the bright tubular structure within the "cavity", seen east of the Hourglass.

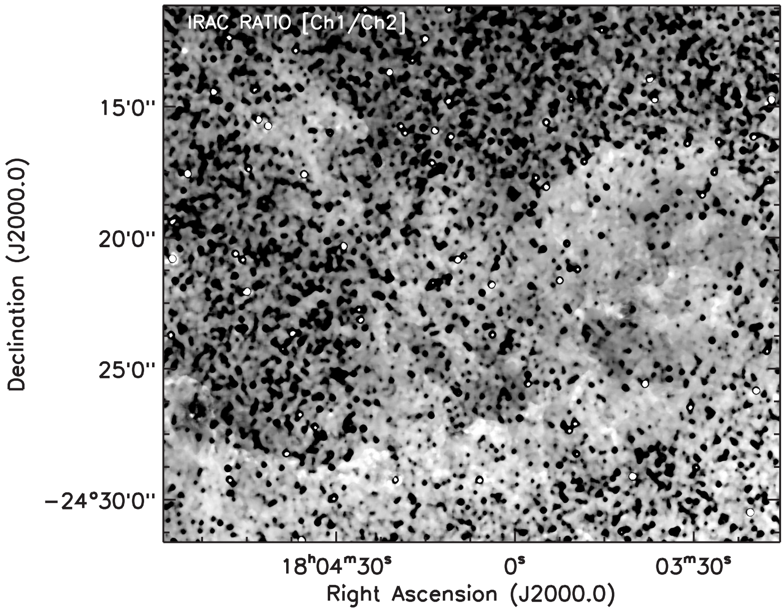

Fig. 4.9: Ratio maps of Ch1/Ch2 in log scale (in a region of size $\sim$ 24.2 $\times$ 20.0 arcmin^2), showing the ridges and filamentary structures (towards east/south-east of Her 36). The dominance of Ch1 (bright portions) over Ch2 in the ridge region and filamentary regions can be noticed, which may be attributed to the PAH emission in these regions. The black and white dots are the result of the residueing process.

flux of Pfγ and Pfδ in Ch1 can exceed that of Pfα in Ch4.

Elsewhere in M8 the ratio maps seem to have a different story to tell. Figs. 4.9, 4.10 and 4.11 give the ratio maps Ch1/Ch2, Ch3/Ch2 and Ch4/Ch2 respectively, of the ridge regions in M8 complex in an area of 24.2 $\times$ 20.0 arcmin^2 to the east/south-east of Her 36. The ratio images show bright rims corresponding to the filamentary structures all along and perpendicular to the east-west ridge region. These regions seem to be bright in all bands, except Ch2 that is free of PAH features. Hence it is tempting to attribute the bright regions seen in the ratio images in Figs. 4.9, 4.10 and 4.11 to the PAH features. It is unlikely that these bright regions are a result of molecular hydrogen emission; since they occur in all the bands though at different excitation temperatures (mostly rotational lines) and should have canceled each other in the ratio maps. Elsewhere in M8 the ratio maps seem to have a different story to tell. Figs. 4.9, 4.10 and 4.11 give the ratio maps Ch1/Ch2, Ch3/Ch2 and Ch4/Ch2 respectively, of the ridge regions in M8 complex in an area of 24.2 $\times$ 20.0 arcmin^2 to the east/south-east of Her 36. The ratio images show bright rims corresponding to the filamentary structures all along and perpendicular to the east-west ridge region.

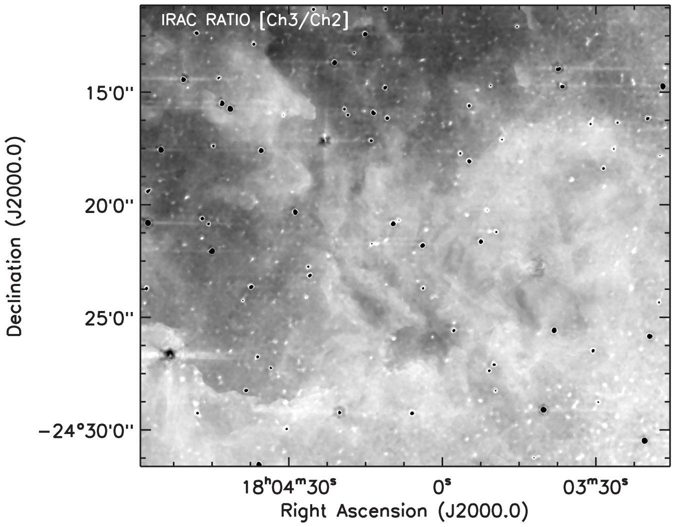

Fig. 4.10: Ratio maps of Ch3/Ch2 in log scale (in a region of size $\sim 24.2 \times 20.0$ arcmin^2), showing the ridges and filamentary structures (towards east/south-east of Her 36). The dominance of Ch3 (bright portions) over Ch2 in the ridge region and filamentary regions can be noticed, which may be attributed to the PAH emission in these regions. The black and white dots are the result of the residueing process.

These regions seem to be bright in all bands, except Ch2 that is free of PAH features. Hence it is tempting to attribute the bright regions seen in the ratio images in Figs. 4.9, 4.10 and 4.11 to the PAH features. It is unlikely that these bright regions are a result of molecular hydrogen emission; since they occur in all the bands though at different excitation temperatures (mostly rotational lines) and should have canceled each other in the ratio maps.

4.4 Conclusions

The important conclusions of this work are as follows:

1. *Spitzer*-IRAC photometry of the M8 region have revealed 64 Class 0/I and 168 Class II YSOs. About 60% of these are present in about 7 small clusters with spatial surface densities of 10-20 YSOs/pc^2;

2. These sources are positioned close to the sub-mm gas clumps and the filamentary or pillar like structures present in M8. It is possible that the formation of these sources could have been triggered by stellar winds or expanding HII regions associated with the massive stars in the region;

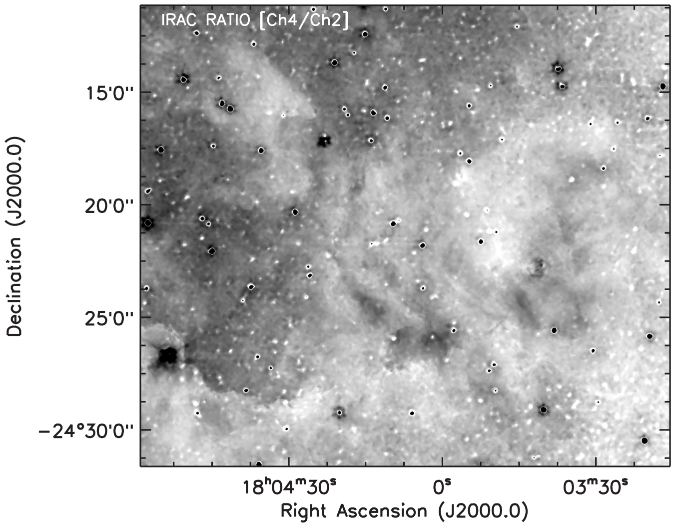

Fig. 4.11: Ratio maps of Ch4/Ch2 in log scale (in a region of size $\sim 24.2 \times 20.0$ arcmin^2), showing the ridges and filamentary structures (towards east/south-east of Her 36). The dominance of Ch4 (bright portions) over Ch2 in the ridge region and filamentary regions can be noticed, which may be attributed to the PAH emission in these regions. The black and white dots are the result of the residueing process.

3. The ratio map Ch2/Ch4 reveals Brα emission corresponding to the Hourglass HII region powered by Her 36 and its inverted ratio (Ch4/Ch2) identifies PAH emission in a cavity east of the Hourglass;

4. The ratio maps Ch1/Ch2, Ch3/Ch2 and Ch4/Ch2 indicate the presence of PAH emission in both the ridges oriented along E-W and NE-SW directions.

Chapter 5

Infrared photometric study of the massive star forming region S235

Following the mid-IR photometric studies on AFGL 437 and M8 in the preceding chapters, we present here a combined study of near-infrared (NIR) and *Spitzer*-IRAC photometry of the young star forming region, IRAS 05375+3540 (in the vicinity of S235A and S235B region). We show here that the NIR data can be effectively combined with the *Spitzer* Space Telescope observations to identify additional young stellar objects (YSOs) in the region.

5.1 Introduction

The S235 is a large extended HII region associated with a star forming complex and situated at a distance between 1.6 kpc and 2.5 kpc (Georgelin et al. 1973; Israel and Felli 1978), in the Perseus Spiral Arm. Georgelin et al. (1973) found that the S235 region is excited by the massive star BD +35^{o}1201 of O9.5V type that has ionised and dispersed the surrounding molecular gas. The earlier studies on this complex show that it is a site of active star formation (Israel and Felli 1978; Felli et al. 1997, 2004, 2006; Allen et al. 2005; Kirsanova et al. 2008). This region covers some well known star forming sites called East 1, East 2, Central (Kirsanova et al. 2008) and S235A, S235B and S235C (Felli et al. 1997).

Using molecular gas kinematics and density distribution from ^{13}CO(1-0) and CS(2-1) emission observations in the mm region, Kirsanova et al. (2008) presented evidences to argue that the expanding HII region in S235 triggered fresh star formation in the north-east and north-west regions of the complex ("East 1, East 2, Central and North-West"). Kirsanova et al. (2008) argued that the star formation may have been triggered either by the "Collect and Collapse" process or by shocking the already clumpy regions and that the denser East 1 cluster is probably younger than the Central and East 2 clusters. Allen et al. (2005) presented *Spitzer*-IRAC photometry on the S235 complex and Felli et al. (2006) studied some selected sources in the S235A and S235B regions (henceforth called as S235A-B) and identified several young protostars. Felli et al. (2004) studied the region S235A-B with high-resolution mm lines (from the molecules HCO^+, $C^{34}S$, H_2CS, SO_2, and CH_3CN) and continuum observations, together with far-IR observations and reported two molecular outflows in HCO^+(1-0) centred on the compact molecular core (traced by the 1.2 mm continuum observations). Later on, from radio observations at the VLA and with *Spitzer*-IRAC observations on the S235A-B region Felli et al. (2006) argued that the expanding HII region from the massive star in S235A triggered the star formation in the dense cluster between the S235A and S235B regions. They also found a new embedded source S235AB-MIR in three IRAC bands (except in Ch1) in the mm core. Felli et al. (2006) detected two compact radio-sources VLA-1 and VLA-2, that coincide with the source M1 and the centre of S235B respectively. Saito et al. (2007) identified dense clumps from their observations of $C^{18}O$ emission (that traces dense gas). Krassner et al. (1982) found recombination lines of Hydrogen and the PAH emission features at 3.3, 8.7 and 11.3 μm associated with S235B that was attributed to a rare class of early type Herbig Be star by Boley et al. (2009).

In the backdrop of the existing observations and interpretations of the S235 complex, our aim to revisit the *Spitzer*-IRAC archival data is: (i) to find YSOs (systematically taking care of all possible contaminations), (ii) to estimate YSO surface densities, (iii) to identify some interesting YSOs and derive their physical parameters using the SED modeling and (iv) to try and delineate regions of different emission lines/features (Brα, H_2 and PAH). To our knowledge these were not done before. In addition, we have made NIR photometric observations in the vicinity of S235A-B from the Mt. Abu observatory. These are deeper observations than the 2MASS archive on the complex. Using the NIR photometry in conjunction with IRAC photometry, we attempted to extract more YSOs in the clusters.

In Section 5.2, we describe the data used for the present study and the analysis tasks utilised. Section 5.3 presents the results and discussion on infrared photometry of embedded sources associated with the S235 complex. In this section, we also present the results and discussion on the ratio maps. In Section 5.4, we give the conclusions.

5.2 Observations and Data Analysis

Near-infrared (NIR) photometric observations were made on the massive star forming region using the Physical Research Laboratory (PRL) 1.2 m telescope at Mt. Abu, India. The source IRAS 05375+3540 (in the vicinity of S235A and S235B regions in the S235 complex) was observed during 20-21 January 2010 under photometric conditions using the newly commissioned Near-Infrared Camera and Spectrograph (NICS: Anandarao et al. (2008)) that has a 1024 $\times$ 1024 HgCdTe array Wide-area Infrared Imager-I (HAWAII-1; Teledyne, USA) in the J(1.17-1.33 μm), H(1.49-1.78 μm) and K(2.03-2.37 μm) bands. NICS has a field of view of 8 $\times$ 8 sq. arcmin with a plate scale of 0.5 arcsec/pixel. Limiting magnitudes of 17, 16.5 and 16.0 mag were achieved in integration times of 300, 200 and 200 seconds in J, H and K bands respectively. These limiting magnitudes are deeper than the 2MASS survey for this object.

The reduction of data from the Mt. Abu 1.2m telescope was done using the standard tasks in IRAF software (Tody 1993). All the images were processed using standard pipeline procedures like dark and sky subtraction and flat-fielding. The images were then co-added and averaged to obtain a final image in each band (J, H and K). PSF photometry is performed on the images using DAOPHOT (digi.daophot) (Stetson 1987) task in IRAF to obtain individual point source magnitudes (details of the procedures of PSF photometry are given in Longmore and Burton (2009)).

Spitzer-IRAC archival data around the source S235 (encompassing IRAS 05375+3540) were obtained from the Spitzer Science Center (SSC) on 6 May 2009. The observations for S235 were taken by *Spitzer* in the High Dynamic Range (HDR) mode with 12s integration time in all four filters on 12 March 2004 as a part of the GTO program id “201” with project title “The Role of Photodissociation Regions in High Mass Star Formation” (PI: G. Fazio). A total number of 72 BCD images of size 5.2 $\times$ 5.2 arcmin^2 were mosaiced to obtain a final image of size 22.5 $\times$ 16.6 arcmin^2 commonly in all the four bands. The detailed procedures for mosaicing are given in Chapters 3 and 4. Aperture photometry was performed on the mosaiced images with 2.8 pixel aperture and sky annuli of 2.8 and 8.5 pixels using APPHOT task in the IRAF package. The zero points for these apertures (including aperture corrections) are, 17.80, 17.30, 16.70 and 15.88 mag for the 3.6, 4.5, 5.8, 8.0 μm bands, here onwards called as Ch1, Ch2, Ch3 and Ch4 respectively. The photometric uncertainties were found to vary between 0.01 to 0.25 for the four channels, with those for longer wavelengths (i.e., 5.8 and 8.0 μm) being on the higher side.

5.3 Results and Discussion

Our work is mainly focused on S235A-B, East 1 and East 2 regions of the S235 molecular cloud complex. We have divided this sub-section into two parts: the first in which we discuss IRAC photometry of the sources in the entire region, we look into each region separately (i.e., S235A-B, East 1 and East 2) and we describe the modeling of important and interesting sources and their possible formation scenario; and the second in which we describe the ratio maps produced from the IRAC images for the entire complex and discuss possible interpretations along with their implications.

5.3.1 IRAC Photometry

In this sub-section, we present a photometric study carried out on the whole S235 complex using four IRAC bands. A 3-colour-composite image of the IRAC bands (Ch4(red), Ch2(green) and Ch1(blue)) is shown in Fig. 5.1, encompassing the East 1, East 2, Central and S235A-B regions.

As described in Chapters 3 and 4, we have removed all possible contaminations from the sample. We have obtained a total of 603 point sources that are commonly identified in all the four IRAC bands. Of these 603 sources, 71 are found to be contaminations (33 PAH galaxy, 2 AGN, 2 shocked emissions, 34 PAH aperture-contaminations), while there are 286 YSOs and 246 purely photospheric sources.

We have applied criteria based on the spectral index, to classify the identified YSOs into different evolutionary classes (Billot et al. 2010). The histogram plot of the spectral index (α_{IRAC}) of YSOs and Photoshperic/Class III sources is shown in Fig. 5.2. Using criteria based on the spectral index (detailed in Section 4.3.1 of Chapter 4), we have obtained 84 Class 0/I, 192 Class II sources (now 276 YSOs) and 10 Class III sources. The locations of these identified YSOs (Class 0/I, II), Class III as well as the photospheric sources are plotted in the IRAC colour-colour diagram shown in Fig. 5.3. The sky coordinates, IRAC magnitudes and spectral indices of Class 0/I and Class II sources are given in the Table E.1 and E.2 of Appendix E respectively.

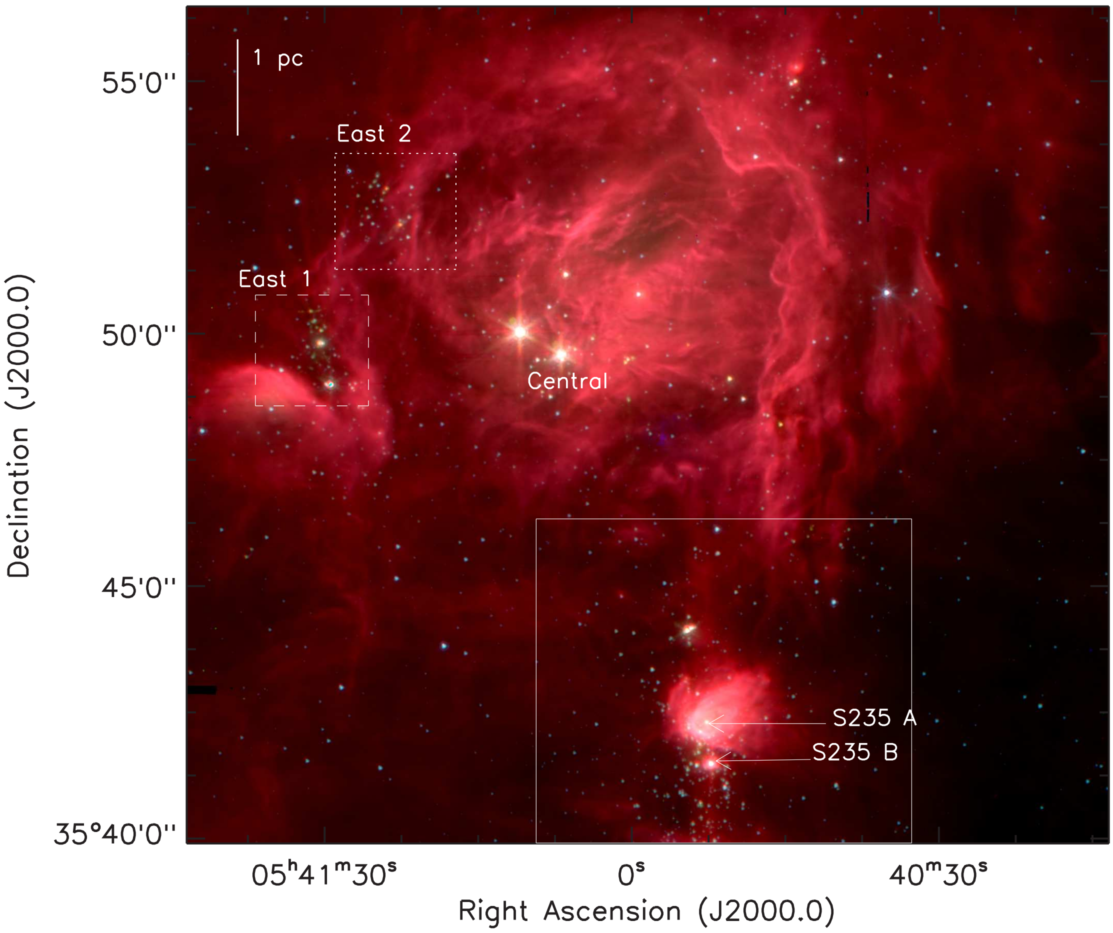

Fig. 5.1: IRAC 3-colour-composite image (size $\sim$ 22.5 $\times$ 16.6 arcmin^2) of S235 complex is presented here (8.0 (red), 4.5 (green) and 3.6 μm (blue)). Different regions identified by Kirsanova et al. (2008) are labeled in the region within S235 complex. Two of such regions in the complex are shown by dashed and dotted boxes for East 1 and East 2 respectively. The solid line box in the complex represents the region covered by our JHK observations.

In order to estimate the clustering of YSOs in the S235 complex, we have calculated the un-biased surface density of YSOs using a 5 arcsec grid size, following the same procedure as described in Chapter 3. The surface density of YSOs is estimated using 6 nearest-neighbour (NN) YSOs for each grid point. Fig. 5.4 shows the spatial distribution of YSOs (Class 0/I (red open circles) and Class II (violet open triangles) sources) in the IRAC Ch2 image (4.5 μm). The surface density contours are overlaid in the figure. The contour levels of surface density of YSOs plotted in Fig. 5.4 are 30, 10 and 5 YSOs/pc^2 decreasing from inner to outer side. It is noted that the distribution of YSOs is mostly concentrated in the East 1, East 2 and the vicinity of S235A-B region, while very small density of YSOs is also found around the Central region. The maximum densities are about 50 YSOs/pc^2 in the complex.

In addition, we have calculated the empirical cumulative distribution as a function of nearest-neighbour distance (see Chapter 4 for more details) to identify the YSO cluster and its members as against the isolated or scattered ones. The spatial distribution of all the 278 YSOs and 10 Class III sources are plotted in the Fig. 5.5 with surface density contours of YSOs (Fig. 5.5a) and the contaminants (Fig. 5.5b) using similar levels as used in Fig. 5.4. We have used somewhat arbitrarily the distance of inflection d_c = 0.62 pc ($\sim$ 0.02^o at 1.8 kpc distance) to identify the size of clusters of YSOs (see Fig. E.1 of Appendix E).

Finally, we have applied the "red sources" criteria (Robitaille et al. 2008) to our identified scattered sources outside the clusters and have estimated nearly 8% of the sources as the AGB contaminations (see details in Chapter 4 and also, the criterion for Red source selection in Section D.3 of Appendix D). We find that 75% of the YSOs are present in clusters concentrated in three main regions i.e., East 1, East 2 and the vicinity of S235A-B.

Our determination of surface densities of YSOs is consistent with the dense regions traced out by CS(2-1) emission, except in the Central region. We have found the highest density of YSOs in the S235A-B region among all the clusters in the entire S235 complex.

S235-East 1

The East 1 region is shown magnified in Fig. 5.6 using IRAC 3-colour-composite image from Fig. 5.1 (dashed box). We have found 11 Class 0/I and 8 Class II sources in the East 1 region, which are marked in Fig. 5.6. Some of the Class 0/I sources are labeled

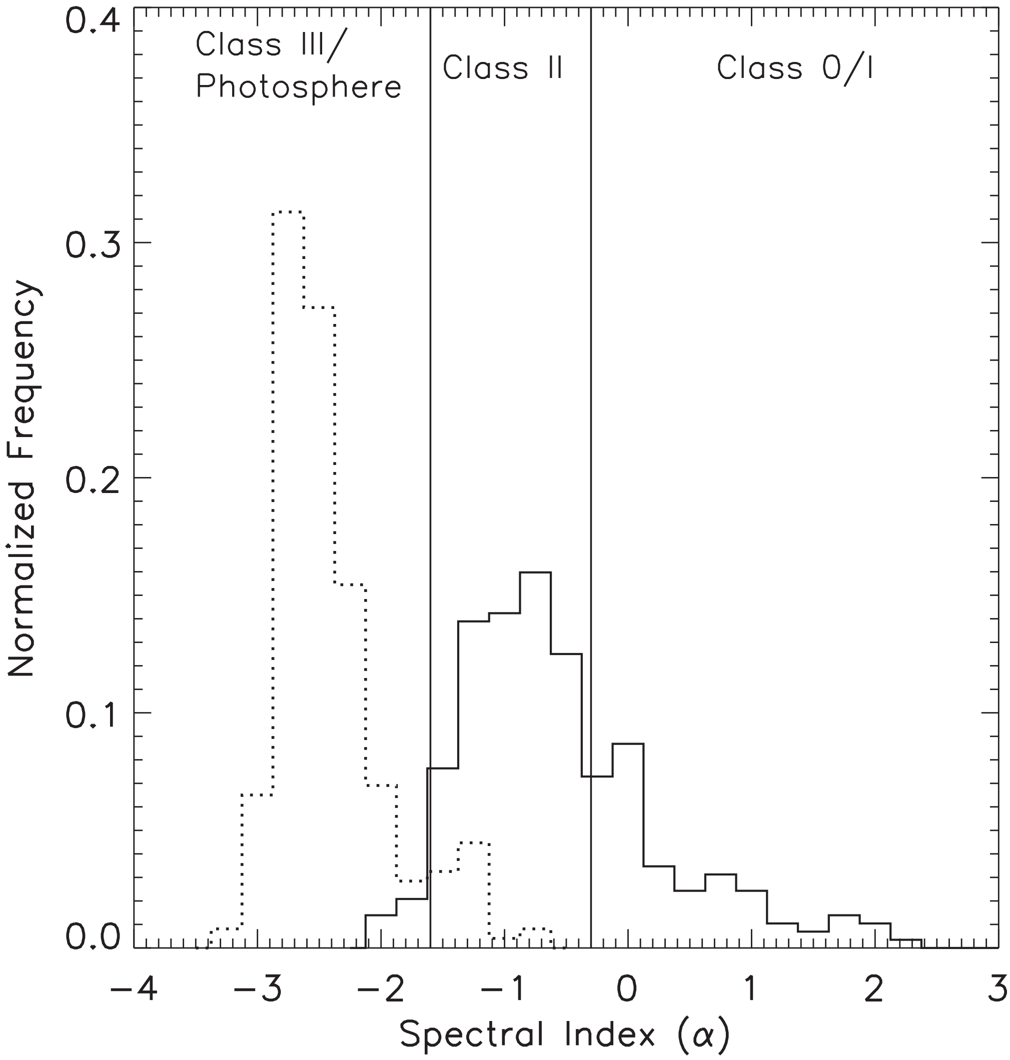

Fig. 5.2: Histogram of spectral index (α_{IRAC}) of sources in S235 complex is shown here with regions of different evolutionary stages of star formation shown by vertical lines (see text for more details). Dotted line represents the distribution of photospheric sources and distribution of YSOs is shown by solid line.

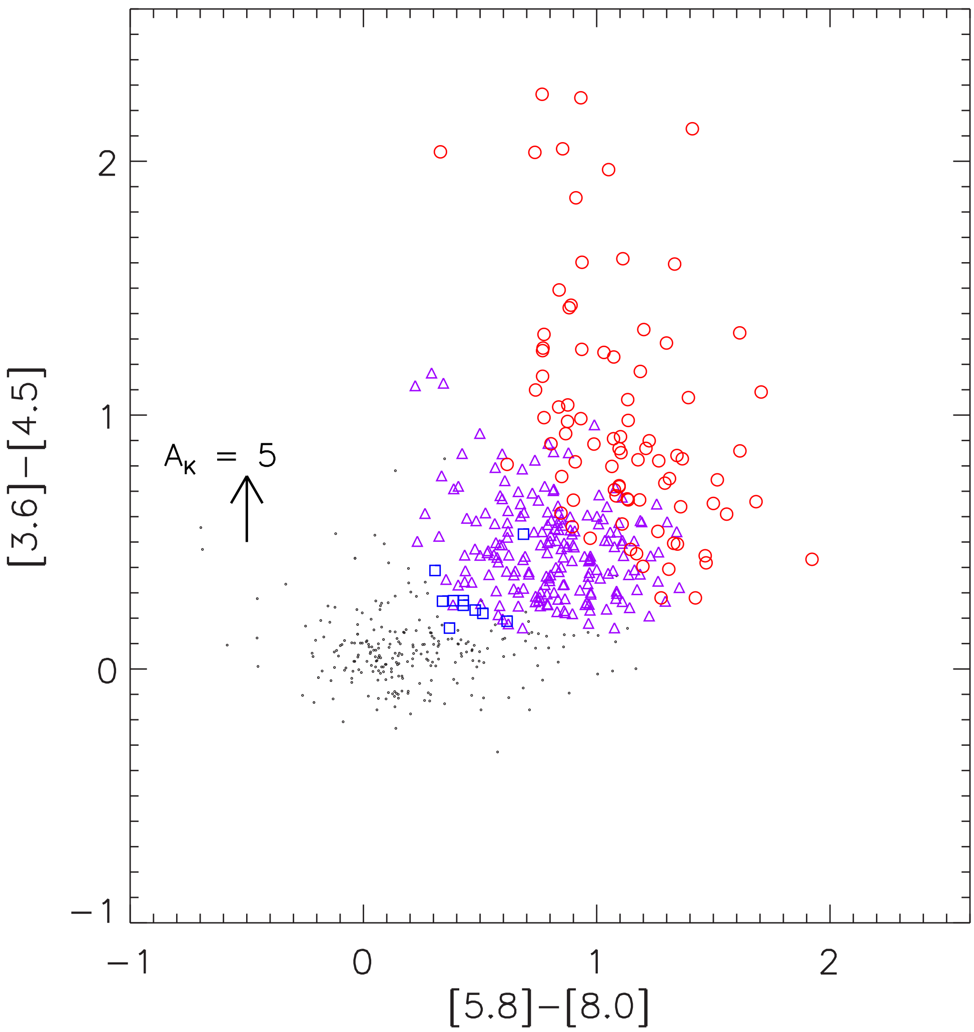

Fig. 5.3: Mid-IR colour-colour diagram using the *Spitzer*-IRAC bands for all the sources identified within the region shown in Fig. 5.1. The extinction vector for A_K = 5 mag is shown by the arrow on the left side, using average extinction law from Flaherty et al. (2007). The black dots around the centre (0,0) locate the stars with only photospheric emissions. The open squares (blue), open triangles (violet) and open circles (red) represent respectively, Class III, Class II and Class 0/I sources, classified using the α_{IRAC} criteria.

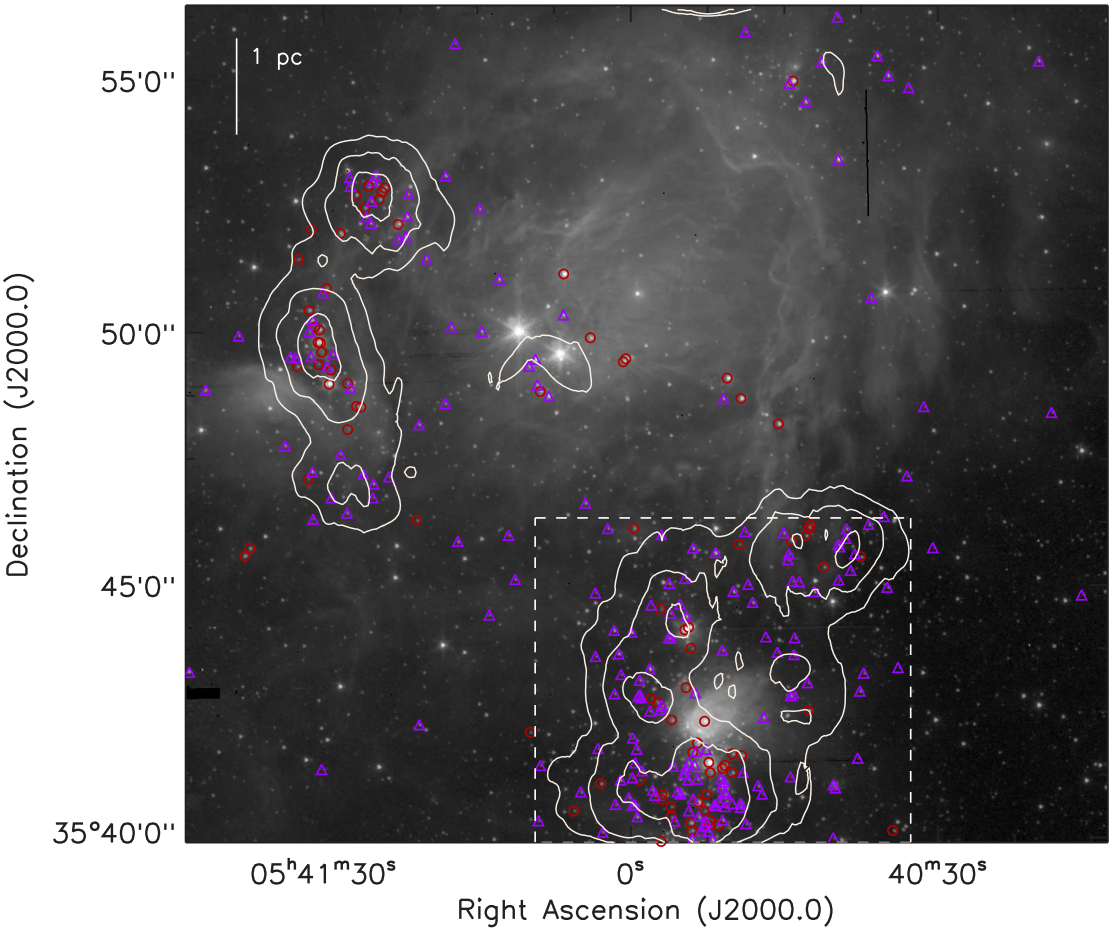

Fig. 5.4: *Spitzer*-IRAC Ch2 (4.5 μm) image of S235 (similar size as shown in Fig. 5.1) over-plotted by IRAC Class 0/I and II sources. The open circles (red) and open triangles (violet) show the IRAC Class 0/I and II sources respectively. The overlaid contours (white) are YSO density contours generated by using a grid size of 5 arcsec: the inner to outer contour levels are 30, 10 and 5 YSOs/pc^2. Dashed box represents the NIR observed region as shown in Fig. 5.1 by a solid box.

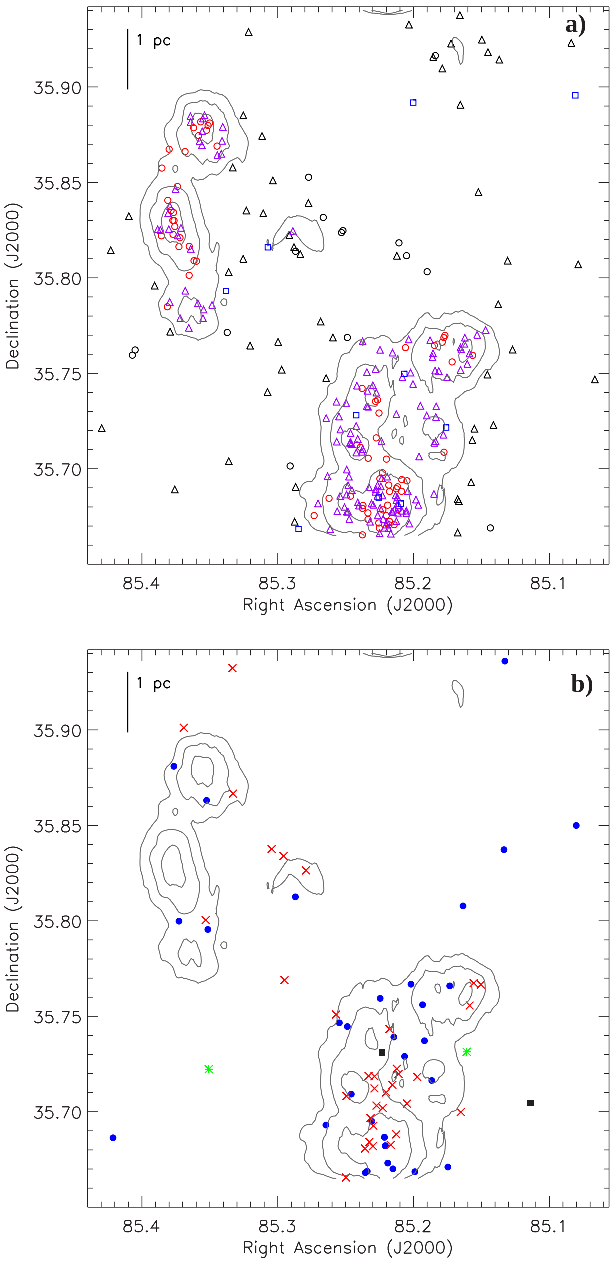

Fig. 5.5: a: *Spitzer*-IRAC S235 region with distribution of all the 286 sources (276 YSOs and 10 Class III): open circles show Class 0/I sources, open triangles show Class II and open squares show Class III sources. The value for d_c = 0.62 pc is used to distinguish the clustered and scattered members. YSOs outside the d_c value are shown by black circles and black triangles for Class 0/I and Class II sources respectively. The distribution of all the cluster members within $d_c \leqslant 0.62$ pc are shown by open circles (red) for Class 0/I sources, and open triangles (violet) for Class II sources; b: *Spitzer*-IRAC S235 region showing contaminants: crosses (red) show resolved PAH aperture contaminations, filled squares (black) show unresolved shocked emission knots, green asterisk show AGNs and the filled circle (blue) the PAH galaxy contaminant. In both the figures, the contours show YSO iso-density at 5, 10 and 30 YSOs/pc^2 from outer to inner side.

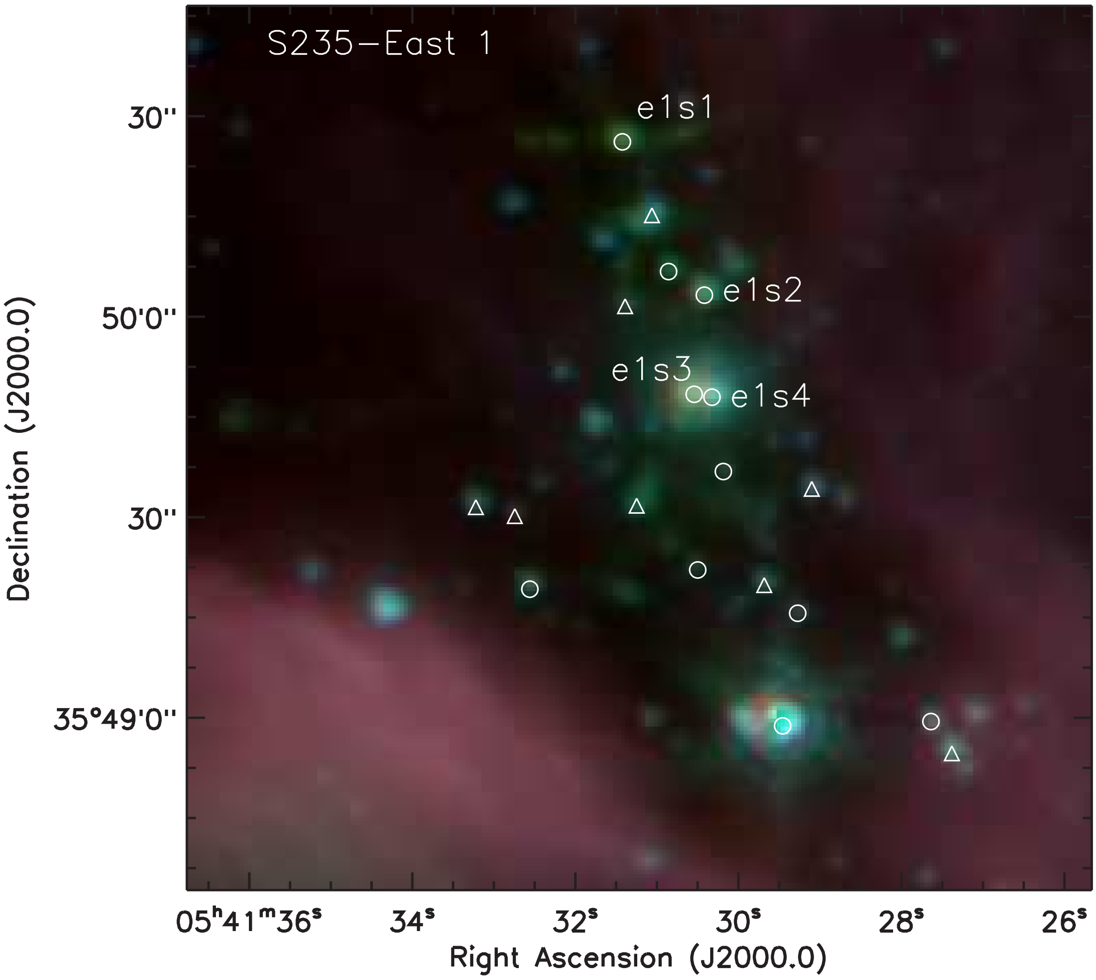

Fig. 5.6: IRAC 3-colour-composite (Ch4(red), Ch2(green) and Ch1(blue)) zoomed-in image of East 1 region (Fig. 5.1: dashed box). Classified YSOs (Class 0/I in white circles and Class II in white triangles) are overlaid on the image. The marked sources are Class 0/I sources that are not detected in 2MASS JHK image. The image shows that the green colour (i.e., IRAC Ch2 (4.5 μm)) is more dominant around the marked sources. They may be associated with the shock-excited molecular H_2 emission because IRAC Ch2 (4.5 μm) is sensitive for shock-excited molecular H_2 emission.

(e1s1-4) in Fig. 5.6. These are sources, which do not have JHK counterparts. The labeled sources are given in Table 5.1 with positions and observed IRAC magnitudes. The IRAC colour-composite image shows the presence of the shock-excited molecular H_2 emission in the East 1 region due to the predominance of Ch2 band. We have done the SED modeling of labeled sources and the fitted plots are shown in Fig. 5.8a for all the labeled sources in S235 East 1 region. The weighted mean values of the physical parameters derived from SED modeling for all selected sources are given in Table 5.2. The SED model results show that all the four labeled sources are young and still going through the accretion. Details of these SED results are also discussed in the IRAC ratio map sub-section.

S235-East 2

Figure 5.7 shows the East 2 region in IRAC 3-colour-composite image zoomed from Fig. 5.1 (dotted box). We have obtained 8 Class 0/I and 13 Class II sources in the East 2 region as displayed in the Fig. 5.7. We have found some interesting Class 0/I sources (labeled e2s1-3, in Fig. 5.7), which do not have JHK counterparts and are detected only in (all the four) IRAC bands. The labeled sources are given in Table 5.3 with position and observed IRAC magnitudes. The SED modeling results of the labeled sources are shown in Fig. 5.8b and the weighted mean values of their physical properties are given in Table 5.4. All these 3 selected sources are young and still passing through the accretion stage. The IRAC colour-composite image indicates the presence of shock-excited molecular H_2 emission in the East 2 region. Fig. 5.7 exhibits the extended “green (Ch2)” emission (about 0.22 pc in SE-NW direction) associated with the Class 0/I source “e2s3”. It could be possible that the source “e2s3” is probably associated with outflows. The SED modeling results indicate that the source “e2s3” is a massive but very young protostar not yet being able to excite an HII region. Our results suggest that “e2s3” is a very interesting source in the S235 East 2 region which may be a new high mass protostellar object (HMPO) associated with outflows. Details of the SED results are also discussed in the light of IRAC ratio maps (see IRAC ratio map sub-section).

S235A-B

Fig. 5.9 represents the zoomed IRAC 3-colour-composite image in the the vicinity of the S235A-B region (solid box in Fig. 5.1). We have obtained 164 YSOs (Class 0/I (44) and Class II (120)) in this region using the four IRAC bands and their positions are overlaid on the image (Fig. 5.9). *Spitzer*-IRAC Ch1 and Ch2 are known to be more sensitive for

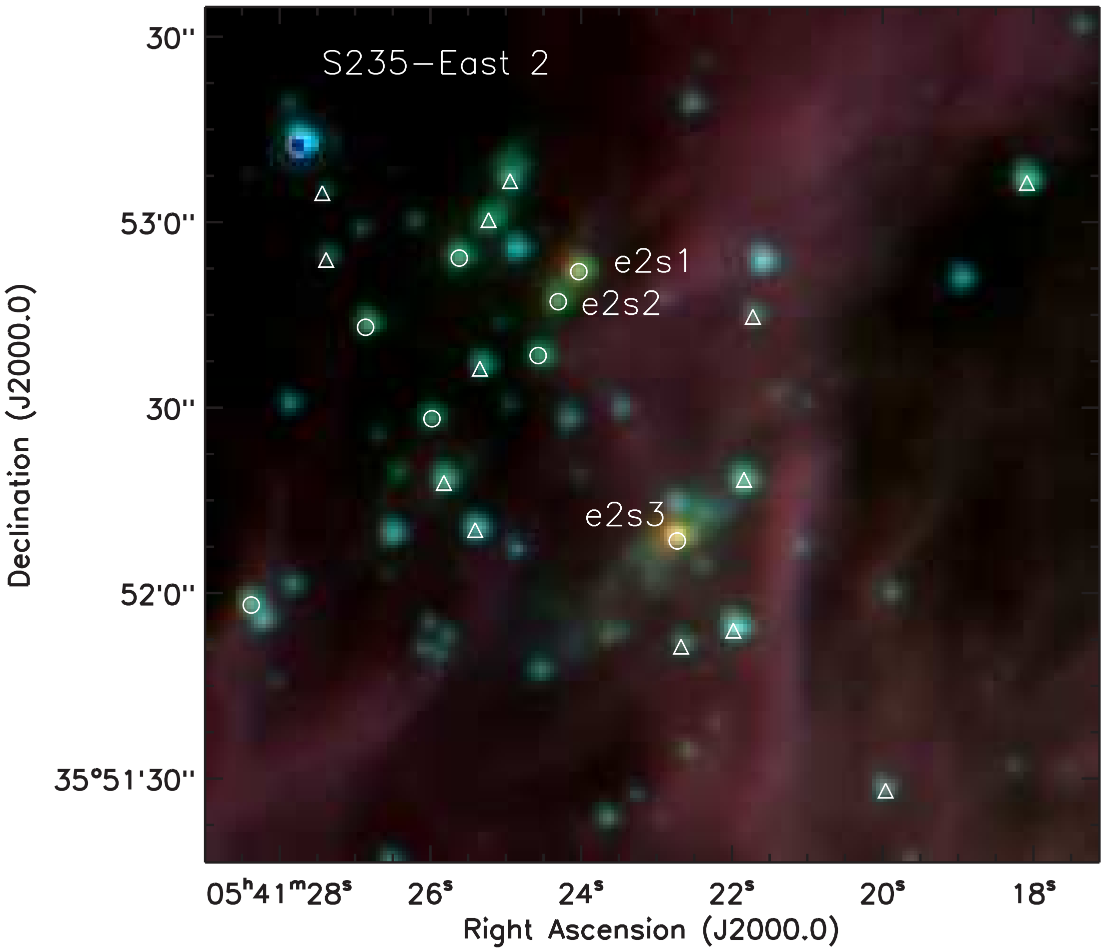

Fig. 5.7: IRAC 3-colour-composite (Ch4(red), Ch2(green) and Ch1(blue)) zoomed-in image of East 2 region (Fig. 5.1: dotted box). Classified YSOs (Class 0/I in white circles and Class II in white triangles) are overlaid on the image. The marked sources are Class 0/I sources that are not detected in 2MASS JHK image. IRAC Ch2 (4.5 μm) is sensitive for shock-excited molecular H_2 emission and the emission around source "e2s3" in the colour-composite image is dominated by green colour i.e., IRAC Ch2 band. Therefore, the "green" emission around the marked source "e2s3" may be due to the shock-excited molecular H_2 emission and may be showing the signature of outflows associated with source "e2s3" (see details about the emission in ratio map section of the chapter).

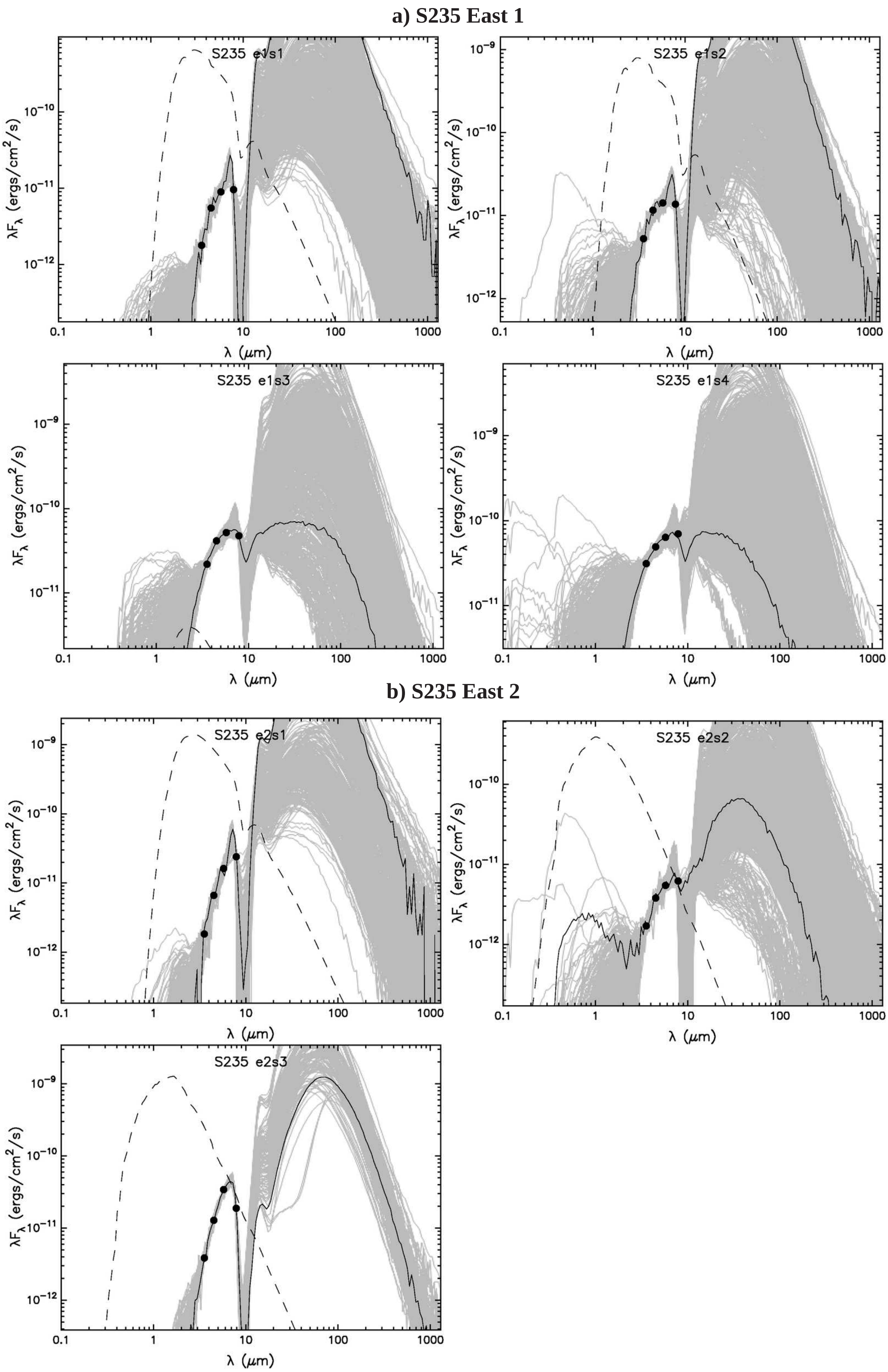

Fig. 5.8: SED model plots of selected sources in the East 1 and East 2 regions are shown here.

Table 5.1: Some of the selected sources in S235 East 1 region; the numbers in parentheses in the Object column are common sources from Table E.1 designations from Appendix E (see Fig. 5.6 and text)

Object	RA [2000]	Dec [2000]	Ch1	Ch2	Ch3	Ch4	α_{IRAC}	class
e1s1(79)	5:41:31.42	35:50:26.2	12.81	10.84	9.56	8.51	2.01	0/I
e1s2(74)	5:41:30.42	35:50:03.2	11.64	10.04	9.07	8.13	1.11	0/I
e1s3(76)	5:41:30.54	35:49:48.4	10.09	8.65	7.66	6.77	0.91	0/I
e1s4(73)	5:41:30.32	35:49:48.0	9.70	8.47	7.44	6.36	0.97	0/I

Table 5.2: Physical parameters derived from SED modeling of the labeled sources from Table 5.1 in S235 East 1 region (see text)

Source	Age	M_*	T_*	L_*	M$_{env}$	$\dot{M}_{env}$	M$_{disk}$	$\dot{M}_{disk}$
Name	log(yr)	M$_\odot$	log(T(K))	log(L$_\odot$)	log(M$_\odot$)	log(M$_\odot$ yr^{-1})	log(M$_\odot$)	log(M$_\odot$ yr^{-1})
e1s1(79)	3.94±0.64	3.53±3.73	3.63±0.10	1.92±0.88	0.05±1.37	-4.46±0.90	-1.86±0.86	-6.26±1.21
e1s2(74)	4.41±0.83	3.85±3.33	3.67±0.14	1.99±0.77	-0.18±2.00	-4.38±1.41	-1.85±0.87	-6.64±1.27
e1s3(76)	4.61±0.96	4.51±2.39	3.73±0.20	2.25±0.50	-0.46±2.54	-4.37±1.85	-1.82±0.86	-6.67±1.23
e1s4(73)	5.33±1.19	4.58±2.04	3.91±0.28	2.39±0.51	-2.62±3.59	-4.80±2.25	-2.09±0.96	-7.04±1.38

Table 5.3: Some of the selected sources in S235 East 2 region; the numbers in parentheses in the Object column are common sources from Table E.1 designations from Appendix E (see Fig. 5.7 and text)

Object	RA [2000]	Dec [2000]	Ch1	Ch2	Ch3	Ch4	α_{IRAC}	class
e2s1(58)	5:41:24.03	35:52:52.0	12.78	10.65	8.93	7.52	3.17	0/I
e2s2(59)	5:41:24.30	35:52:47.1	12.86	11.25	10.11	8.99	1.54	0/I
e2s3(57)	5:41:22.73	35:52:08.4	11.97	9.93	8.11	7.78	2.03	0/I

Table 5.4: Physical parameters derived from SED modeling of the labeled sources from Table 5.3 in S235 East 2 region (see text)

Source	Age	M_*	T_*	L_*	M$_{env}$	$\dot{M}_{env}$	M$_{disk}$	$\dot{M}_{disk}$
Name	log(yr)	M$_\odot$	log(T(K))	log(L$_\odot$)	log(M$_\odot$)	log(M$_\odot$ yr^{-1})	log(M$_\odot$)	log(M$_\odot$ yr^{-1})
e2s1(58)	3.87±0.67	5.37±4.48	3.68±0.16	2.49±0.81	0.52±1.52	-4.19±0.88	-1.74±1.03	-5.91±1.59
e2s2(59)	4.32±0.95	2.58±2.50	3.66±0.16	1.65±0.78	-0.61±1.83	-4.84±1.31	-2.07±0.84	-6.76±1.23
e2s3(57)	4.45±0.56	7.14±2.49	3.71±0.11	2.76±0.48	1.78±0.76	-3.44±0.43	-1.49±0.84	-6.36±1.07

stellar photospheres compared to the two longer IRAC bands (Ch3 and Ch4). Therefore, using NIR photometry, in combination with IRAC Ch1 and Ch2, we may identify additional YSOs which are not detected in Ch3 and Ch4. Gutermuth (2005) and Gutermuth et al. (2009) demonstrated the separation of protostars, stars with disks and disk-less photospheres using dereddened K - [3.6] versus [3.6] - [4.5] colour space obtained from the colour excess ratios and the reddening law of Flaherty et al. (2007). The details of the calculation of dereddened colours (K - [3.6] and [3.6] - [4.5]) are given in the Section E.1 of Appendix E. We have used our new Mt. Abu NIR JHK observations in combination with IRAC Ch1 and Ch2 bands in the vicinity of the S235A-B region. Fig. 5.10 shows the 3-colour-composite NIR (J(blue), H(green) and K(red)) images in the vicinity of the S235A-B region, marked as a solid box in Fig. 5.1. We have used all the common sources in H, K, Ch1 and Ch2 bands to identify the additional new YSOs in the region (see Fig. 5.10). We have eliminated the contaminations obtained from the IRAC photometry, before applying the selection criteria for YSOs in this region. Figure 5.11 shows the dereddened $[K - [3.6]]_0$ and $[[3.6] - [4.5]]_0$ colour-colour diagram with the newly identified YSOs (Class I and Class II sources). The separation between Class I and Class II sources are shown by the dashed line in the diagram. Fig. E.2 of Appendix E shows the colour-colour diagram used for measuring the extinction for dereddening, along with the identified YSOs shown by solid red circles. The newly identified YSOs are shown overlaid on the 3-colour-composite image in Fig. 5.12. We have obtained an additional 63 new YSOs (18 Class I and 45 Class II) using NIR (H and K) photometry combined with IRAC (Ch1 and Ch2) bands. Adding these sources to the IRAC identified sources (164 YSOs with 44 identified Class I and 120 Class II sources), we get a total number of YSOs in the vicinity of the region S235A-B as 227, with 62 Class I and 165 class II sources.

We have re-estimated the surface density for all the YSOs in the S235A-B region using a 5 arcsec grid size. We have used a similar procedure for the calculation of surface density using 6 NN as described in Chapter 3. The surface density contours are shown overlaid on the Ch2 band in Fig. 5.13. It is very clear that all the Class I sources are lying within the surface density contours. The maximum surface density is about 120 YSOs/pc^2. We have calculated the empirical cumulative distribution as a function of nearest-neighbour distance for YSOs and found a distance of inflection d_c = 0.33 pc (0.01^o at 1.8 kpc distance) for the clustering of YSOs (see Fig. E.3 of Appendix E). Figure 5.14 shows the clustering of YSOs obtained by using d_c = 0.33 pc. We find 71% of the YSOs to be present in 4 clusters. We used only IRAC identified YSOs to look for the clustering of YSOs to compare with all

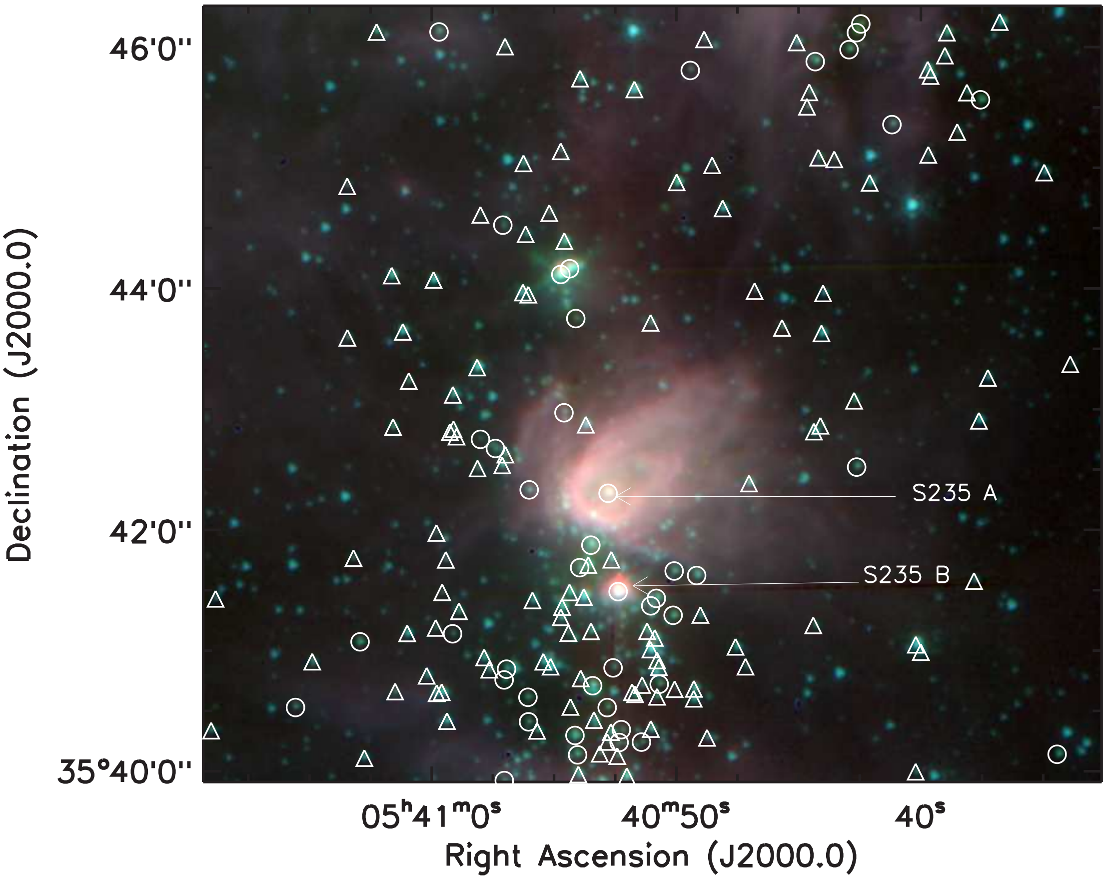

Fig. 5.9: IRAC 3-colour-composite (Ch4(red), Ch2(green) and Ch1(blue)) zoomed-in image of S235A-B region (shown in Fig. 5.1 by solid box). Classified YSOs (Class 0/I in white circles and Class II in white triangles) are overlaid on the image. Image shows the horseshoe shaped structure around the source S235A and small nebulous region associated with S235B. It appears that the structure is expanding towards south-east due to the expansion of HII region and may be triggering fresh star formation.

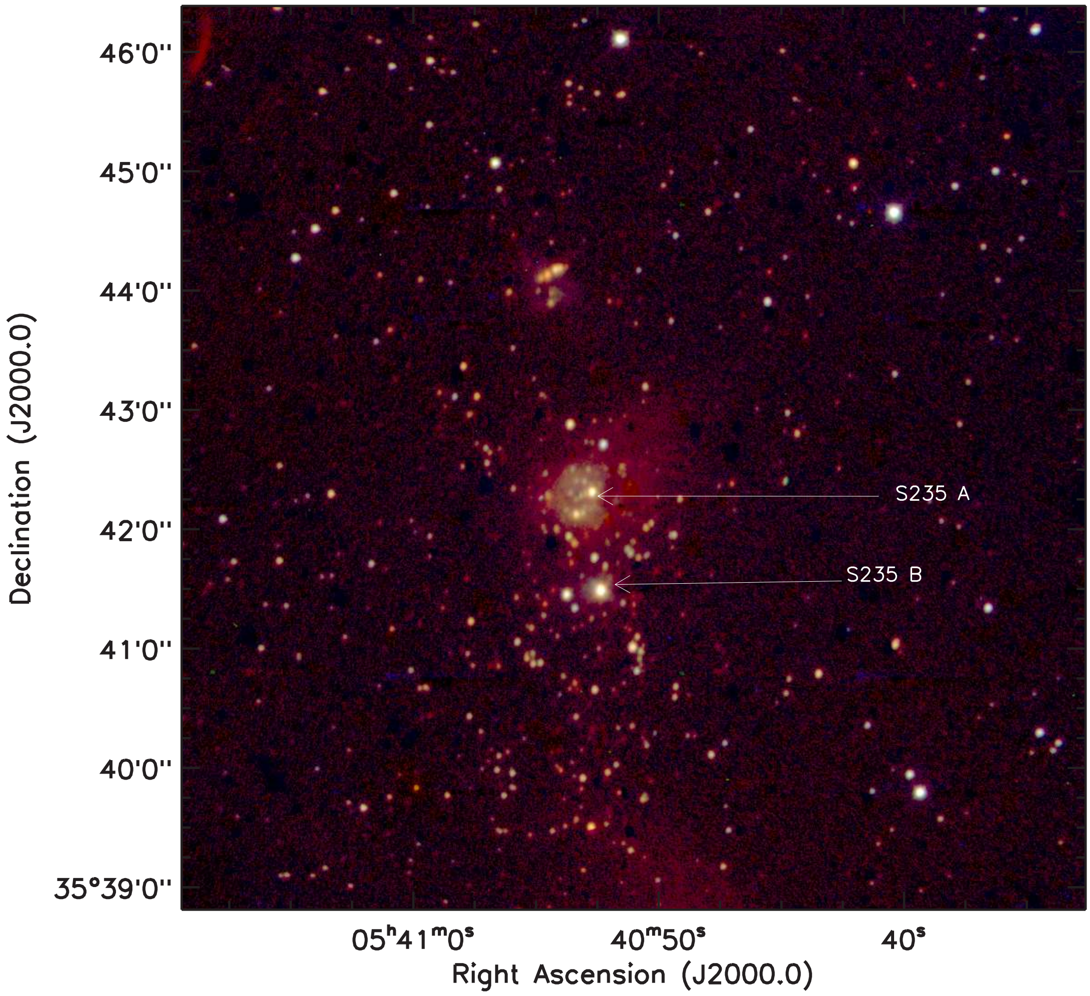

Fig. 5.10: Exhibits the Mt. Abu NIR 3-colour-composite K(red), H(green) and J(blue) image of the vicinity of S235A-B region.

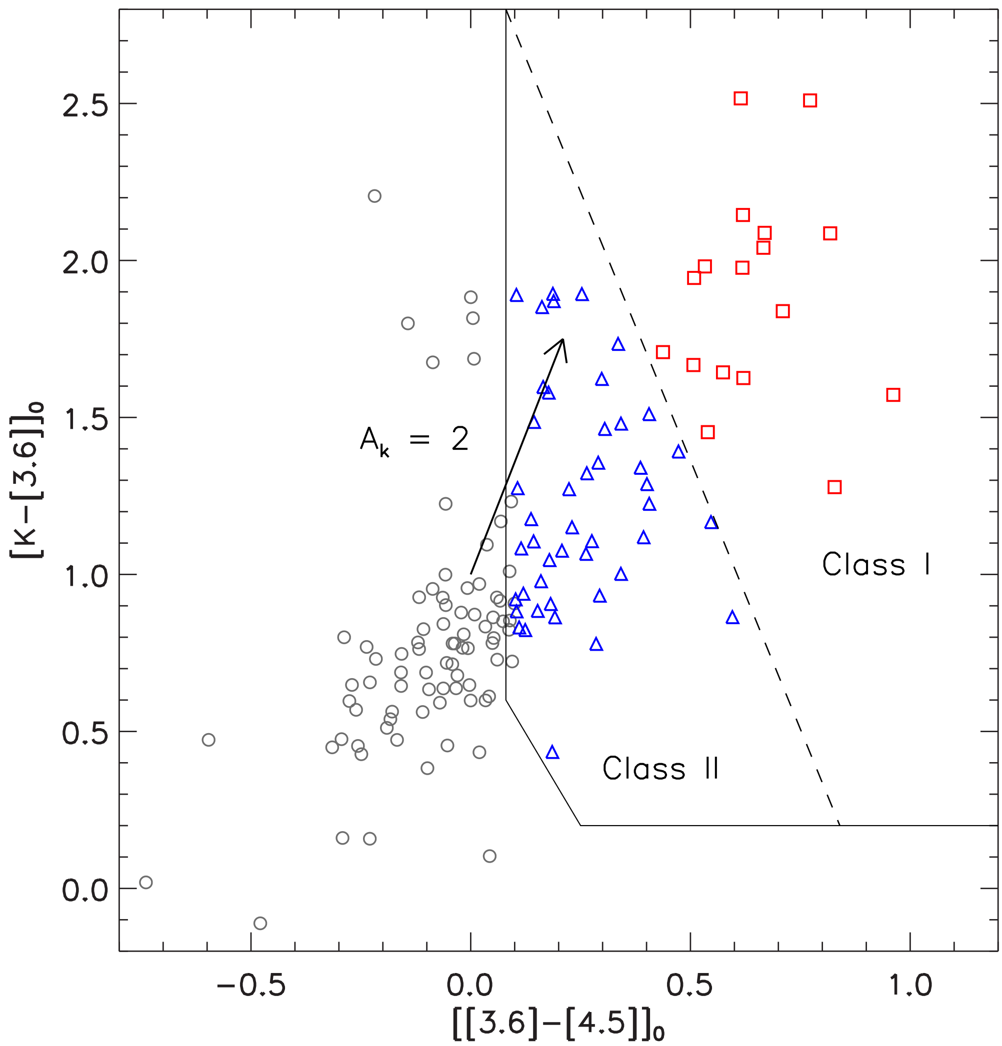

Fig. 5.11: De-reddened [K - [3.6]]$_0$ and [[3.6] - [4.5]]$_0$ colour-colour (CC-D) diagram with identified new YSOs (Class I and Class II) in the S235A-B region. Open squares in red represent Class I and triangles in blue represent Class II sources and the rest are shown by grey open circles. The dotted line makes division between Class I and Class II sources. The extinction vector for A$_K$ = 2 mag is shown by the arrow, calculated using average extinction law from Flaherty et al. (2007).

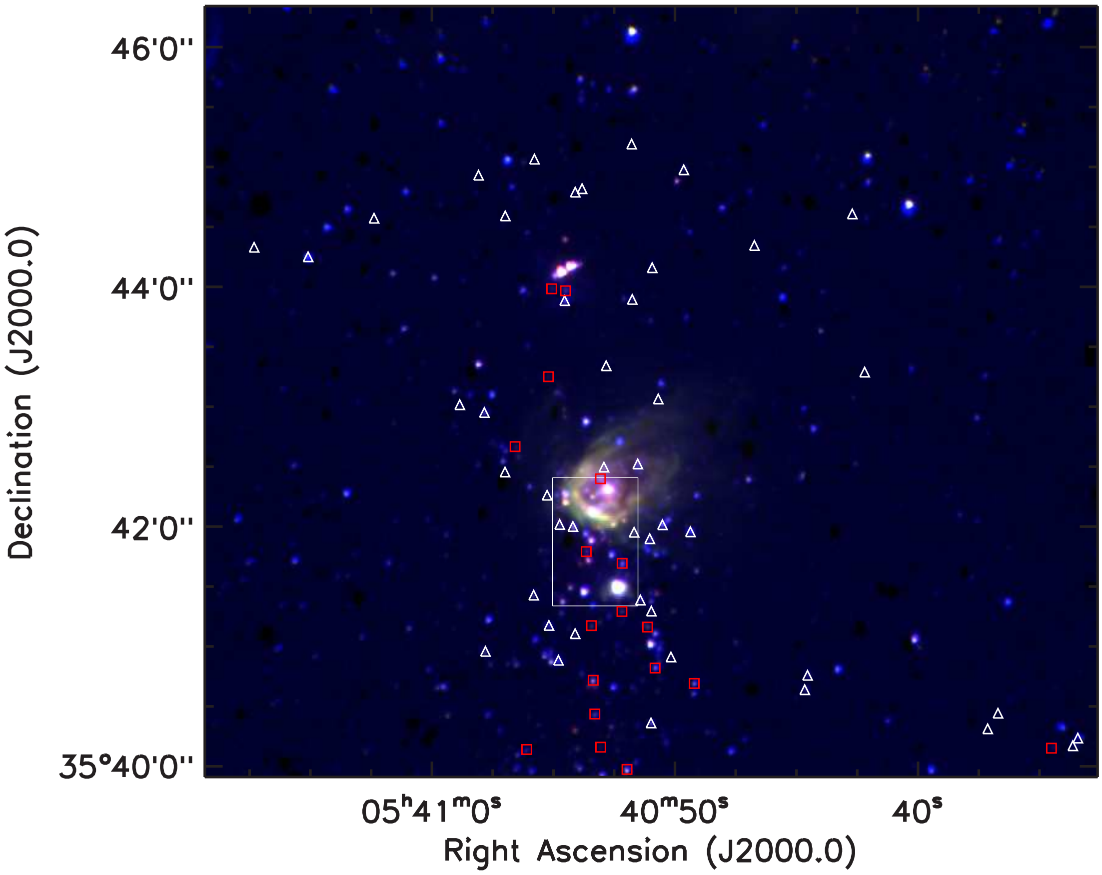

Fig. 5.12: Newly identified YSOs (see Figure 5.11) are overlaid on the 3-colour-composite image (K-band (blue), Ch1 (green) and Ch2 (red)). Symbols are similar to those used in Figure 5.11 for Class I (red squares) and Class II (white triangles) sources.

YSOs in this region and have found d_c = 0.39 pc, which gives about 72% YSOs inside the clusters. The positions of the dense clumps (detected in $C^{18}O$ measurements by Saito et al. (2007)) associated with the S235A-B region are over-plotted in Fig. 5.14b. The presence of $C^{18}O$ emission supports the dense clustering of YSOs in the S235A-B region.

The S235A-B region was well studied by Felli et al. (1997, 2004, 2006), who found evidences for fresh star formation in the region, through the interaction of an expanding classical HII region into an ambient molecular core. Figure 5.15 exhibits the zoomed image of the dashed box shown in Fig. 5.12. We have marked some of the interesting sources in the right side of Fig. 5.15. Felli et al. (2006) studied some of these sources using IRAC images in the S235A-B region. We focus particularly on the ring-like structure formed by the sources in the region (see the left side of Fig. 5.15) which are associated with the dense clump identified by Saito et al. (2007). This ring-like structure is also associated with the 850 μm (obtained from JCMT archival data base) dust continuum observations in the S235A-B region. The location of the ring-like structure sources (s3 to s10 and s13) is shown in the right-side of Fig. 5.15 for a better view, represented by the solid cyan coloured line (see Table 5.5). The formation of these sources in a ring-like structure may have been triggered by the interaction of S235A HII region with the ambient dense molecular region. The right-side of Fig. 5.15 shows the horse-shoe shaped structure in the contours of IRAC bands expanding towards the south. The 850 μm dust continuum contours (dashed lines) are also shown in the figure. The horse-shoe shaped structure forms the outer boundary of the expanding HII region (see the red contours in Fig. 5.15). The ring-like structure of sources is just located at the interface between the horse-shoe shaped structure (the red contours in Fig. 5.15) and the peak of the dust continuum (in Fig. 5.15). Felli et al. (2006) found a source S235AB-MIR (which is labeled as s9 in our image) at the peak position of the 1.2 mm observations which has been detected only in IRAC Ch2, Ch3 and Ch4 bands but not in Ch1. The ring-like structure of sources (s3 to s10 and s13; connected by a cyan coloured line) is more prominent in the IRAC Ch2 band (4.5 μm) than the other bands. It is interesting that the source S235AB-MIR (s9) is one of the “members” in the ring-like structure.

One may notice that there is another ring-like structure starting from s1 to s12 (i.e., s1, s2, s8, s9 (S235AB-MIR), s10, s11(M1) and s12; shown by the solid blue line). The positions and photometric magnitudes of the labeled sources are given in Table 5.5. We have done the SED modeling of the labeled sources that have at least 3 data points using the

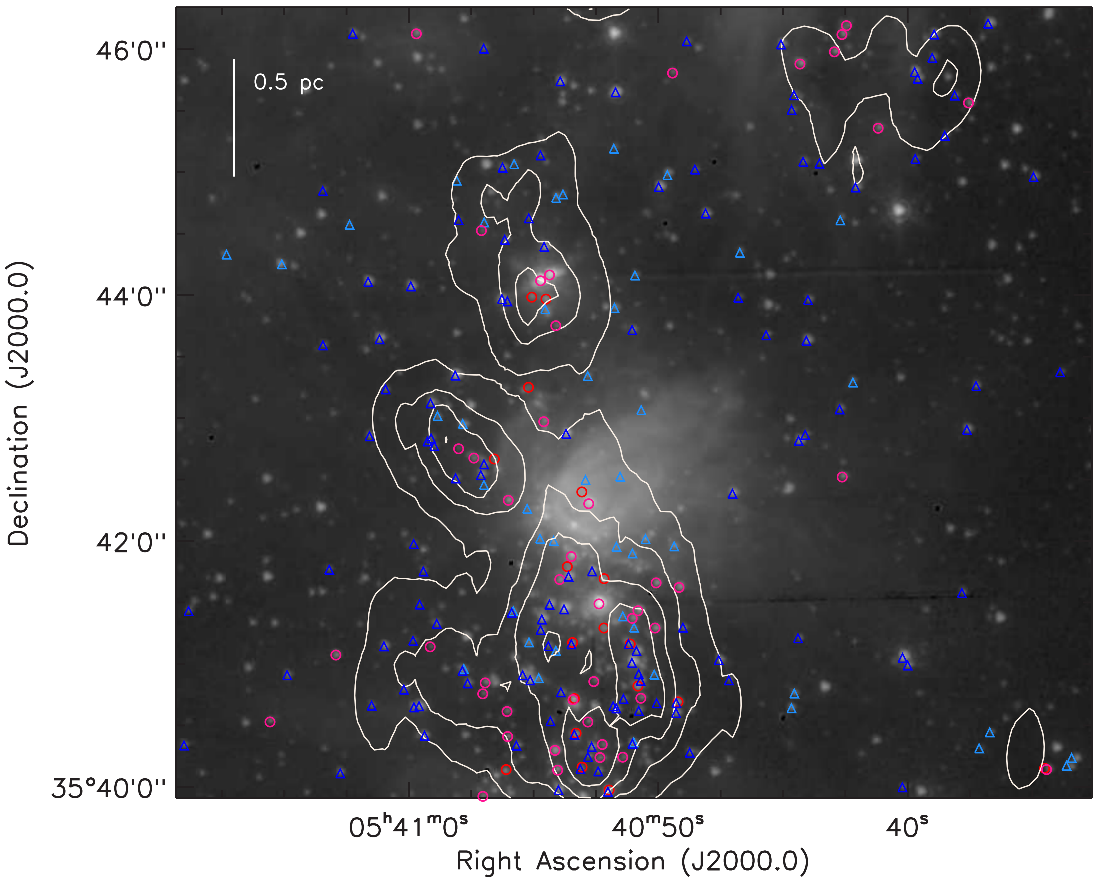

Fig. 5.13: Surface density map of YSOs overlaid on IRAC Ch2 image. Circles and triangles represent Class I and Class II sources respectively. Red circles show the Class I sources identified through H, K, CH1, CH2 bands and deep pink circles represent the Class 0/I sources selected from IRAC four bands criteria. Similarly, Class II sources identified through H, K, CH1, CH2 bands are represented by light blue triangle and dark blue triangles show the Class II sources identified through four IRAC bands criteria. The levels of surface density contours are 20, 40, 70 and 120 YSOs/pc^2 from outer to inner side.

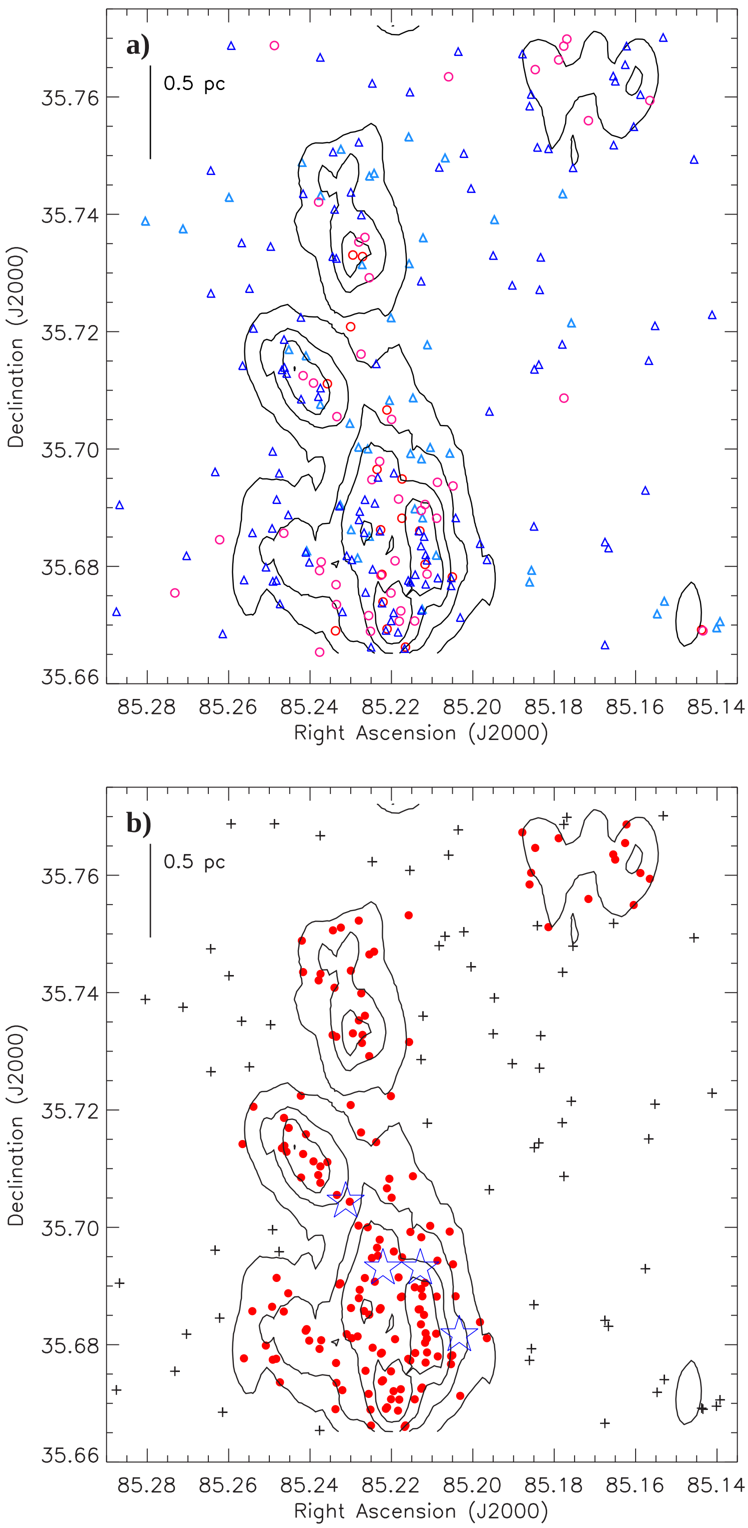

Fig. 5.14: a: The plot is the same as the one shown in Fig. 5.13, except that the image is removed, for a better view; b: The distribution of all cluster members ($d_c \leqslant 0.33$ pc) are shown by filled circles (red) for YSOs and plus symbols (black) for the YSOs outside d_c. The positions of dense clumps associated with the region (shown by blue star symbols) are detected from $C^{18}O$ observations by Saito et al. (2007).

model tool. We do not have the required minimum of 3 data points for the sources s3, s4, s5, s6, s7, s8 and s13 to do the SED modeling. Therefore, we have modeled only 8 sources (6 sources from the second ring which are connected by solid blue line except s8 and S235B) which are labeled in the Fig. 5.15. The SED model fits are shown in Fig. 5.16. The SED model weighted mean values of the physical parameters are given in Table 5.6. The model-derived parameters show that the source S235AB-MIR is a young and accreting massive protostar that is not yet being able to excite an HII region. We used 450 and 850 μm fluxes associated with the S235AB region from Felli et al. (2004) and considered 50% of the 450 μm flux to be associated with S235AB-MIR source. Thus, we used 3 IRAC and one 450 μm fluxes as data points for the SED fitting. Our SED modeling results show that s1 and s2 are much evolved and are low-mass stars (compared to the other 4 sources in the ring). The SED results of sources s10 and s12 show that they are low mass stars still accreting matter. Also, the results of SED modeling of the source M1 shows that it is a low-mass star but not highly evolved (see Table 5.6). Felli et al. (2006) reported that the radio source VLA-1 coincides with the source M1 and that it could be a B2-B3 star with a UCHII region. But, our SED modeling results of M1 are not consistent with the suggestion of Felli et al. (2006). Our SED modeling results indicate that the second ring-like structure sources (i.e., s1, s2, s8, s9(S235AB-MIR), s10, s11(M1) and s12) are mostly low-mass stars except s9(S235AB-MIR).

Triggered star formation by the “Collect and Collapse” process (Elmegreen and Lada 1977) could be responsible for the existence of these IRAC sources, possibly started by the expanding HII regions associated with the nearby massive stars. There is also the possibility for the formation of stars due to the propagation of a shock wave from a nearby HII region which may lead to the contraction of pre-existing dense molecular clumps. This possibility is supported by the detection of dense $C^{18}O$ emission clumps in the S235A and S235B regions (Saito et al. 2007). Li (2001) and Li and Nakamura (2002) made a simulation for the formation of ring-like structures and multiple-star formation in magnetically sub-critical clouds. They demonstrated that a magnetically sub-critical cloud breaks up into fragments as multiple magnetically supercritical clumps leading to the formation of a new generation of stars in small clusters (in a ring-like formation). A supportive observational evidences in the source IRAS 22134+5834 was reported by Kumar et al. (2003). In our study, the location of these two ring-like structures coincide with the peak position of 850 μm, as well as dense clumps (Saito et al. 2007).

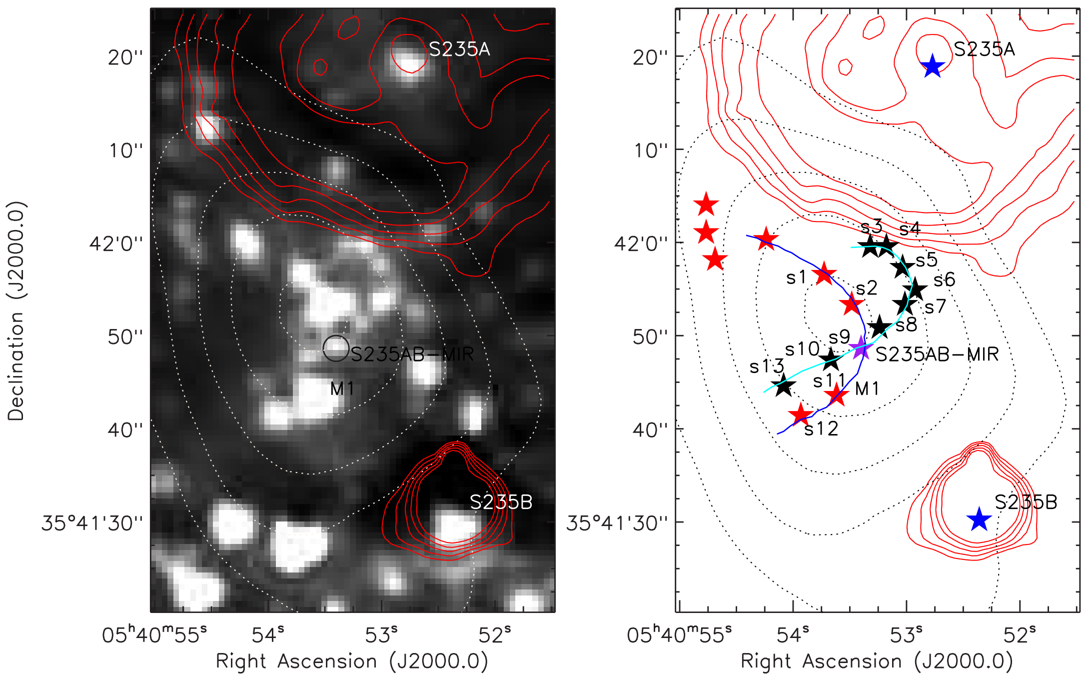

Fig. 5.15: The image on the left represents the zoomed-in IRAC ratio map of Ch2/Ch4 in a region showed by the dashed box in Fig. 5.12. Right side image shows the positions of sources seen atleast in any one of the IRAC bands with contours (red) of IRAC Ch4 image overlaid having levels between min = 420 and max = 1300 MJy/Sr. Source S235AB-MIR is represented by star symbol with violet colour and blue stars show the position of sources S235A and S235B. Public archival Scuba 850 μm contours (dotted curves) of the region are overlaid on both figures with levels between min = 1100 and max = 9900 Jy. There is a ring-like structure of sources (s3 to s10 and s13; connected by cyan colour line in right side figure) most prominent only in IRAC Ch2 band, while a second ring-like structure of sources (s1, s2, s9, s11 and s12; connected by blue colour line in right side figure) is seen atleast in 3 IRAC bands. Both the ring-like structures are shown in the right side figure for better view (see text for more details). One may notice that the source S235AB-MIR is common for both the rings.

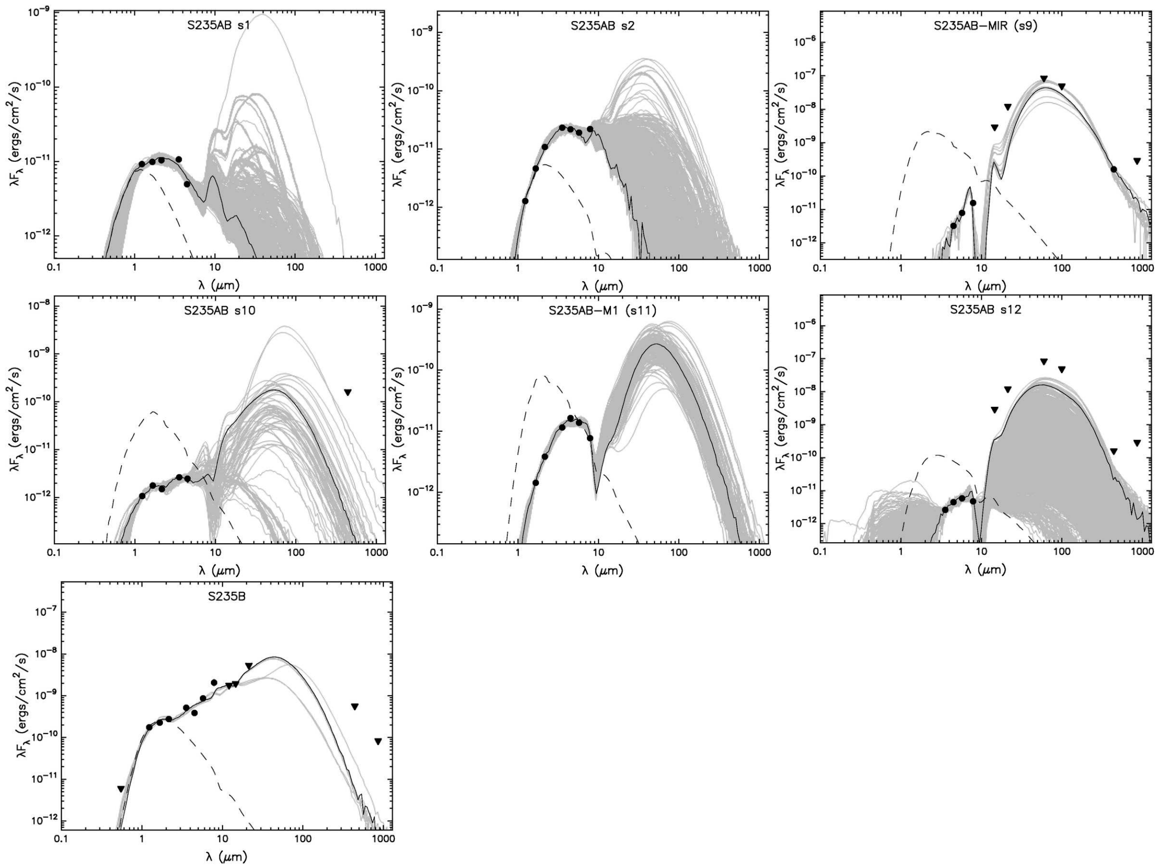

Fig. 5.16: SED model plots of selected sources in the S235A-B region (labeled in Fig. 5.9).

Table 5.5: Some of the selected sources in S235A-B region; the numbers in parentheses in the Object column are common sources from Table E.1 and E.2 designations from Appendix E (see Fig. 5.15 and text)

Object	RA [2000]	Dec [2000]	Jmag	Hmag	Kmag	Ch1	Ch2	Ch3	Ch4	α_{IRAC}	class
s1	5:40:53.72	35:41:56.0	14.60	13.18	12.38	10.87	10.96	—	—	—	—
s2(29)	5:40:53.49	35:41:52.4	16.21	14.00	12.33	10.02	9.35	8.75	7.61	-0.10	0/I
s3	5:40:53.34	35:41:59.5	—	—	—	—	—	—	—	—	—
s4	5:40:53.16	35:41:59.3	—	—	—	—	10.11	—	—	—	—
s5	5:40:53.02	35:41:57.6	—	—	—	—	—	—	—	—	—
s6	5:40:52.92	35:41:55.3	—	—	—	—	—	—	—	—	—
s7	5:40:53.02	35:41:53.3	—	—	—	—	11.31	9.88	—	—	—
s8	5:40:53.23	35:41:50.8	—	—	—	—	—	—	—	—	—
s9(MIR-AB)	5:40:53.43	35:41:48.4	—	—	—	—	11.43	9.70	7.98	—	—
s10	5:40:53.66	35:41:47.4	16.39	15.04	14.48	12.38	11.72	—	—	—	—
s11(81;M1)	5:40:53.60	35:41:42.6	—	15.28	13.46	10.78	9.66	9.10	8.76	-0.59	II
s12(30)	5:40:53.95	35:41:41.2	—	—	—	12.39	11.07	10.04	9.27	0.72	0/I
s13	5:40:54.02	35:41:43.0	—	—	—	12.92	12.20	—	—	—	—
S235B(24)	5:40:52.38	35:41:29.3	10.86	9.78	8.81	6.66	6.23	4.61	2.69	1.94	0/I

Table 5.6: Physical parameters derived from SED modeling of the labeled sources from Table 5.5 in S235A-B region (see text)

Source Name	Age log(yr)	M_* $M_\odot$	T_* log(T(K))	L_* log($L_\odot$)	M_{env} log($M_\odot$)	$\dot{M}_{env}$ log($M_\odot$ yr^{-1})	M_{disk} log($M_\odot$)	$\dot{M}_{disk}$ log($M_\odot$ yr^{-1})
s1	6.74±0.19	2.88±0.78	4.02±0.11	1.73±0.41	-5.65±1.60	-6.75±0.16	-5.57±1.74	-11.45±1.64
s2(29)	6.56±0.32	3.84±1.42	4.09±0.12	2.17±0.47	-6.12±1.87	-6.58±0.60	-4.60±1.73	-9.99±1.45
s9(MIR-AB)	3.93±0.64	13.79±3.53	3.88±0.30	3.88±0.34	2.58±0.35	-3.01±0.17	-1.36±0.84	-5.48±1.36
s10	5.63±0.89	2.32±1.21	3.74±0.17	1.38±0.43	-2.25±2.52	-4.84±2.44	-3.27±1.54	-8.78±1.87
s11(81;M1)	5.03±0.40	3.18±1.25	3.66±0.05	1.76±0.26	-0.15±0.87	-4.58±0.61	-2.11±0.82	-7.66±1.05
s12(30)	4.56±0.75	2.55±2.26	3.64±0.11	1.61±0.66	-0.34±1.50	-4.55±1.08	-1.99±0.85	-7.06±1.26
S235B(24)	4.43±0.71	6.26±1.72	3.76±0.14	2.78±0.36	0.37±0.58	-4.15±0.38	-1.84±1.01	-6.62±1.18

5.3.2 IRAC Ratio Maps

We mentioned in Chapters 3 & 4 that the IRAC bands contain a number of prominent molecular emissions lines (see Table 3.2 of Chapter 3). We have used IRAC ratio Ch2/Ch4 images to find out the emission regions in the S235 complex. The detailed procedure for generating the IRAC ratio maps is described in Chapters 3 & 4. Fig. 5.17 shows the IRAC ratio Ch2/Ch4 of the entire S235 complex with some important regions shown by the boxes. IRAC zoomed-in ratio map (Ch2/Ch4) of the East 1 region is shown in Fig. 5.18. We have found a very strong bright region corresponding to East 1 in the ratio map which could be due to molecular H_2 emission. The results of SED modeling of important sources (i.e., e1s1, e1s2, e1s3 and e1s4) in the region show the lack of an associated HII region. But these sources are young, still accreting material and may be associated with outflows, especially the Class 0/I sources e1s1, e1s3 and e1s4. The IRAC zoomed-in ratio map (Ch2/Ch4) of the East 2 region is shown in Fig. 5.19. The ratio map shows an extended bright emission (about 0.22 pc in SE-NW direction) possibly associated with the source “e2s3”. This could represent the outflow lobes in the source due to shock-excited molecular H_2 emission. The size of the bright region is about 0.22 pc in SE-NW direction. The SED modeling of the source “e2s3” shows that it is a young massive protostar still accreting the material. Our results are only indicative/speculative about the nature of these sources; therefore, it requires further study at longer wavelengths i.e., sub-mm/mm.

Figs. 5.20 shows the IRAC ratio map of Ch2/Ch4 in the S235A-B region. We have found very strong bright emission in the Ch2/Ch4 map in the S235A-B region. The IRAC horse-shoe shaped structure seen in Ch4 band is over-plotted as contours in Figs. 5.20. We have found that the Brα emission is present within the horse-shoe structure around S235A and represents an HII region. But bright emission outside of the IRAC horse-shoe structure

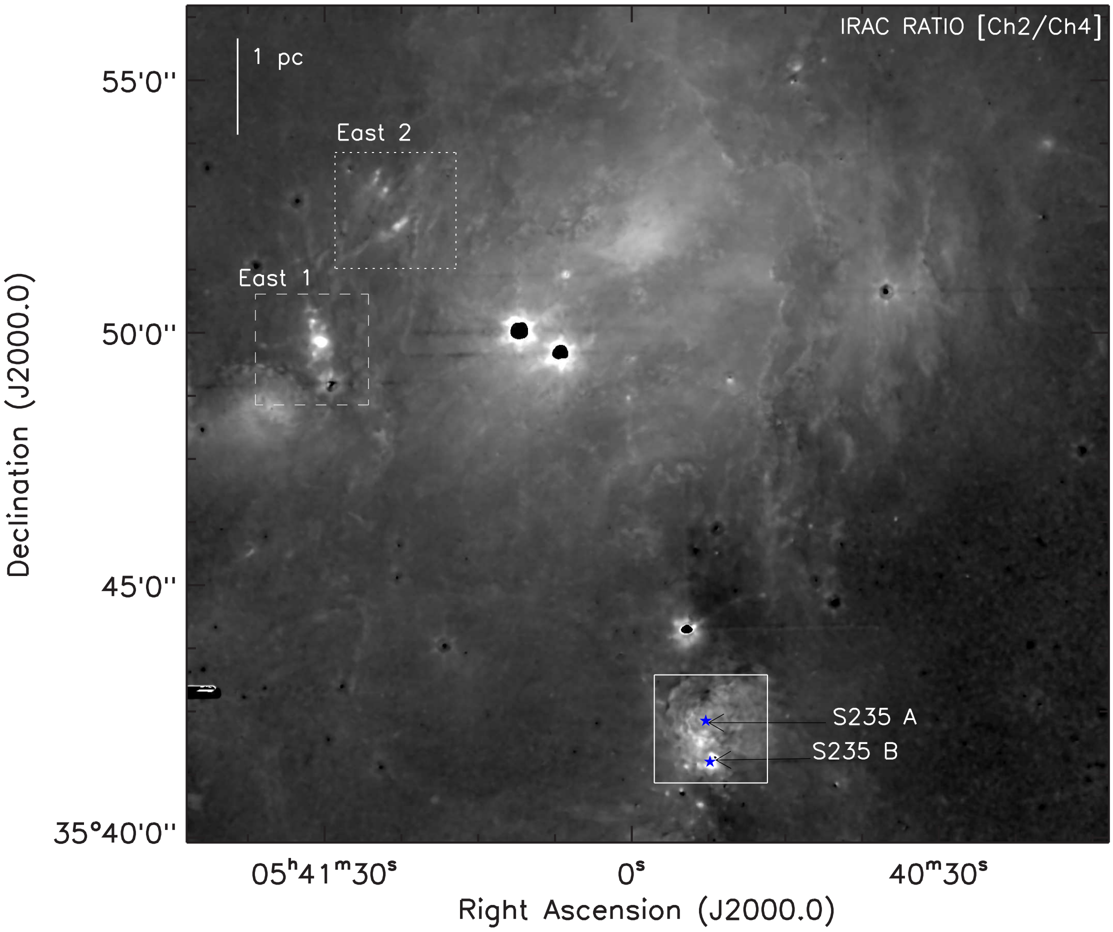

Fig. 5.17: IRAC ratio map of Ch2/Ch4 for the entire S235 complex. Box regions marked here are shown zoomed-in Figs. 5.18, 5.19 and 5.20.

may be due to the H_2 emission. This interpretation is consistent with the narrow band Brγ and H_2 imaging of the region by Felli et al. (1997). We have also found that the source S235B is associated with Brα emission due to the presence of an HII region. Recently, using spectroscopy, Boley et al. (2009) reported that S235B is a source that belongs to a rare class of early- type Herbig Be stars. SED modeling of the source S235B shows that it is an intermediate mass young star and our model results are consistent with the Boley et al. (2009) results.

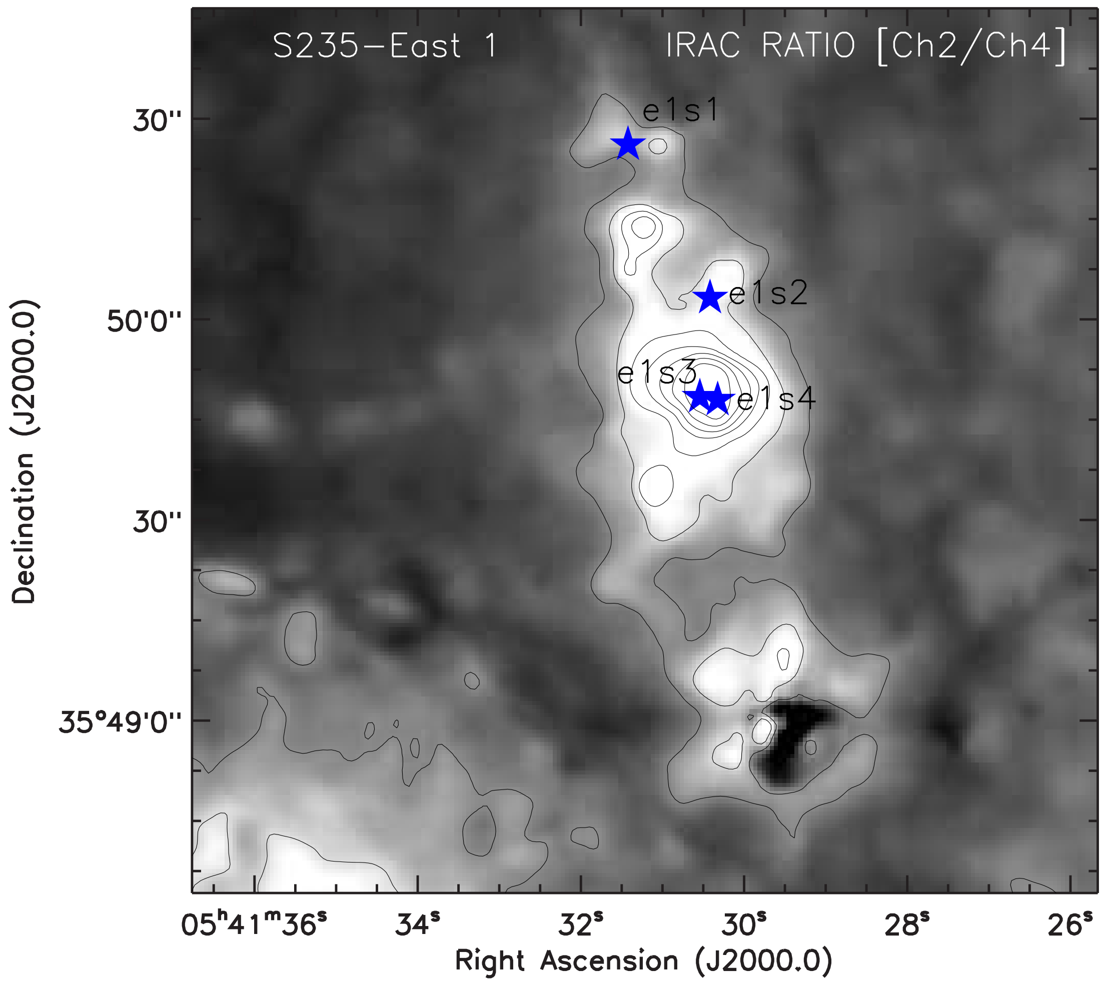

Fig. 5.18: IRAC ratio map of Ch2/Ch4 in East 1 region revealing bright regions. Contours of the ratio map of Ch2/Ch4 are over-plotted with labeled sources (blue stars) from Fig. 5.6. The contour levels are min 0.039 and max 0.33.

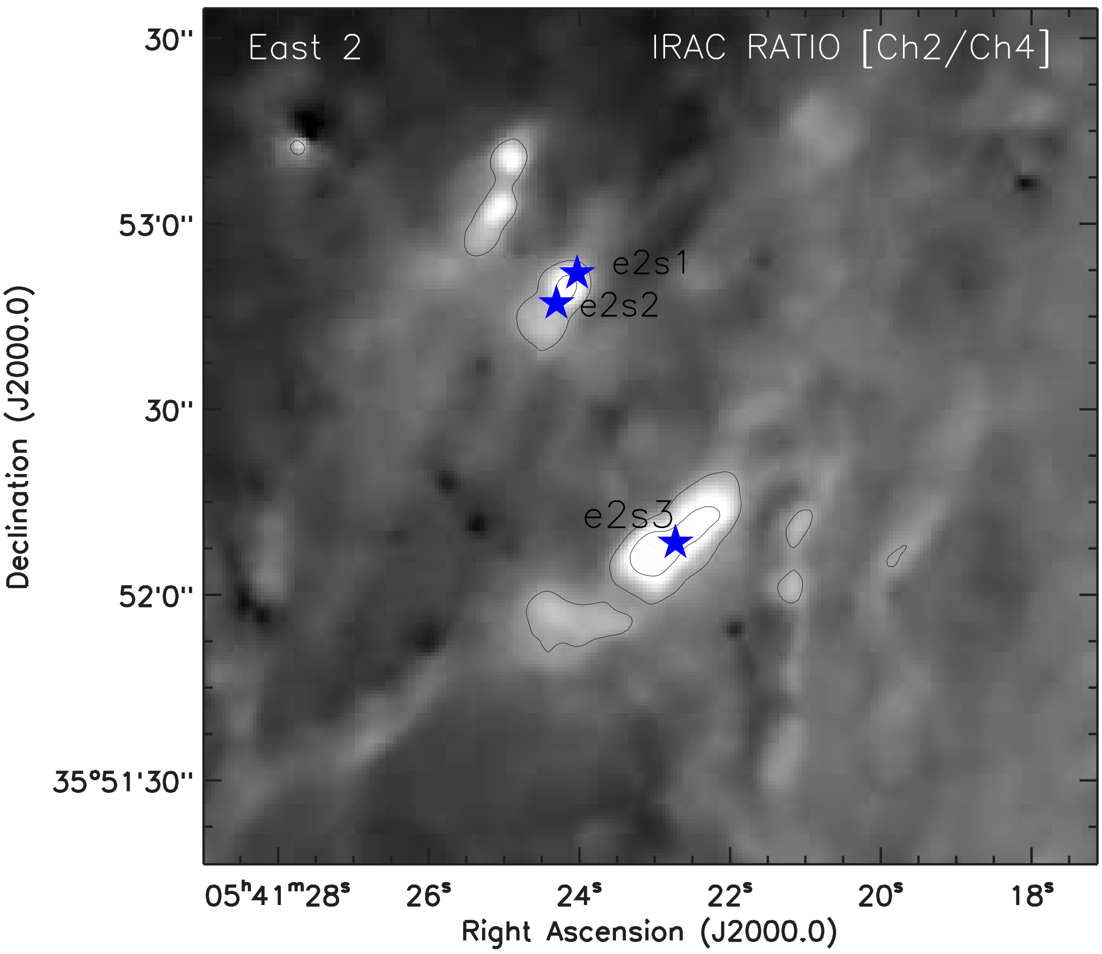

Fig. 5.19: IRAC ratio map of Ch2/Ch4 in East 2 region revealing bright regions. Contours of the ratio map of Ch2/Ch4 are over-plotted with labeled sources (blue stars) from Fig. 5.7. The contour levels are min = 0.044 and max = 0.33. Source "e2s3" may be associated with an outflow due to shock-excited H_2 emission. The extension of bright regions associated with source "e2s3" is about 0.22 pc in SE-NW direction.

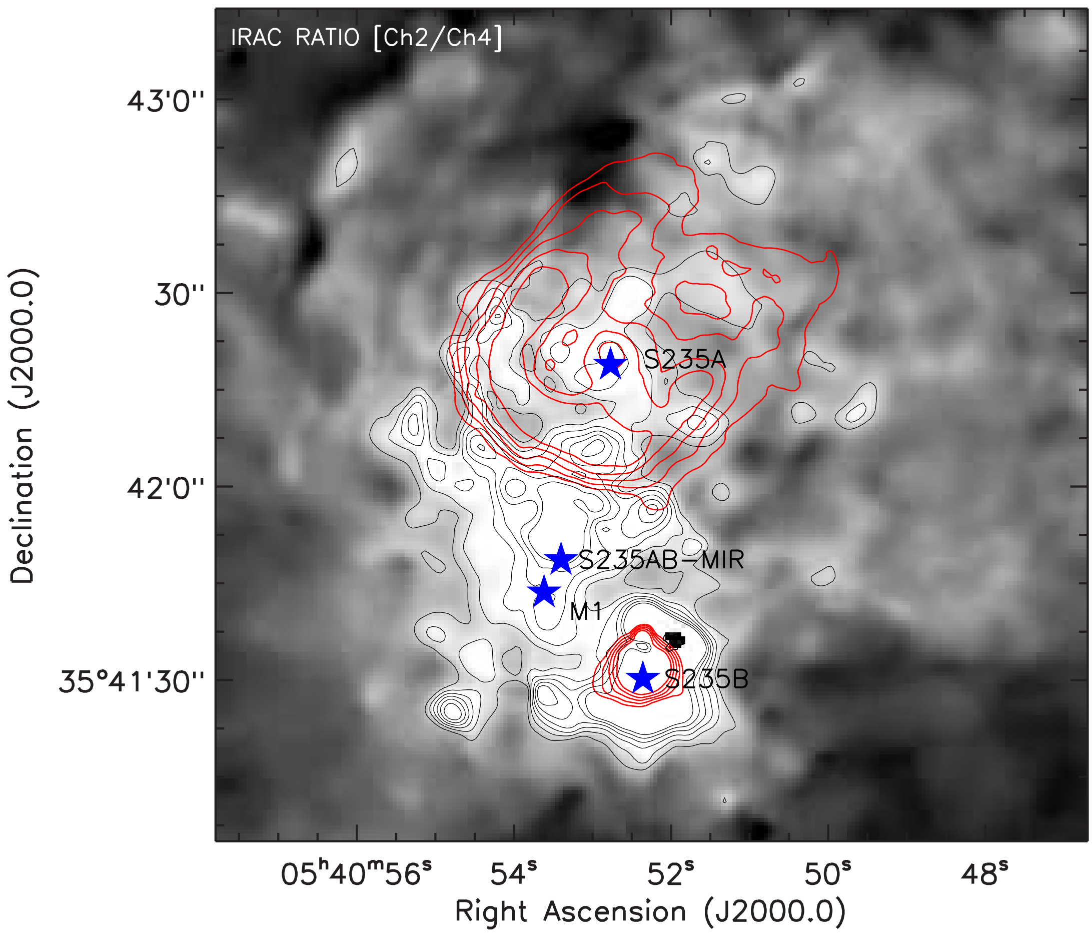

Fig. 5.20: IRAC ratio map of Ch2/Ch4 in the S235A-B region revealing bright regions. Contours of IRAC Ch4 are over-plotted in red colour, with same levels as shown in Fig. 5.15. Bright emission regions within red contours are probably due to Brα emission. The bright regions outside towards south of the red contours are probably due to molecular H_2 emission. Also, the contours of the IRAC ratio map of Ch2/Ch4 are overlaid with levels of min=0.05 and max=0.1. The position of important sources are marked by blue star symbols on the image. It is noticed that the S235B is also associated with a bright regions that could be due to Brα emission due to the presence of an HII region.

5.4 Conclusions

The important conclusions of this work are as follows:

1. *Spitzer*-IRAC photometry of the S235 complex has revealed 84 Class 0/I and 192 Class II YSOs. About 75% of these are present in clusters concentrated in 3 main regions (i.e., East 1, East 2 and the vicinity of S235A-B) with surface densities of 20-30 YSOs/pc^2;

2. A total of 227 YSOs (62 Class I and 165 Class II) have been identified in the vicinity of the S235A-B region using a combination of NIR and IRAC bands. About 71% of these sources are present in 4 clusters with maximum YSO surface density of about 120 YSOs/pc^2;

3. Clustering of YSOs is found in all the three regions viz. East 1, East 2 and the vicinity of S235A-B. The S235A-B cluster is found to be the richest for YSOs;

4. Ring-like structures of sources are found in the interface between the horse-shoe structure and sub-mm dust continuum emission region. Also, one embedded source S235AB-MIR has been detected in three IRAC bands except Ch1 band which forms a part of the ring-like structure. SED modeling shows that the source S235AB-MIR is a young, massive star that is still accreting material. The ring-like structure may be an evidence for magnetically super-critical collapse;

5. The HII region associated with S235A is traced by the presence of Brα emission within the IRAC observed horse-shoe structure using the IRAC ratio Ch2/Ch4 map. Outside of the horse-shoe structure, the map indicates molecular H_2 emission;

6. Brα emission is also found around S235B using the ratio map Ch2/Ch4. The map reveals the presence of an ionised region around it and the SED modeling shows that the source S235B is a young intermediate mass star;

7. The SED modeling shows that the source M1 is a low-mass star, relatively young in its evolution;

8. New Class 0/I sources are identified in the East 1 and East 2 region that do not have NIR JHK counterparts. IRAC colour-composite image reveals the presence of shock-excited H_2 emission in both regions. This is confirmed in IRAC ratio map of Ch2/Ch4, which reveals that the source “e2s3” in the East 2 region may be associated

with shock-excited H_2 emission outflow. The SED modeling of the source “e2s3” in the East 2 region indicates that it is a massive but very young protostar not yet being able to drive an HII region

Chapter 6

Conclusions and Future Work

The Chapter-wise conclusions and future directions of work are given below.

1. In the first part of Chapter 2, we studied the driving engine-outflow relationships for a sample of HMPOs using an online SED fitting tool. The resulting physical properties of the infrared counterparts (the putative driving engines) are compared against the properties of the associated molecular outflows obtained from the literature. Our study shows that the outflow mass and momentum are directly proportional to the (proto)stellar mass and inversely proportional to the (proto)stellar age. These results, limited by the dataset, are valid up to a mass of 25 $M_\odot$ and an age of 1Myr. The outflow mass and momentum are also proportional to the disk and envelope accretion rates. The modeled disk accretion rates are two orders of magnitude smaller than the envelope accretion rates and can not explain the observed mass loss rates. Therefore it is the mass accreted in the envelope that appears to contribute to the outflow entrainment rate. We point out that the massive molecular outflows scale high in terms of mass and momenta compared to their low mass counterparts, but their terminal velocities are less than half of the values found in low mass jet-like flows, resulting in missing “intermediate and extremely high velocity (IHV and EHV)” components. We may speculate that the massive outflows are launched in the large scale infalling envelopes, with typical properties of poorly collimated low velocity flows.

Unambiguous identification and characterisation of disks and envelopes in isolated massive protostars with outflows are necessary to understand the true connection between the outflow and the protostar. Also, it is necessary to identify independent indicators of accretion rates, similar to the emission lines of magnetospheric origin in low mass stars. Such results are expected to be possible with future high resolution facilities.

2. In the second part of Chapter 2, we have presented the identification and SED modeling of the driving engines of 42 UCHII regions; and obtained important physical parameters for all the driving engines. The observed SEDs of all the driving engines are described with stellar masses in the range of 5 - 43 $M_\odot$ (median of about 13 $M_\odot$) and with ages in the range of $10^{3.5-6.5}$ yr (median age of $10^{4.5}$ yr). The radii range between 3 - 250 $R_\odot$ and the temperatures range between 4300 - 40000 K. We obtained median disk and envelope accretion rates of $\sim 10^{-5.8}$ and $10^{-3.6}$ $M_\odot$ yr^{-1} respectively. It is found that mass and luminosity have a tight relation; L $\sim 10^{0.4\pm0.1} \times M^{3.2\pm0.1}$ for the identified central sources. It is also found that the envelope accretion rate has power law relation with stellar mass: $\dot{M}_{env}$ = $10^{-6.6\pm0.7} \times M^{2.6\pm0.6}$.

It is known that some of the UCHII regions are associated with ionised inward flow, therefore it may possible that the ionised accretion with high rate is important for massive star formation. However, our SED modeling results predict very high (envelope) accretion rates, even without taking ionised accretion flows into account. Therefore, it calls for (i) improved SED modeling to take into account the ionised flows, non-spherical accretion and envelope accretion luminosity; and (ii) observations that unambiguously identify and characterise disks and envelopes.

3. In Chapter 3, we have presented *Spitzer*-IRAC imaging photometric study of the massive star forming region AFGL 437. The IRAC ratio maps indicate molecular outflow corresponding to the source WK34, which is possibly due to H_2. The SED modeling of the outflow driving source WK34 indicates that it is a massive but very young protostar not yet able to drive a HII region. Several new embedded YSOs are identified within 64 arcsec of the central compact cluster with a maximum surface density about 25 YSOs/pc^2. SED modeling of the cluster sources gives their masses in the range 1-10 $M_\odot$, ages $10^{4.1-6.4}$ yr and luminosities $10^{0.47-3.48}$ $L_\odot$.

4. In Chapter 4, *Spitzer*-IRAC images and photometry of another star forming region M8 are discussed. *Spitzer*-IRAC photometry of M8 region revealed 64 Class 0/I and 168 Class II YSOs. About 60% of these are present in about 7 small clusters with spatial surface densities of 10-20 YSOs/pc^2. These sources are positioned close to the sub-mm gas clumps and the filamentary or pillar like structures present in M8. It is possible that the formation of these sources could have been triggered by stellar winds or expanding HII regions associated with the massive stars in the region. The IRAC ratio map Ch2/Ch4 reveals Brα emission corresponding to the Hourglass HII region powered by Her 36 and its inverted ratio Ch4/Ch2 identifies PAH emission in a cavity east of the Hourglass. The ratio maps Ch1/Ch2, Ch3/Ch2 and Ch4/Ch2 indicate the presence of PAH emission in both the ridges oriented along E-W and NE-SW directions.

5. In Chapter 5, we have presented the ground-based NIR photometric study of the young star forming region, IRAS 05375+3540 (in the vicinity of S235A and S235B region). For the source IRAS 05375+3540, our NIR data is effectively combined with the *Spitzer*-IRAC observations to identify additional young stellar objects (YSOs) in this complex. Our study revealed several clusters of young stellar objects with surface density varying from 20 - 120 YSOs/pc^2. Fresh star formation occurring in the region could be triggered by the interaction of expanding HII regions into the ambient molecular core. Both the mechanisms, viz. "Collect and Collapse" scenario and/or the passage of a shock wave into pre-existing dense clumps in the region could be responsible for triggered star formation in the region. Ring-like structures of sources are found in the interface between the horse-shoe structure and sub-mm dust continuum emission region. Also, one embedded source S235AB-MIR has been detected in three IRAC bands except Ch1 band which forms a part of the ring-like structure. The SED modeling shows that the source S235AB-MIR is a young, massive star that is still accreting material. The ring-like structure may be an evidence for magnetically super-critical collapse. IRAC ratio Ch2/Ch4 map traces Brα in the HII region of S235A in horse shoe shaped structure. Outside of the horse-shoe structure the map indicates molecular H_2 emission. Brα emission is found around S235B using the IRAC ratio map Ch2/Ch4 which reveals the presence of an ionised region around it and SED modeling shows that the source S235B is a young intermediate mass star. The SED modeling shows that the source M1 is a low-mass star relatively young in its evolution. Several new YSOs have been identified in East 1 and East 2 regions as well as shock-excited H_2 emission have identified in both regions using the IRAC ratio map of Ch2/Ch4. One new young massive protostar in accretion phase have been detected in East 2 region and this source is not yet being able to drive an HII region.

Further study of the three massive star forming regions is required in longer wavelengths (i.e., sub-mm/mm) at higher spatial resolution. Such observations will help confirming the true nature of the sources such as WK 34 in AFGL 437 and those in the East 1 and East 2 (source "e2s3") regions of S235 complex.

Appendix A

HMPOs outflow driving engines: Images and SED Modeling

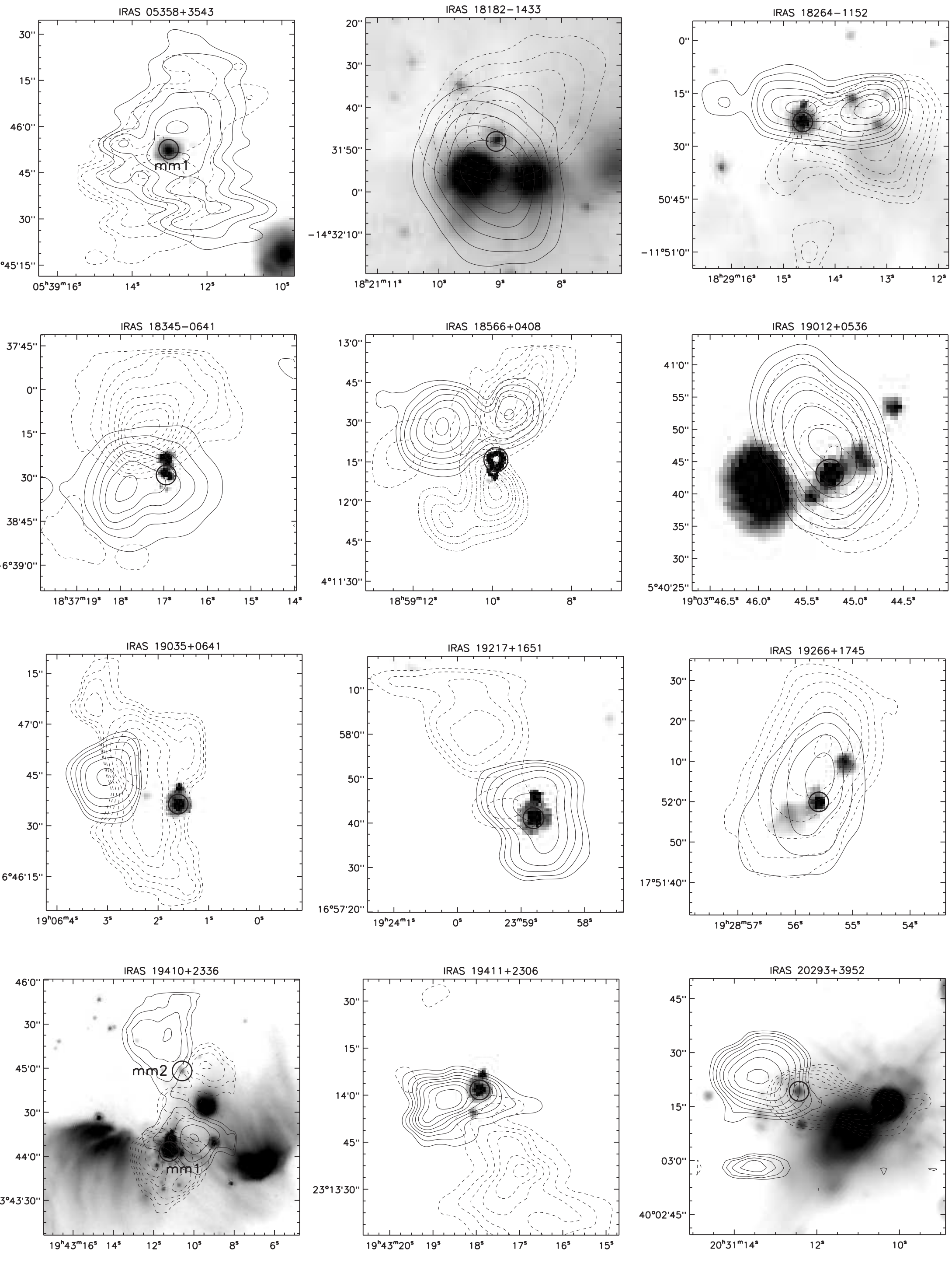

Fig. A.1: Outflow associations for 13 IRC(s). *Spitzer*-IRAC 8μm images of the IRC(s) are represented by grey scale. The CO outflow data (Beuther et al. 2002a) are shown using dashed (red-shifted lobe) and solid (blue-shifted lobe) contours. Black circles mark the IRC(s) modeled as driving engines.

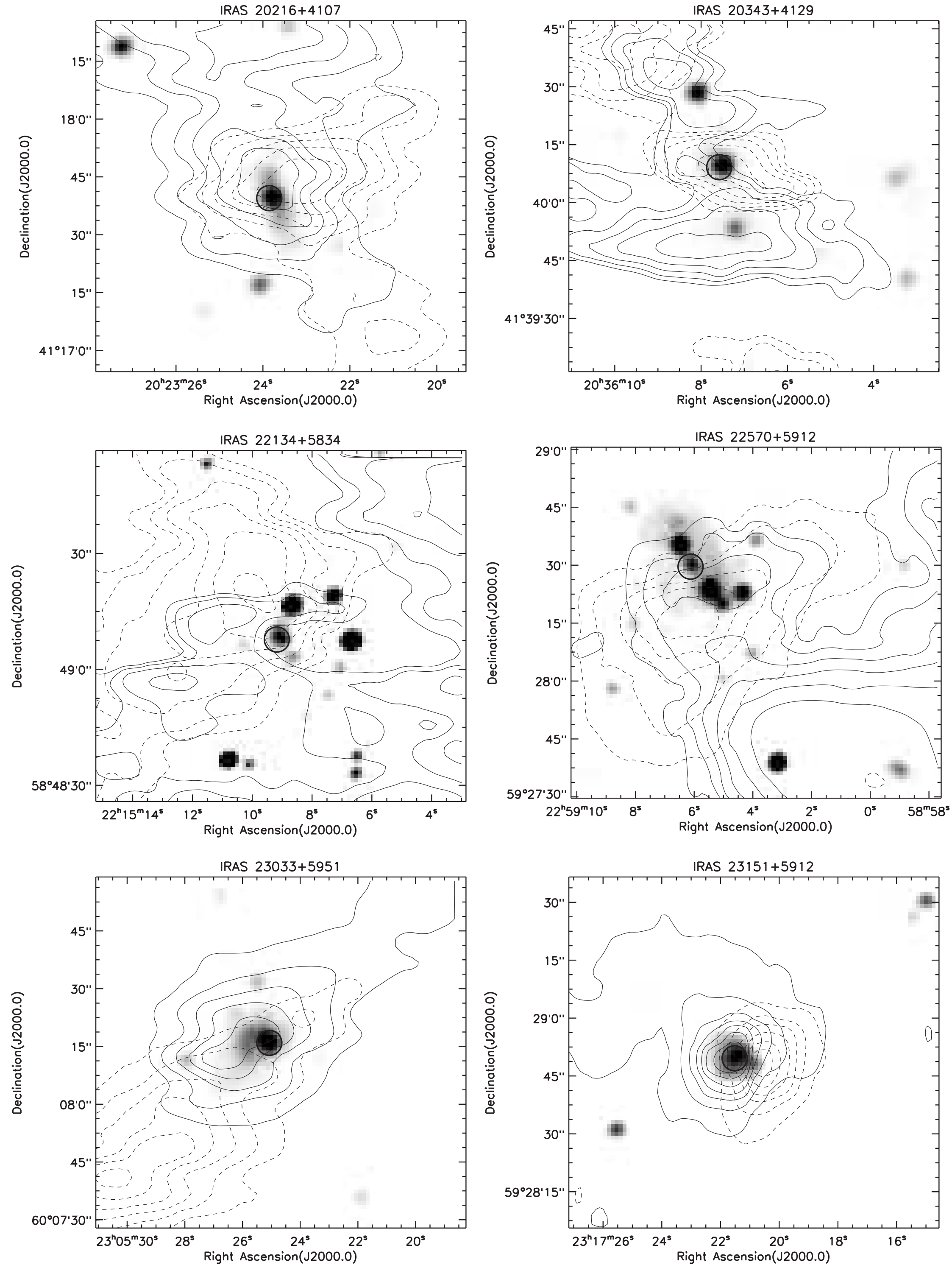

Fig. A.2: Outflow associations for 6 IRC(s) for which *Spitzer*-IRAC data are unavailable. 2MASS K-band images are represented by grey scale. The CO outflow data (Beuther et al. 2002a) are shown using dashed (red-shifted lobe) and solid (blue-shifted lobe) contours. Black circles mark the IRC(s) modeled as driving engines.

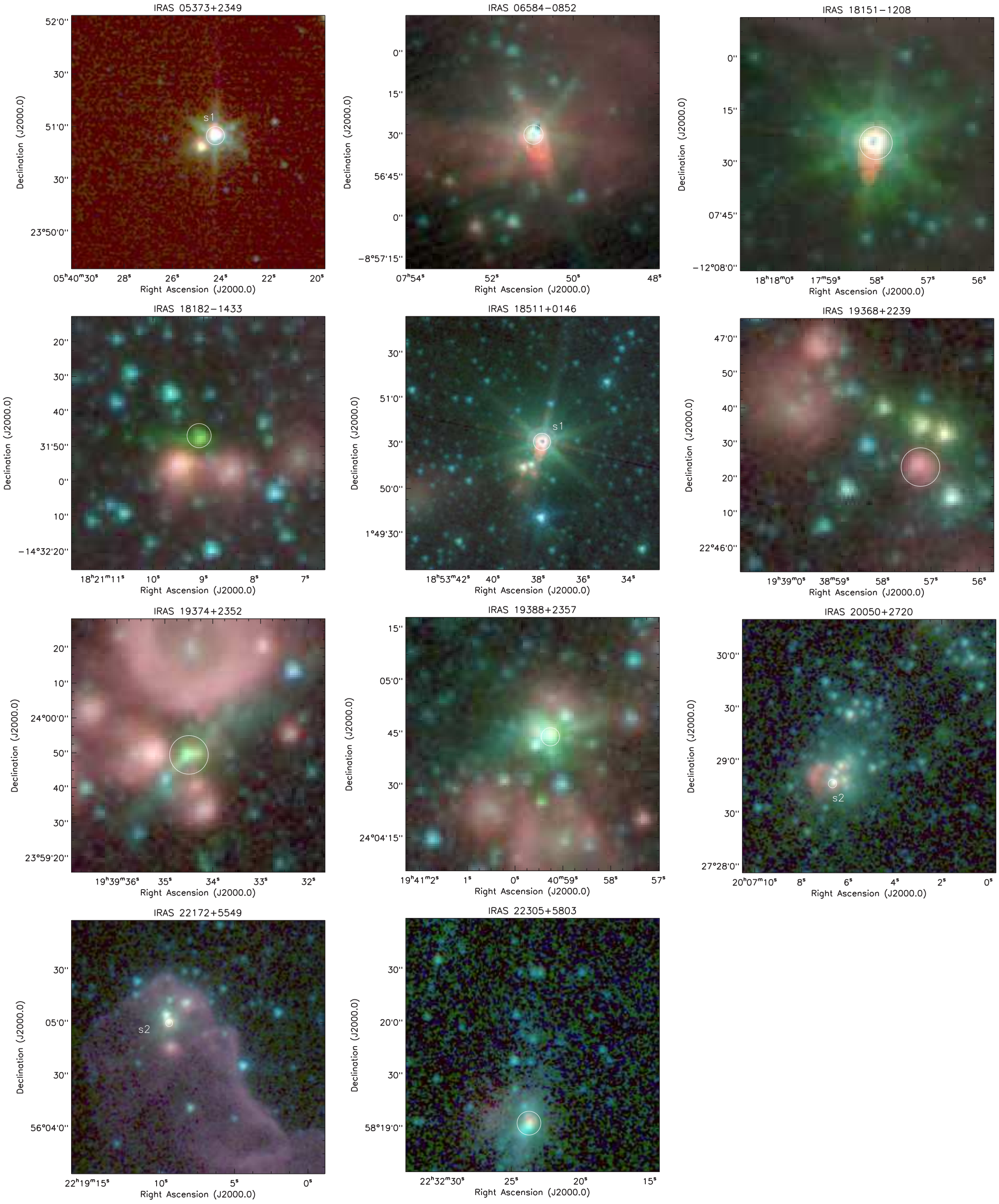

Fig. A.3: 3-colour-composite *Spitzer*-IRAC images made from Ch4, Ch2 and Ch1 shown as red, green and blue respectively. White circles mark the IRC(s) modeled as driving engines. The circled source from IRAS 18182-1433 region is associated with the jet structure, possibly be due to the shock-excited molecular H_2 emission.

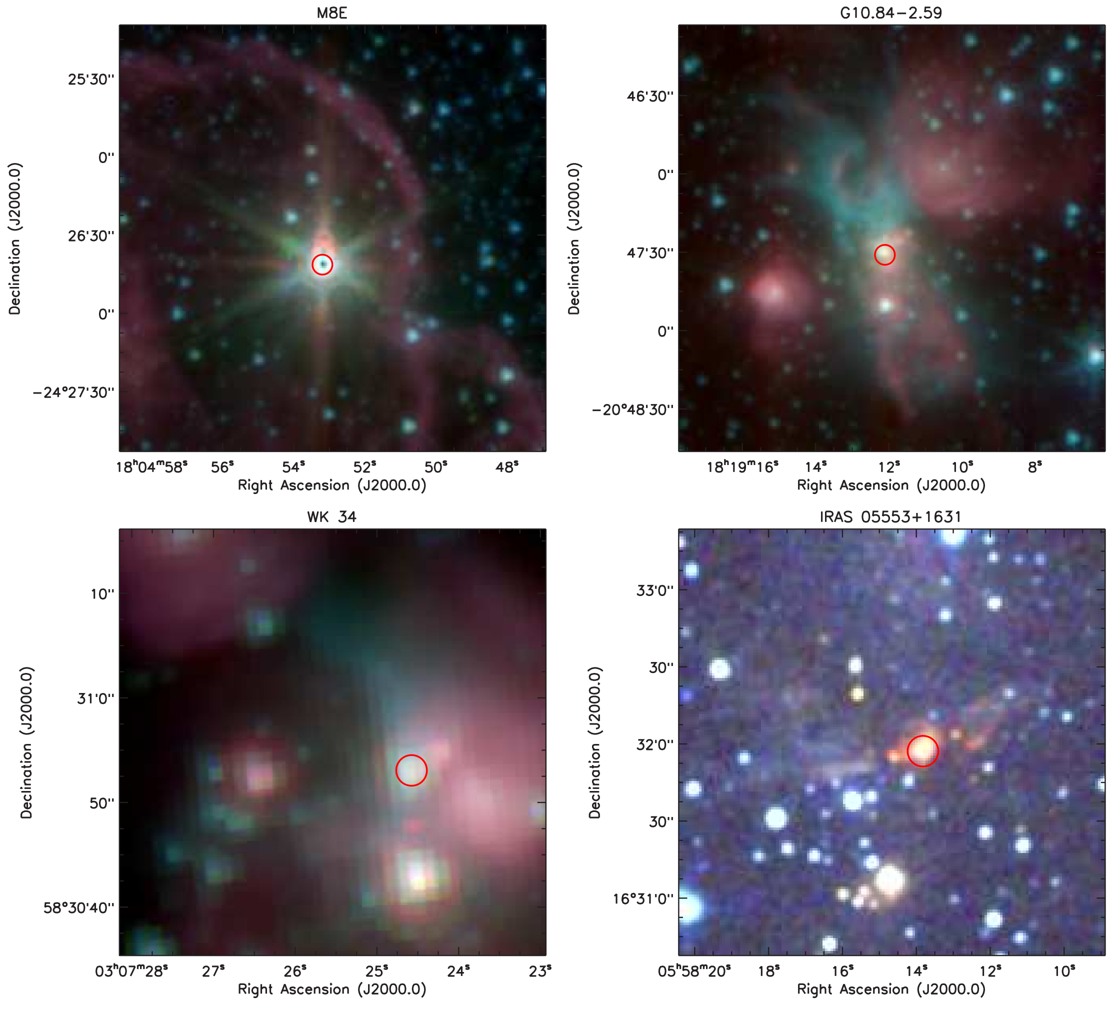

Fig. A.4: 3-colour-composite *Spitzer*-IRAC images Ch4 (red), Ch2 (green) and Ch1 (blue) for three sources; and 2MASS K(red), H(green) and J(blue) images for one source namely, IRAS 05553+1631.) Red circles mark the IRC(s) modeled as driving engines.

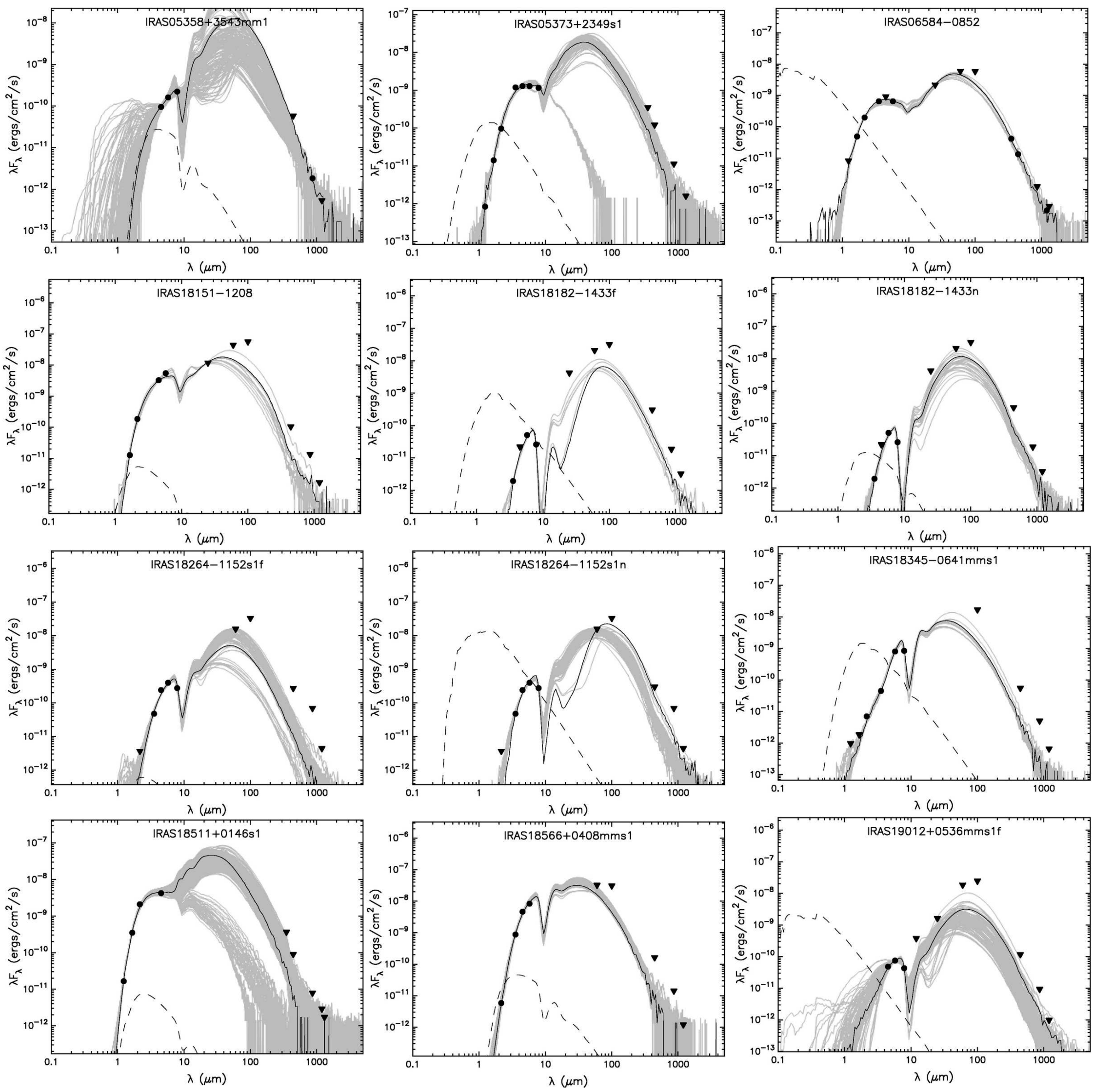

Fig. A.5: SED model plots: The solid line is the best fit model interpolated to different apertures at different wavelengths. The grey bunch of lines are the models that satisfy the criteria $\chi^2 - {\chi^2}_{best} < 3$. The dotted line represents the input photosphere. Filled circles and triangles show good data points and upper limits respectively.

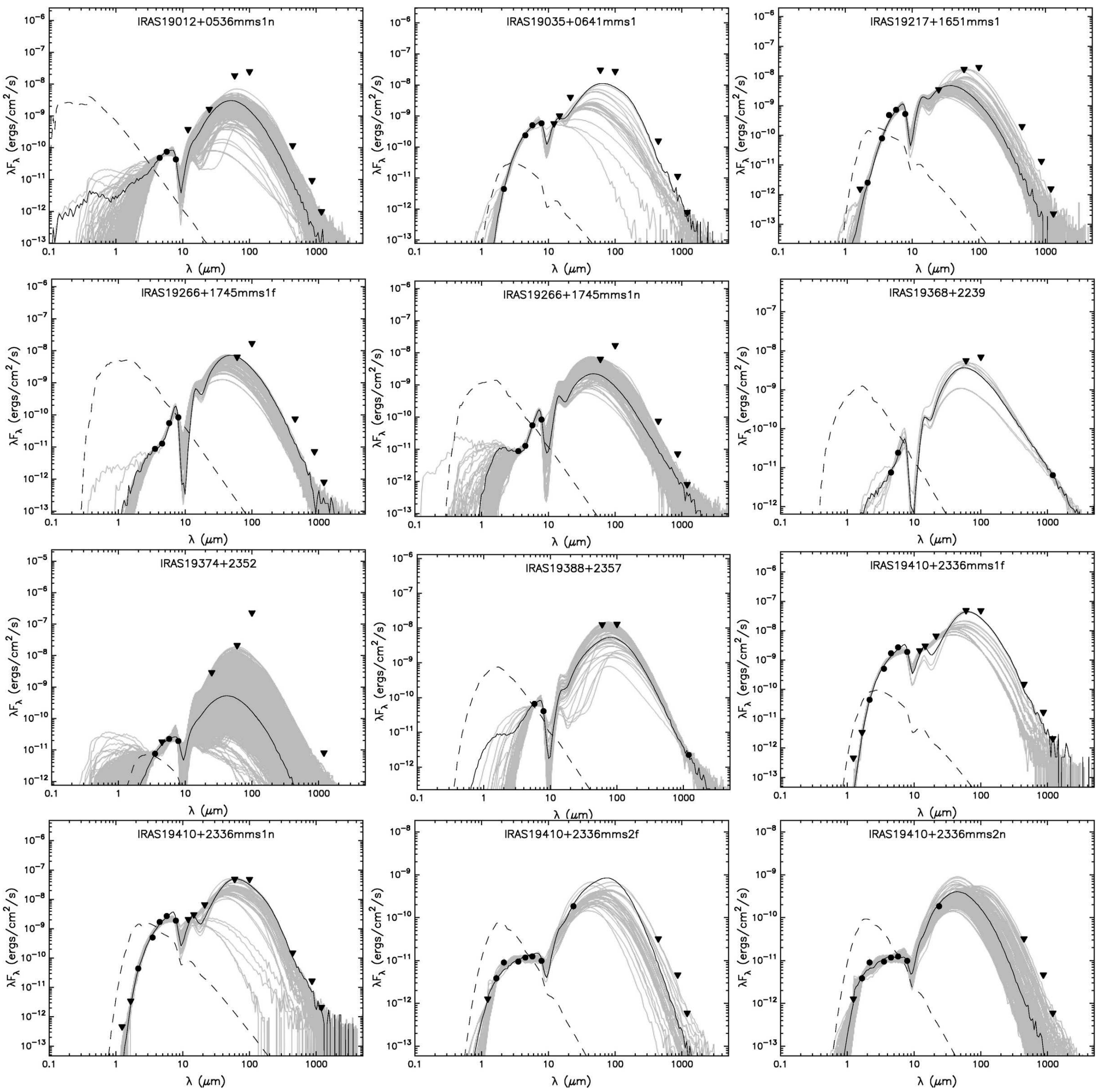

Fig. A.5: SED model plots: contd.

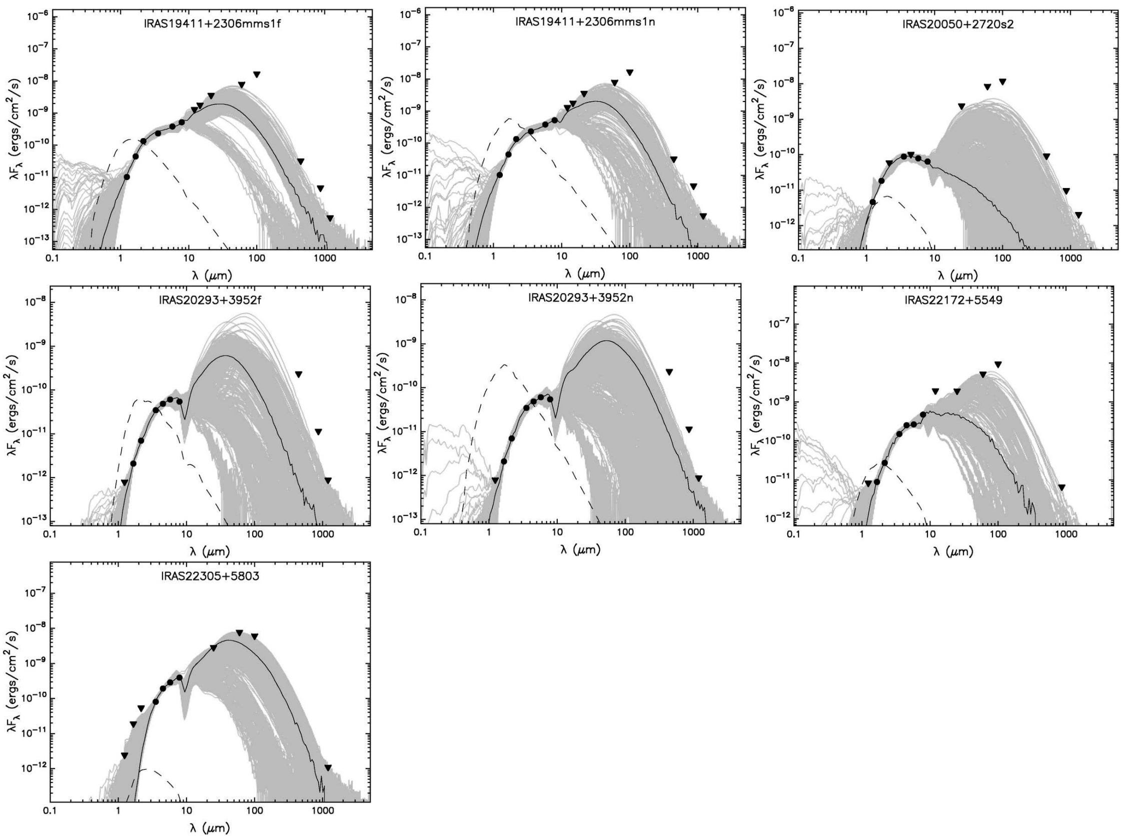

Fig. A.5: SED model plots: contd.

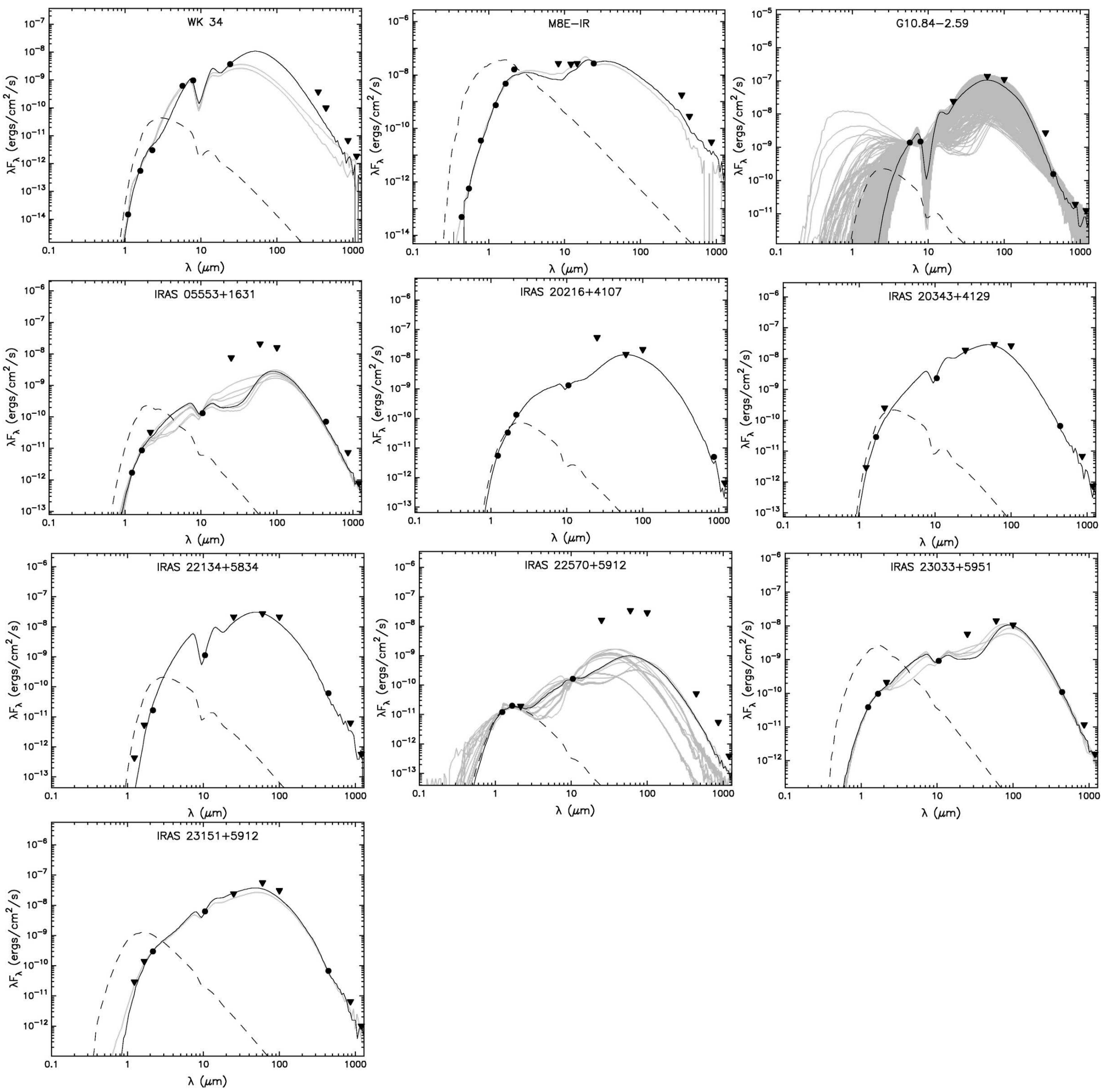

Fig. A.5: SED model plots: contd.

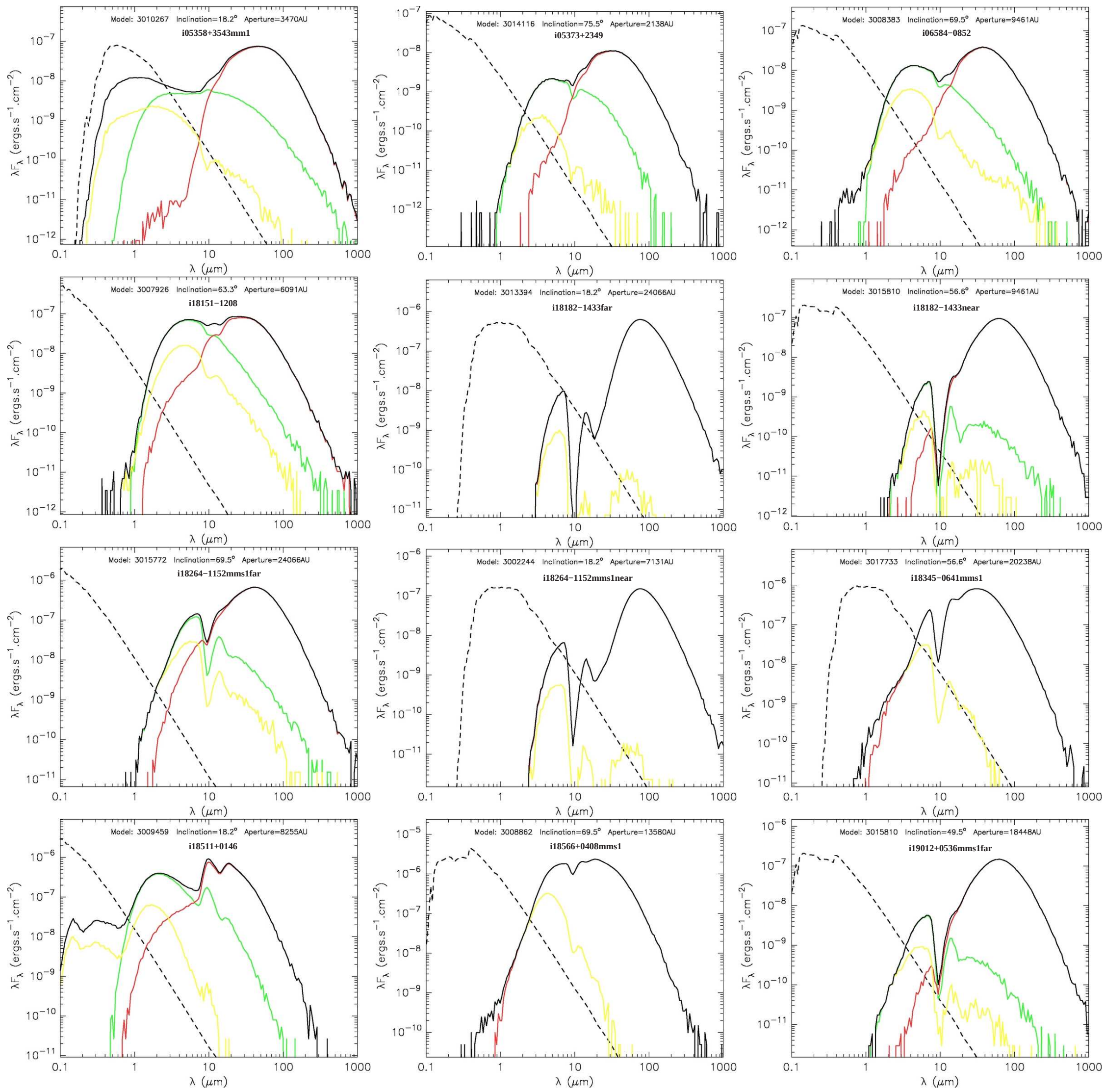

Fig. A.6: The best fit SED models are shown decomposed into the disk (green), envelope (red) and scattered light (yellow) components. The dotted line shows the input photospheric emission and the solid black line shows the best fit model for a single aperture corresponding to 2.4″ at the distance of the source (see Table 2.1 for distance).

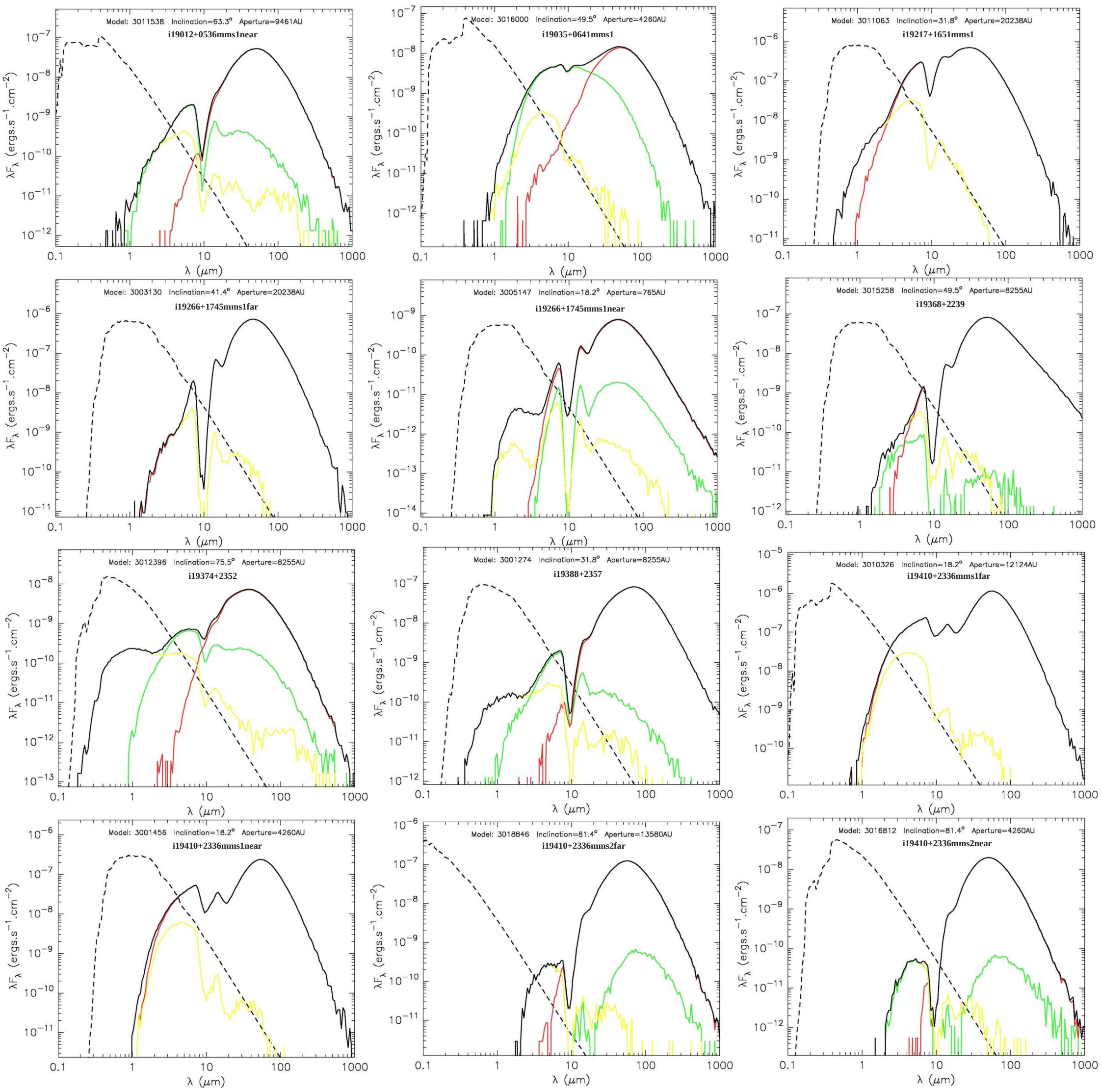

Fig. A.6: The best fit SED models: contd.

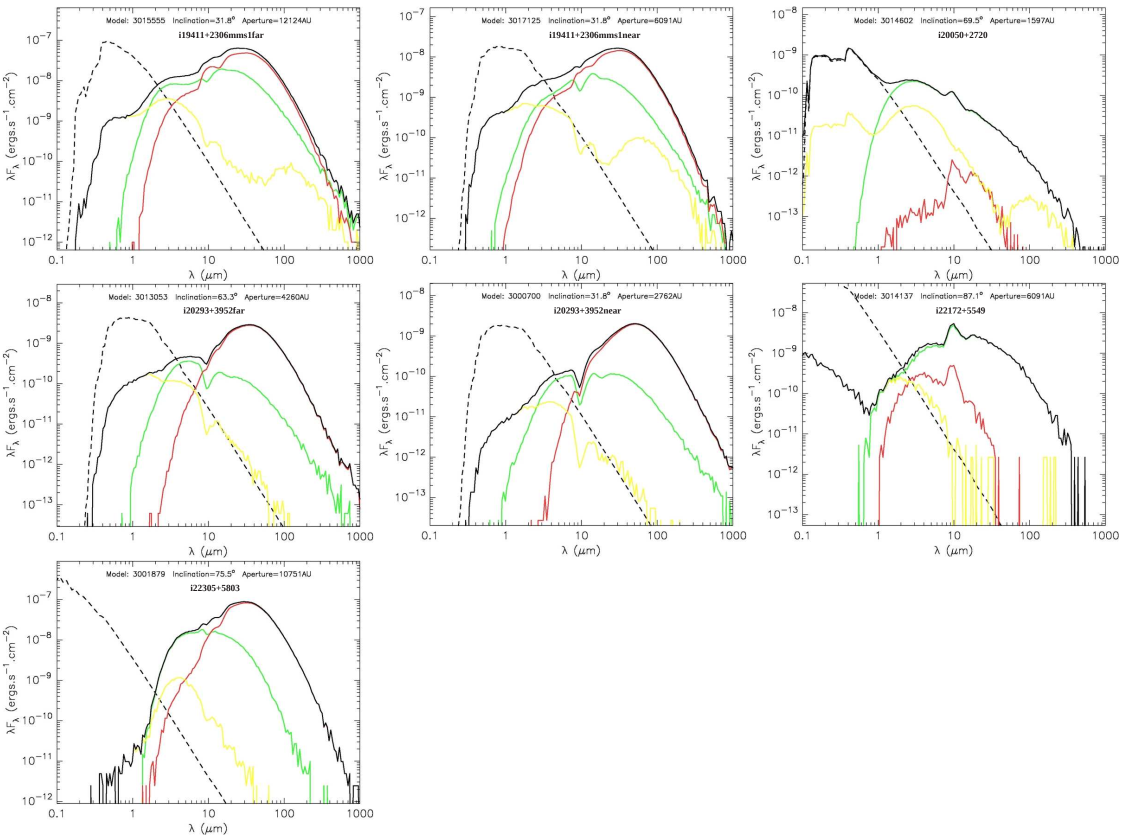

Fig. A.6: The best fit SED models: contd.

Table A.1: Physical parameters of the HMPO sources. “$*$” represents the observed outflow parameters

Source	distance	χ^2	M_*		L_*		Age		M$_{env}$		$\dot{M}_{env}$		M$_{disk}$		$\dot{M}_{disk}$		$M_{out}{}^*$	p*	$\dot{M}_{out}{}^*$ (10^{-4})
IRAS	kpc	per data point	M$_\odot$		log(L$_\odot$)		log(yr)		log(M$_\odot$)		log($M_\odot$ yr^{-1})		log(M$_\odot$)		log(M$_\odot$ yr^{-1})		M$_\odot$	M$_\odot$ km s^{-1}	$M_\odot$ yr^{-1}
05358+3543mm1	01.80	0.03	7.42	3.12	2.92	0.54	4.03	0.46	1.89	0.98	-3.24	0.65	-1.14	0.70	-5.58	0.73	21.0	288.0	5.6
05373+2349	01.20	1.74	9.23	1.31	3.43	0.27	4.91	0.70	0.51	2.84	-3.91	0.33	-2.17	1.59	-6.91	1.59	03.4	27.1	1.6
05553+1631	2.5	5.84	5.93	1.13	2.61	0.14	3.76	0.40	2.01	0.18	-2.76	0.16	-1.96	0.26	-7.22	0.53	37.9	609	3.4
06584-0852	04.50	0.12	9.04	0.39	3.72	0.02	5.09	0.11	2.03	0.04	-3.75	0.04	-2.26	0.70	-7.20	0.87	04.6	25.2	0.74
18151-1208	03.00	2.46	14.52	1.85	4.07	0.19	4.71	0.97	1.72	0.40	-4.39	0.97	-1.13	0.74	-5.62	1.03	12.0	106.0	1.7
18182-1433far	11.70	1.14	22.76	5.64	4.50	0.11	3.89	0.83	3.29	0.13	-2.37	0.14	-0.85	1.05	-4.82	1.31	203.0	1665.0	13.0
18182-1433near	04.50	1.43	11.29	1.97	3.92	0.21	4.71	0.34	2.95	0.20	-2.80	0.18	-1.23	0.73	-5.69	0.92	30.0	246.0	3.4
18264-1152mms1far	12.50	3.87	24.87	3.95	4.85	0.26	4.68	0.55	2.68	0.35	-2.94	0.42	-1.02	0.95	-5.11	1.02	405.0	6818.0	58.0
18264-1152mms1near	03.50	1.51	11.39	1.75	3.94	0.13	4.87	0.52	2.62	0.30	-3.09	0.28	-1.23	1.06	-5.86	0.99	31.0	534.0	8.6
18345-0641mms1	09.50	1.11	29.84	2.53	4.54	0.10	3.15	0.11	2.11	0.08	-3.61	0.11	-0.81	0.03	-4.61	0.03	143.0	1841.0	9.5
18511+0146	03.90	1.17	21.25	3.23	4.73	0.15	5.61	0.37	1.15	2.15	-5.01	1.63	-1.96	1.40	-6.65	1.70	18.8	248.7	3.7
18566+0408mms1	06.70	1.56	38.48	3.81	5.35	0.12	3.61	0.37	1.95	0.11	-3.84	0.10	-0.90	0.50	-5.28	0.35	32.0	540.0	4.3
19012+0536mms1far	08.60	0.05	11.42	2.13	3.87	0.21	4.62	0.45	2.64	0.43	-3.08	0.40	-1.29	0.90	-5.77	1.09	134.0	1339.0	11.0
19012+0536mms1near	04.60	0.01	9.37	1.24	3.46	0.24	4.64	0.41	2.03	0.64	-3.40	0.32	-1.54	0.81	-6.34	0.90	38.0	383.0	2.9
19035+0641mms1	02.20	0.92	6.48	1.77	2.97	0.36	4.05	1.01	0.81	2.08	-4.01	0.62	-1.90	0.78	-6.41	1.39	3.0	28.0	0.9
19217+1651mms1	10.50	2.08	22.41	5.93	4.48	0.16	3.70	0.52	2.18	0.43	-3.54	0.46	-1.29	0.98	-5.52	1.35	108.0	1961.0	14.0
19266+1745mms1far	10.00	0.80	19.57	4.51	4.40	0.18	4.04	0.71	2.17	0.29	-3.49	0.27	-1.52	1.35	-5.66	1.95	35.0	311.0	1.9
19266+1745mms1near	00.30	0.21	1.90	1.41	1.55	0.52	4.04	0.61	-0.50	0.77	-4.72	0.41	-2.33	0.88	-6.57	1.06	0.04	0.3	0.03
19368+2239	04.40	0.21	9.15	2.05	3.51	0.24	3.34	0.28	2.05	0.14	-3.38	0.31	-0.33	0.54	-3.44	0.29	35.6	113.2	4.5
19374+2352	04.30	0.00	8.52	4.71	2.99	0.66	3.97	0.76	1.11	1.00	-3.94	0.62	-1.68	1.17	-6.04	2.62	17.1	122.0	3.8
19388+2357	04.30	0.01	11.20	1.20	3.69	0.17	4.35	0.28	2.98	0.22	-2.59	0.11	-1.39	0.94	-5.63	1.36	16.1	94.4	...
19410+2336mms1far	06.40	0.93	19.06	4.77	4.54	0.09	4.91	0.73	2.25	0.61	-3.68	1.19	-0.65	0.33	-5.46	0.71	1423.0	31896.0	240
19410+2336mms1near	02.10	0.78	11.49	4.66	3.81	0.22	4.91	0.91	1.59	2.37	-3.44	1.30	-1.51	1.23	-6.14	1.48	153.0	3434.0	40.0
19410+2336mms2far	06.40	1.19	7.40	1.13	2.80	0.21	4.31	0.50	1.98	0.71	-3.32	0.65	-1.48	0.71	-6.32	0.87	173.0	3766.0	28.0
19410+2336mms2near	02.10	1.01	3.28	1.29	1.86	0.24	4.75	0.53	0.22	0.98	-4.25	0.66	-1.95	0.84	-7.24	1.28	18.0	405.0	4.6
19411+2306mms1far	05.80	0.81	9.90	1.84	3.69	0.21	5.26	0.85	0.19	2.84	-4.78	1.86	-1.75	1.20	-6.69	1.77	46.0	649.0	6.7
19411+2306mms1near	02.90	0.75	7.59	1.90	3.21	0.34	5.38	1.01	-1.16	3.06	-5.08	2.09	-2.04	1.09	-6.91	1.36	12.0	162.0	1.7
20050+2720	00.73	0.01	2.88	1.02	1.82	0.35	5.98	0.98	-4.08	2.96	-4.90	2.00	-2.92	1.30	-8.27	1.47	2.0	17.8	3.6
20216+4107	1.7	4.57	8.06	0.00	3.34	0.00	5.02	0.00	2.35	0.00	-3.15	0.00	-2.48	0.00	-8.50	0.00	6	43	1.7
20293+3952far	02.00	0.02	4.74	1.61	2.34	0.31	5.07	1.03	-1.45	3.07	-4.66	2.07	-1.83	1.06	-6.89	1.31	9.0	270.0	8.6
20293+3952near	01.30	0.02	2.98	1.76	1.84	0.46	4.91	1.02	-1.56	2.68	-4.70	1.82	-2.00	1.04	-7.06	1.33	4.0	114.0	3.0
20343+4129	1.4	3.26	8.93	2.03	3.13	0.22	4.49	0.68	1.24	0.32	-3.27	0.22	-1.46	0.38	-6.92	0.23	2	9	0.6
22134+5834	2.6	8.07	10.19	1.40	3.81	0.10	4.78	0.38	2.29	0.17	-3.45	0.06	-1.70	0.69	-5.53	0.35	17	242	4.9
22172+5549	02.87	0.24	7.40	2.28	3.23	0.40	5.91	0.76	-2.40	3.32	-5.87	2.26	-2.55	1.30	-7.59	1.55	9.0	37.1	...
22305+5803	05.40	0.21	11.48	1.71	3.91	0.23	5.20	0.81	0.94	2.14	-4.69	2.02	-1.45	0.95	-6.04	1.35	15.6	79.4	2.3
22570+5912	5.1	0.08	7.27	1.26	3.04	0.31	5.24	0.54	0.80	1.40	-4.03	0.94	-2.36	1.59	-6.98	1.76	73	911	6.1
23033+5951	3.5	0.17	10.85	0.57	3.55	0.08	3.29	0.26	2.53	0.20	-2.44	0.10	-1.35	0.45	-6.22	0.31	32	566	6.4
23151+5912	5.7	0.90	18.91	3.00	4.50	0.06	3.96	0.42	2.88	0.03	-2.85	0.01	-1.81	0.45	-6.58	0.41	21	597	10.0
M8E-IR	1.5	6.81	11.02	0.63	3.62	0.18	4.30	0.37	1.81	0.10	-4.09	0.16	-1.49	0.54	-6.22	1.17	23.1	94.8	6.6
WK34	2.0	8.26	7.23	1.91	3.00	0.30	3.94	0.57	0.48	0.64	-4.06	0.55	-1.67	0.75	-4.69	0.39	620	13559	110.
HH80	1.9	0.00	12.26	2.60	3.66	0.36	3.74	0.43	2.60	0.36	-2.93	0.21	-1.41	1.28	-5.31	1.55	570	536	5.7

Appendix B

Driving engines of UCHII regions: Images and SED Modeling

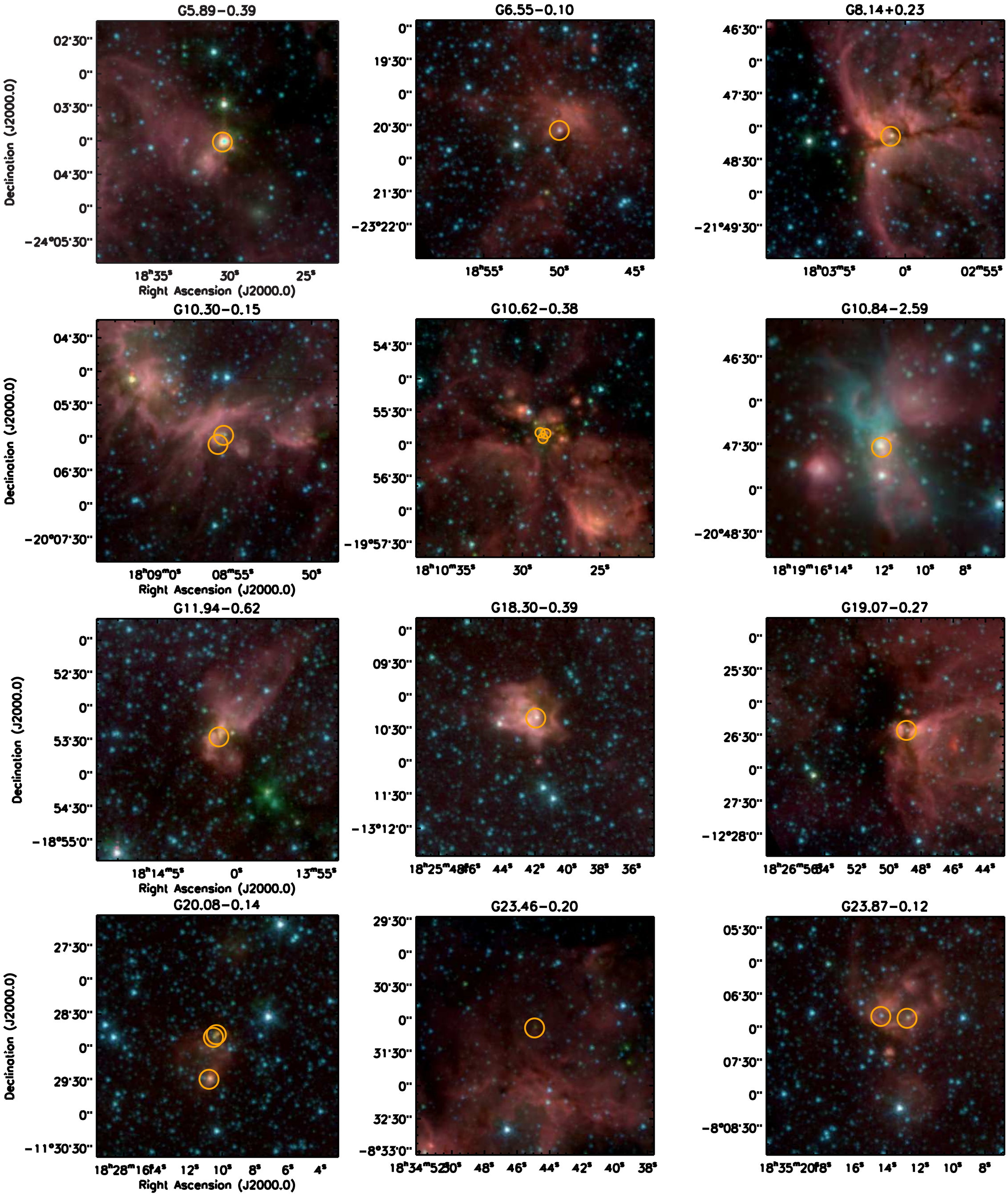

Fig. B.1: *Spitzer*-IRAC 3-colour-composite images of UCHII regions (Ch4(red), Ch2(green) and Ch1(blue)). Orange circles represent the locations of IRC(s) driving engines.

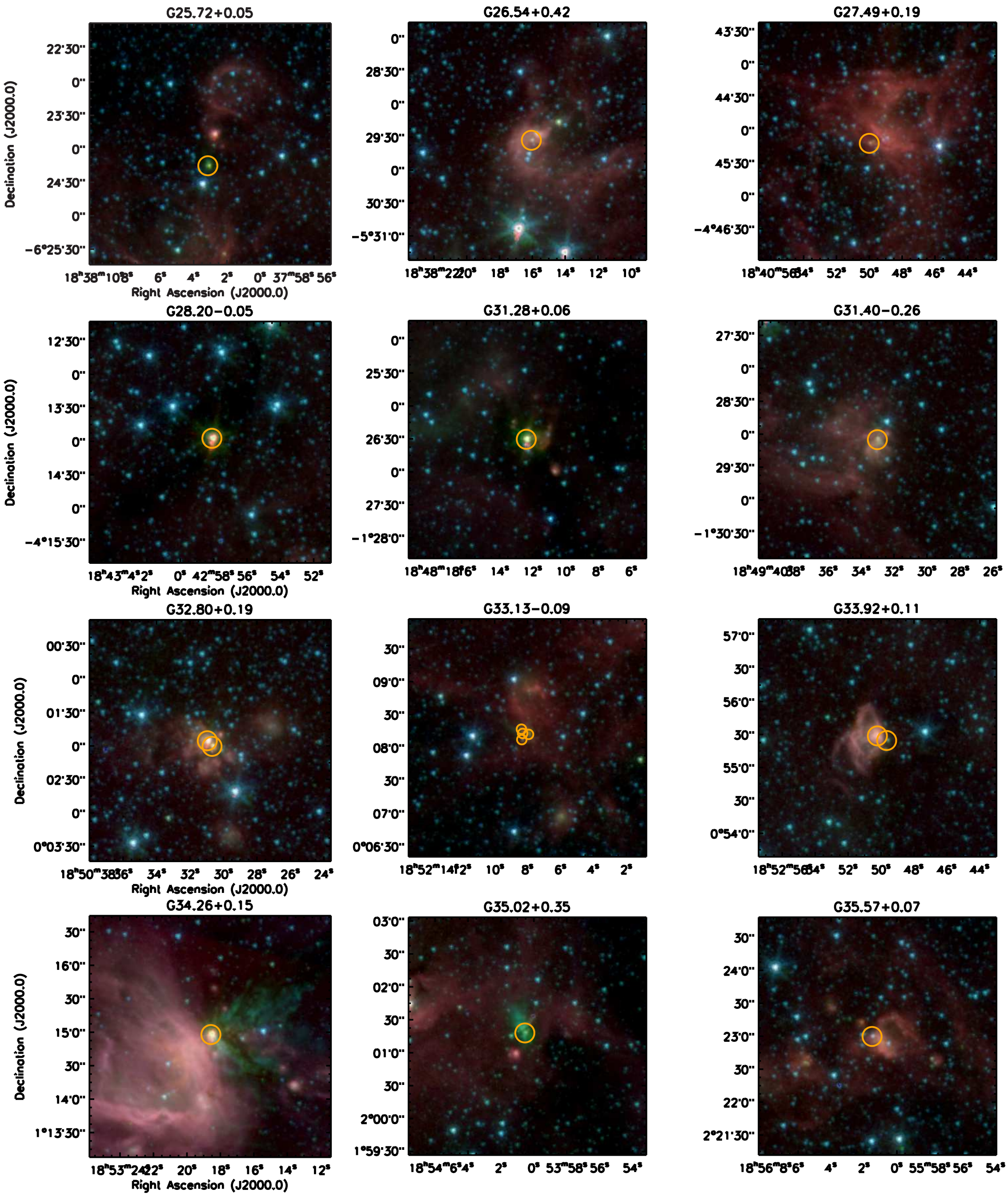

Fig. B.1: *Spitzer*-IRAC 3-colour-composite images of UCHII regions: contd.

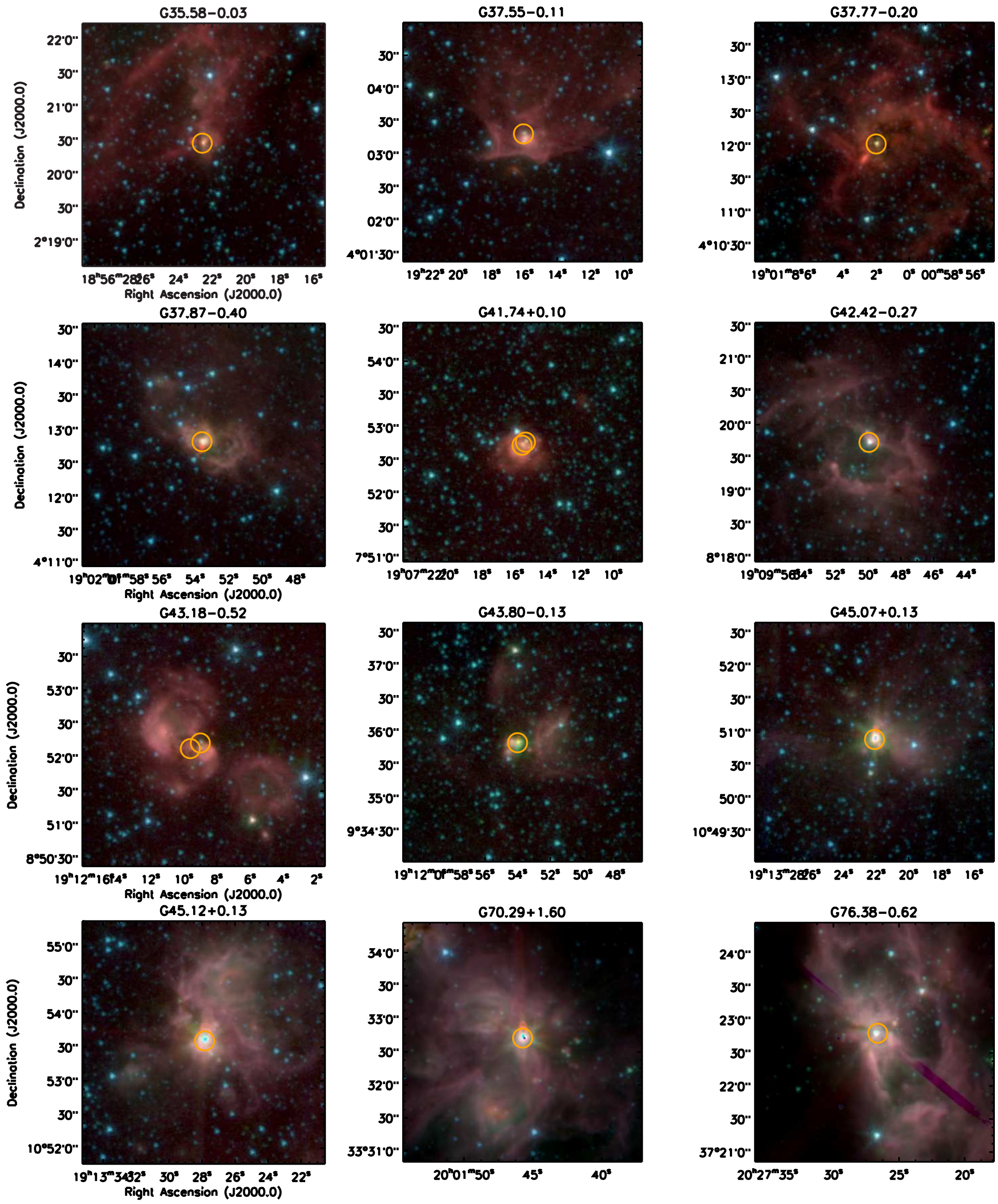

Fig. B.1: *Spitzer*-IRAC 3-colour-composite images of UCHII regions: contd.

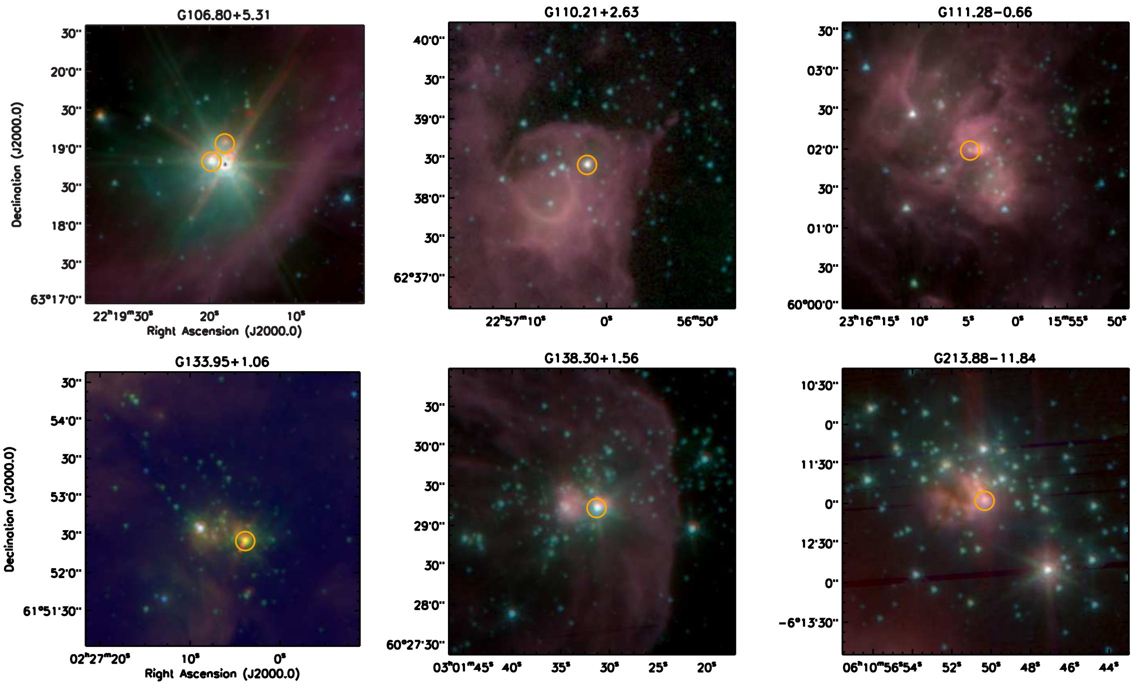

Fig. B.1: *Spitzer*-IRAC 3-colour-composite images of UCHII regions: contd. 2MASS K-band image is used as blue instead of Ch1 for the source G133.95+1.06.

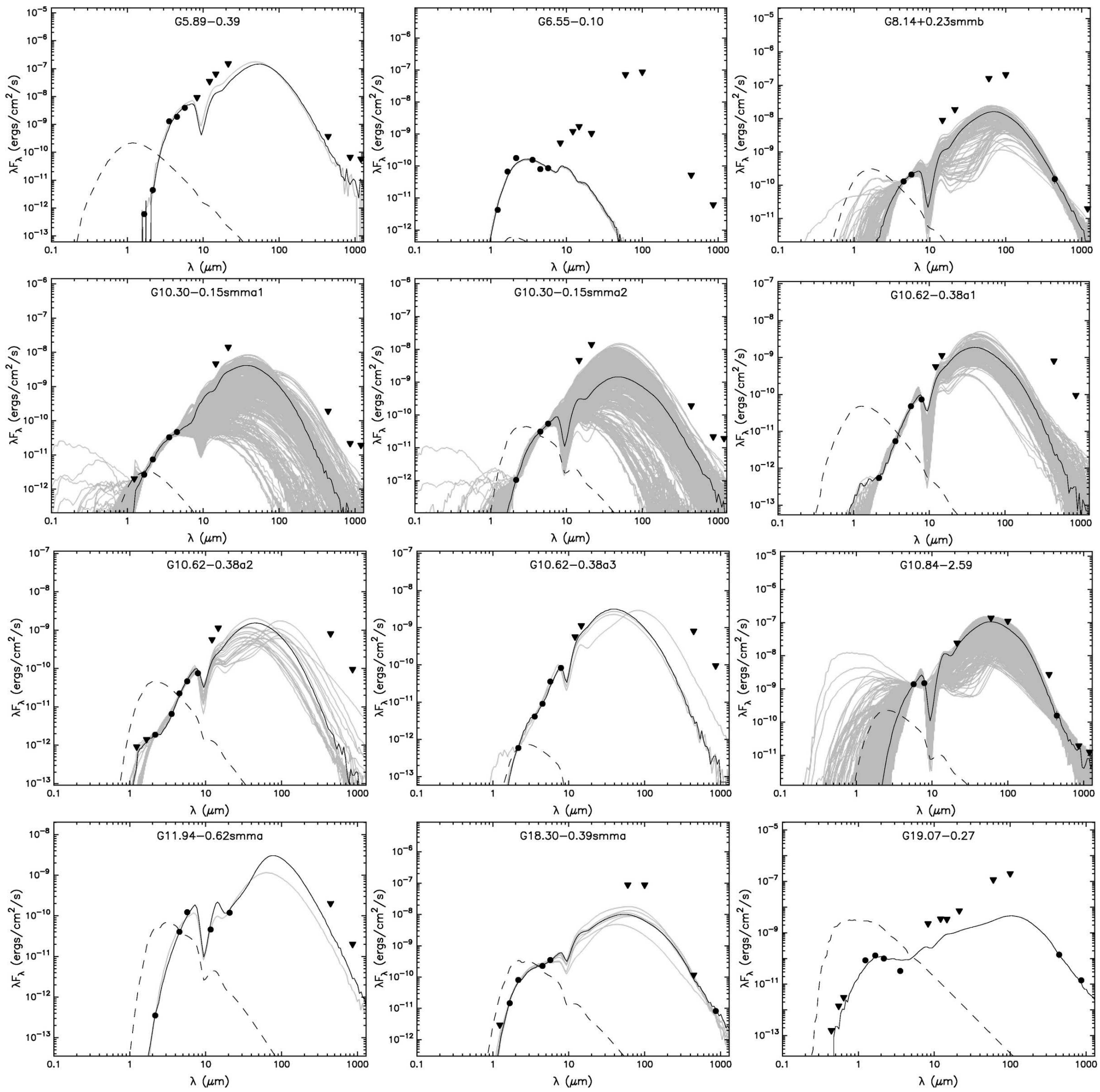

Fig. B.2: SED model plots of the driving engine of UCHII regions (plot details are the same as in Fig A.5).

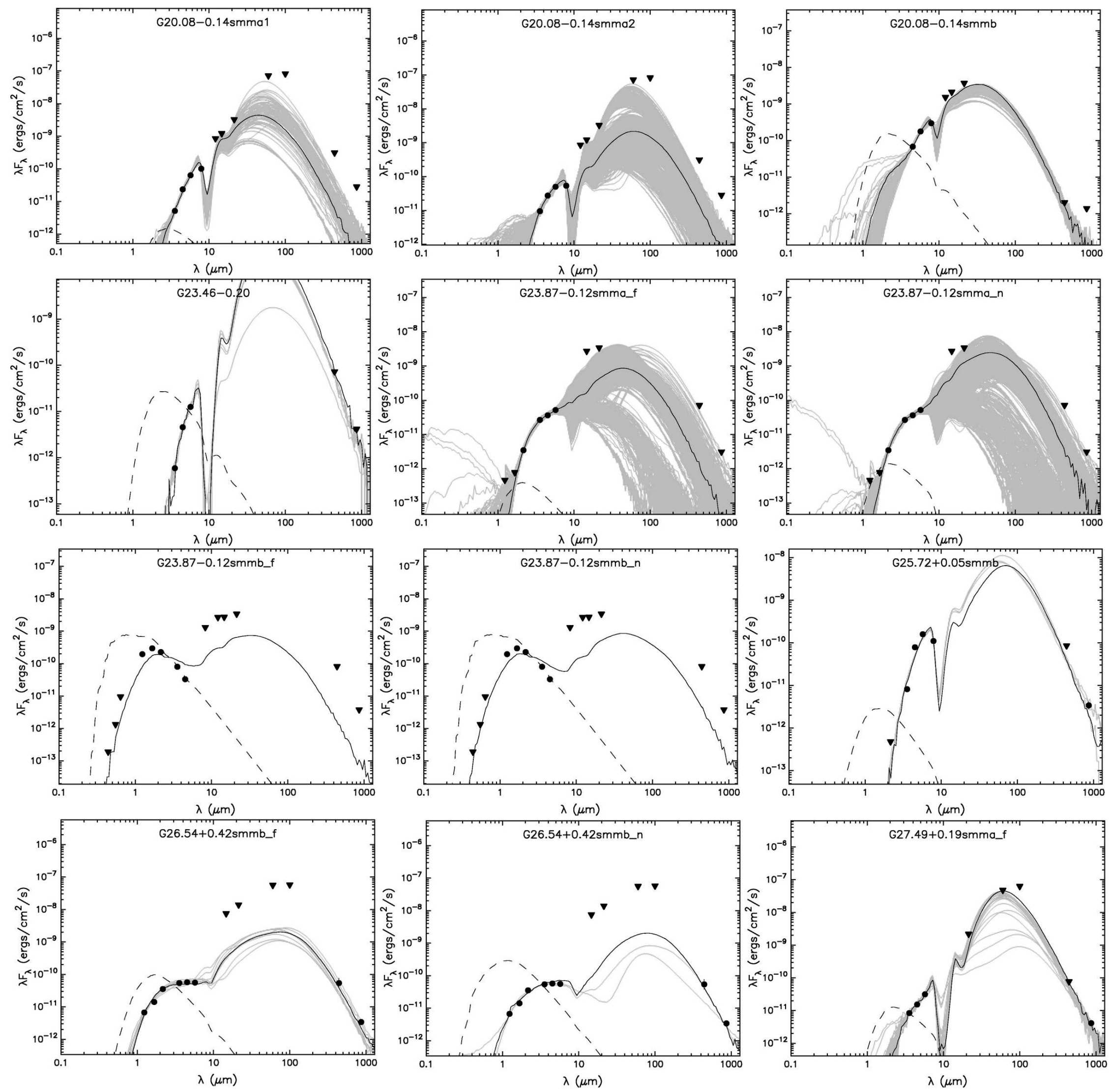

Fig. B.2: SED model plots of the driving engine of UCHII regions: contd.

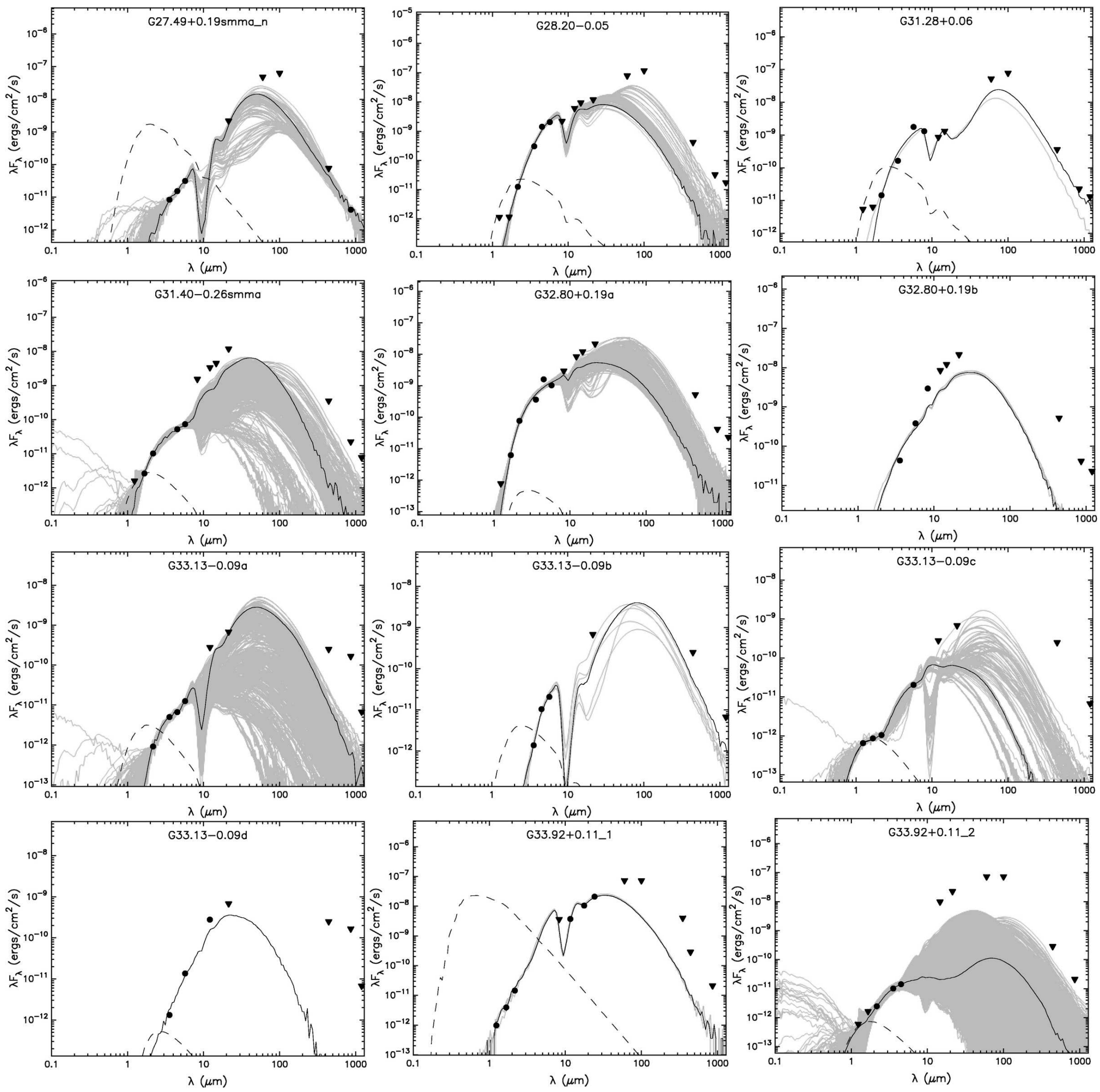

Fig. B.2: SED model plots of the driving engine of UCHII regions: contd.

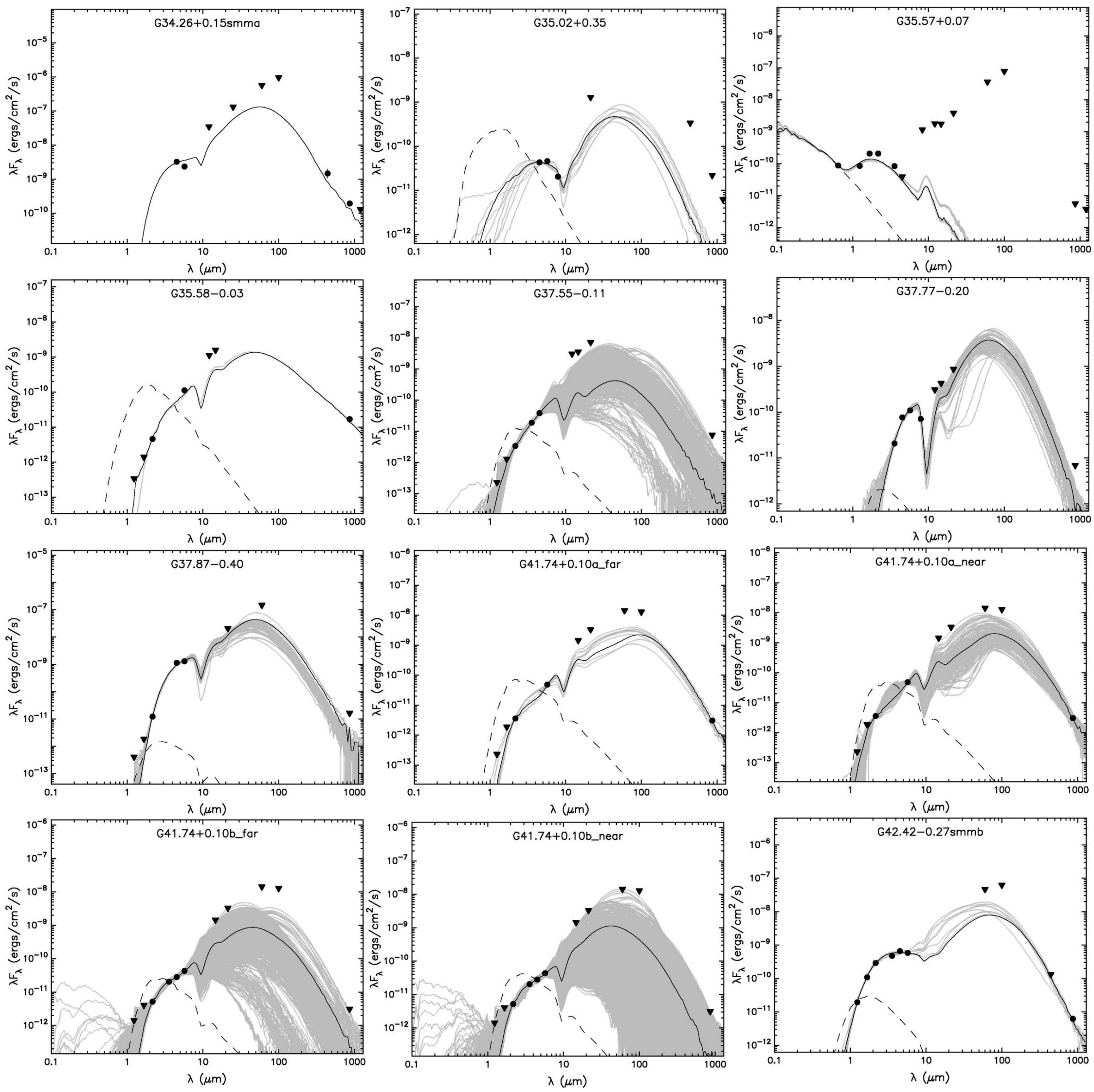

Fig. B.2: SED model plots of the driving engine of UCHII regions: contd.

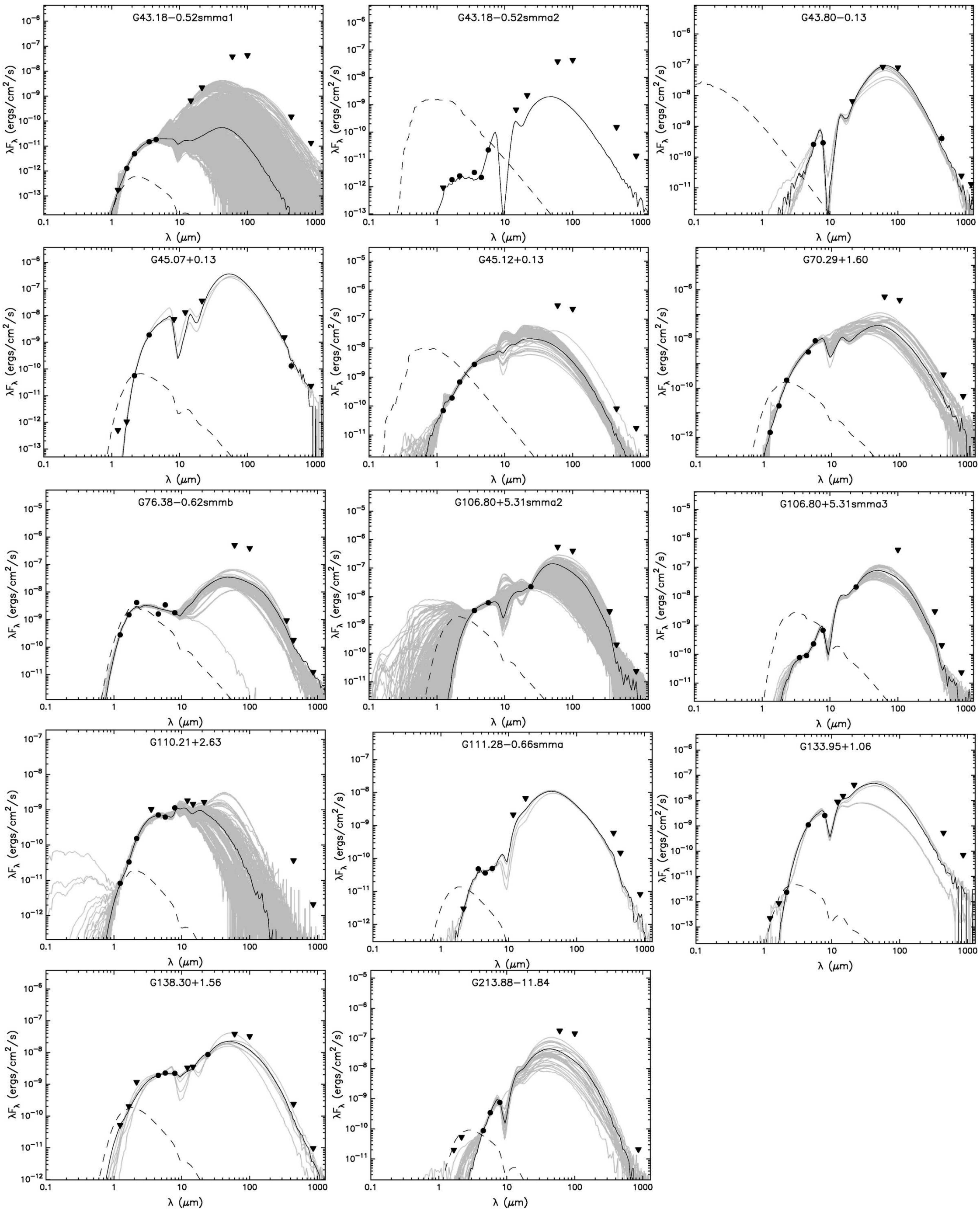

Fig. B.2: SED model plots of the driving engine of UCHII regions: contd.

Table B.1: Physical parameters of the driving engine(s) of UCHII regions

Source	χ^2 per data point	Age log(yr)		M_* $M_\odot$		T_* log($T_\odot$)		L_* log($L_\odot$)		R_* log($R_\odot$)		M_{env} log($M_\odot$)		$\dot{M}_{env}$ log($M_\odot$ yr^{-1})		M_{disk} log($M_\odot$)		$\dot{M}_{disk}$ log($M_\odot$ yr^{-1})	
G5.89-0.39	6.59	4.85	0.15	17.05	2.84	4.51	0.04	4.47	0.19	0.75	0.04	2.73	0.10	-2.98	0.12	-2.03	0.57	-5.73	0.44
G6.55-0.10	11.88	6.17	0.02	17.61	0.44	4.53	0.00	4.51	0.03	0.73	0.01	-6.84	0.31	—	—	-4.28	0.24	-9.66	0.17
G8.14+0.23smmb	0.01	4.08	0.37	12.87	1.67	3.83	0.19	3.82	0.22	1.76	0.31	3.08	0.23	-2.52	0.15	-1.21	0.90	-5.32	1.24
G10.30-0.15smma1	0.01	5.11	0.87	9.23	2.46	4.15	0.32	3.52	0.44	0.96	0.50	0.86	1.88	-4.67	1.66	-1.83	1.19	-6.75	1.79
G10.30-0.15smma2	0.00	4.99	0.75	11.17	2.12	4.19	0.31	3.79	0.37	1.03	0.48	1.03	1.24	-4.08	1.27	-1.59	0.64	-6.34	1.04
G10.62-0.38a1	0.04	3.91	0.67	9.08	2.23	3.74	0.17	3.34	0.23	1.68	0.32	1.15	0.61	-4.07	0.24	-1.46	1.13	-5.76	2.21
G10.62-0.38a2	0.83	4.01	0.61	7.62	2.05	3.70	0.11	3.04	0.28	1.61	0.21	1.07	0.71	-4.05	0.51	-1.31	1.00	-5.49	1.69
G10.62-0.38a3	1.96	4.96	0.34	9.05	0.62	4.12	0.24	3.53	0.12	1.05	0.43	2.14	0.67	-3.66	0.64	-2.63	0.36	-7.61	1.31
G10.84-2.59	0.00	3.74	0.43	12.26	2.60	3.78	0.21	3.66	0.36	1.79	0.30	2.60	0.36	-2.93	0.21	-1.41	1.28	-5.31	1.55
G11.94-0.62smma	2.64	3.86	0.97	9.25	0.83	3.79	0.21	3.51	0.05	1.70	0.44	2.99	0.14	-2.86	0.11	-2.16	0.02	-7.33	0.03
G18.30-0.39smma	1.32	3.96	0.43	10.30	1.42	3.71	0.12	3.40	0.16	1.78	0.22	2.37	0.57	-3.14	0.38	-0.81	0.69	-5.13	0.80
G19.07-0.27	28.12	3.51	0.00	14.65	0.00	3.64	0.00	3.67	0.00	2.07	0.00	3.64	0.00	-2.14	0.00	-1.52	0.00	-4.44	0.00
G20.08-0.14smma1	0.42	4.33	0.49	21.54	6.86	4.30	0.35	4.62	0.44	1.24	0.52	2.41	0.56	-3.22	0.50	-1.45	1.41	-5.52	1.45
G20.08-0.14smma2	0.11	4.29	0.68	17.22	8.52	4.14	0.38	4.21	0.61	1.34	0.57	2.28	0.72	-3.30	0.56	-1.48	1.30	-5.72	2.07
G20.08-0.14smmb	0.01	3.91	0.53	20.19	3.67	3.98	0.30	4.49	0.08	1.80	0.60	1.67	0.17	-3.93	0.09	-1.07	1.54	-4.74	2.34
G23.46-0.20	0.17	4.05	0.53	26.82	9.02	4.24	0.27	4.83	0.71	1.45	0.46	2.87	0.61	-2.71	0.39	-2.13	0.75	-5.99	0.80
G23.87-0.12smma-far	0.11	5.53	0.57	10.56	2.29	4.35	0.17	3.82	0.26	0.74	0.31	0.43	2.75	-4.94	1.95	-2.15	1.16	-7.12	1.42
G23.87-0.12smma-near	0.06	5.61	0.81	7.83	1.78	4.19	0.25	3.29	0.35	0.79	0.44	-0.88	3.34	-5.38	2.12	-2.24	1.09	-7.14	1.49
G23.87-0.12smmb-far	61.78	3.71	0.00	13.61	0.00	3.65	0.00	3.64	0.00	2.04	0.00	1.73	0.00	-3.87	0.00	-1.39	0.00	-5.41	0.00
G23.87-0.12smmb-near	45.15	4.09	0.00	8.70	0.00	3.66	0.00	2.96	0.00	1.68	0.00	1.74	0.00	-3.75	0.00	-1.96	0.00	-7.95	0.00
G25.72+0.05smmb	12.36	4.59	0.29	22.09	2.98	4.48	0.18	4.79	0.18	0.95	0.29	3.21	0.19	-2.42	0.19	-1.42	0.63	-4.90	0.78
G26.54+0.42smmb-far	3.59	4.33	0.25	11.58	1.88	3.89	0.10	3.74	0.16	1.59	0.18	3.22	0.23	-2.51	0.18	-1.43	0.80	-5.77	1.39
G26.54+0.42smmb-near	2.12	3.96	0.58	6.57	3.37	3.68	0.09	3.03	0.29	1.49	0.27	2.41	1.04	-2.81	0.32	-1.17	0.62	-4.79	1.07
G27.49+0.19smma-far	0.26	4.06	0.54	29.44	9.63	4.27	0.35	4.98	0.58	1.46	0.55	3.18	0.28	-2.43	0.25	-0.81	0.95	-4.25	1.45
G27.49+0.19smma-near	0.00	3.58	0.22	10.15	2.43	3.64	0.03	3.34	0.29	1.88	0.16	1.25	0.51	-3.44	0.23	-0.77	0.48	-4.76	0.85
G28.20-0.05	3.54	4.02	0.47	25.03	3.78	4.23	0.30	4.87	0.13	1.50	0.59	2.24	0.44	-3.50	0.48	-1.21	0.95	-5.36	0.87
G31.28+0.06	16.38	3.69	0.00	20.39	1.81	3.85	0.08	4.54	0.11	2.09	0.11	3.10	0.07	-2.54	0.14	-0.59	0.58	-4.31	1.37
G31.40-0.26smma	0.01	5.33	0.80	11.32	2.87	4.25	0.31	3.82	0.45	0.93	0.46	0.60	1.94	-5.04	1.96	-2.09	1.46	-7.05	2.24
G32.80+0.19a	13.13	4.98	0.54	28.62	4.04	4.56	0.14	5.05	0.15	0.92	0.25	2.11	0.32	-3.95	1.00	-1.35	1.37	-5.82	1.61
G32.80+0.19b	24.93	5.67	0.20	28.86	0.88	4.60	0.00	5.06	0.03	0.85	0.01	1.75	0.15	-5.08	0.93	-0.93	1.25	-6.86	1.32
G33.13-0.09a	0.06	4.80	1.16	7.92	3.60	3.96	0.34	3.13	0.64	1.14	0.58	-0.12	2.89	-4.22	2.11	-2.01	2.17	-6.75	2.75
G33.13-0.09b	2.44	4.62	0.61	10.50	2.88	4.12	0.28	3.72	0.48	1.13	0.42	2.62	0.96	-3.01	0.57	-1.57	1.04	-6.22	1.29
G33.13-0.09c	0.01	5.58	1.04	5.75	1.09	4.09	0.27	2.82	0.23	0.74	0.48	-3.29	2.86	-4.67	2.17	-2.21	0.71	-6.91	1.23

Table B.1: contd.

Source	χ^2	Age		M_*		T_*		L_*		R_*		M_{env}		$\dot{M}_{env}$		M_{disk}		$\dot{M}_{disk}$	
thomposon list	per data point	log(yr)		$M_\odot$		log($T_\odot$)		log($L_\odot$)		log($R_\odot$)		log($M_\odot$)		log($M_\odot$ yr^{-1})		log($M_\odot$)		log($M_\odot$ yr^{-1})	
G33.13-0.09d	15.54	6.01	0.33	11.12	1.64	4.43	0.03	3.91	0.22	0.62	0.04	-1.30	1.34	-4.80	0.00	-1.12	0.55	-7.55	0.62
G33.92+0.11s1	1.57	3.46	0.00	24.44	0.00	3.75	0.00	4.76	0.00	2.40	0.00	2.16	0.00	-3.52	0.00	—-	—-	—-	—-
G33.92+0.11s2	0.00	5.60	0.85	7.77	2.35	4.16	0.25	3.23	0.49	0.81	0.41	-1.35	3.24	-5.16	1.92	-2.30	1.49	-7.49	1.90
G34.26+0.15smma	9.35	4.66	0.00	14.72	0.00	4.46	0.00	4.76	0.00	0.81	0.00	3.24	0.00	-2.47	0.00	-0.58	0.00	-3.26	0.00
G35.02+0.35	1.89	4.48	0.45	9.95	1.14	3.87	0.18	3.49	0.13	1.52	0.36	2.15	0.39	-3.61	0.37	-1.09	0.84	-5.49	1.09
G35.57+0.07	14.81	6.37	0.12	9.35	0.30	4.39	0.01	3.70	0.05	0.58	0.01	-6.90	0.29	—-	—-	-6.41	0.67	-11.10	0.58
G35.58-0.03	3.13	3.46	0.00	13.22	0.00	3.64	0.00	3.77	0.00	2.04	0.00	2.34	0.00	-3.44	0.00	-0.09	0.00	-3.19	0.00
G37.55-0.11	0.00	4.41	0.62	13.30	3.41	4.05	0.32	3.92	0.49	1.38	0.48	1.65	0.84	-3.93	0.78	-1.62	1.87	-6.25	2.28
G37.77-0.20	1.43	4.77	0.52	12.88	2.56	4.30	0.23	4.09	0.17	0.96	0.45	2.73	0.28	-2.98	0.28	-1.38	1.03	-5.94	1.10
G37.87-0.40	1.46	4.86	0.36	29.50	5.06	4.58	0.09	5.08	0.17	0.91	0.17	2.51	0.31	-3.09	0.39	-1.14	0.85	-5.39	1.09
G41.74+0.10a-far	0.00	4.16	0.20	15.48	0.88	4.01	0.11	4.17	0.05	1.59	0.19	3.36	0.07	-2.34	0.07	-0.88	0.25	-4.80	0.37
G41.74+0.10a-near	0.00	4.04	0.62	1.63	1.33	3.61	0.02	1.46	0.38	1.01	0.16	1.15	0.41	-3.61	0.26	-2.22	0.86	-6.69	0.84
G41.74+0.10b-far	0.02	5.04	0.97	12.13	3.04	4.19	0.36	3.87	0.43	1.07	0.57	0.96	1.95	-4.66	1.90	-2.13	1.99	-7.01	2.62
G41.74+0.10b-near	0.01	4.76	0.95	2.00	1.58	3.67	0.17	1.41	0.55	0.86	0.25	-1.21	2.09	-4.90	1.47	-2.43	0.97	-7.54	1.36
G42.42-0.27smmb	0.91	4.52	0.35	12.72	1.76	4.11	0.19	4.04	0.14	1.32	0.37	3.03	0.37	-2.58	0.17	-1.20	0.65	-5.47	1.08
G43.18-0.52smma1	0.01	5.79	0.86	5.80	1.52	4.05	0.25	2.75	0.34	0.79	0.44	-2.69	3.35	-5.21	2.16	-2.65	1.52	-7.93	1.73
G43.18-0.52smma2	17.31	3.55	0.00	8.78	0.00	3.63	0.00	3.20	0.00	1.85	0.00	0.93	0.00	-3.67	0.00	-1.49	0.00	-4.86	0.00
G43.80-0.13	1.96	4.17	0.28	31.71	5.79	4.47	0.21	5.21	0.28	1.18	0.35	3.46	0.10	-2.14	0.08	-0.86	0.96	-5.01	1.18
G45.07+0.13	0.78	3.64	0.30	43.45	0.73	4.24	0.30	5.59	0.04	1.84	0.61	3.21	0.07	-2.35	0.07	—-	—-	—-	—-
G45.12+0.13	0.40	4.90	0.84	29.62	5.32	4.42	0.34	5.01	0.26	1.18	0.58	1.92	0.20	-4.24	0.63	-1.24	1.37	-6.16	1.83
G70.29+1.60	4.10	4.29	0.57	30.89	6.37	4.39	0.27	5.12	0.21	1.30	0.48	2.47	0.50	-3.19	0.53	-1.24	1.41	-5.44	1.79
G76.38-0.62smmb	11.24	5.74	0.87	7.75	1.75	4.12	0.31	3.19	0.42	0.86	0.49	-3.84	3.99	-4.52	2.27	-2.73	2.03	-7.51	2.02
G106.80+5.31smma2	0.00	4.75	0.54	9.73	2.13	4.05	0.27	3.53	0.40	1.18	0.42	1.37	0.68	-4.14	0.43	-1.91	0.96	-6.77	1.31
G106.80+5.31smma3	1.31	4.13	0.46	10.26	2.37	3.74	0.12	3.36	0.35	1.73	0.24	1.46	0.53	-3.99	0.22	-1.43	0.56	-6.13	1.01
G110.21+2.63smmb	0.27	6.47	0.24	5.29	1.39	4.22	0.07	2.72	0.38	0.44	0.06	-5.37	1.67	-8.25	0.01	-3.98	1.38	-9.50	1.39
G111.28-0.66smma	1.83	4.57	0.55	11.10	1.57	4.07	0.29	3.75	0.21	1.26	0.51	2.10	0.14	-3.66	0.11	-1.27	0.54	-5.71	1.28
G133.95+1.06	0.09	4.26	0.78	15.17	1.32	4.23	0.39	4.22	0.27	1.16	0.65	2.04	0.25	-3.74	0.27	-1.33	0.40	-5.34	0.59
G138.30+1.56	0.19	4.35	0.48	13.96	3.82	4.06	0.22	4.03	0.12	1.42	0.44	2.64	0.28	-2.97	0.13	-2.14	0.43	-6.18	0.55
G213.88-11.84	0.42	4.60	0.66	9.00	2.16	3.90	0.23	3.35	0.36	1.37	0.38	1.25	0.87	-4.12	0.32	-1.70	1.32	-6.66	1.55

Appendix C

AFGL 437: List of Class II sources; SED modeling of selected sources

Table C.1: *Spitzer*-IRAC 4-channel photometry (in mag) of the Class II sources in the AFGL 437 region

id	RA [2000]	Dec [2000]	Ch1	Ch2	Ch3	Ch4	α_{IRAC}
1	3:06:41.46	58:27:56.7	13.80	13.69	13.64	13.02	-1.99
2	3:06:43.92	58:42:41.9	13.52	13.51	13.74	13.12	-2.46
3	3:07:08.50	58:28:33.8	9.90	9.85	9.70	9.11	-1.93
4	3:07:10.39	58:29:28.5	12.61	12.57	12.33	11.70	-1.77
5	3:07:12.87	58:34:47.6	13.82	13.78	13.31	12.38	-1.12
6	3:07:13.60	58:28:31.6	12.39	12.29	12.23	11.44	-1.78
7	3:07:17.35	58:30:47.8	12.96	12.84	11.56	10.74	-0.06
8	3:07:22.61	58:31:40.7	12.21	11.94	11.91	10.95	-1.48
9	3:07:29.07	58:30:09.2	12.00	11.77	11.52	10.71	-1.38
10	3:07:31.11	58:41:59.4	13.66	13.60	13.94	13.48	-2.74
11	3:07:31.65	58:27:03.4	14.30	14.21	14.20	13.65	-2.14
12	3:07:31.80	58:31:31.3	12.34	12.34	12.46	11.81	-2.29
13	3:07:32.86	58:39:28.7	13.76	13.69	13.15	12.07	-0.84
14	3:07:33.45	58:28:53.9	11.77	11.65	11.71	11.29	-2.34
15	3:07:35.02	58:31:25.4	11.41	11.02	10.73	10.19	-1.46
16	3:07:35.48	58:33:40.0	13.53	13.43	13.12	12.58	-1.72
17	3:07:35.80	58:30:11.5	13.22	13.05	13.22	12.34	-1.94
18	3:07:37.02	58:29:40.7	13.01	12.70	12.57	11.81	-1.52
19	3:07:40.69	58:28:23.0	12.87	12.73	12.47	11.59	-1.38
20	3:07:43.32	58:28:35.3	14.13	13.84	13.62	12.85	-1.40
21	3:07:43.51	58:37:51.4	14.19	14.14	13.88	13.43	-1.94
22	3:07:45.03	58:28:49.4	13.69	13.52	13.53	12.71	-1.78
23	3:07:45.66	58:29:54.7	13.35	13.32	13.19	12.36	-1.72
24	3:07:57.05	58:27:38.1	13.97	13.79	13.64	12.82	-1.55
25	3:07:57.13	58:36:23.3	13.91	13.87	13.80	13.14	-1.98
26	3:08:05.58	58:36:26.3	13.59	13.58	13.87	13.38	-2.69
27	3:08:06.89	58:42:55.5	13.32	13.27	13.56	12.83	-2.39
28	3:08:17.06	58:30:38.8	11.21	10.85	10.56	9.67	-1.11
29	3:08:21.57	58:29:46.8	13.34	13.19	13.23	12.80	-2.28
30	3:08:22.25	58:38:17.6	13.80	13.77	13.61	12.94	-1.85
31	3:08:22.71	58:38:51.8	13.58	13.52	13.51	13.04	-2.25
32	3:08:31.97	58:41:24.2	13.20	13.06	13.21	12.81	-2.47
33	3:08:36.15	58:29:02.0	13.55	13.55	13.61	13.16	-2.43
34	3:08:39.09	58:31:05.8	13.57	13.19	12.74	11.86	-0.88
35	3:08:41.66	58:29:12.8	13.66	13.56	13.56	12.89	-2.00
36	3:08:45.97	58:37:25.7	14.53	14.42	13.68	13.01	-0.98
37	3:08:50.93	58:34:22.3	14.11	14.08	14.10	13.45	-2.12
38	3:08:57.79	58:25:44.2	14.41	14.12	13.98	12.88	-1.16
39	3:08:59.55	58:35:25.8	13.19	13.15	13.23	12.80	-2.44
40	3:08:59.99	58:32:19.5	14.91	14.60	14.35	13.57	-1.33
41	3:09:00.13	58:33:18.6	12.91	12.83	12.88	12.41	-2.32
42	3:09:00.66	58:32:23.4	14.50	14.28	13.84	13.14	-1.24
43	3:09:01.39	58:27:32.5	14.43	14.25	13.94	13.30	-1.53
44	3:09:04.73	58:41:52.0	13.27	13.23	13.49	13.01	-2.63
45	3:06:39.09	58:29:47.8	13.55	12.99	12.54	11.71	-0.75
46	3:07:14.77	58:31:09.4	13.35	12.66	12.04	11.27	-0.46
47	3:07:20.80	58:30:39.0	11.92	11.13	10.72	9.73	-0.42
48	3:07:31.66	58:30:54.3	12.70	12.19	11.86	11.44	-1.42
49	3:07:33.53	58:30:49.3	13.32	12.89	12.59	12.03	-1.39
50	3:07:36.64	58:29:46.9	14.24	13.77	13.19	12.42	-0.74
51	3:07:41.22	58:30:48.1	12.31	11.71	11.41	10.44	-0.77
52	3:08:51.38	58:32:59.8	13.88	13.34	13.29	12.69	-1.58

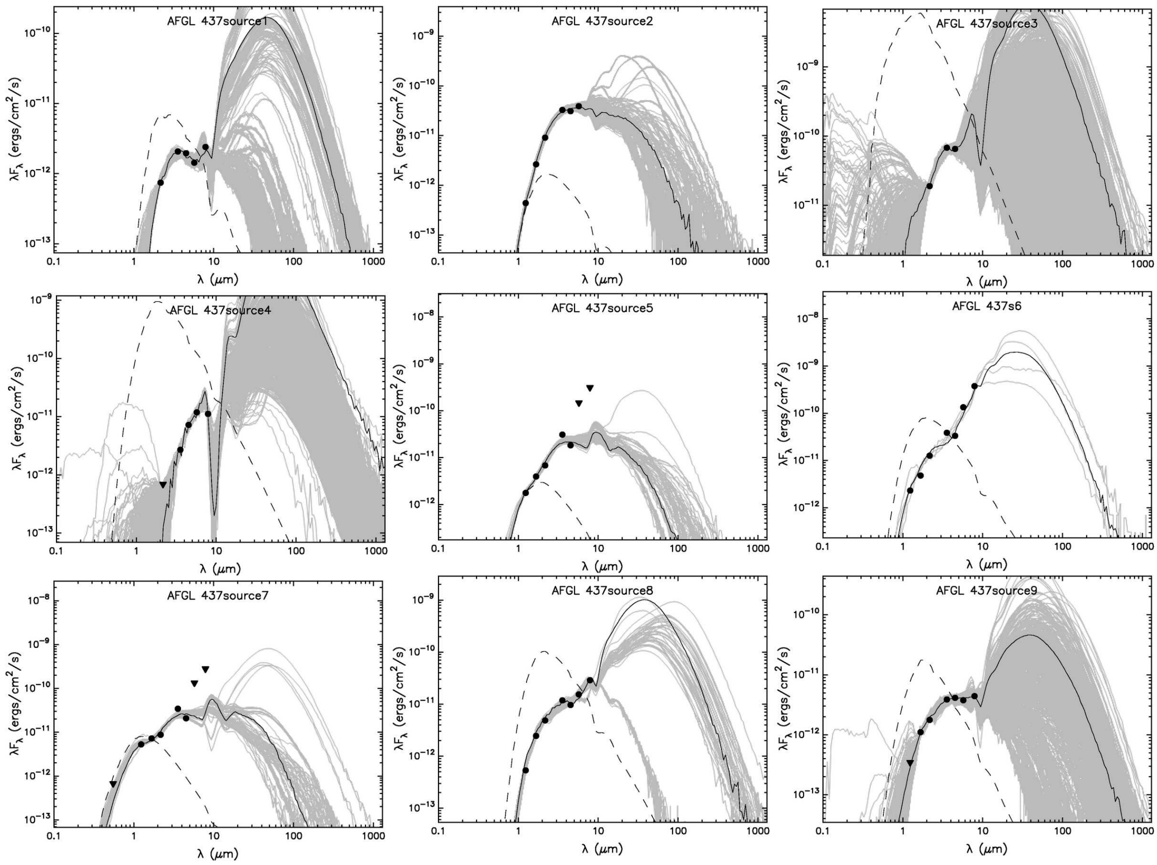

Fig. C.1: SED model plots of s1-s9 sources (from Table 3.1) and details of the plots are the same as in Fig A.5.

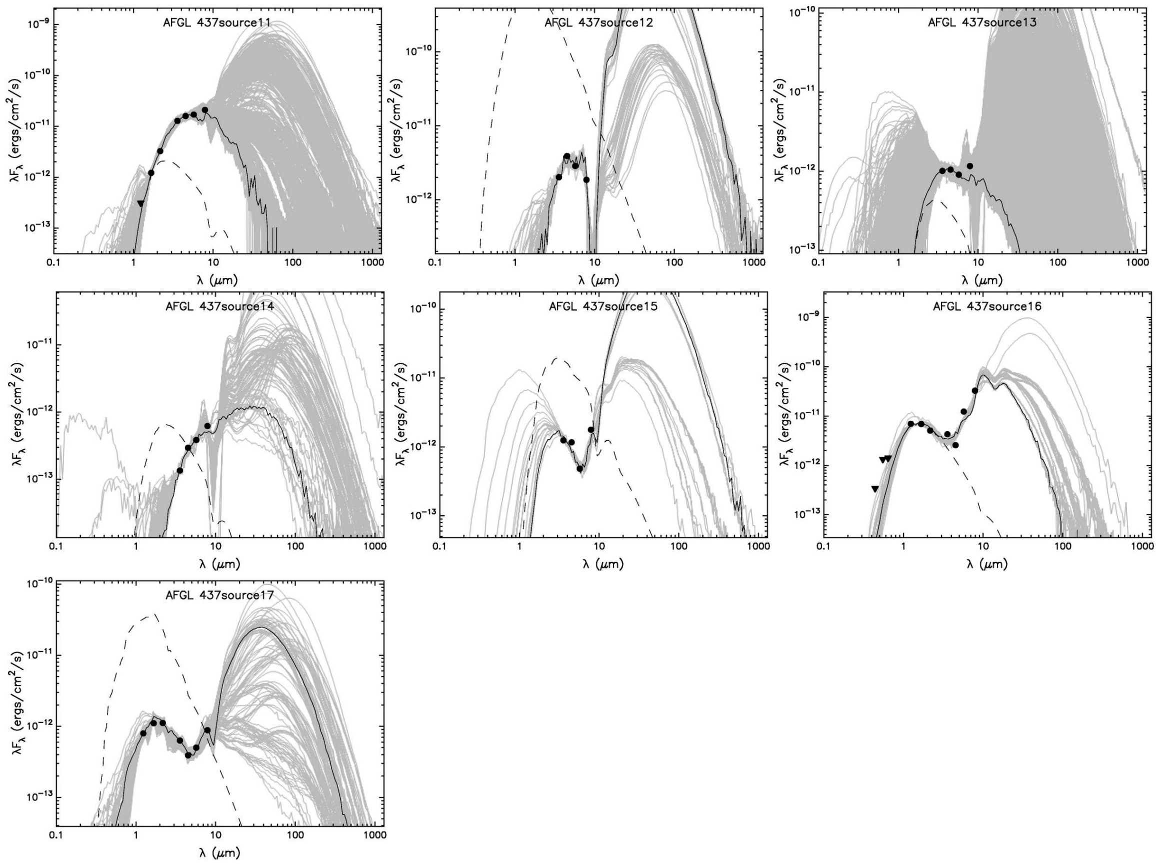

Fig. C.2: SED model plots of s10-s17 (from Table 3.1) and details of the plots are the same as in Fig A.5.

Table C.2: Physical parameters derived from SED modeling of the 17 sources (s1-s17). Weighted mean and standard deviation of each physical parameters are shown in the table. (see Chapter 3 for detail)

Source	M_* $M_\odot$		L_* $\log(L_\odot)$		Age $\log(yr)$		T_* $\log(K)$		$\dot{M}_{env}$ $\log(M_\odot\ yr^{-1})$		M_{disk} $\log(M_\odot)$		$\dot{M}_{disk}$ $\log(M_\odot\ yr^{-1})$		M_{env} $\log(M_\odot)$	
s1	2.83	1.09	1.75	0.45	6.11	0.93	3.92	0.22	-4.83	0.61	-5.02	2.09	-10.68	2.21	-4.05	2.74
s2	4.77	1.51	2.54	0.45	6.44	0.28	4.17	0.10	-6.72	0.76	-4.53	1.74	-9.84	1.89	-5.45	2.39
s3	6.15	1.95	2.84	0.42	5.86	0.86	4.10	0.25	-5.23	2.09	-3.46	1.80	-8.68	1.92	-3.09	3.55
s4	2.68	2.35	1.74	0.59	4.02	0.68	3.62	0.07	-4.55	0.72	-1.93	0.76	-6.50	1.10	-0.12	1.24
s5	3.46	0.61	2.06	0.24	6.62	0.26	4.10	0.06	-5.05	0.15	-3.77	1.39	-9.26	1.41	-6.04	1.59
s6	7.70	1.55	3.32	0.39	5.66	0.44	4.21	0.19	-5.03	0.40	-2.57	1.29	-7.68	0.83	-0.34	2.18
s7	3.44	0.48	2.05	0.18	6.58	0.40	4.08	0.10	-4.65	0.83	-3.35	1.38	-8.93	1.36	-5.77	2.03
s8	3.27	2.07	2.02	0.63	4.99	0.98	3.81	0.27	-4.16	0.98	-3.21	2.08	-8.41	2.59	-1.71	3.07
s9	1.95	1.23	1.28	0.46	5.50	1.04	3.74	0.19	-5.50	1.84	-3.07	1.73	-8.40	1.96	-3.01	2.68
s10	6.35	2.12	2.76	0.50	4.47	0.78	3.80	0.25	-4.32	0.26	-1.92	0.67	-6.54	1.18	0.56	1.38
s11	3.77	1.90	2.13	0.60	5.78	1.03	3.95	0.27	-5.00	2.07	-3.45	1.97	-8.71	2.19	-4.09	3.16
s12	2.74	2.27	1.58	0.64	4.93	0.47	3.65	0.06	-4.37	0.50	-2.20	0.87	-7.65	1.20	0.15	0.92
s13	1.79	0.90	1.07	0.53	5.93	0.88	3.78	0.20	-5.83	2.04	-4.65	2.06	-10.22	2.06	-4.37	2.79
s14	1.03	1.24	0.75	0.69	4.49	1.27	3.61	0.21	-5.17	1.31	-2.81	0.79	-7.55	1.18	-2.16	2.51
s15	2.87	1.22	1.63	0.36	6.32	0.84	3.88	0.14	-4.90	0.23	-2.95	1.70	-8.75	1.72	-3.83	2.53
s16	3.66	0.75	2.16	0.27	6.50	0.27	4.10	0.08	-5.15	0.10	-3.55	1.10	-9.44	1.24	-5.06	2.22
s17	0.75	0.68	0.46	0.48	4.99	1.00	3.57	0.08	-5.75	2.00	-2.61	0.74	-7.59	1.11	-2.78	2.72

Appendix D

M8: IRAC images, YSO lists and YSO selection criteria

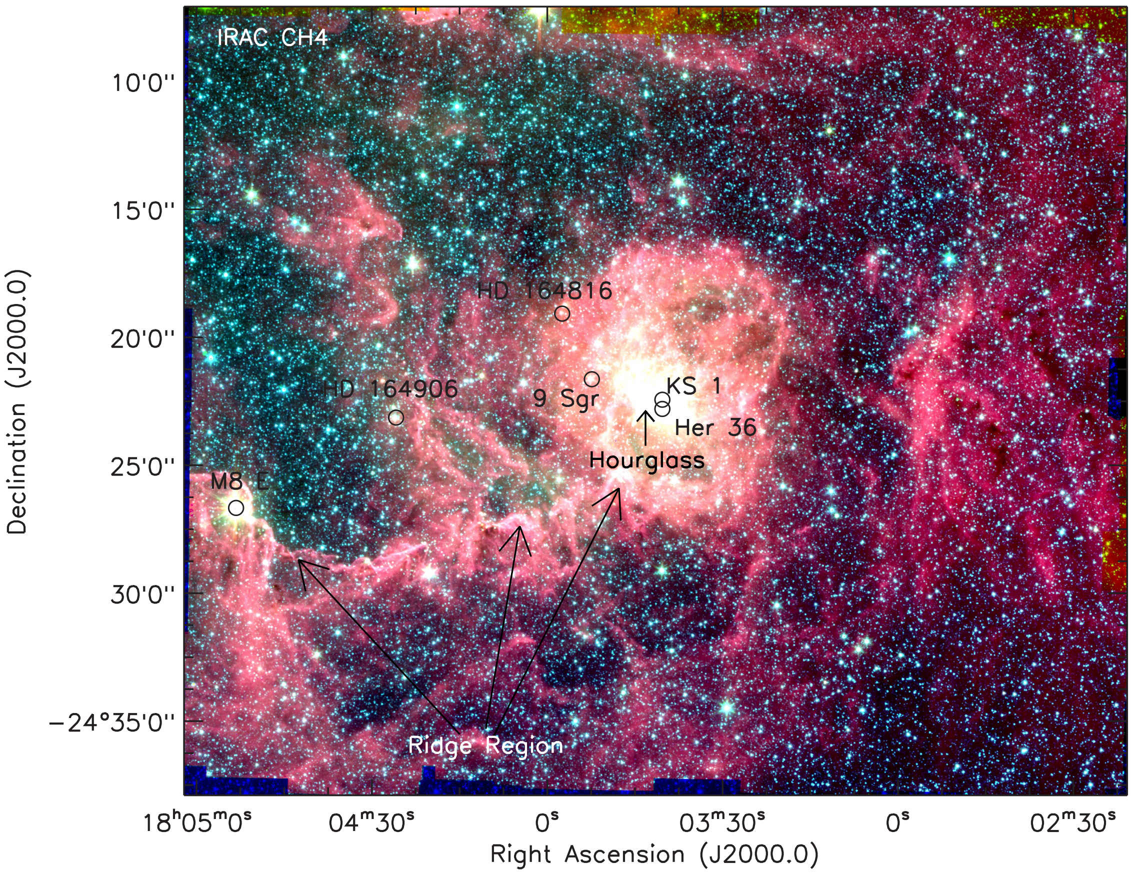

Fig. D.1: IRAC 3-colour-composite image (3.6 (blue), 4.5 (green) and 8.0 μm (red)) of the entire M8 region ($\sim 42.5 \times 30.0$ arcmin^2) available in *Spitzer* archives (see more details in the caption of Fig 4.1).

D.1 Criteria for the selection of contaminations:

The following gives the selection criteria for various possible contaminations, based on IRAC colour indices (see Gutermuth et al. (2009) for more details):

a) PAH Galaxies:

$$[4.5] - [5.8] < \frac{1.05}{1.2} \times ([5.8] - [8.0] - 1)$$

&

$$[4.5] - [5.8] < 1.05$$

&

$$[5.8] - [8.0] > 1$$

&

$$[4.5] > 11.5$$

Another set of conditions for **PAH galaxies**, in addition to above mentioned conditions, is the following:

$$[3.6] - [5.8] < \frac{1.5}{2} \times ([4.5] - [8.0] - 1)$$

&

$$[3.6] - [5.8] < 1.5$$

&

$$[4.5] - [8.0] > 1$$

&

$$[4.5] > 11.5$$

b) AGNs:

$$[4.5] - [8.0] > 0.5$$

&

$$[4.5] > 13.5 + ([4.5] - [8.0] - 2.3)/0.4$$

&

$$[4.5] > 13.5$$

In addition, one needs to consider any one of the following conditions along with the above mentioned conditions:

$$[4.5] > 14 + ([4.5] - [8.0] - 0.5)$$

OR

$$[4.5] > 14.5 - ([4.5] - [8.0] - 1.2)/0.3$$

OR

$$[4.5] > 14.5$$

c) Shocked Emission:

$$[3.6] - [4.5] > \frac{1.2}{0.55} \times ((([4.5] - [5.8]) - 0.3) + 0.8$$

&

$$[4.5] - [5.8] \leqslant 0.85$$

&

$$[3.6] - [4.5] > 1.05$$

d) PAH-emission aperture:

$$[3.6] - [4.5] \leqslant 1.4 \times ((([4.5] - [5.8]) - 0.7) + 0.15$$

&

$$[3.6] - [4.5] \leqslant 1.65$$

D.2 Criteria for the YSO selection:

Once the above mentioned contaminations are removed from the sources then the YSOs can be identified using the following criteria (see Gutermuth et al. (2009) for more details):

$$[4.5] - [8.0] > 0.5$$

&

$$[3.6] - [5.8] > 0.35$$

&

$$[3.6] - [5.8] \leqslant \frac{0.14}{0.04} \times (([4.5] - [8.0]) - 0.5) + 0.5$$

&

$$[3.6] - [4.5] > 0.15$$

D.3 Criteria for the "Red sources":

Additionally, the "Red sources" that include AGB stars may be removed from the YSO list following the criteria give below (see Robitaille et al. (2008)):

$$13.89 \geqslant [4.5] \geqslant 6.50$$

&

$$9.52 \geqslant [8.0] \geqslant 4.01$$

&

$$[4.5] - [8.0] \geqslant 1$$

Table D.1: *Spitzer*-IRAC 4-channel photometry (in mag) of the Class 0/I YSOs identified in the M8 (see text for details); the JHK photometry is taken from literature with the numbers in the last column referring to: 1. 2MASS; 2. Arias et al. (2006); 3. Arias et al. (2007)

Object	RA [2000]	Dec [2000]	Ch1	Ch2	Ch3	Ch4	α_{IRAC}	H	J-H	H-K	NIR Ref.
1	18:02:25.56	-24:32:41.7	12.63	11.88	10.87	9.76	0.51				
2	18:02:29.28	-24:08:15.8	5.79	5.12	4.41	3.45	-0.15	9.46	3.16	1.96	1
3	18:02:42.07	-24:19:13.2	12.19	10.63	9.54	8.62	1.20				
4	18:02:42.97	-24:23:25.5	11.28	10.13	9.28	8.33	0.51				
5	18:02:49.71	-24:22:26.6	11.36	9.90	9.13	8.82	-0.01				
6	18:02:52.85	-24:20:46.6	11.52	10.27	9.54	8.85	0.15				
7	18:02:53.21	-24:20:17.3	8.91	8.31	7.82	5.94	0.49	9.79	0.16	0.19	1
8	18:03:06.89	-24:20:57.6	11.08	10.29	9.52	8.24	0.40				
9	18:03:06.99	-24:21:20.1	8.78	7.87	6.86	5.94	0.46				
10	18:03:11.64	-24:11:57.0	6.63	5.57	4.28	3.41	0.94				
11	18:03:12.28	-24:33:30.5	8.12	7.13	6.16	5.88	-0.22				
12	18:03:25.59	-24:21:08.3	10.88	10.21	9.42	8.55	-0.13				
13	18:03:27.38	-24:21:04.0	11.81	9.98	9.08	8.63	0.69				
14	18:03:29.22	-24:21:49.9	10.34	9.89	9.05	7.80	0.13	13.27	1.44	1.08	1
15	18:03:30.84	-24:20:03.1	11.73	9.94	8.63	7.36	2.12				
16	18:03:35.58	-24:22:04.6	11.86	10.75	9.51	7.37	2.31				
17	18:03:36.21	-24:18:13.7	9.87	8.67	7.91	7.11	0.27				
18	18:03:36.28	-24:17:51.1	8.75	7.66	6.68	5.53	0.85				
19	18:03:37.05	-24:22:31.6	10.34	9.36	8.25	7.06	0.96	13.87	1.13	0.98	1,2
20	18:03:37.41	-24:13:56.9	4.64	4.04	3.09	2.43	-0.21	6.83	1.95	1.28	1
21	18:03:37.74	-24:25:30.3	11.24	10.18	9.47	8.17	0.61				
22	18:03:38.31	-24:33:59.8	11.71	10.59	9.67	8.56	0.75				
23	18:03:38.65	-24:22:24.3	9.00	7.90	6.96	5.22	1.45	12.52	1.01	0.92	1,2,3
24(KS 1)	18:03:40.37	-24:22:38.6	6.19	5.29	4.46	2.51	1.34	10.61	1.63	1.08	2
25(Her 36)	18:03:40.43	-24:22:43.6	5.42	4.72	3.86	2.27	0.79	7.45	0.49	0.54	1,2
26(KS 4)	18:03:41.50	-24:22:44.3	9.36	8.58	—	—	—	12.99	2.17	1.46	2
27	18:03:44.95	-24:16:08.7	11.13	10.66	9.88	8.58	0.13				
28	18:03:45.16	-24:23:25.0	8.88	8.20	7.54	6.24	0.18	11.36	1.30	0.92	2,3
29	18:03:47.05	-24:25:37.4	8.45	7.86	6.95	6.08	-0.05	11.81	1.74	1.37	1
30	18:03:47.37	-24:18:44.4	8.73	8.16	7.29	6.33	-0.03				
31	18:03:47.47	-24:25:34.5	8.73	7.87	6.99	6.13	0.16				
32	18:03:48.44	-24:26:32.0	9.77	8.64	7.75	7.29	0.00				
33	18:03:48.47	-24:25:58.6	10.47	9.09	8.40	7.66	0.28				
34	18:03:50.26	-24:22:23.4	10.03	9.54	8.95	7.80	-0.28	11.96	0.85	0.56	1
35	18:03:54.23	-24:25:33.3	10.15	9.40	8.28	6.88	0.98	13.27	1.72	1.04	1
36	18:04:05.11	-24:16:42.3	10.80	10.04	9.56	8.43	-0.19	12.59	0.83	0.32	1
37	18:04:08.81	-24:27:27.5	10.36	9.54	8.90	8.11	-0.28				
38	18:04:10.55	-24:26:56.1	9.00	8.32	7.84	6.59	-0.13	11.10	0.99	0.62	1,3
39	18:04:11.03	-24:27:20.5	11.66	9.48	8.11	7.10	2.29				
40	18:04:11.07	-24:21:31.5	6.56	5.72	4.83	3.96	0.17				
41	18:04:11.08	-24:26:54.2	10.07	8.46	7.35	6.39	1.33				
42	18:04:17.06	-24:28:10.9	11.32	10.62	9.87	8.72	0.15	13.67	1.13	0.65	1
43	18:04:20.09	-24:29:14.7	5.56	4.33	2.95	2.77	0.46				
44	18:04:20.74	-24:28:22.1	10.06	9.35	8.57	7.50	0.11	13.03	1.87	1.20	1
45	18:04:20.95	-24:21:07.9	11.40	10.78	10.44	9.01	-0.19	13.10	1.06	0.56	1

Table D.1: contd.

Object	RA [2000]	Dec [2000]	Ch1	Ch2	Ch3	Ch4	α_{IRAC}	H	J-H	H-K	NIR Ref.
46	18:04:21.24	-24:28:03.5	9.86	9.45	8.60	7.39	0.07	12.49	1.31	0.88	1,3
47	18:04:21.63	-24:11:26.3	9.33	8.68	7.92	7.08	-0.23	12.61	2.35	1.51	1
48	18:04:21.70	-24:21:14.6	11.47	10.98	10.29	9.05	-0.04				
49	18:04:23.98	-24:21:27.0	9.19	8.79	8.30	6.58	0.12	9.25	0.07	0.03	1
50	18:04:24.31	-24:20:59.7	9.45	9.17	8.49	6.82	0.20	9.83	0.04	0.01	1
51	18:04:26.52	-24:29:00.3	9.72	9.30	8.59	7.36	-0.09	11.82	1.04	0.50	1
52	18:04:28.09	-24:22:41.8	11.25	10.82	10.10	8.89	-0.10				
53	18:04:28.90	-24:14:02.6	8.46	8.05	7.30	6.06	-0.04	10.19	0.42	0.32	1
54	18:04:30.74	-24:28:45.6	6.75	6.02	5.34	4.27	-0.01	10.52	1.99	1.49	1
55	18:04:35.78	-24:28:35.6	9.03	8.44	7.71	6.74	-0.19				
56	18:04:40.67	-24:12:16.9	11.06	10.66	9.96	8.78	-0.19	13.01	1.06	0.52	1
57	18:04:44.19	-24:15:25.1	10.67	10.25	9.57	8.32	-0.11	12.01	0.91	0.37	1
58	18:04:47.09	-24:27:55.4	9.05	8.08	7.36	6.51	0.04				
59	18:04:48.42	-24:27:53.8	10.99	10.66	9.92	8.64	-0.09				
60	18:04:50.37	-24:14:25.8	5.02	4.27	3.29	2.31	0.32				
61	18:04:50.62	-24:25:42.2	8.73	8.11	7.67	5.87	0.36	10.16	0.29	0.43	3
62	18:04:51.13	-24:26:33.7	9.48	9.03	8.52	6.93	0.05	12.68	1.95	1.13	1
63	18:04:56.77	-24:27:16.4	10.30	9.24	8.44	7.56	0.27				
64	18:04:58.82	-24:26:24.1	9.54	8.47	7.82	6.89	0.13				
65	18:05:00.47	-24:13:26.8	9.51	8.88	8.25	6.94	0.08	10.89	0.62	0.37	1

Table D.2: *Spitzer*-IRAC 4-channel photometry (in mag) of the Class II YSOs identified in the M8 (see text for details); the JHK photometry is taken from literature with the numbers in the last column referring to: 1. 2MASS; 2. Arias et al. (2006); 3. Arias et al. (2007)

Object	RA [2000]	Dec [2000]	Ch1	Ch2	Ch3	Ch4	α_{IRAC}	H	J-H	H-K	NIR Ref.
1	18:02:23.78	-24:08:49.4	10.76	10.41	10.04	9.26	-1.13	12.29	0.94	0.42	1
2	18:02:24.95	-24:36:08.4	7.92	7.57	7.12	6.86	-1.59	9.59	2.31	1.02	1
3	18:02:25.98	-24:27:31.8	6.83	6.25	5.59	4.74	-0.42	11.46	3.65	2.14	1
4	18:02:27.52	-24:22:52.9	8.12	7.53	6.69	6.49	-0.88				
5	18:02:27.65	-24:11:38.0	11.53	11.20	10.43	9.70	-0.66				
6	18:02:29.49	-24:24:53.7	10.58	10.05	9.81	8.97	-1.07	12.71	1.08	0.69	1
7	18:02:36.33	-24:21:07.9	8.10	7.83	7.23	6.94	-1.43	11.15	3.46	1.78	1
8	18:02:37.34	-24:16:24.4	10.40	9.98	9.55	8.86	-1.08	12.47	0.92	0.56	1
9	18:02:41.45	-24:10:35.3	8.26	7.91	7.36	7.20	-1.56	10.85	3.13	1.48	1
10	18:02:41.65	-24:33:55.0	7.92	7.55	6.94	6.11	-0.73	9.60	2.07	0.93	1
11	18:02:42.67	-24:17:18.9	6.34	6.06	5.42	4.88	-1.09				
12	18:02:43.91	-24:15:23.1	10.71	10.26	9.85	9.03	-0.93	12.55	0.77	0.56	1
13	18:02:45.65	-24:13:49.7	8.47	7.92	7.53	7.24	-1.44	10.85	2.89	1.47	1
14	18:02:48.85	-24:21:08.8	9.56	9.24	8.87	7.88	-0.92	12.34	0.84	0.62	1
15	18:02:49.10	-24:28:15.8	7.32	6.91	6.47	6.13	-1.46	10.59	2.99	1.62	1
16	18:02:49.15	-24:08:52.3	6.50	6.04	5.73	4.96	-1.12	9.75	2.88	1.59	1
17	18:02:49.33	-24:11:19.0	5.80	5.34	5.00	4.63	-1.51	9.30	2.55	1.47	1
18	18:02:50.81	-24:17:56.6	9.95	9.29	9.03	8.29	-1.02	12.50	1.43	0.95	1
19	18:02:50.95	-24:22:20.1	10.65	10.21	9.83	8.82	-0.76				
20	18:02:51.10	-24:19:23.4	9.59	9.20	8.84	8.02	-1.05	12.64	1.32	0.95	1
21	18:02:51.12	-24:16:57.2	5.29	4.20	3.38	3.18	-0.43				
22	18:02:51.15	-24:18:07.9	10.45	9.78	9.50	8.74	-0.96	12.95	0.96	0.71	1
23	18:02:51.39	-24:17:13.3	9.48	9.15	8.59	8.26	-1.38				
24	18:02:52.47	-24:18:44.7	8.56	8.14	7.64	6.78	-0.79	10.72	0.90	0.75	1
25	18:02:53.83	-24:20:19.8	9.22	8.68	8.60	7.92	-1.45				
26	18:02:53.96	-24:20:11.3	9.97	9.51	9.16	8.41	-1.09	12.61	1.29	1.00	1
27	18:02:54.30	-24:20:56.5	8.85	8.35	8.01	7.20	-0.99	11.23	0.92	0.77	1
28	18:02:54.72	-24:19:56.9	9.57	9.14	8.75	8.47	-1.57				
29	18:02:56.79	-24:23:34.8	10.17	9.89	9.62	8.98	-1.49	12.32	2.42	1.10	1
30	18:02:56.88	-24:35:40.7	8.08	7.79	7.28	7.04	-1.59	10.20	2.84	1.29	1
31	18:03:01.50	-24:27:47.1	10.53	10.13	9.47	8.48	-0.45	12.93	1.70	0.90	1
32	18:03:05.14	-24:31:54.2	5.57	5.16	4.61	3.81	-0.80				
33	18:03:06.56	-24:32:13.1	5.60	4.96	4.44	3.56	-0.53	8.46	2.91	1.63	1
34	18:03:09.96	-24:33:50.4	8.10	7.50	6.97	6.67	-1.19	10.79	2.63	1.38	1
35	18:03:10.31	-24:26:59.5	6.49	5.89	5.43	4.59	-0.69	10.50	2.93	1.92	1
36	18:03:17.69	-24:20:53.2	10.74	10.25	9.77	8.93	-0.77	12.20	1.08	0.45	1
37	18:03:18.30	-24:25:58.7	8.19	7.44	6.70	6.20	-0.53	10.30	2.58	1.45	1
38	18:03:20.03	-24:20:20.4	10.45	10.21	9.81	9.05	-1.21	12.45	2.12	0.99	1
39	18:03:20.53	-24:30:29.8	5.27	5.09	4.69	4.18	-1.54	8.31	2.35	1.44	1
40	18:03:23.06	-24:23:41.8	7.03	6.61	6.22	5.82	-1.45	11.43	2.97	1.82	1
41	18:03:23.09	-24:21:33.1	9.80	9.53	8.88	8.65	-1.42				
42	18:03:24.06	-24:21:23.3	8.58	7.94	7.17	6.95	-0.91				
43	18:03:25.06	-24:19:02.2	8.07	7.72	7.07	6.93	-1.44	10.34	3.06	1.45	1
44	18:03:25.12	-24:21:28.4	11.06	10.06	9.49	8.85	-0.36				
45	18:03:26.71	-24:22:11.3	8.91	8.68	8.27	7.22	-0.88				

Table D.2: contd.

Object	RA [2000]	Dec [2000]	Ch1	Ch2	Ch3	Ch4	α_{IRAC}	H	J-H	H-K	NIR Ref.
46	18:03:34.15	-24:24:59.7	8.17	7.83	7.19	7.07	-1.50	10.50	2.96	1.44	1
47	18:03:34.74	-24:18:53.7	6.44	6.20	5.68	5.32	-1.50	10.57	3.94	2.21	1
48	18:03:35.86	-24:09:11.9	9.61	8.85	8.82	7.90	-1.04	11.63	0.91	0.64	1
49	18:03:36.29	-24:09:48.2	6.11	5.74	5.31	4.38	-0.85	10.88	2.82	1.78	1
50	18:03:36.68	-24:10:32.6	8.59	8.39	8.00	7.52	-1.58	10.50	2.04	0.86	1
51	18:03:36.84	-24:24:15.1	10.23	9.71	9.39	8.20	-0.58	12.26	0.89	0.37	1
52	18:03:37.32	-24:22:46.9	9.01	8.44	7.99	6.88	-0.44	11.47	1.34	0.66	2
53	18:03:38.49	-24:22:31.7	8.81	8.11	7.57	6.63	-0.38	10.80	1.22	0.80	1,2
54	18:03:38.81	-24:08:58.8	5.43	5.08	4.59	3.86	-1.02	8.58	2.92	1.55	1
55	18:03:39.05	-24:28:10.8	8.16	7.74	7.09	6.81	-1.23	9.97	2.41	1.11	1
56	18:03:39.38	-24:25:24.2	9.54	9.06	8.54	7.38	-0.37	11.85	1.14	0.69	1
57	18:03:40.23	-24:22:03.8	9.54	9.15	8.74	7.84	-0.90	11.66	1.31	0.63	1
58	18:03:40.24	-24:29:08.2	5.05	4.51	3.84	2.93	-0.38	8.93	2.76	1.92	1
59	18:03:40.33	-24:25:05.2	10.39	9.78	9.54	8.58	-0.86	12.25	1.04	0.54	1
60	18:03:40.74	-24:23:16.3	8.67	8.29	7.83	6.87	-0.77	11.24	1.10	0.80	1,2,3
61	18:03:41.05	-24:25:45.6	8.54	8.21	7.73	7.23	-1.30				
62	18:03:42.26	-24:23:22.4	9.68	9.10	8.70	7.76	-0.69	12.48	1.40	0.94	1,2
63	18:03:42.89	-24:16:26.4	8.17	7.79	7.21	7.03	-1.47	9.83	2.26	1.07	1
64	18:03:43.09	-24:21:29.6	8.49	8.29	7.87	7.08	-1.20	10.84	2.75	1.25	1
65	18:03:43.29	-24:28:07.1	8.14	7.90	7.19	7.09	-1.52	10.13	2.62	1.29	1
66	18:03:45.07	-24:22:05.6	8.61	8.45	8.15	6.37	-0.30	9.13	0.11	0.10	1,2
67	18:03:47.93	-24:18:02.1	9.05	8.45	8.00	7.37	-0.94	12.65	1.94	1.43	1
68	18:03:49.38	-24:26:14.6	8.47	8.04	7.42	7.27	-1.40				
69	18:03:49.61	-24:22:09.3	10.85	10.36	9.99	8.85	-0.59	12.65	0.99	0.42	1
70	18:03:50.73	-24:20:13.3	9.81	9.57	9.31	8.44	-1.29				
71	18:03:50.79	-24:21:10.9	6.46	6.14	5.61	4.60	-0.68	9.21	0.86	0.85	1,3
72	18:03:51.65	-24:28:26.7	9.51	9.21	8.91	8.12	-1.25	11.58	0.80	0.64	1
73	18:03:53.05	-24:14:51.6	8.17	7.59	7.17	6.89	-1.38				
74	18:03:57.82	-24:20:51.3	10.21	9.67	9.43	8.52	-0.97				
75	18:03:57.84	-24:25:34.9	6.09	5.54	5.09	4.25	-0.76	8.84	0.94	0.83	1
76	18:03:58.29	-24:16:49.3	9.95	9.26	8.95	8.10	-0.81	12.24	1.02	0.71	1,3
77	18:03:58.54	-24:24:58.8	9.66	9.31	8.90	8.18	-1.14	11.24	0.87	0.41	1
78	18:03:59.27	-24:23:08.2	9.01	8.79	8.59	7.76	-1.44	11.16	1.24	0.93	1
79	18:04:01.13	-24:22:35.6	10.49	10.30	9.93	8.96	-1.06	12.33	2.19	0.99	1
80	18:04:03.10	-24:25:19.5	9.53	9.17	8.70	7.60	-0.63	11.72	0.66	0.58	1
81	18:04:04.65	-24:08:49.8	8.03	7.69	7.13	6.92	-1.51	9.89	2.31	1.12	1
82	18:04:07.89	-24:26:06.3	10.69	10.27	9.69	8.55	-0.37				
83	18:04:08.11	-24:20:55.6	10.90	10.39	10.04	9.04	-0.75	13.03	1.00	0.47	1
84	18:04:08.47	-24:20:49.5	10.76	10.44	10.08	8.93	-0.76	12.39	0.93	0.38	1
85	18:04:09.94	-24:25:32.7	9.72	9.27	9.02	8.20	-1.15	11.15	0.94	0.38	1
86	18:04:10.19	-24:25:49.6	9.09	8.62	8.20	7.27	-0.78	11.80	1.17	0.69	1
87	18:04:11.57	-24:28:42.1	12.10	11.85	11.11	10.95	-1.40				
88	18:04:11.99	-24:26:28.1	10.18	9.57	9.07	8.18	-0.57	11.81	0.96	0.43	1
89	18:04:12.48	-24:11:51.6	10.83	10.10	9.70	8.67	-0.44	12.83	1.00	0.73	1
90	18:04:12.52	-24:35:47.1	8.15	7.83	7.43	7.07	-1.58	9.39	2.02	0.81	1

Table D.2: contd.

Object	RA [2000]	Dec [2000]	Ch1	Ch2	Ch3	Ch4	α_{IRAC}	H	J-H	H-K	NIR Ref.
91	18:04:13.10	-24:26:13.3	10.88	10.43	9.90	8.80	-0.46	12.38	0.99	0.43	1
92	18:04:15.75	-24:19:01.7	10.07	9.80	9.64	8.80	-1.43	11.71	0.80	0.41	1,3
93	18:04:15.77	-24:25:15.8	10.71	10.17	9.79	9.09	-1.02				
94	18:04:15.91	-24:18:46.2	10.05	9.35	9.12	8.48	-1.13	12.44	1.11	0.81	1,3
95	18:04:16.06	-24:27:57.4	10.05	9.70	9.34	8.79	-1.40				
96	18:04:16.14	-24:19:52.5	9.41	8.86	8.44	7.45	-0.63	11.45	0.92	0.62	1
97	18:04:16.41	-24:24:38.8	9.67	9.17	8.79	7.74	-0.67	11.88	1.10	0.78	1,3
98	18:04:16.93	-24:24:14.9	9.16	8.75	8.38	7.84	-1.33	10.96	0.70	0.38	1
99	18:04:17.42	-24:19:09.8	8.83	8.42	8.00	7.53	-1.34	11.37	1.57	0.98	1,3
100	18:04:17.89	-24:17:46.8	10.39	9.84	9.60	8.44	-0.69	12.02	0.94	0.57	1
101	18:04:19.09	-24:27:58.8	10.28	9.70	9.17	8.18	-0.46	12.43	1.20	0.73	1
102	18:04:19.31	-24:22:54.9	9.95	9.60	9.33	8.70	-1.42	11.50	0.94	0.47	1,3
103	18:04:19.58	-24:24:04.7	9.00	8.77	8.37	7.81	-1.44	11.79	1.48	1.16	1
104	18:04:19.87	-24:28:23.7	9.45	8.86	8.46	7.73	-0.91				
105	18:04:20.07	-24:22:48.2	10.58	10.26	9.66	8.51	-0.44	12.09	0.89	0.83	3
106	18:04:20.26	-24:20:24.8	10.14	9.79	9.41	8.65	-1.14	12.32	1.04	0.73	1
107	18:04:20.34	-24:24:34.6	10.75	9.93	9.51	9.07	-0.96				
108	18:04:20.52	-24:23:04.1	9.96	9.48	8.97	8.12	-0.73				
109	18:04:20.61	-24:23:01.1	10.24	9.89	9.45	8.47	-0.81				
110	18:04:20.82	-24:23:22.5	10.33	9.92	9.68	8.88	-1.22	12.46	1.05	0.83	1
111	18:04:21.01	-24:13:41.8	5.42	5.01	4.51	3.69	-0.85	8.69	2.32	1.39	1
112	18:04:21.11	-24:23:25.5	10.08	9.81	9.42	8.66	-1.20				
113	18:04:21.12	-24:20:47.7	10.46	10.24	9.84	8.79	-0.91				
114	18:04:21.19	-24:24:22.4	10.39	9.96	9.55	8.89	-1.13				
115	18:04:21.47	-24:23:19.1	9.46	9.16	8.62	7.94	-1.05				
116	18:04:21.69	-24:23:19.7	9.75	9.27	8.63	7.75	-0.51				
117	18:04:21.82	-24:22:15.6	10.84	10.58	10.09	9.03	-0.74	13.02	0.91	0.52	1
118	18:04:21.84	-24:16:26.2	9.83	9.50	9.27	8.23	-1.05	11.67	0.89	0.49	1
119	18:04:21.86	-24:11:37.5	10.57	10.24	9.80	8.53	-0.51	11.77	0.51	0.22	1
120	18:04:22.77	-24:22:09.7	8.53	8.09	7.65	6.87	-0.95	8.86	0.22	0.30	1
121	18:04:23.05	-24:24:15.2	10.12	9.88	9.27	8.94	-1.40				
122	18:04:23.54	-24:22:47.6	9.69	9.15	8.76	8.46	-1.45				
123	18:04:24.23	-24:16:25.2	9.95	9.53	9.04	8.29	-0.94	12.71	1.47	1.01	1
124	18:04:26.15	-24:22:45.1	6.73	6.24	5.77	5.03	-0.90	10.23	1.65	1.27	1
125	18:04:26.75	-24:22:42.0	11.17	10.85	10.35	9.08	-0.43	13.08	1.09	0.62	1
126	18:04:26.84	-24:23:23.5	9.07	8.71	8.44	7.71	-1.30	11.30	0.88	0.66	1
127	18:04:27.09	-24:21:06.8	10.84	10.37	10.16	9.07	-0.89	12.36	0.95	0.51	1
128	18:04:27.27	-24:20:57.0	9.41	9.06	8.82	8.23	-1.52	12.59	1.47	1.03	1
129	18:04:27.36	-24:14:27.3	9.84	9.38	8.74	8.05	-0.75	12.69	1.31	1.09	1
130	18:04:27.48	-24:07:31.1	8.03	7.76	7.19	6.85	-1.42				

Table D.2: contd.

Object	RA [2000]	Dec [2000]	Ch1	Ch2	Ch3	Ch4	α_{IRAC}	H	J-H	H-K	NIR Ref.
131	18:04:28.03	-24:21:43.2	8.03	7.57	7.16	6.04	-0.59	7.97	-0.04	0.07	1
132	18:04:28.25	-24:25:48.0	10.14	9.76	9.39	8.62	-1.11				
133	18:04:28.66	-24:20:20.0	5.77	5.47	5.16	4.44	-1.33	8.19	2.12	1.18	1
134	18:04:29.67	-24:25:19.4	7.09	6.90	6.26	6.03	-1.52	10.36	2.07	1.31	1
135	18:04:29.93	-24:14:29.8	10.46	10.08	9.76	9.05	-1.24	12.67	1.13	0.63	1
136	18:04:30.59	-24:26:06.9	8.16	7.69	7.25	6.85	-1.33	10.29	1.94	1.00	1
137	18:04:31.07	-24:29:09.9	10.59	10.41	9.89	9.04	-1.00				
138	18:04:32.35	-24:19:28.1	10.07	9.53	9.07	8.02	-0.52	12.48	0.96	0.59	1
139	18:04:32.39	-24:27:55.2	10.33	9.95	9.61	8.82	-1.13	13.36	1.62	1.04	1
140	18:04:33.22	-24:27:18.0	9.68	9.02	8.77	8.17	-1.18	11.56	1.15	0.77	1
141	18:04:33.58	-24:21:54.8	8.70	8.45	7.81	6.89	-0.70	10.42	0.97	0.61	1
142	18:04:34.61	-24:09:02.0	5.30	4.66	4.23	3.43	-0.75	9.29	2.80	1.74	1
143	18:04:34.94	-24:22:51.9	10.70	10.27	9.92	8.84	-0.75	12.99	0.99	0.58	1
144	18:04:36.50	-24:19:13.7	10.23	9.73	9.38	8.96	-1.40				
145	18:04:38.90	-24:19:28.2	8.24	7.87	7.32	7.11	-1.49				
146	18:04:39.31	-24:32:24.4	5.64	5.25	4.61	3.77	-0.65	10.00	2.60	1.61	1
147	18:04:39.46	-24:27:09.2	10.46	9.99	9.57	8.65	-0.79	12.26	1.10	0.53	1
148	18:04:39.86	-24:23:05.2	9.55	9.05	8.53	7.57	-0.58	12.28	1.22	0.83	1
149	18:04:40.90	-24:17:10.8	9.29	9.01	8.71	8.15	-1.54	11.70	1.05	0.70	1,3
150	18:04:41.27	-24:15:44.9	5.14	4.58	4.14	3.83	-1.35	7.66	2.63	1.41	1
151	18:04:41.63	-24:26:31.8	8.11	7.49	7.02	6.71	-1.24	10.05	2.07	1.11	1
152	18:04:43.53	-24:27:38.7	8.40	7.76	7.22	6.46	-0.64	10.78	1.21	0.76	3
153	18:04:43.65	-24:27:59.1	10.26	9.86	9.63	9.00	-1.44	13.01	1.47	0.94	1
154	18:04:44.06	-24:19:39.7	10.48	10.02	9.75	8.99	-1.18	12.07	0.84	0.43	1
155	18:04:44.46	-24:10:17.5	10.15	9.85	9.64	8.85	-1.38				
156	18:04:46.41	-24:26:08.0	10.42	10.05	9.52	8.52	-0.65	12.54	1.13	0.53	1
157	18:04:48.05	-24:27:24.6	7.20	6.59	6.16	5.74	-1.18				
158	18:04:48.56	-24:26:40.7	8.89	8.46	8.04	7.29	-1.02	11.02	1.58	0.95	1,3
159	18:04:50.23	-24:27:59.4	10.40	10.09	9.36	8.82	-0.93				
160	18:04:51.53	-24:24:17.4	10.06	9.45	9.00	8.08	-0.61	12.28	1.21	0.61	1
161	18:04:51.57	-24:26:10.9	10.72	10.02	9.96	9.00	-1.01				
162	18:04:51.63	-24:25:15.8	10.37	9.88	9.40	8.91	-1.16	12.02	0.97	0.47	1
163	18:04:52.64	-24:27:30.8	10.72	10.42	9.67	8.99	-0.76	13.28	1.16	0.70	1
164	18:04:53.48	-24:26:08.7	8.45	7.91	7.21	6.66	-0.74				
165	18:04:54.08	-24:26:23.7	7.05	6.33	5.96	5.45	-1.06				
166	18:04:55.00	-24:27:18.1	9.15	8.77	8.29	7.42	-0.84	12.59	2.04	1.33	1
167	18:04:56.18	-24:09:00.9	8.16	7.78	7.55	6.98	-1.52	10.06	2.02	0.99	1
168	18:04:57.35	-24:20:48.4	4.49	4.30	3.58	3.28	-1.33				

Appendix E

S235: Supplementary plots, YSO lists and YSO selection criteria

E.1 Criteria for YSO selection for combined JHK and IRAC data:

YSOs can be identified using H, K, Ch1 and Ch2 bands with following conditions (see Gutermuth et al. (2009) for more details):

$$[[3.6] - [4.5]]_0 > 0.101$$

&

$$[K - [3.6]]_0 > 0$$

&

$$[K - [3.6]]_0 > -2.85714 \times ([[3.6] - [4.5]]_0 - 0.101) + 0.5.$$

where, the subscript '0' indicates dereddened indices.

These YSOs can be further classified into Class I and II sources with following criteria:

$$[K - [3.6]]_0 > -2.85714 \times ([[3.6] - [4.5]]_0 - 0.401) + 1.7$$

Further, Class I sources must have

$$[3.6]_0 < 15$$

and Class II sources must have

$$[3.6]_0 < 14.5$$

to minimize extragalactic contaminants.

The dereddened colours used in the above criteria are obtained by using the following relations:

$$[H-K]_0 = \frac{1.33 \times (C[H-K]_{meas} - [[3.6]-[4.5]]_{meas}) - 0.133}{1.33C - 1}$$

$$[K-[3.6]]_0 = [K-[3.6]]_{meas} - ([H-K]_{meas} - [H-K]_0) \times \frac{E_{K-[3.6]}}{E_{H-K}}$$

$$[[3.6]-[4.5]]_0 = [[3.6]-[4.5]]_{meas} - ([H-K]_{meas} - [H-K]_0) \times \frac{E_{[3.6]-[4.5]}}{E_{H-K}}$$

where,

$\frac{E_{J-H}}{E_{H-K}} = 1.73$, $\frac{E_{H-K}}{E_{K-[3.6]}} = 1.49$, $\frac{E_{H-K}}{E_{K-[4.5]}} = 1.17$ and C = $\frac{E_{[3.6]-[4.5]}}{E_{H-K}} = 0.18$.

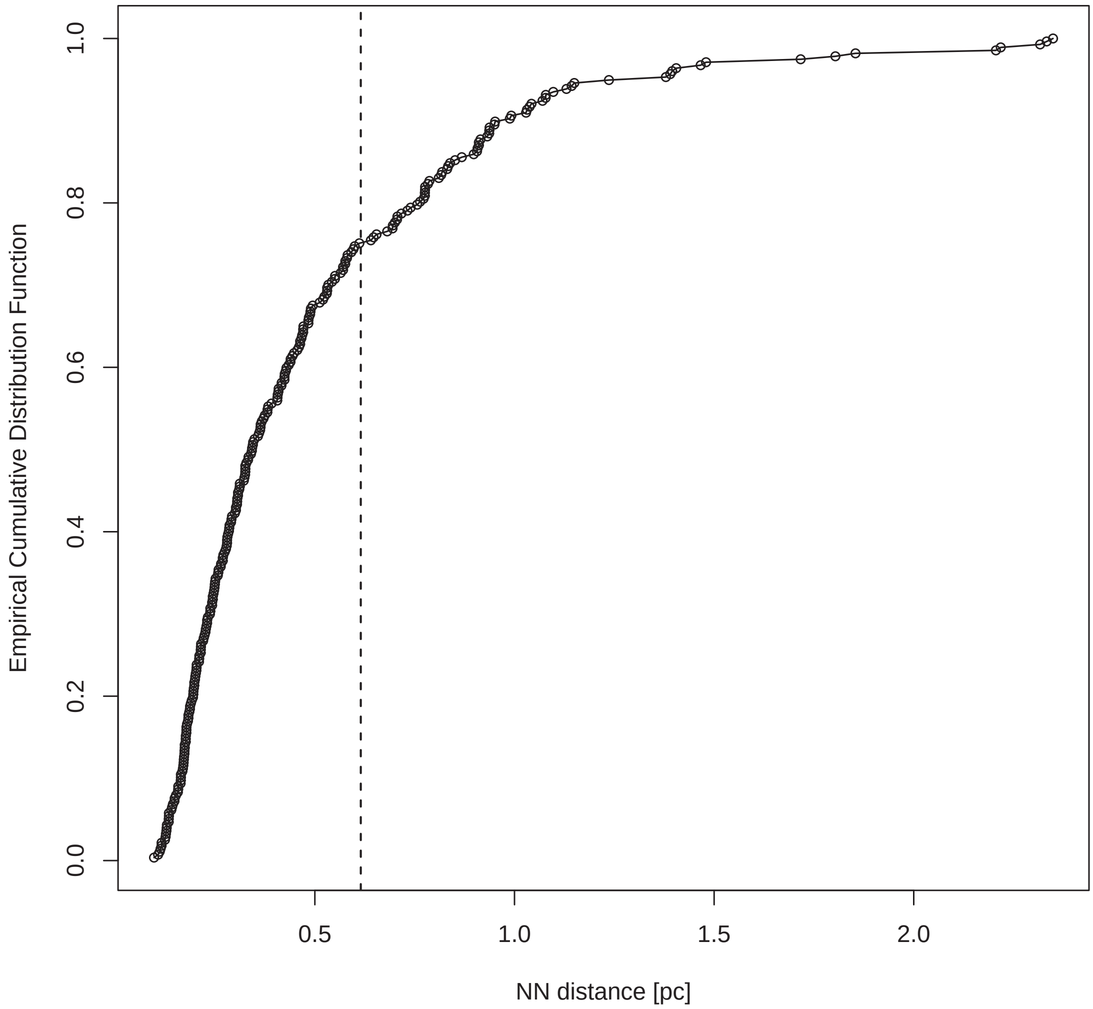

Fig. E.1: Empirical cumulative distribution function of nearest-neighbour distance for the YSOs in the entire S235 complex. The separation between clustered and scattered YSOs was estimated using (arbitrary) distance of inflection (d_c) of 0.62 pc (0.02^o at a distance of 1.8 kpc).

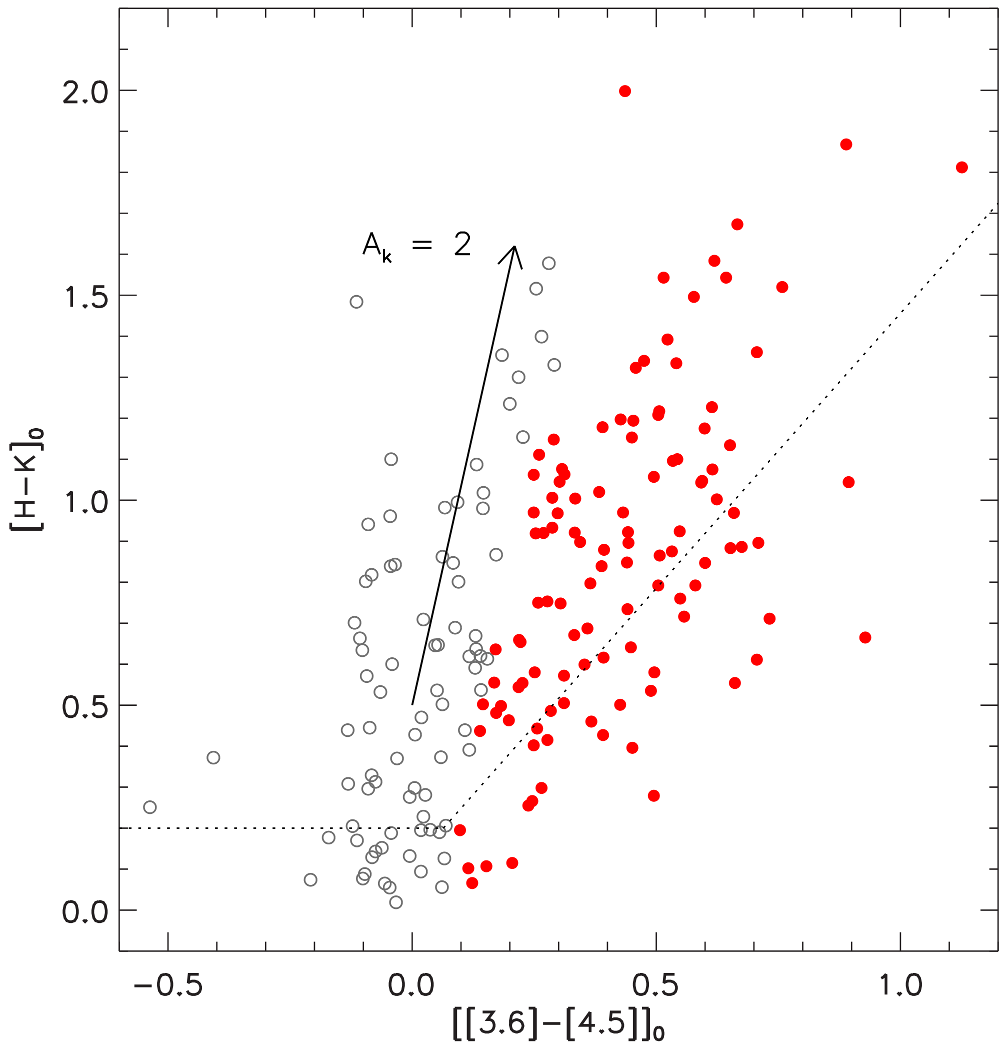

Fig. E.2: Colour-colour diagram used for measuring extinction for dereddening. Filled red circles represent the identified YSOs and the rest of the sources are shown by gray open circles. The extinction calculations are plotted as dotted line obtained by given conditions in section E.1 of appendix E. The extinction vector for A_K = 2 mag is shown by the arrow, obtained using the average extinction law of Flaherty et al. (2007).

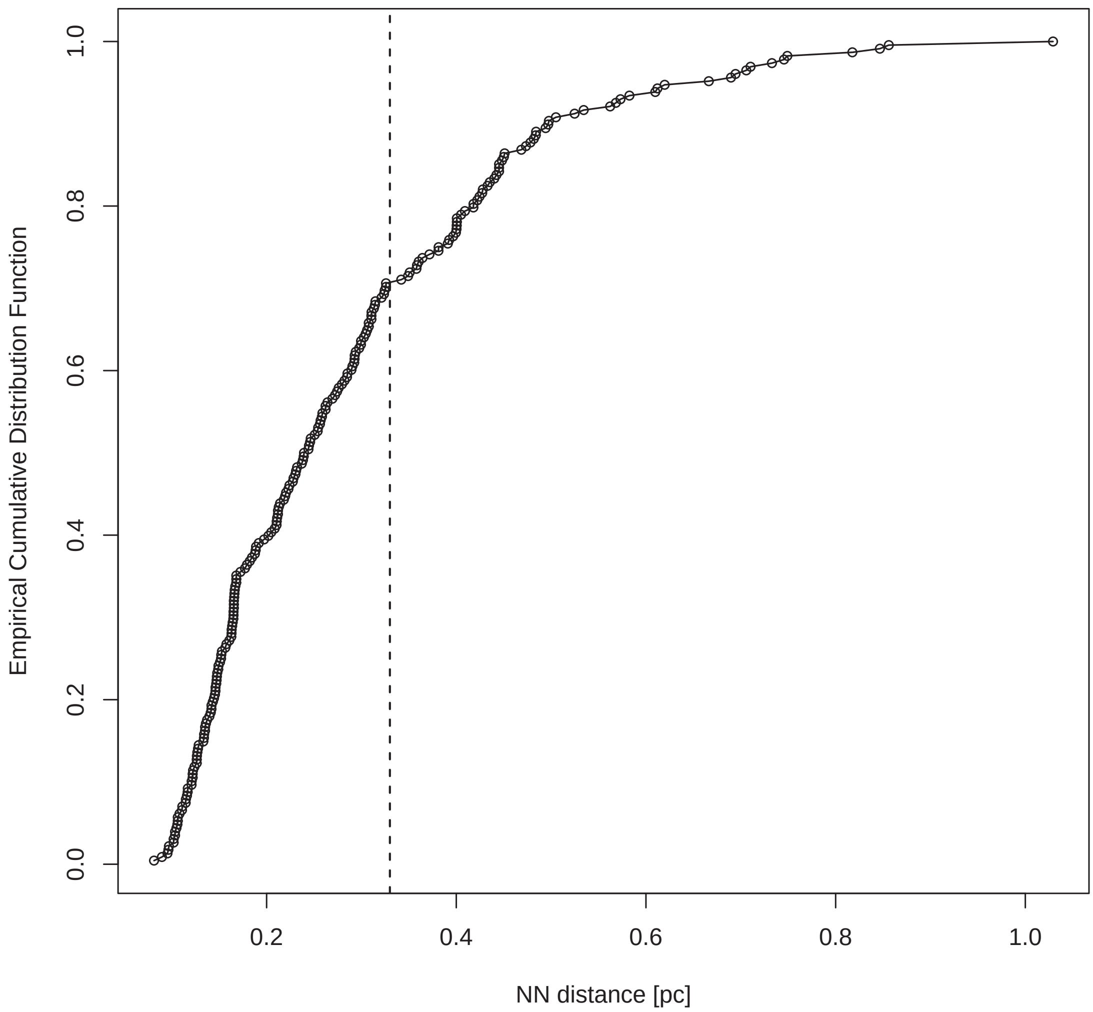

Fig. E.3: Empirical cumulative distribution function of nearest-neighbour distance for the YSOs in Mt. Abu NIR observed region (the vicinity of S235A-B). The separation between clustered and scattered YSOs was obtained using (arbitrary) distance of inflection value (d_c) of 0.33 pc (0.01^o at a distance of 1.8 kpc).

Table E.1: *Spitzer*-IRAC 4-channel photometry (in mag) of the Class 0/I YSOs identified in S235 (see text for details).

Object	RA [2000]	Dec [2000]	Ch1	Ch2	Ch3	Ch4	α_{IRAC}
1	5:40:34.43	35:40:08.4	13.28	12.55	11.93	10.64	0.16
2	5:40:37.56	35:45:33.8	13.17	12.25	11.08	10.22	0.63
3	5:40:41.18	35:45:21.4	12.97	12.22	11.19	9.88	0.76
4	5:40:42.46	35:46:11.5	14.76	12.72	11.83	11.09	1.20
5	5:40:42.63	35:42:31.2	12.66	12.17	11.59	10.26	-0.09
6	5:40:42.64	35:46:07.2	14.41	12.16	10.83	9.90	2.22
7	5:40:42.94	35:45:58.7	13.17	11.90	11.19	10.42	0.24
8	5:40:44.15	35:54:59.0	9.55	8.30	7.49	6.46	0.64
9	5:40:44.32	35:45:52.8	12.20	11.35	10.68	9.57	0.13
10	5:40:45.60	35:48:11.6	11.37	9.32	8.13	7.28	1.74
11	5:40:49.17	35:41:37.3	11.54	11.03	10.27	9.29	-0.22
12	5:40:49.24	35:48:41.8	9.20	8.65	8.03	6.77	-0.06
13	5:40:49.43	35:45:48.4	13.74	13.13	12.51	10.96	0.33
14	5:40:50.09	35:41:39.5	12.21	11.34	10.42	9.21	0.61
15	5:40:50.13	35:41:17.5	12.35	11.36	10.82	10.05	-0.27
16	5:40:50.58	35:49:06.0	9.57	8.08	7.14	6.30	0.84
17	5:40:50.70	35:40:43.2	13.24	12.44	11.50	10.88	-0.08
18	5:40:50.82	35:41:25.9	11.68	10.76	10.02	8.92	0.30
19	5:40:51.05	35:41:22.2	11.83	11.55	11.04	9.62	-0.30
20	5:40:51.43	35:40:14.5	13.62	13.12	12.55	11.21	-0.09
21	5:40:52.24	35:41:17.1	12.26	11.60	10.66	8.98	0.96
22	5:40:52.25	35:40:20.7	13.54	12.82	12.28	11.19	-0.19
23	5:40:52.34	35:40:14.3	13.66	12.69	12.01	11.13	0.02
24(S235B)	5:40:52.38	35:41:29.3	6.66	6.23	4.61	2.69	1.94
25	5:40:52.59	35:40:51.4	13.66	12.92	12.17	10.65	0.59
26(S235A)	5:40:52.79	35:42:18.2	8.52	7.87	6.99	5.49	0.66
27	5:40:52.83	35:40:31.7	13.65	12.55	11.36	9.65	1.76
28	5:40:53.42	35:40:42.5	10.95	10.20	9.43	8.58	-0.11
29	5:40:53.49	35:41:52.4	10.02	9.35	8.75	7.61	-0.10
30	5:40:53.95	35:41:41.2	12.39	11.07	10.04	9.27	0.72
31	5:40:54.03	35:40:08.2	12.33	11.53	11.04	9.98	-0.21
32	5:40:54.11	35:43:45.1	15.14	12.88	11.98	11.21	1.46
33	5:40:54.15	35:40:17.8	11.67	10.63	9.68	8.80	0.45
34	5:40:54.36	35:44:09.8	8.61	7.90	7.15	6.08	0.07
35	5:40:54.59	35:42:58.2	12.45	11.78	10.89	9.99	0.03
36	5:40:54.72	35:44:07.0	8.12	6.52	5.48	4.14	1.63
37	5:40:56.02	35:42:19.9	11.70	11.30	10.56	9.25	0.01
38	5:40:56.04	35:40:24.6	13.43	12.58	11.88	10.53	0.44
39	5:40:56.07	35:40:36.8	13.48	12.66	11.79	10.88	0.17
40	5:40:56.94	35:40:50.7	13.02	12.13	11.37	10.57	-0.04
41	5:40:57.03	35:39:55.4	13.68	12.61	11.81	10.41	0.86
42	5:40:57.04	35:40:45.4	14.28	13.29	12.45	11.51	0.32
43	5:40:57.09	35:44:31.5	13.75	13.18	12.53	11.42	-0.17
44	5:40:57.40	35:42:40.5	13.14	12.32	11.73	10.55	0.08
45	5:40:58.01	35:42:45.0	14.96	14.07	12.89	11.66	1.02

Table E.1: contd.

Object	RA [2000]	Dec [2000]	Ch1	Ch2	Ch3	Ch4	α_{IRAC}
46	5:40:59.15	35:41:08.3	14.27	13.66	12.75	11.90	-0.06
47	5:40:59.70	35:46:07.5	12.38	11.82	11.06	10.17	-0.26
48	5:41:00.48	35:49:29.0	10.08	8.82	7.98	7.04	0.58
49	5:41:00.73	35:49:25.4	11.10	9.25	7.97	7.06	1.74
50	5:41:02.93	35:41:04.4	12.53	12.06	11.34	10.19	-0.12
51	5:41:03.95	35:49:54.0	10.50	9.40	8.62	7.89	0.12
52	5:41:05.57	35:40:31.7	13.52	13.06	12.30	11.13	-0.05
53	5:41:06.55	35:51:09.8	8.08	6.79	5.96	4.66	1.00
54	5:41:08.85	35:48:50.1	11.45	10.19	9.33	8.56	0.43
55	5:41:09.81	35:42:05.2	13.79	13.12	12.59	11.46	-0.20
56	5:41:20.92	35:46:17.0	13.45	12.72	12.07	10.97	-0.03
57	5:41:22.73	35:52:08.4	11.97	9.93	8.11	7.78	2.03
58	5:41:24.03	35:52:52.0	12.78	10.65	8.93	7.52	3.17
59	5:41:24.30	35:52:47.1	12.86	11.25	10.11	8.99	1.54
60	5:41:24.57	35:52:38.4	11.93	11.25	10.63	9.55	-0.12
61	5:41:25.62	35:52:54.2	11.79	10.90	10.42	9.43	-0.22
62	5:41:25.98	35:52:28.2	12.48	11.61	10.96	9.87	0.12
63	5:41:26.36	35:48:31.4	11.74	11.46	10.82	9.55	-0.28
64	5:41:26.79	35:48:32.4	12.08	11.66	11.06	9.60	0.01
65	5:41:26.86	35:52:43.0	12.16	11.26	10.54	9.46	0.23
66	5:41:27.64	35:48:59.4	11.65	11.20	10.58	9.11	0.07
67	5:41:27.66	35:48:04.8	13.72	13.08	12.72	11.37	-0.22
68	5:41:28.38	35:51:58.1	11.37	10.70	10.18	9.00	-0.16
69	5:41:29.27	35:49:15.6	13.07	12.66	11.90	10.71	-0.08
70	5:41:29.46	35:48:58.8	7.47	6.44	5.76	4.92	0.03
71	5:41:29.72	35:50:52.3	13.21	12.35	11.32	9.70	1.20
72	5:41:30.18	35:49:36.8	14.36	12.94	12.21	11.33	0.53
73	5:41:30.32	35:49:48.0	9.70	8.47	7.44	6.36	0.97
74	5:41:30.42	35:50:03.2	11.64	10.04	9.07	8.13	1.11
75	5:41:30.50	35:49:22.1	13.86	13.04	12.42	11.15	0.21
76	5:41:30.54	35:49:48.4	10.09	8.65	7.66	6.77	0.91
77	5:41:30.86	35:50:06.8	13.04	11.89	11.12	10.35	0.20
78	5:41:31.19	35:52:02.5	14.73	13.75	12.83	11.69	0.64
79	5:41:31.42	35:50:26.2	12.81	10.84	9.56	8.51	2.01
80	5:41:31.50	35:47:05.5	14.86	13.53	12.84	11.22	1.19
81	5:41:32.47	35:51:27.0	14.32	12.99	12.17	10.96	0.93
82	5:41:32.56	35:49:19.2	12.48	11.65	11.28	9.91	-0.01
83	5:41:37.20	35:45:44.0	12.63	11.57	11.13	9.99	0.05
84	5:41:37.69	35:45:34.2	12.47	11.29	10.50	9.31	0.71

Table E.2: *Spitzer*-IRAC 4-channel photometry (in mag) of the Class II YSOs identified in S235 complex (see text for details).

Object	RA [2000]	Dec [2000]	Ch1	Ch2	Ch3	Ch4	α_{IRAC}
1	5:40:15.96	35:44:48.5	13.97	13.64	13.13	12.73	-1.37
2	5:40:18.91	35:48:25.3	12.91	12.64	12.36	11.25	-0.97
3	5:40:20.14	35:55:22.9	11.60	11.42	10.89	10.27	-1.25
4	5:40:30.51	35:45:44.7	13.94	13.69	13.15	12.49	-1.12
5	5:40:31.38	35:48:32.4	13.85	13.26	13.09	11.90	-0.72
6	5:40:32.86	35:54:51.5	13.99	13.83	13.26	12.18	-0.71
7	5:40:33.04	35:47:10.1	13.66	13.33	12.81	11.95	-0.86
8	5:40:33.89	35:43:22.3	14.45	14.19	13.83	12.86	-1.02
9	5:40:34.85	35:55:05.5	10.78	9.99	9.43	8.74	-0.53
10	5:40:34.96	35:44:57.6	12.26	12.01	11.71	11.13	-1.55
11	5:40:35.28	35:46:21.7	13.20	12.83	12.24	11.46	-0.81
12	5:40:35.93	35:55:29.1	10.37	10.02	9.71	8.91	-1.20
13	5:40:36.54	35:50:41.7	12.65	12.35	11.96	11.30	-1.29
14	5:40:36.78	35:46:12.5	11.35	10.96	10.31	9.87	-1.08
15	5:40:37.26	35:43:15.6	12.75	12.59	12.35	11.66	-1.59
16	5:40:37.63	35:42:54.2	11.88	11.66	11.52	10.66	-1.49
17	5:40:37.83	35:41:34.6	13.42	13.07	12.55	12.20	-1.39
18	5:40:38.12	35:45:37.4	13.74	13.00	12.57	11.97	-0.86
19	5:40:38.52	35:45:17.7	13.75	13.41	12.98	12.51	-1.40
20	5:40:38.94	35:46:07.2	12.20	11.37	10.72	9.99	-0.33
21	5:40:39.02	35:45:55.8	12.98	12.38	11.88	10.92	-0.50
22	5:40:39.60	35:45:45.6	12.41	11.85	11.09	10.23	-0.30
23	5:40:39.70	35:45:06.5	13.81	13.50	13.07	12.51	-1.32
24	5:40:39.72	35:45:48.8	11.54	10.86	10.46	9.87	-0.98
25	5:40:39.74	35:53:26.3	8.92	8.53	8.25	7.18	-0.89
26	5:40:39.82	35:56:15.3	13.35	13.12	12.55	11.69	-0.89
27	5:40:40.00	35:40:59.2	12.37	11.83	11.32	10.26	-0.44
28	5:40:40.21	35:41:02.9	10.09	9.80	9.43	8.69	-1.23
29	5:40:40.21	35:39:59.8	13.62	13.26	13.04	12.25	-1.32
30	5:40:41.38	35:55:21.7	10.55	10.03	9.37	8.75	-0.74
31	5:40:42.10	35:44:52.5	11.66	11.36	10.95	9.98	-0.91
32	5:40:42.73	35:43:04.2	13.06	12.68	12.36	11.65	-1.24
33	5:40:42.92	35:54:34.8	10.38	9.80	9.29	8.48	-0.68
34	5:40:43.54	35:45:04.2	13.94	13.56	13.24	12.53	-1.25
35	5:40:44.00	35:43:57.6	12.97	12.66	12.34	11.41	-1.06
36	5:40:44.07	35:43:37.7	11.46	11.20	10.71	9.76	-0.87
37	5:40:44.11	35:42:51.8	13.64	13.32	12.99	11.64	-0.58
38	5:40:44.20	35:45:05.0	13.08	12.58	12.33	11.54	-1.14
39	5:40:44.38	35:42:48.9	11.34	11.01	10.64	9.87	-1.15
40	5:40:44.40	35:41:12.5	13.89	13.39	13.23	12.18	-0.96
41	5:40:44.55	35:54:56.5	9.11	8.62	8.13	7.24	-0.70
42	5:40:44.56	35:45:37.5	13.04	12.78	12.50	11.71	-1.33
43	5:40:44.66	35:45:30.4	13.57	12.86	12.40	11.32	-0.31
44	5:40:45.08	35:46:02.3	11.76	11.19	10.89	9.88	-0.75
45	5:40:45.68	35:43:40.4	13.36	12.85	12.65	11.54	-0.84
46	5:40:46.80	35:43:58.7	14.07	13.80	13.67	12.93	-1.58
47	5:40:47.03	35:42:23.1	11.14	10.52	10.30	9.51	-1.06
48	5:40:47.17	35:40:52.0	13.86	13.37	13.02	12.16	-0.93

Table E.2: contd.

Object	RA [2000]	Dec [2000]	Ch1	Ch2	Ch3	Ch4	α_{IRAC}
49	5:40:47.58	35:41:01.9	12.44	11.72	11.30	10.89	-1.10
50	5:40:48.10	35:44:39.8	11.60	11.27	11.19	10.34	-1.46
51	5:40:48.54	35:45:01.3	13.92	13.38	13.06	11.72	-0.39
52	5:40:48.74	35:40:16.6	12.74	12.52	12.07	11.24	-1.08
53	5:40:48.82	35:55:57.5	12.68	12.27	11.81	10.96	-0.87
54	5:40:48.86	35:46:03.8	13.55	13.04	12.73	11.70	-0.77
55	5:40:49.02	35:41:17.7	12.84	12.54	12.27	11.46	-1.28
56	5:40:49.28	35:40:41.0	11.35	10.91	10.38	9.53	-0.74
57	5:40:49.29	35:40:36.0	11.76	11.39	10.87	9.91	-0.71
58	5:40:49.99	35:44:52.8	10.95	10.40	9.98	9.09	-0.74
59	5:40:50.07	35:40:40.8	14.41	14.16	13.72	12.58	-0.73
60	5:40:50.71	35:40:51.8	12.41	11.92	11.36	10.48	-0.62
61	5:40:50.78	35:40:55.0	12.87	12.63	12.20	11.23	-0.94
62	5:40:50.79	35:40:37.0	12.97	12.27	11.74	11.07	-0.69
63	5:40:50.88	35:41:06.3	10.96	10.41	10.03	9.41	-1.10
64	5:40:50.95	35:48:41.6	11.63	10.96	10.73	10.14	-1.22
65	5:40:51.04	35:40:21.0	11.63	11.13	11.10	10.30	-1.43
66	5:40:51.05	35:43:42.9	12.67	12.14	11.71	10.82	-0.75
67	5:40:51.06	35:41:00.5	9.28	9.01	8.49	7.41	-0.67
68	5:40:51.20	35:41:09.6	11.79	11.15	10.86	10.02	-0.88
69	5:40:51.40	35:40:42.9	13.08	12.82	12.24	11.74	-1.23
70	5:40:51.69	35:40:38.3	12.94	12.09	11.50	10.91	-0.54
71	5:40:51.72	35:45:38.9	10.31	9.94	9.57	8.60	-0.90
72	5:40:51.81	35:40:39.3	12.80	12.21	11.58	11.14	-0.91
73	5:40:52.02	35:39:57.6	10.62	9.97	9.79	9.11	-1.20
74	5:40:52.41	35:40:07.5	13.36	12.51	12.09	11.21	-0.47
75	5:40:52.66	35:41:45.2	10.62	10.36	9.75	8.96	-0.88
76	5:40:52.67	35:40:19.5	12.09	11.24	10.66	9.85	-0.31
77	5:40:52.82	35:40:14.6	13.32	12.64	12.43	11.32	-0.66
78	5:40:53.13	35:40:08.7	13.46	12.91	12.39	11.55	-0.66
79	5:40:53.37	35:40:25.5	11.86	11.26	10.60	9.72	-0.38
80	5:40:53.49	35:41:09.6	12.19	11.57	10.84	10.22	-0.55
81(M1)	5:40:53.60	35:41:42.6	10.78	9.66	9.10	8.76	-0.59
82	5:40:53.70	35:42:52.3	9.79	9.51	9.24	8.37	-1.24
83	5:40:53.78	35:41:26.6	9.15	8.76	8.20	7.20	-0.58
84	5:40:53.91	35:40:46.1	12.60	12.11	11.53	10.77	-0.72
85	5:40:53.94	35:45:44.3	11.22	10.65	10.44	9.88	-1.37
86	5:40:54.00	35:39:58.4	11.45	10.83	10.71	10.03	-1.32
87	5:40:54.33	35:40:32.0	13.79	13.29	12.76	11.65	-0.40
88	5:40:54.37	35:41:28.9	11.13	10.34	9.61	9.04	-0.44
89	5:40:54.41	35:41:08.7	13.37	12.93	12.77	12.19	-1.55
90	5:40:54.58	35:44:23.6	11.19	10.26	9.78	9.28	-0.72
91	5:40:54.67	35:41:21.6	10.90	10.01	9.52	8.72	-0.42
92	5:40:54.72	35:41:16.6	12.11	11.69	11.33	10.36	-0.86
93	5:40:54.73	35:45:08.2	13.45	12.84	12.23	11.97	-1.12
94	5:40:55.14	35:40:52.0	10.62	10.16	9.62	9.09	-1.06
95	5:40:55.20	35:44:37.5	13.52	13.18	12.83	11.57	-0.64
96	5:40:55.44	35:40:54.4	11.16	10.71	9.95	9.25	-0.59

Table E.2: contd.

Object	RA [2000]	Dec [2000]	Ch1	Ch2	Ch3	Ch4	α_{IRAC}
97	5:40:55.70	35:40:20.1	12.87	12.32	11.82	11.00	-0.71
98	5:40:55.88	35:41:24.9	12.00	11.74	11.11	10.73	-1.30
99	5:40:56.05	35:43:57.0	13.40	12.70	12.18	11.79	-1.00
100	5:40:56.16	35:44:27.0	12.74	12.29	12.00	11.47	-1.41
101	5:40:56.25	35:45:02.2	12.54	11.95	11.48	10.46	-0.48
102	5:40:56.27	35:43:58.0	11.48	11.03	10.83	10.27	-1.50
103	5:40:56.99	35:42:37.4	12.28	11.70	11.38	10.07	-0.39
104	5:40:57.00	35:46:00.3	13.15	12.66	12.17	11.10	-0.50
105	5:40:57.12	35:42:32.1	11.57	10.99	10.62	9.43	-0.44
106	5:40:57.65	35:40:50.5	12.46	12.09	11.52	10.98	-1.09
107	5:40:57.86	35:40:56.6	11.86	11.55	10.78	10.02	-0.64
108	5:40:58.01	35:44:36.6	14.79	14.29	13.61	13.38	-1.16
109	5:40:58.13	35:42:30.5	13.05	12.61	11.88	10.90	-0.32
110	5:40:58.15	35:43:20.7	10.16	9.66	9.31	8.48	-0.95
111	5:40:58.89	35:41:19.5	12.81	12.47	12.03	11.59	-1.41
112	5:40:58.99	35:42:46.3	14.22	13.26	12.92	11.93	-0.35
113	5:40:59.11	35:42:50.0	13.33	12.95	12.60	11.98	-1.30
114	5:40:59.14	35:43:07.1	11.64	11.21	11.02	10.13	-1.17
115	5:40:59.26	35:42:48.6	14.25	13.40	12.98	12.56	-0.96
116	5:40:59.38	35:40:24.9	11.79	11.27	10.88	10.56	-1.44
117	5:40:59.42	35:41:45.1	13.26	12.81	12.44	11.94	-1.34
118	5:40:59.57	35:41:29.0	14.25	13.85	13.34	12.51	-0.83
119	5:40:59.59	35:40:39.3	11.28	10.68	10.21	9.53	-0.86
120	5:40:59.80	35:40:38.8	11.92	11.43	10.90	10.33	-1.00
121	5:40:59.81	35:41:58.5	14.12	13.67	13.32	12.09	-0.56
122	5:40:59.84	35:41:11.3	13.91	13.43	12.83	11.92	-0.55
123	5:40:59.92	35:44:04.2	11.48	10.77	10.26	9.45	-0.55
124	5:41:00.21	35:40:47.5	12.65	12.44	12.13	11.56	-1.58
125	5:41:00.94	35:43:14.0	13.52	12.94	12.70	11.61	-0.74
126	5:41:01.00	35:41:08.6	11.84	11.27	10.95	10.33	-1.15
127	5:41:01.18	35:43:38.4	11.33	10.79	10.51	9.74	-1.08
128	5:41:01.50	35:40:39.6	13.30	13.00	12.51	11.42	-0.67
129	5:41:01.58	35:42:51.1	12.89	12.34	11.82	10.92	-0.59
130	5:41:01.64	35:44:06.4	11.44	10.83	10.29	9.77	-0.92
131	5:41:02.25	35:46:07.5	12.44	11.92	11.65	10.85	-1.08
132	5:41:02.75	35:40:06.6	12.69	12.24	11.88	11.45	-1.42
133	5:41:03.20	35:41:46.0	13.70	13.38	13.04	12.35	-1.30
134	5:41:03.45	35:43:35.5	13.29	12.89	12.67	11.51	-0.86
135	5:41:03.46	35:44:50.8	13.72	13.47	12.89	12.13	-0.96
136	5:41:04.42	35:46:37.6	11.74	11.37	10.91	10.11	-0.96
137	5:41:04.89	35:40:54.5	12.76	12.45	12.20	11.55	-1.48
138	5:41:06.59	35:50:21.3	10.19	9.74	9.55	8.44	-0.91
139	5:41:08.02	35:48:44.8	9.57	8.88	8.32	7.60	-0.59
140	5:41:08.84	35:41:25.7	13.56	13.18	12.84	12.19	-1.29
141	5:41:09.02	35:40:20.2	13.29	12.84	12.47	11.52	-0.85
142	5:41:09.13	35:48:58.0	10.77	10.39	9.73	8.89	-0.64
143	5:41:09.32	35:49:28.4	9.10	8.38	7.70	6.92	-0.34
144	5:41:09.95	35:49:20.4	11.03	10.27	9.88	9.55	-1.20

Table E.2: contd.

Object	RA [2000]	Dec [2000]	Ch1	Ch2	Ch3	Ch4	α_{IRAC}
145	5:41:11.31	35:45:06.9	12.85	12.31	12.03	11.30	-1.12
146	5:41:11.95	35:45:59.3	12.93	12.51	12.19	11.61	-1.35
147	5:41:12.86	35:51:03.7	10.78	10.33	10.03	9.41	-1.30
148	5:41:13.81	35:44:24.7	13.14	12.90	12.74	11.70	-1.24
149	5:41:14.56	35:50:01.6	10.94	10.51	10.13	9.45	-1.15
150	5:41:14.78	35:52:27.4	11.76	11.54	11.36	10.47	-1.40
151	5:41:16.89	35:45:52.1	12.17	11.58	11.38	10.53	-1.05
152	5:41:17.16	35:55:43.6	13.80	13.43	13.02	11.88	-0.65
153	5:41:17.55	35:50:06.9	11.67	11.16	11.04	9.88	-0.89
154	5:41:18.09	35:53:06.4	11.06	10.42	9.92	8.88	-0.38
155	5:41:18.12	35:48:35.8	12.22	11.95	11.72	10.97	-1.43
156	5:41:19.96	35:51:28.1	11.82	11.48	11.19	10.23	-1.05
157	5:41:20.65	35:42:14.2	12.45	12.14	11.96	10.99	-1.22
158	5:41:20.68	35:48:10.8	11.51	11.31	10.94	10.35	-1.48
159	5:41:21.72	35:52:44.7	12.42	11.86	11.44	10.65	-0.85
160	5:41:21.84	35:52:18.3	10.86	10.28	9.61	8.78	-0.44
161	5:41:21.98	35:51:53.9	10.25	9.66	9.34	8.86	-1.29
162	5:41:22.68	35:51:51.4	12.15	11.97	11.66	10.70	-1.17
163	5:41:23.61	35:47:08.8	13.45	13.14	12.57	11.40	-0.46
164	5:41:24.94	35:53:06.6	11.58	10.87	10.41	9.60	-0.62
165	5:41:25.11	35:47:00.2	12.01	11.57	11.10	10.13	-0.70
166	5:41:25.21	35:46:43.9	13.69	13.25	12.82	11.85	-0.75
167	5:41:25.23	35:53:00.3	12.32	11.15	10.56	10.27	-0.55
168	5:41:25.34	35:52:36.3	11.77	11.31	10.98	10.19	-1.06
169	5:41:25.41	35:52:10.2	10.89	10.62	10.46	9.63	-1.43
170	5:41:25.82	35:52:17.9	11.17	10.74	10.40	9.43	-0.88
171	5:41:26.12	35:47:12.1	12.54	12.08	11.62	10.35	-0.36
172	5:41:27.38	35:48:54.7	11.03	10.34	9.87	8.86	-0.41
173	5:41:27.38	35:52:53.9	13.13	12.64	12.26	11.68	-1.19
174	5:41:27.43	35:53:04.7	13.88	13.23	12.94	11.68	-0.41
175	5:41:27.72	35:46:25.7	12.53	12.15	11.80	10.75	-0.83
176	5:41:28.35	35:47:35.7	12.57	12.21	12.05	11.04	-1.15
177	5:41:29.10	35:49:34.2	11.92	11.55	11.25	10.06	-0.76
178	5:41:29.25	35:46:43.9	13.07	12.46	11.87	11.03	-0.50
179	5:41:29.68	35:49:19.9	12.38	11.91	11.78	10.93	-1.26
180	5:41:30.07	35:50:47.5	12.16	11.90	11.37	10.08	-0.43
181	5:41:30.20	35:41:21.0	15.02	14.81	14.40	13.18	-0.72
182	5:41:31.02	35:46:18.4	13.70	13.33	13.16	12.52	-1.54
183	5:41:31.06	35:50:15.2	11.13	10.46	10.03	9.28	-0.76
184	5:41:31.10	35:47:14.7	11.05	10.74	10.31	9.22	-0.74
185	5:41:31.25	35:49:31.7	12.64	11.53	10.85	10.62	-0.56
186	5:41:31.39	35:50:01.6	13.05	12.51	12.13	11.04	-0.58
187	5:41:32.74	35:49:30.2	13.66	13.40	13.02	12.06	-1.01
188	5:41:33.22	35:49:31.5	12.11	11.83	11.69	10.94	-1.54
189	5:41:33.76	35:47:45.4	11.72	11.42	11.16	10.37	-1.32
190	5:41:38.31	35:49:56.3	12.84	12.37	11.92	11.44	-1.23
191	5:41:41.51	35:48:52.0	12.21	11.60	11.33	10.33	-0.77
192	5:41:43.11	35:43:16.5	11.34	10.85	10.37	9.77	-1.05

Table E.3: Mt. Abu J, H, K and *Spitzer*-IRAC Ch1 and Ch2 band photometry (in mag) of the Class I YSOs identified in vicinity of S235A-B region (see text for details).

Object	RA [2000]	Dec [2000]	Jmag	Hmag	Kmag	Ch1	Ch2
1	5:40:34.51	35:40:09.1	16.30	14.92	14.21	13.28	12.55
2	5:40:49.21	35:40:41.5	15.03	13.80	13.07	11.35	10.91
3	5:40:50.82	35:40:49.2	13.99	13.29	12.89	11.21	10.76
4	5:40:51.13	35:41:09.7	—	15.77	14.23	11.79	11.15
5	5:40:51.97	35:39:58.4	15.51	13.86	12.72	10.62	9.97
6	5:40:52.17	35:41:41.6	15.18	14.06	13.17	11.46	10.79
7	5:40:52.18	35:41:17.5	—	15.28	14.31	12.26	11.60
8	5:40:53.06	35:40:09.6	—	15.77	15.01	13.46	12.91
9	5:40:53.07	35:42:23.9	15.11	13.98	13.16	13.57	11.54
10	5:40:53.30	35:40:26.2	15.40	14.26	13.41	11.86	11.26
11	5:40:53.36	35:40:43.1	—	14.85	13.33	10.95	10.20
12	5:40:53.44	35:41:10.4	—	15.74	14.74	12.19	11.57
13	5:40:53.65	35:41:47.5	16.39	15.04	14.48	12.38	11.72
14	5:40:54.50	35:43:58.1	16.35	14.61	13.56	12.24	11.35
15	5:40:55.07	35:43:59.0	16.25	15.00	14.39	12.71	12.01
16	5:40:55.20	35:43:15.0	16.44	15.25	14.97	13.28	12.79
17	5:40:56.10	35:40:08.4	16.63	15.34	14.16	12.49	11.89
18	5:40:56.58	35:42:40.0	16.91	15.50	14.70	13.05	12.54

Table E.4: Mt. Abu J, H, K and *Spitzer*-IRAC Ch1 and Ch2 band photometry (in mag) of the Class II YSOs identified in vicinity of S235A-B region (see text for details).

Object	RA [2000]	Dec [2000]	Jmag	Hmag	Kmag	Ch1	Ch2
1	5:40:33.42	35:40:14.1	14.02	13.34	13.15	12.13	12.03
2	5:40:33.63	35:40:10.3	—	13.86	13.75	12.88	12.73
3	5:40:36.71	35:40:26.6	16.75	15.59	15.09	14.10	13.92
4	5:40:37.13	35:40:18.8	—	16.75	15.82	15.01	14.72
5	5:40:42.20	35:43:17.3	—	15.76	15.18	13.81	13.56
6	5:40:42.71	35:44:36.5	15.61	14.70	14.44	13.84	13.60
7	5:40:44.55	35:40:45.6	15.65	14.33	13.83	12.75	12.61
8	5:40:44.66	35:40:38.4	15.40	14.23	13.67	12.56	12.39
9	5:40:46.73	35:44:20.7	16.14	15.21	14.78	13.84	13.70
10	5:40:49.37	35:41:57.4	14.35	13.36	12.89	11.81	11.45
11	5:40:49.64	35:44:58.6	15.99	14.96	14.30	12.24	12.02
12	5:40:50.17	35:40:54.7	—	16.05	15.13	13.15	12.88
13	5:40:50.52	35:42:00.9	15.97	13.97	12.86	11.02	10.76
14	5:40:50.69	35:43:03.9	16.55	15.53	14.98	13.01	12.79
15	5:40:50.94	35:44:09.6	—	14.32	14.21	13.36	13.15
16	5:40:50.97	35:41:17.7	—	15.99	14.60	12.76	12.24
17	5:40:50.99	35:40:21.7	15.83	14.71	13.50	11.63	11.13
18	5:40:51.04	35:41:53.9	16.57	15.07	13.89	12.36	11.97
19	5:40:51.42	35:41:23.2	15.28	14.28	13.79	12.46	12.18
20	5:40:51.53	35:42:31.3	16.36	14.55	13.36	11.95	11.49
21	5:40:51.68	35:41:57.1	—	15.38	14.32	11.97	11.66
22	5:40:51.76	35:43:53.7	—	16.31	14.31	12.35	11.91
23	5:40:51.78	35:45:11.5	—	15.83	15.26	13.77	13.46
24	5:40:52.83	35:43:20.5	—	16.51	15.17	12.92	12.45
25	5:40:52.92	35:42:29.8	15.28	14.31	13.42	11.97	11.53
26	5:40:53.82	35:44:49.1	16.48	15.55	14.91	13.78	13.61
27	5:40:54.10	35:44:47.4	—	15.55	14.40	12.67	12.38
28	5:40:54.11	35:41:06.4	16.39	15.20	14.36	12.71	12.32
29	5:40:54.20	35:42:00.1	15.72	14.19	13.13	10.71	10.46
30	5:40:54.54	35:43:53.1	15.68	13.86	12.94	11.64	11.20
31	5:40:54.74	35:42:01.0	16.40	14.95	13.87	11.82	11.51
32	5:40:54.79	35:40:53.1	14.76	13.63	13.14	11.93	11.76
33	5:40:55.19	35:41:10.5	16.06	14.39	13.42	12.17	11.87
34	5:40:55.26	35:42:15.7	—	15.98	14.75	13.34	12.73
35	5:40:55.78	35:45:03.9	16.62	15.49	15.09	13.82	13.57
36	5:40:55.81	35:41:25.7	16.24	14.80	13.88	12.00	11.74
37	5:40:56.98	35:44:35.5	16.96	15.53	14.81	14.09	13.53
38	5:40:56.99	35:42:27.3	16.45	15.36	14.89	13.93	13.73
39	5:40:57.80	35:40:57.5	15.79	14.69	13.94	11.86	11.55
40	5:40:57.84	35:42:57.1	16.31	14.57	13.47	11.86	11.32
41	5:40:58.08	35:44:55.9	15.98	15.39	15.12	14.36	14.12
42	5:40:58.85	35:43:01.0	—	15.70	14.70	13.17	12.83
43	5:41:02.38	35:44:34.3	—	15.02	14.96	14.12	13.99
44	5:41:05.09	35:44:15.0	—	12.21	12.11	11.29	11.18
45	5:41:07.32	35:44:19.8	—	15.73	15.32	13.77	13.49

Bibliography

Allen, D. A. 1986, *MNRAS*, **319**, 35

Allen, L. E. et al. 2004, *ApJS*, **154**, 363

Allen, L. E., Hora, J. L., Megeath, S. T., Deutsch, L. K., Fazio, G. G., Chavarria L. and Dell R. W. 2005, in Cesaroni R., Felli M., Churchwel E., Walmsley M., eds, Proc. *IAU Symp. 227, Massive star birth: A crossroads of Astrophysics.* Cambridge University Press, Cambridge, p. 352

Alvarez, C., Feldt, M., Henning, T., Puga, E., Brandner, W. and Stecklum, B. 2004, *ApJS*, **155**, 123

Anandarao, B. G., Chakraborty, A., Ojha, D. K. and Testi, L. 2004, *A&A*, **421**, 1045

Anandarao, B. G., Richardson, E. H., Chakraborty, A. and Epps, H. 2008, *Ground-based and Airborne Instrumentation for Astronomy II*, Edited by McLean, Ian S.; Casali, Mark M. Proceedings of the SPIE, Volume **7014**, pp. 70142Y-70142Y-8

André, P., Ward-Thompson, D. and Barsony, M. 1993, *ApJ*, **406**, 122

André, P., Ward-Thompson, D. and Barsony, M. 2000, *Protostars and Planets IV*, (**Tucson: Univ. Arizona Press**), 59

Arce, H. G., Shepherd, D., Gueth, F., Lee, C. F., Bachiller, R., Rosen, A. and Beuther, H. 2007, *in Protostars and Planets V*, Eds: B. Reipurth, D. Jewitt & K. Keil, University of Arizona Press, Tucson, **p.245-260**

Arias, J. I., Barba, R. H., Maiz Apellaniz, J., Morrell, N. I. and Rubio, M. 2006, *MNRAS*, **366**, 739

Arias, J. I., Barba, R. H. and Morrell, N. I. 2007, *MNRAS*, **374**, 1253

Arquilla, R. and Goldsmith, P. F. 1984, *ApJ*, **279**, 664

Bachiller, R. and Cernicharo, J. 1990, *A&A*, **239**, 276

Bachiller, R., Martin-Pintado, J., Tafalla, M., Cernicharo, J. and Lazareff, B. 1990, *A&A*, **236**, 461

Bachiller, R. 1996, *ARA&A*, **34**, 111

Banerjee, R. and Pudritz, R. E. 2007, *ApJ*, **660**, 479

Barba, R. H. and Arias, J. I. 2007, *A&A*, **471**, 841

Beltrán, M. T., Cesaroni, R., Neri, R., Codella, C., Furuya, R. S., Testi, L. and Olmi, L. 2004, *ApJ*, **601**, L187

Benedettini, M., Molinari, S., Testi, L. and Noriega-Crespo, A. 2004, *MNRAS*, **347**, 295

Bergin, E. A. and Tafalla, M. 2007, *ARA&A*, **45**, 339

Bernasconi, P. A. and Maeder, A. 1996, *A&A*, **307**, 829

Beuther, H., Schilke, P., Menten, K. M., Motte, F., Sridharan, T. K. and Wyrowski, F. 2002, *ApJ*, **566**, 945

Beuther, H., Schilke, P., Sridharan, T. K., Menten, K. M., Walmsley, C. M. and Wyrowski, F. 2002a, *A&A*, **383**, 892

Beuther, H., Schilke, P., Gueth, F., McCaughrean, M., Andersen, M., Sridharan, T. K. and Menten, K. M. 2002b, *A&A*, **387**, 931

Beuther, H., Schilke, P. and Wyrowski, F. 2004, *ApJ*, **615**, 832

Beuther, H., Zhang, Q., Sridharan, T. K. and Chen, Y. 2005, *ApJ*, **628**, 800

Beuther, H., Churchwell, E. B., McKee, C. F. and Jonathan, C. T. 2007, *Protostars and Planets V.* Tucson: Univ.Ariz. Press., p. 165

Billot, N., Noriega-Crespo, A., Carey, S., Guieu, S., Shenoy, S., Paladini, R. and Latter, W. 2010, *ApJ*, **712**, 797

Bjorkman, J. E. 1997, *Stellar Atmospheres: Theory and Observations*, ed. J. P. De Greve, R. Blomme & H. Hensberge (**New York: Springer**), 239

Bjorkman, J. E. and Wood, K. 2001, *ApJ*, **554**, 615

Boley, P. A., Sobolev, A. M., Krushinsky, V. V., van Boekel, R., Henning, T., Moiseev, A. V. and Yushkin, M. V. 2009, *MNRAS*, **399**, 778

Bonnell, I. A., Bate, M. R., Clarke, C. J. and Pringle, J. E. 1997, *MNRAS*, **285**, 201

Bonnell, I. A., Bate, M. R. and Zinnecker, H. 1998, *MNRAS*, **298**, 93

Bonnell, I. A., Bate, M. R., Clarke, C. J. and Pringle, J. E. 2001, *MNRAS*, **323**, 785

Bontemps, S., André, P., Tereby, S. and Cabrit, S. 1996, *A&A*, **311**, 858

Brand, P. W. J. L. and Zealey, W. J. 1978, *A&A*, **63**, 345

Burrows, C. J. et al. 1996, *ApJ*, **473**, 437

Burton, M. G. 2002, *PASA*, **19**, 260

Cabrit, S. and Bertout, C. 1992, *A&A*, **261**, 274

Cabrera-Lavers, A., Garzón, F., Hammersley, P. L., Vicente, B. and González-Fernández, C. 2006, *A&A*, **453**, 371

Campbell,M. F., Sridharan, T. K., Beuther, H., Hora,J., Kassis, M., Adams, J. D. and Fung, S. H. 2005, *IAU Symp.*, **227**

Caratti o Garatti, A., Froebrich, D., Eislöffel, Giannini, T. and Nisini, B. 2008, *A&A*, **485**, 137

Casertano, S. and Hut, P. 1985 *ApJ*, **298**, 80

Cesaroni, R., Felli, M., Testi, L., Walmsley, C. M. and Olmi, L. 1997, *A&A*, **325**, 725

Cesaroni, R., Felli, M., Jenness, T., Neri, R., Olmi, L., Robberto, M., Testi, L. and Walmsley, C. M. 1999, *A&A*, **345**, 949

Cesaroni, R., Codella, C., Furuya, R. S. and Testi, L. 2003, *A&A*, **401**, 227

Cesaroni, R., Neri, R., Olmi, L., Testi, L., Walmsley, C. M. and Hofner, P. 2005, *A&A*, **434**, 1039

Cesaroni, R., Galli, D., Lodato, G., Walmsley, M. and Zhang, Q. 2006, *Nature*, **444**, 703

Chakraborty, A. and Anandarao, B. G. 1997, *AJ*, **114**, 1576

Chavarria, L. A., Allen, L. E., Hora, J. L., Brunt, C. M. and Fazio, G. G. 2008, *ApJ*, **682**, 445

Churchwell, E. 2002 *in Hot Star Workshop III:* The Earliest Stages of Massive Star Birth, ed. P. A. Crowther (ASP), 3

Cohen, M. and Kuhi, L. V. 1977, *PASP*, **89**, 829

Crowther, P. A. and Conti, P. S. 2003, *MNRAS*, **343**, 143

Curiel, S. et al. 2006 *ApJ*, **638**, 878

Damiani, F., Flaccomio, E., Micela, G., Sciortino, S., Harnden, F. R., Jr. and Murray, S. S., 2004, *ApJ*, **608**, 781

Davis, C. J.,G. Moriarty-schieven, G., Eisloffel, J., Hoare, M. G. and Ray, T. P. 1998, *AJ*, **115**, 1118

De Buizer, J. M., Radomski, J. T., Telesco, C. M. and Piña, R. K. 2003, *ApJ*, **598**, 1127

de Muizon Jourdain, M., d'Hendecourt, L. and Geballe, T. R. 1990, *A&A*, **227**, 526

Dent, W. R. F., Matthews, H. E. and Ward-Thompson, D. 1998, *MNRAS*, **301**, 1049

Devine, K. E., Churchwell, E. B., Indebetouw, R., Watson, C. and Crawford, S. M. 2008, *AJ*, **135**, 2095

de Wit, W. J. et al., 2009, *A&A*, **494**, 157

Dyson, J. E. and Williams, D. A. 1980, *Physics of the interstellar medium*, (New York, Halsted Press)

Egan, M. P., Shipman, R. F., Price, S. D. et al. 1998, *ApJ*, **494**, 199L

Elmegreen, B. G. and Lada, C. J. 1977, *ApJ*, **214**, 725

Elmegreen, B. G. and Starrfield, S. 1999, *A&A*, **527**, 266

Evans II, N. J. 1999, *ARA&A*, **37**, 311

Evans II, N. J., Shirley, Y. L., Mueller, K. E. and Knez, C. 2002, *In Hot Star Workshop*

III: The Earliest Stages of Massive Star Birth. ASP Conference Proceedings, **Vol. 267**, Edited by Paul A. Crowther pages 17

Evans II, N. J. et al. 2009, *ApJS*, **181**, 321

Fang, M. and Yao, Yong-Giang 2004, *ChA&A*, **28**, 308

Faundez, S., Bronfman, L., Garay, G., Chini, R., Nyman, L.-Å and May, J. 2004, *A&A*, **426**, 97

Fazio, G. G. et al. 2004, *ApJS*, **154**, 10

Felli, M., Testi, L., Valdettaro, R. and Wang, J. J. 1997, *A&A*, **320**, 594

Felli, M., Massi, F., Navarrini, A., Neri, R., Cesaroni, R. and Jenness, T. 2004, *A&A*, **420**, 553

Felli, M., Massi, F., Robberto, M. and Cesaroni, R. 2006, *A&A*, **453**, 911

Flaherty, K. M., Pipher, J. L., Megeath, S. T., Winston, E. M., Gutermuth, R. A., Muzerolle, J., Allen, L. E. and Fazio, G. G. 2007, *ApJ*, **663**, 1069

Franco, J., Tenorio-tagle, G. and Bodenheimer, P. 1990, *ApJ*, **349**, 126

Fuller, G. A., Williams, S. J. and Sridharan, T. K. 2005, *A&A*, **442**, 949

Furuya, R. S., Cesaroni, R., Takahashi, S., Codella, C., Momose, M. and Beltrán, M. T. 2008, *ApJ*, **673**, 363

Gaume, R. A., Goss, W. M., Dickel, H. R., Wilson, T. L. and Johnston, K. J. 1995, *ApJ*, **438**, 776

Georgelin, Y. M., Georgelin, Y. P. and Roux, S. 1973, *A&A*, **25**, 337

Giveon, U., Richter, M. J., Becker, R. H. and White, R. L. 2007, *AJ*, **133**, 639

Gomez, J. F., Torelles, J. M., Estalalella, R., Anglada, G., Vades-Montenegro, L. and Ho, P. T. P. 1992, *ApJ*, **397**, 492

Goto, M., Stecklum, B., Linz, H., Feldt, M., Henning, Th., Pascucci, I. and Usuda, T. 2006, *ApJ*, **649**, 299

Goudis, C. 1976, *Ap&SS*, **40**, 281

Grave, J. M. C. and Kumar M. S. N. 2009, *A&A*, **498**, 147

Greene, T. P., Wilking, B. A., Andre, P., Young, E. T., and Lada, C. J., 1994, *ApJ*, **434**, 614

Guieu, S. et al. 2009, *ApJ*, **697**, 787

Gutermuth, R. A. 2005, *Ph.D. thesis, Univ. Rochester*

Gutermuth, R. A., et al. 2008, *ApJ*, **674**, 336

Gutermuth, R. A., Megeath, S. T., Myers, P. C., Allen, L. E., Pipher, J. L. and Fazio G. G. 2009, *ApJS*, **184**, 18

Harvey, P. M. et al. 2006, *ApJ*, **644**, 307

Harvey, P. M., Merin, B., Huard, T. L., Rebull, L. M., Chapman, N., Evans II, N. J. and

Myers, P. C. 2007, *ApJ*, **663**, 1149

Hill, T., Burton, M. G., Minier, V., Thompson, M. A. et al. 2005, *MNRAS*, **363**, 405

Hill, T., Thompson, M. A., Burton, M. G., Walsh, A. J., Minier, V., Cunningham, M. R. and Pierce-Price, D. 2006, *MNRAS*, **368**, 1223

Hogerheijde, M. R., van Dishoeck, E. F. and Salverda, J. M. 1999, *ApJ*, **513**, 350

Hummer, D. G. and Storey P. J., 1987, *MNRAS*, **224**, 801

Hunter, T. R., Brogan, C. L., Indebetouw, R. and Cyganowski, C. J. 2008 *ApJ*, **680**, 1271

Hunter, T. R., Churchwell, E., Watson, C., Cox, P., Benford, D. J. and Roelfsema, P. R. 2000, *ApJ*, **119**, 2711

Israel, F. P. and Felli, M. 1978, *A&A*, **63**, 325

Jeans, J. H. 1902, *Phil. Trans. R. Soc. Lond. A*, **199**, 1

Jijina, J. and Adams, F. C. 1996, *ApJ*, **462**, 874

Johnson, C. O., Depree, C. G. and Goss, W. M. 1998, *ApJ*, **500**, 302

Keto, E. R., Welch, W. J., Reid, M. J. and Ho, P. T. P. 1995, *ApJ*, **666**, 976

Keto, E. 2002, *ApJ*, **580**, 980

Keto, E. 2002a, *ApJ*, **568**, 754

Keto, E. and Wood, K. 2006, *ApJ*, **637**, 850

Keto, E. 2007, *ApJ*, **666**, 976

Kim, kee-tae and Kurtz, S. K. 2006, *ApJ*, **643**, 978

Kirsanova, M. S., Sobolev, A. M., Thomasson, M., Wiebe, D. S., Johansson, L. E. B. and Seleznev, A. F. 2008, *MNRAS*, **388**, 729

Kleinmann, S. G., Sargent, D. G., Gillet, F. C., Grasdalen, G. L., and Joyce, R. R. 1977, *ApJ*, **215**, L79

Konigl, A. and Pudritz, R. E. 2000, *Protostars and Planets IV*, eds: Mannings, V., Boss, A. P., & Russell, S. S., **University of Arizona Press**, p 579

Krassner, J., Pipher, J. L., Sharpless, S. and Herter, T. 1982, *A&A*, **109**, 223

Krumholz, M. R., McKee, C. F. and Klein, R. I. 2005, *ApJ*, **618**, L33

Kumar, M. S. N., Bachiller, R. and Davis, C. J. 2002, *ApJ*, **576**, 313

Kumar, M. S. N., Ojha, D. K. and Davis, C. J. 2003, *ApJ*, **598**, 1107

Kumar, M. S. N. and Grave, J. M. C. 2007, *A&A*, **472**, 155

Kumar, M. S. N., Velusamy, T., Davis, C. J., Varricatt, W. P. and Dewangan, L. K. 2010, accepted in *A&A*

Kurtz, S., Churchwell, E. and Wood, D. O. S. 1994, *ApJS*, **91**, 659

Kurtz, S., Cesaroni, R., Churchwell, E., Hofner, P. and Walmsley, C. M. 2000 *Protostars and Planets IV*, (**Tucson: Univ. Arizona Press**), 299

Lada, C. J., Gull, T. R., Gottlieb, C. A. and Gottlieb, E. W. 1976, *ApJ*, **203**, 159

Lada, C. J. and Wilking, B. A. 1984, *ApJ*, **287**, 610

Lada, C. J. 1985, *ARA&A*, **23**, 267

Lada, C. J. 1987, *IAU Symposium*, **462**, 874

Lada, C. J. and Lada, E. A. 2003, *ARA&A*, **41**, 57

Lada, C. J. et al. 2006, *AJ*, **131**, 1574

Larson, R. B. and Starrfield, S. 1971, *A&A*, **13**, 190

Larson, R. B. 1998, *MNRAS*, **301**, 569

Lebrón, M., Beuther, H., Schilke, P. and Stanke, Th. 2006, *A&A*, **448**, 1037

Li, Z. Y. 2001, *ApJ*, **556**, 813

Li, Z. Y. and Nakamura, F. 2002, *ApJ*, **578**, 256

Linz, H. et al. 2009, *A&A*, **505**, 655

Longmore, S. N. and Burton, M. G. 2009, *PASA*, **26**, 439L

Lynds, B. T., and Oneil, E. J., Jr. 1982, *ApJ*, **263**, 130

Mathis, J. S. 1990, *ARA&A*, **28**, 37

Machida, M. N., Inutsuka, S. and Matsumoto, T. 2008, *ApJ*, **676**, 1088

Makovoz, D. and Marleau, F. R. 2005, *PASP*, **117**, 1113

McKee, C. F. and Tan, J. C. 2003, *ApJ*, **585**, 850

McKee, C. F. and Ostriker, E. C. 2007, *ARA&A*, **45**, 565

Meakin, C. A., Hines D. C. and Thompson, R. I. 2005, *ApJ*, **634**, 1146

Megeath, S. T. et al. 2004, *ApJS*, **154**, 367

Megeath, S. T., Wilson, T. L. and Corbin, M. R. 2005, *ApJ*, **622**, 141

Mitchell, G. F., Maillard, J. P. and Hasegawa, T. I. 1991, *ApJ*, **371**, 342

Mueller, K. E., Shirley, Y. L., Evans II, N. J. and Jacobson, H. R. 2002, *ApJS*, **143**, 469

Muench, A. A., Lada, C. J., Luhman, K. L., Muzerolle, J. and Young, E. 2007, AJ, 134, 411 *AJ*, **134**, 411

Mundy, L. G. et al. 1996, *ApJ*, **464**, 169

Neufeld, D. A. and Yuan, Y., 2008, *ApJ*, **678**, 974

Palla, F. and Stahler, S. W. 1993, *ApJ*, **418**, 414

Palau, A., Estalella, R., Ho, P. T. P., Beuther, H. and Beltrán, T. M. 2007a, *A&A*, **465**, 219

Palau, A., Estalella, R., Ho, P. T. P., Beuther, H. and Beltrán, T. M. 2007b, *A&A*, **474**, 911

Panagia, N. 1973, *AJ*, **78**, 929

Patel, N. A. et al. 2005, *Nature*, **437**, 109

Perault, M., Omont, A., Simon, G. et al. 1996, *A&A*, **315**, L165

Povich, M. S. et al., 2007, *ApJ*, **660**, 346

Pozzo, M., Naylor, T., Jeffries, R. D. and Drew, J. E. 2003, *MNRAS*, **341**, 805

Pringle, J. E. 1981, *ARA&A*, **19**, 137

Puga, E. et al. 2009, *A&A*, **503**, 107

Qin, S. L., Wang, J. J., Zhao, G., Miller, M. and Zhao, J. H. 2008, *A&A*, **484**, 361

Qiu, K., Zhang, Q., Megeath, S. T., Gutermuth, R. A., Beuther, H., Shepherd, D. S., Sridharan, T. K., Testi, L. and De Pree, C. G. 2008, *ApJ*, **685**, 1005

Rainer, J. and McLean, I. 1987, *Infrared Astronomy with Arrays*, ed. C. G. Wynn-Williams, E. E. Becklin & L. H. Good (**Honolulu: Univ. of Hawaii169**), 272

Rathborne, J. M., Jackson, J. M., Chambers, E. T., Stojimirovic, I., Simon, R., Shipman, R. and Frieswijk, W. 2010, *arXiv*, **1003**, 3193

Reach, W. T. et al. 2005, *PASP*, **117**, 978

Ridge, N. A. and Moore, T. J. T. 2001, *A&A*, **378**, 495

Robitaille, T. P., Whitney, B. A., Indebetouw, R., Wood, K. and Denzmore, P. 2006, *ApJS*, **167**, 256

Robitaille, T. P., Whitney, B. A., Indebetouw, R. and Wood, K. 2007, *ApJS*, **169**, 328

Robitaille, T. P. et al. 2008, *AJ*, **136**, 2413

Robitaille, T. P. 2008, *ASPC*, **387**, 290

Saito, H., Saito, M., Moriguchi, Y. and Fukui, Y. 2006, *PASJ*, **58**, 343

Saito, H., Saito, M., Sunada, K. and Yonekura, Y. 2007, *ApJ*, **659**, 459

Salpeter, E. E. 1955, *ApJ*, **121**, 161

Santiago-Garcia, J., Tafalla, M., Johnstone, D. and Bachiller, R. 2009, *A&A*, **495**, 169

Shepherd, D. S. and Churchwell, E. 1996, *ApJ*, **472**, 225

Shepherd, D. S. and Kurtz, S. E. 1999, *ApJ*, **523**, 690

Shepherd, D. S., Yu, K. C., Bally, J. and Testi, L. 2000, *ApJ*, **535**, 833

Shu, F. H, Adams, F. C. and Lizano, S. 1987, *ARA&A*, **25**, 23

Shull, J. M. and Beckwith, S. 1982, *ARA&A*, **20**, 163

Siess, L., Dufour, E. and Forestini, M. 2000, *A&A*, **358**, 593

Simon, M., Cassar, L., Felli, M., Fischer, J., Massi, M. and Sanders, D., 1984, *ApJ*, **278**, 170

Simon, M., Dutrey, A. and Guilloteau, S. 2000, *ApJ*, **545**, 1034

Skrutskie, M. F. et al. 2006, *AJ*, **131**, 1163

Smith, M. D. 2004, *The Origin of Stars*, **Imperial College Press**, London, p. 123

Smith, M. D. and Rosen, A., 2005, *MNRAS*, **357**, 1370

Stecklum, B., Henning, T., Eckart, A., Howell, R. R. and Hoare, M. G. 1995, *ApJ*, **445**, 153L

Stecklum, B., Henning, T., Feldt, M., Hayward, T. L., Hoare, M. G., Hofner, P. and Richter, S. 1998, *AJ*, **115**, 767

Stetson, P. B. 1987, *PASP*, **99**, 191

Su, Y. N., Liu, S. Y., Chen, H. R., Zhang, Q. and Cesaroni, R. 2007, *ApJ*, **671**, 571

Takashi, H. and Kazuyuki, O. 2009, *ApJ*, **691**, 823

Thompson, M. A., Hatchell, J., Walsh, A. J., Macdonald, G. H. and Millar, T. J. 2006, *A&A*, **453**, 1003

Trinidad, M. A. et al. 2003, *ApJ*, **589**, 386

Tody, D. 1993, *"IRAF in the Nineties" in Astronomical Data Analysis Software and Systems II*, **589**, A. S. P. Conference Ser., Vol 52, eds. R. J. Hanisch, R. J. V. Brissenden, & J. Barnes, 173

Torrelles, J. M., Gomez, J. F., Anglada, G., Estalella, R., Mauersberger, R. and Eiroa, C. 1992, *ApJ*, **392**, 616

Tothill, N. F. H., White, G. J., Matthews, H. E., McCutcheon, W. H., McCaughrean, M. J. and Kenworthy, M. A. 2002, *ApJ*, **580**, 285

Tothill, N. F. H., Gagne, M., Stecklum, B. and Kenworthy, M. A. 2008, *Handbook of Star Forming Regions Vol II*, **Astron. Soc. Pacific, Ed. B. Reipurth**

van der Tak, E. F. S. and Menten,K. M. 2005, *ApJ*, **437**, 947

van Dishoeck, E. F., Blake, G. A., Jansen, D. J. and Groesbeck,T. D. 1995, *ApJ*, **447**, 760

van Kempen, T. A., Doty, S. D., van Dishoeck, E. F., Hogerheijde, M. R. and Jørgensen, J. K. 2008, *A&A*, **487**, 975

Ward-Thompson, D. 2002, *Science*, **295**, 76

Weintraub, D. A., Kastner, J. H., Gatley, I. and Merrill, K. M. 1996, *ApJ*, **468**, L45

Weintraub, D. A. and Kastner, J. H. 1996, *ApJ*, **458**, 670

Werner, M. W. et al. 2004, *ApJS*, **154**, 1

White, G. J., Tothill, N. F. H., Matthews, H. E., McCutcheon W. H., Huldtgren M. and McCaughrean, M. J. 1997, *A&A*, **323**, 529

Whitney, B. A., Wood, K., Bjorkman, J. E. and Wolff, M. J. 2003a, *ApJ*, **591**, 1049

Whitney, B. A., Wood, K., Bjorkman, J. E. and Cohen, M. 2003b, *ApJ*, **598**, 1079

Whitney, B. A., Indebetouw, R., Bjorkman, J. E. and Wood, K. 2004, *ApJ*, **617**, 1177

Whitney, B. A. et al. 2008, *AJ*, **136**, 18

Williams, S. J., Fuller, G. A. and Sridharan, T. K. 2004, *A&A*, **417**, 115

Wolfire, M. G. and Cassinelli, J. P. 1987, *ApJ*, **319**, 850

Woodward, C. E. et al. 1986, *AJ*, **91**, 870

Woodward, C. E., Pipher, J. L., Helfer, H. L. and Forrest, W. J. 1990, *ApJ*, **365**, 252

Woolf, N. J. 1961, *PASP*, **73**, 206

Wright, E. L., Lada, C. J., Fazio, G. G., Kleinmann, D. E. and Low, F. J. 1977, *AJ*, **82**, 132

Wu, Y., Huang, M. and He, J. 1996, *A&AS*, **115**, 283W

Wu, Y., Wei, Y., Zhao, M., Shi, Y., Yu, W., Qin, S. and Huang, M. 2004, *A&A*, **426**, 503

Wynn-Williams, C. G., Becklin, E. E., Beichman, C. A., Capps, R. and Shakeshaft, J. R. 1981, *ApJ*, **246**, 801

Zhang, Q., Hunter, T. R. and Sridharan, T. K. 1998 *ApJ*, **505**, 151

Zhang, Q., Hunter, T. R., Brand, J., Sridharan, T. K., Molinari, S., Kramer, M. A. and Cesaroni, R. 2001 *ApJ*, **552**, 167

Zhang, Q., Hunter, T. R., Brand, J., Sridharan, T. K., Cesaroni, R., Molinari, S., Wang, J. and Kramer, M. 2005, *ApJ*, **625**, 864

Zhang, Q., Sridharan, T. K., Hunter, T. R., Chen, Y., Beuther, H. and Wyrowski, F. 2007, *A&A*, **470**, 269

Zinnecker, H. and Yorke, H. W. 2007, *ARA&A*, **45**, 481

List of Publications

In Refereed Journals

1. "*Spitzer*-IRAC imaging photometric study of the massive star forming region AFGL 437"
   Kumar Dewangan, L. and Anandarao, B. G. 2010, MNRAS, 402, 2583

2. "A study of the massive star forming region M8 using *Spitzer*-IRAC images"
   Dewangan, L. K. and Anandarao, B. G. 2010, accepted in MNRAS

3. "Ring-like features around young B stars"
   Kumar, M. S. N., Velusamy, T. , Davis, C. J., Varricatt, W. P. and **Dewangan, L. K.** 2010, accepted in A&A

Papers to be communicated

1. "*Spitzer*-IRAC GLIMPSE of high mass protostellar objects III.
   The outflow and driving source relationships"
   Kumar, M. S. N., **Dewangan, L. K.** and Grave, J. M. C.

2. "*Spitzer*-IRAC GLIMPSE of Ultra-Compact HII Regions:
   Physical Properties from SED modelling"
   Dewangan, L. K., Kumar, M. S. N. and Anandarao, B. G

3. "Infrared photometric study of the massive star forming region S235"
   Dewangan, L. K. and Anandarao, B. G.

Conferences, Workshops and Circulars

1. "Near-Infrared Photometric Study of Massive Star Forming Regions"
   Dewangan, L. K. and Anandarao, B. G.
   27^{th} ASI meeting (2009) at IIA, Bangalore, INDIA

2. "*Spitzer*-IRAC GLIMPSE of high mass protostellar objects
   The outflow and driving source relationships"
   Dewangan, L. K., Kumar, M. S. N. and Grave, J. M. C.
   International Workshop on Interstellar Matter and Star Formation,
   October 5–7th (2009) at Hyderabad, INDIA

3. "GCN CIRCULAR (7191) **Transient XRF 080109 / SN 2008D**: Mount Abu NIR observations"
   Dewangan, L. K., Venkat, V., Purohit, R., Jain, J., Vadawale, S. and Anandarao, B. G.

4. "GCN CIRCULAR (7321) **GRB 080212**: Mount Abu NIR observations"
   Dewangan, L. K., Venkat, V., Jain, J., Vadawale, S. and Anandarao, B. G.